

FAULT TOLERANT CONTROL OF SPACECRAFT

by

Godard

B.Eng., Aerospace Engineering, Ryerson University, 2004

M.A.Sc., Aerospace Engineering, Ryerson University, 2006

A dissertation presented to Ryerson University
in partial fulfillment of the requirements for the degree of

DOCTOR OF PHILOSOPHY

in the Program of

Aerospace Engineering

Toronto, Ontario, Canada, 2010

© Godard 2010

All rights reserved

For ... Uppa, Umma, Azra, and Ruru

AUTHOR'S DECLARATION

I hereby declare that I am the sole author of this thesis.

I authorize Ryerson University to lend this thesis to other institutions or individuals for the purpose of scholarly research.

I further authorize Ryerson University to reproduce this thesis by photocopying or by other means, in total or in part, at the request of other institutions or individuals for the purpose of scholarly research.

ABSTRACT

FAULT TOLERANT CONTROL OF SPACECRAFT

Godard, Doctor of Philosophy, Aerospace Engineering
Ryerson University, Toronto, April 2010

Autonomous multiple spacecraft formation flying space missions demand the development of reliable control systems to ensure rapid, accurate, and effective response to various attitude and formation reconfiguration commands. Keeping in mind the complexities involved in the technology development to enable spacecraft formation flying, this thesis presents the development and validation of a fault tolerant control algorithm that augments the AOCS on-board a spacecraft to ensure that these challenging formation flying missions will fly successfully. Taking inspiration from the existing theory of nonlinear control, a fault-tolerant control system for the *RyePicoSat* missions is designed to cope with actuator faults whilst maintaining the desirable degree of overall stability and performance.

Autonomous fault tolerant adaptive control scheme for spacecraft equipped with redundant actuators and robust control of spacecraft in underactuated configuration, represent the two central themes of this thesis. The developed algorithms are validated using a hardware-in-the-loop simulation. A reaction wheel testbed is used to validate the proposed fault tolerant attitude control scheme. A spacecraft formation flying experimental testbed is used to verify the performance of the proposed robust control scheme for underactuated spacecraft configurations. The proposed underactuated formation flying concept leads to more than 60% savings in fuel consumption when compared to a fully actuated spacecraft formation configuration. We also developed a novel attitude control methodology that requires only a single thruster to stabilize three axis attitude and angular velocity components of a spacecraft. Numerical simulations and hardware-in-the-loop experimental results along with rigorous analytical stability analysis shows that the proposed methodology will greatly enhance the reliability of the spacecraft, while allowing for potentially significant overall mission cost reduction.

ACKNOWLEDGEMENTS

All the hardwork and time spent at Ryerson University since September 2000 (I landed in Toronto to pursue my B.Eng. in Aerospace Engineering) has come down to this 265 page document, my Doctoral Dissertation, called Fault Tolerant Control of Spacecraft. To say I am finally relieved is an understatement. The feeling has slowly sunk in. I have earned my Ph.D degree. The work presented in this thesis has been carried out over a period of 45 months, starting September 2006, under the supervision of Dr. Krishna Dev Kumar and Dr. Bo Tan. Thank you, Dr. Kumar and Dr. Tan, for steering me towards all these interesting and challenging open problems out there, and for your ideas and suggestions that helped me make significant contributions in the field of Spacecraft Dynamics and Control. Especially Dr. Kumar: Sir, your enthusiasm is an inspiration to everyone around.

Second, I would like to take this opportunity to thank my M.A.Sc. supervisor Dr. John Enright. I was his first graduate student and he was my first graduate supervisor. You certainly top my list of most intelligent people in this world and it has been my privilege to work with you at the Space Avionics and Instrumentation Laboratory. Thank you for your invaluable help, guidance, and friendship.

Additionally, I want to thank all the members of my Ph.D defence committee: Dr. Jeffrey Yokota, Prof. Kamran Behdinan, Dr. Simant Upreti, and Dr. Puren Ouyang. I would like to thank my external examiner Prof. Chris Damaren (University of Toronto, Institute of Aerospace Studies) for reviewing my work and calling it an "*Excellent piece of work that makes many important contributions to the field of spacecraft control systems*". Coming from an established and world-renowned professor, this meant a lot.

The longest part of my life at Ryerson University has been spent at the Space Systems Dynamics and Control (SSDC) Laboratory. I have to thank all my colleagues: Dr. Youdong Pan (Sir, you've taught me Sliding Mode Control, way better than any textbook could have, thank you!), Dr. Anmin Zou, Dr. Xi Liu, Surjit Varma (thank you for implementing my control algorithm on the SAFE testbed), Junquan Li, Suketu Patel, and Daren Lee. Special mention: Tarun Patel, Geoff McVitti, and Mike Alger. I would also like to thank Noel Abreu, and Bryan Stuurman for helping me with the hardware-in-the-loop simulations and

developing an efficient experimental reaction wheel testbed. Other wannabe PhD's: Tom Dzamba (thanks for helping me out with LaTeX) and Dmitri Ignakov, thank you for those stress relieving sessions of Rainbow Six and Hawx. Mr. Karthik Narayan, thank you for all those perfect assignments which I've used as a template to study during my undergrad years. Without a doubt the next thank you must go to Dr. Sajan Abdul. Sajo, you've been a great friend and a mentor. I miss those coffee breaks, marathon movie sessions, and discussions on pretty much everything.

To all my friends in Toronto, who have always been ready to lend a helping hand, I thank you. Pavan Gopala Krishna, thanks for everything with regards to PowerPoint. You've helped me so much in getting this 265 page document crunched to 40 slides. Also, feels great to have another Manchester United supporter who is as obsessed about the club as I am. Manoj Mohanty, always up for Wandas and always ready to help, thank you. I also want to thank Kavitha, Sharanya, Raghu, and Sky for helping me sort out many problems during those trial-run's of my thesis presentation. How can I forget to thank Suhas Swamy, fellow devotee of Sachin Tendulkar, for those stress-busting Jägerbomb explorations and cinema analyses. Last, but certainly not the least, Ankit Garg, thank you brother for being there for me whenever I required any form of assistance.

Members of the TP family, especially Alfán, Noah, and Laban: thank you for consulting me when it came to academic choices and ensuring that my opinion mattered. The added pressure of being a role model for you guys ensured that I always made the right choices in life. Shifa, Afza, Afshan, Bhaiji, and Khurram: thank you for constantly checking that my motivation level never hit rock-bottom. Special thanks to my in-laws: Mr. & Mrs. Khayum and Shahid Khan, for always being a source of strength, guidance, and support. The talks we had were very helpful to me during the most trying moments.

During the course of my intellectual exile, two people deserve a very special mention, my parents, Dr. TP Nazar and Dr. Ramla Nazar. Both of you have been an unwavering source of support. I thank you for your unyielding love and the choices you've made for me earlier in my life. By prioritizing education and instilling good moral values within me, both of you have made sure that I always succeeded. Not many parents would take that bold step of investing in their son's education by sending him abroad for undergraduate

study. The astronomical sum you've paid for my fees and expenses (by working over-time and attending patients day and night) made sure that I didn't have to worry about financial stability and just concentrate on my studies. By just earning this doctoral degree, I know I've not returned those investments, but I do know that I've made you proud.

I would also like to thank my brother, an aspiring film director, Fellini. The struggles you've gone through, the rock-bottoms you've hit, only to pursue what you want in life, and the way you've overcome all of those obstacles, has been (and will be) a learning experience for me as well. Not many people can say that they've learned a lot from their younger brother, but I can proudly say that I've learned to be patient and go for my dreams even when stuck with no success for the long haul.

Finally, a huge *spasibo* to my wife, Azra, because it would have been practically impossible to do any of this without her. By persistently asking me when I will complete my thesis, she made sure that I finished the write-up in no time. Thanks for understanding and being there for me when I needed you the most. Sorry for not finding time to spend with you, but now since I am done with this thesis, I have no excuse (okay, am joking!). Thanks for putting up with a year and a half of (very) late nights, sweetheart, your love means everything. Above everything else, thank you, my love, for saying "Yes" to me about 5 years ago, and for you I continue to exist.

Contrary to the existing template of "Acknowledgements", I would like to end this section by thanking Kam Shahid. We did our undergrad together, worked in the same lab space during our M.A.Sc., submitted our master's thesis at the same time, and have been working under the same supervisor for our PhD. I was his best man and he was mine at our respective wedding ceremonies. No matter what I write about him here, nothing can do justice to the kind of support I've had from Kam during the past 8 years. Kam shares my passion for rocket science and stood by the work presented in this dissertation even when it appeared it was too simple a contribution to ever see the light of day. Thank you Kam, for keeping me sane. You are the only person who understands every bit of effort I've put in each topic presented in this dissertation. You are my best friend, finest critic, and a loyal colleague who has shaped every chapter in this dissertation with keen insight.

LIST OF PUBLICATIONS

Articles published or accepted in refereed journals:

1. Godard, Kumar, K.D., "Fault Tolerant Reconfigurable Satellite Formations Using Adaptive Variable Structure Techniques," *AIAA Journal of Guidance, Control, and Dynamics*, Vol. 33, No. 3, pp. 969-984, 2010.
2. Godard, Kumar, K.D., Tan, B., "Nonlinear Optimal Control of Tethered Satellite Systems Using Tether Offset in the Presence of Tether Failure," *Acta Astronautica*, Vol. 66, No. 9-10, pp. 1434-1448, 2010.
3. Godard, Kumar, K.D., Tan, B., "Fault Tolerant Stabilization of a Tethered Satellite System Using Offset Control," *AIAA Journal of Spacecraft and Rockets*, Vol. 45, No. 5, pp. 1070-1084, 2008.

Articles submitted to refereed journals:

1. Godard, Kumar, K.D., "Robust Station-keeping and Reconfiguration of Underactuated Spacecraft Formations," (Ref. No.: TAES-200900264, Submitted: July 30, 2009) *IEEE Transactions on Aerospace and Electronic Systems*, pp. 1-25, 2009.
2. Godard, Kumar, K.D., "Robust Attitude Stabilization of Underactuated Spacecraft Based on Sliding Mode Control," (Ref. No.: AA-S-09-00388, Submitted: June 15, 2009) *Acta Astronautica*, pp. 1-20, 2009.

Articles published in refereed conference proceedings:

1. Godard, Kumar, K.D., "A Novel Single Thruster Control Strategy for Spacecraft Attitude Stabilization," *Proceedings of AIAA Guidance, Navigation, and Control Conference*, Toronto, Canada, pp. 1-19, Aug. 2-5, 2010.
2. Godard, Kumar, K.D., "Robust Control of Underactuated Spacecraft Formations," *Proceedings of the 15th Canadian Aeronautics and Space Institute (CASI) ASTRO Conference*, Toronto, Canada, pp. 1-6, May 4-6, 2010.

3. Godard, Abreu, N., Kumar, K.D., "Fault Tolerant Attitude Control of Miniature Satellites Using Reaction Wheels," *Advances in Astronautical Sciences, Proceedings of the 20th AAS/AIAA Space Flight Mechanics Meeting - AAS 10-111*, San Diego, CA, , pp. 1-20, Feb. 14-17, 2010.
4. Godard, Kumar, K.D., Tan, B., "Adaptive Control of Tethered Satellite Systems in Presence of Tether Failure," *Proceedings of the 58th International Astronautical Congress, International Astronautical Federation*, Hyderabad, India, Vol. 6, pp. 4128-4141, Sep. 24-28, 2008.
5. Godard, Kumar, K.D., Tan, B., "Attitude Control of Spacecraft Using Space Manipulators," *Proceedings of the 9th IASTED International Conference on Control and Applications*, Montreal, Canada, pp. 45-50, May 30 - June 1, 2007.

CONTENTS

Author's Declaration	v
Abstract	vii
Acknowledgements	ix
List of Publications	xiii
List of Figures	xxi
List of Tables	xxv
Nomenclature	xxvii
Abbreviations	xxxix
1 Introduction	1
1.1 Rationale Behind Fault Tolerant Control Design	2
1.2 Ryerson University Small Satellite Program	6
1.3 Literature Review	10
1.3.1 Spacecraft Formation Control	10
1.3.2 Spacecraft Attitude Control	13
1.3.3 Tethered Spacecraft Systems	15
1.4 Fault-Tolerance in Spacecraft Systems	17
1.4.1 Fault Classification	17
1.4.2 Failure Modes in Reaction Wheels and Thrusters	18
1.4.3 Controller Reconfiguration	20
1.5 Problem Statement	22
1.6 Research Objectives	24
1.7 Main Contributions	26
1.8 Thesis Outline	29
2 Fault Tolerant Control of Spacecraft Formations	31
2.1 SFF Mathematical Model	32
2.1.1 Cartesian Coordinate Frames	32
2.1.2 Coordinate Frame Rotations	33

2.1.3	Equations of Motion	34
2.1.4	Desired Formation Geometry	35
2.1.5	External Disturbances	36
2.2	Design of Control Laws	38
2.2.1	Basics of Variable Structure Control	39
2.2.2	Control Problem	41
2.2.3	Adaptive Sliding Mode Control	44
2.2.4	Adaptive Nonsingular Terminal SMC	49
2.3	Performance Evaluation	55
2.3.1	Nominal Case	56
2.3.2	Fault Case	59
2.3.3	Quantitative Analysis	62
2.4	Summary	64
3	Control of Underactuated Spacecraft Formations	65
3.1	Design of Control Laws	66
3.1.1	System Controllability	66
3.1.2	Design of Sliding Manifold	73
3.1.3	Nonlinear Control Formulation	76
3.1.4	Stability Analysis	79
3.2	Performance Evaluation	83
3.2.1	Ideal Formation-keeping	85
3.2.2	Initial Errors and Formation Reconfiguration	88
3.2.3	Quantitative Analysis	92
3.3	Hardware-in-the-Loop Simulation	96
3.3.1	SAFE Overview	96
3.3.2	SAFE System and Mathematical Model	97
3.3.3	Experimental Results	103
3.4	Summary	106

4	Fault Tolerant Attitude Control of Spacecraft	107
4.1	Spacecraft Mathematical Model	108
4.1.1	Coordinate Frames	108
4.1.2	Spacecraft Dynamics	109
4.1.3	Attitude Kinematics	110
4.1.4	External Disturbances	112
4.1.5	Attitude Tracking	112
4.1.6	Actuator Dynamics	113
4.2	Fault-Tolerant Attitude Tracking Control Law	115
4.2.1	Design of Sliding Manifold	116
4.2.2	Control Law Formulation	117
4.2.3	Stability Analysis	118
4.3	Reaction Wheel Experimental Testbed	122
4.4	Performance Analysis - Numerical Simulation	124
4.4.1	Case I - Three Wheels in Orthogonal Configuration	126
4.4.2	Case II - Traditional Four Wheel Configuration	131
4.4.3	Case III - Four Wheels in Pyramid Configuration	137
4.5	Performance Evaluation - HIL Simulation	140
4.5.1	Case I - Three Wheels in Orthogonal Configuration	141
4.5.2	Case II - Traditional Four Wheel Configuration	147
4.5.3	Case III - Four Wheels in Pyramid Configuration	152
4.6	Summary	157
5	Attitude Control of Underactuated Spacecraft	159
5.1	Spacecraft Mathematical Model	160
5.1.1	Coordinate Frames	160
5.1.2	Spacecraft Angular Velocity	162
5.1.3	Equations of Motion	164
5.1.4	Underactuated Rigid Spacecraft Model	166
5.2	Design of Control Laws	167
5.2.1	Proposed Control Law for Fully Actuated Spacecraft	167

5.2.2	Sliding Mode Control for Underactuated Spacecraft	169
5.3	Performance Evaluation	177
5.3.1	Nominal Performance	179
5.3.2	Variations in Spacecraft Mass Moment of Inertia	182
5.3.3	Eccentricity and External Disturbances	187
5.4	Summary	190
6	Spacecraft Attitude Control Using Single Thruster	191
6.1	Spacecraft Model with Single Thruster	192
6.2	Control Laws - Single Thruster System	194
6.2.1	Design of Sliding Manifold	195
6.2.2	Control Formulation	196
6.2.3	Stability Analysis	197
6.3	Performance Evaluation	199
6.3.1	Nominal Performance	201
6.3.2	Variations in Moment of Inertia	202
6.3.3	Eccentricity and External Disturbances	205
6.4	Summary	208
7	Fault-Tolerant Control of Flexible Spacecraft	209
7.1	Proposed Tethered Satellite System	210
7.1.1	Energy Model and Equations of Motion	211
7.1.2	Offset Control Methodology	214
7.2	Design of Control Laws	216
7.2.1	Nominal Sliding Mode Control	216
7.2.2	Adaptive Sliding Mode Control	218
7.2.3	Tether Failure	221
7.3	Dynamical Features of Proposed TSS	222
7.3.1	Traveling Waves	222
7.3.2	Tether Severance	222
7.4	Performance Evaluation	223

7.4.1	Nominal Sliding Mode Control	225
7.4.2	Fault-tolerant Adaptive Control	228
7.4.3	Quantitative Analysis	236
7.5	Summary	236
8	Conclusions	239
8.1	Summary of Contributions	239
8.1.1	Fault Tolerant Reconfigurable Spacecraft Formations	240
8.1.2	Control of Underactuated Spacecraft Formations	240
8.1.3	Fault Tolerant Attitude Control of Spacecraft	241
8.1.4	Attitude Control of Underactuated Spacecraft	242
8.1.5	Spacecraft Attitude Control Using a Single Thruster	243
8.1.6	Fault Tolerant Attitude Control of Tethered Spacecraft	243
8.2	Future Work	244
8.2.1	Improved Fidelity Attitude Estimation	244
8.2.2	Experimental Validation and Prototyping	245
8.2.3	Applications	245
8.3	Concluding Remarks	246
	Bibliography	247

List of Figures

1.1	Classification of RyeSat AOCS framework based on actuator configuration.	8
1.2	Classification of RyeSat AOCS framework based on non-affine control models.	9
1.3	Schematic of RyeSat AOCS design framework.	9
1.4	Fault classification based on representation and time characteristics.	17
1.5	Schematic of the proposed fault tolerant attitude control system.	20
1.6	Schematic of a control system with actuator faults.	21
1.7	Thesis outline: The main chapters are represented by shaded boxes.	30
2.1	Geometry of orbit motion of leader and follower spacecraft.	33
2.2	Relative J_2 disturbance ($r_p = 6878$ km and $R_d = 0.5$ km).	38
2.3	Phase portrait of the double integrator under VSC.	40
2.4	Relative position errors and thrust demand for formation keeping.	56
2.5	Adaptive parameter estimates for formation keeping.	57
2.6	Tracking errors and thrust demand for formation reconfiguration.	58
2.7	Three-dimensional trajectories of the entire formation maneuver.	59
2.8	Relative position errors and thrust demand for formation keeping when thrusters degrade by 90% after 0.02 orbit.	60
2.9	Relative position errors and thrust demand for formation maneuvering when thrusters 'jam' between 1 and 2 orbits.	61
2.10	Relative position errors and thrust demand for formation keeping when thrusters 'fail' between 0.5 and 1.5 orbits.	62
3.1	Deviation of the relative position errors with no control (no J_2).	85
3.2	Controlled response for Case I (no external disturbances).	86
3.3	Controlled response for Case I (with relative J_2 disturbance).	86
3.4	Controlled response for Case II (no external disturbances).	87
3.5	Controlled response for Case II (with relative J_2 disturbance).	87
3.6	Case I with relative J_2 disturbance and initial offset errors.	89

3.7	Case II with relative J_2 disturbance and initial offset errors.	89
3.8	Case I - Formation reconfiguration from $R_d = 0.5\text{km}$ to $R_d = 1.5\text{km}$	90
3.9	Case II - Formation reconfiguration from $R_d = 0.5\text{km}$ to $R_d = 1.5\text{km}$	91
3.10	Case I - Projected circular to circular formation.	91
3.11	Case II - Projected circular to circular formation.	92
3.12	Comparison of fuel consumption (disturbance free case).	94
3.13	Comparison of fuel consumption (with relative J_2 disturbance).	95
3.14	Block diagram representation of the SAFE test-bed.	96
3.15	Block diagram representation of MATLAB and SAFE interface.	97
3.16	Configuration of thrusters on the SAFE platform.	98
3.17	Positioning of thrusters on the SAFE platform.	98
3.18	Reference frames for SAFE platform.	99
3.19	Tracking errors - Fully actuated configuration ($X_d = 0, Y_d = 0$).	103
3.20	Tracking errors - Underactuated configuration ($X_d = 0, Y_d = 0$).	104
3.21	Thruster profiles - Underactuated configuration ($X_d = 0.4, Y_d = 0.6$).	105
4.1	Geometry of orbit motion of rigid spacecraft.	109
4.2	Schematic of traditional four wheel configuration.	122
4.3	Schematic of four wheels in pyramid configuration.	123
4.4	Schematic of HIL simulation.	124
4.5	Attitude tracking errors for Case I.	127
4.6	Angular velocity errors for Case I.	128
4.7	Reaction wheels' input voltage for Case I.	129
4.8	Reaction wheels' angular speed for Case I.	130
4.9	Attitude tracking errors for Case II.	133
4.10	Angular velocity errors for Case II.	134
4.11	Reaction wheels' input voltage for Case II.	135
4.12	Reaction wheels' angular speed for Case II.	136
4.13	Angular velocity and attitude tracking errors for Case III.	138
4.14	Reaction wheel parameters for Case III.	139
4.15	HIL simulation - Controlled performance for Case I: Fault-free conditions.	142

4.16	HIL simulation - Reaction wheel parameters for Case I: Fault-free conditions.	143
4.17	Difference between the generated faulty and ideal signals.	144
4.18	HIL simulation - Controlled performance for Case I: Faulty conditions. . .	145
4.19	HIL simulation - Reaction wheel parameters for Case I: Faulty conditions.	146
4.20	HIL simulation - Controlled performance for Case II: Fault-free conditions.	148
4.21	HIL simulation - Reaction wheel parameters for Case II: Fault-free conditions.	149
4.22	HIL simulation - Controlled performance for Case II: Faulty conditions. . .	150
4.23	HIL simulation - Reaction wheel parameters for Case II: Faulty conditions.	151
4.24	HIL simulation - Controlled performance for Case III: Fault-free conditions.	153
4.25	HIL simulation - Reaction wheel parameters for Case III: Fault-free conditions.	154
4.26	HIL simulation - Controlled performance for Case III: Faulty conditions. . .	155
4.27	HIL simulation - Reaction wheel parameters for Case III: Faulty conditions.	156
5.1	Geometry of orbit motion of rigid spacecraft.	161
5.2	Comparison between the performance of the conventional control algorithm and the proposed controller for case I.	179
5.3	State space trajectories, sliding surfaces, Lyapunov derivative, and angular velocities for case I.	180
5.4	Comparison between the performance of the conventional control algorithm and the proposed controller for case II.	181
5.5	State space trajectories, sliding surfaces, Lyapunov derivative, and angular velocities for case II.	182
5.6	Controlled performance for an axis-symmetric spacecraft ($k_1 = k_2 = 0.1765$).	183
5.7	Spacecraft attitude response as affected by changes in moment inertia matrix (kg^2m). (a) $I_{xx} = 15, I_{yy} = 17, I_{zz} = 20, I_{xy} = I_{xz} = I_{yz} = 0$; (b) $I_{xx} = 15,$ $I_{yy} = 17, I_{zz} = 20, I_{xy} = 0.5, I_{yz} = 2, I_{xz} = 0.9$	184
5.8	Controlled performance for unstable gravity-gradient inertia configurations. Controller designed based on stable moment of inertias ($k_1 = 0.3, k_2 = 0.2$) applied to a spacecraft in unstable configuration with $k_1 = 0.3, k_2 = -0.2$ for Case I and $k_1 = -0.2, k_2 = -0.3$ for Case II.	186
5.9	Effects of orbital eccentricity ($e = 0.3$) - Case I.	187

5.10	Effects of orbital eccentricity ($e = 0.3$) - Case II.	188
5.11	Effects of time-varying external disturbances.	189
6.1	Thruster azimuth and elevation.	192
6.2	Controlled response for ideal attitude stabilization.	202
6.3	Controlled response for unstable gravity gradient configuration.	203
6.4	Controlled response for an axisymmetric spacecraft.	204
6.5	Effects of orbital eccentricity ($e = 0.3$) on controller performance.	205
6.6	Effects of time-varying external disturbances on RyeSat.	207
7.1	Geometry of the proposed tethered satellite system.	211
7.2	Uncontrolled response of TSS subjected to initial errors and tether failure.	224
7.3	Controlled response of TSS with tether breakage at 0.1 orbit.	225
7.4	Effect of external disturbances and tether breakage.	226
7.5	Effect of external disturbances on linear controller.	227
7.6	Controlled system response using adaptive control law - Case I.	229
7.7	Parameter estimates \hat{I}_r , \hat{C}_1 , and \hat{C}_2	229
7.8	Controlled system response using adaptive control law - Case II.	230
7.9	Parameter estimates $\hat{\eta}_1$ and $\hat{\eta}_2$	231
7.10	Range of parameters with stable solution for $\alpha'_0 = 0.1$ and 0.01	233
7.11	Range of parameters with stable solution for gains $K = 3$ and 5	233
7.12	Blockage of \bar{a}_2 attachment point is simulated at 0.1 orbit.	234
7.13	Sign reversal of \bar{a}_2 attachment point is simulated at 0.1 orbit.	235

List of Tables

1.1	Summary of on-orbit failures of thruster assemblies.	4
1.2	Summary of on-orbit failures of momentum/reaction wheels.	5
2.1	ASMC and ANTSMC parameters	55
2.2	Steady-state stabilization errors	63
2.3	Fuel-consumption per orbit	63
3.1	Leader spacecraft orbital parameters	84
3.2	Controller parameters for underactuated SFF	84
3.3	Formation-keeping steady-state errors	93
3.4	Fuel consumption comparison	93
3.5	SAFE Subsystem	97
4.1	Reaction wheel parameters.	124
4.2	Spacecraft model parameters.	125
4.3	Reaction wheel specification sheet [Kumar & Misra 2009].	140
5.1	Underactuated spacecraft - Simulation parameters	177
5.2	Controller parameters used for numerical analysis	178
5.3	Variations in spacecraft moment of inertia	183
5.4	Unstable gravity-gradient configurations	186
6.1	RyePicoSat inertia and thruster parameters.	200
6.2	Higher-order SMC parameters.	200
6.3	RyePicoSat parameters for disturbance models.	206
6.4	Disturbance torque models for RyePicoSat.	207
7.1	TSS Simulation parameters	224
7.2	Maximum tether offset requirements for various satellite systems.	237

NOMENCLATURE

List of lowercase symbols

a	semi-major axis of the reference orbit
e	eccentricity of the reference orbit
e_a	applied armature voltage (Chapter 4)
e_x	relative radial position tracking error
e_y	relative along-track position tracking error
e_z	relative cross-track position tracking error
f	viscous friction coefficient (Chapter 4)
i_a	armature current (Chapter 4)
i_l	orbit inclination of leader spacecraft
m	mass of the spacecraft (Chapter 5)
m_2	mass of the sub-satellite (Chapter 7)
m_f	mass of the follower spacecraft
n	two-body mean motion of leader spacecraft (Chapter 2 and Chapter 3)
q_v	quaternion parameters - vector component
q_4	quaternion parameters - scalar component
r_e	radius of the Earth
r_f	radial position of the follower spacecraft from the Earth centre
r_l	radial position of the leader spacecraft from the Earth centre
r_{dc}	nominal radius of the desired circular formation
r_{dpc}	nominal radius of the desired projected circular formation
t_r	reaching time
$u_{\bar{j}}$	follower spacecraft control input components, $j = x, y, z$
u_r	required control torque (Chapter 4)
v_j	reaction wheel input voltage, $j = 1, 2, 3, 4$ (Chapter 4)
x	radial separation between leader and follower spacecraft (Chapter 2)
y	along-track separation between leader and follower spacecraft (Chapter 2)
z	cross-track separation between leader and follower spacecraft (Chapter 2)

List of uppercase symbols

A	reaction wheel projection matrix (Chapter 4)
C_j	tether rigidity parameter, $j = 1, 2$ (Chapter 7)
C_L^B	direction cosine matrix
EA	tether modulus of rigidity (Chapter 7)
F_{dj}	relative perturbations due to external forces, $j = x, y, z$ (Chapter 2)
G	upper bound of external perturbations (Chapter 2)
H_{BI}^B	angular momentum vector relative to inertial frame expressed in body frame
I_r	satellite mass distribution parameter (Chapter 7)
J_2	second zonal harmonic coefficient of the Earth's gravity field
J_s	moment of inertia of the spacecraft (Chapter 4)
J_w	axial moment of inertia of the reaction wheels (Chapter 4)
K_b	motor back-EMF constant (Chapter 4)
K_t	motor torque constant (Chapter 4)
L	distance of the auxiliary mass from the satellite mass center (Chapter 7)
L_a	armature inductance (Chapter 4)
L_j	stretched tether lengths, $j = 1, 2$ (Chapter 7)
L_{j0}	unstretched tether lengths, $j = 1, 2$ (Chapter 7)
L_{ref}	reference length (Chapter 7)
M	mass of the main satellite (Chapter 7)
N	control force saturation limit (Chapter 2 and Chapter 3)
N_c	coulomb friction coefficient (Chapter 4)
Q_q	generalized force components corresponding to the generalized coordinate q
S	sliding surface
S_u	underactuated sliding surface (Chapter 5)
S_{1T}	sliding surface for single thruster (Chapter 6)
T	orthogonal state transformation matrix (Chapter 3)
T	kinetic energy function (Chapter 5)
T_{IB}	rotation matrix to transform from the ECI frame to orbital frame
U_p	potential energy function (Chapter 5)

List of Greek symbols

α	spacecraft pitch angle
β	in-plane tether swing angle (Chapter 7)
γ	spacecraft yaw angle
δ	sliding surface boundary layer
ε_j	tether strains in the j -th tether (Chapter 7)
ζ	damping ratio (Chapter 4)
η	positive design scalar to determine sliding surface reaching time
θ	true anomaly
Λ_i	lagrange multiplier for the i -th constraint (Chapter 7)
λ_{min}	minimum eigenvalue
μ_e	geocentric gravitational constant of the Earth
ρ	adaptive gain (Chapter 4)
ρ_j	scalar constants, $j = 1, 2, 3, 4$ (Chapter 3, Chapter 5, and Chapter 6)
σ	linear sliding manifold (Chapter 4)
τ	control torque
τ_d	external disturbance torque (Chapter 4)
τ_f	friction torque (Chapter 4)
τ_g	gravity gradient torque
τ_m	motor torque (Chapter 4)
Φ	principal angle of rotation in Euler's theorem (Chapter 4)
ϕ	spacecraft roll angle
ϕ	in-plane formation phase angle (Chapter 2 and Chapter 3)
φ_j	control gains, $j = 1, 2, 3, 4$
Ω	axial angular velocity of reaction wheels
Ω_l	right ascension of the ascending node of leader spacecraft orbit
ω_0	magnitude of orbital angular velocity of LVLH frame (Chapter 4)
ω_{BI}^B	angular velocity vector relative to inertial frame expressed in body frame
ω_l	argument of perigee of leader spacecraft orbit
ω_n	natural frequency (Chapter 4)

List of reference frames

$\mathfrak{B} - xyz$	spacecraft body-fixed coordinate frame
$\mathfrak{J} - XYZ$	Earth centered inertial reference frame
$\mathfrak{L} - x_o y_o z_o$	local vertical local horizontal orbital reference frame
$S - XY$	SAFE platform inertial reference frame
$S - xy$	SAFE platform body-fixed reference frame

Notational conventions

$ \cdot $	absolute value
$\ \cdot\ $	Euclidean norm for vectors, induced norm for matrices
$(\cdot)_0$	(\cdot) at $t = 0$
$(\dot{\cdot})$	derivative of (\cdot) with respect to time, t
$(\cdot)'$	derivative of (\cdot) with respect to θ
$(\hat{\cdot})$	parameter estimate
$(\tilde{\cdot})$	parameter estimation error
$[a^\times]$	skew-symmetric matrix for vector a

ABBREVIATIONS

ACS	Attitude Control System
AOCS	Attitude and Orbit Control System
ASMC	Adaptive Sliding Mode Control
CW	Clohessy-Wiltshire
ECI	Earth Centered Inertial
EMF	Electromotive Force
FDI	Fault Detection and Isolation
FTC	Fault Tolerant Control
FTCS	Fault Tolerant Control System
FUSE	Far Ultraviolet Spectroscopic Explorer
GN&C	Guidance, Navigation, & Control
HIL	Hardware-In-Loop
LEO	Low Earth Orbit
LIP	Lock in Place
LOE	Loss of Effectiveness
LVLH	Local Vertical Local Horizontal
MTB	Magnetic Torquer Bars
NTSM	Nonsingular Terminal Sliding Mode
RWA	Reaction Wheel Assembly
SAFE	Satellite Airbed Formation Experiment
SDRE	State Dependant Riccati Equation
SFF	Spacecraft Formation Flying
SSDC	Space Systems Dynamics and Control
SMC	Sliding Mode Control
TSM	Terminal Sliding Mode
TSS	Tethered Satellite Systems
VSC	Variable Structure Control

CHAPTER 1

Introduction

AUTONOMOUS on-orbit position maintenance and attitude control of spacecraft is one of the most rapidly-growing innovative field that can implement cross-cutting technologies to significantly enhance future Earth and space-observing missions. The *Attitude and Orbit Control System* (AOCS), the heart of spacecraft, consists of various types of sensors, actuators, and control electronics (on-board computer). The control electronics process attitude and orbit information of the spacecraft from sensors and based on available on-board algorithms, control signals are generated for actuators to correct any attitude and/or orbit errors. Most of the earlier and current spacecraft AOCS generally employ redundant actuators and sensors to achieve required reliability utilizing various control algorithms. These conventional feedback control designs may result in unsatisfactory performance and instability, in the event of unexpected malfunctions in actuators. To prevent fault induced losses and to minimize the potential risks associated with mission failure, new control techniques need to be designed to cope with actuator faults whilst maintaining the desirable degree of overall stability and performance. A control system that possesses such a capability is often known as a *Fault Tolerant Control System*.

Future spacecraft will be expected to achieve high-precision pointing, formation flying, and optimal slew maneuvers from large initial conditions and in the presence of large environmental and non-environmental disturbances, measurement noise, large modeling uncertainties, actuator failures, and hardware as well as software constraints. With increasing demand for performance and capability, and an increasing awareness about risks associated with system malfunction, fault tolerance is becoming an essential concern in spacecraft AOCS design. Redundancy is a widely used approach for integrating mission safety with control hardware failures. Due to increasing mission demands and stringent constraints on weight, power, and cost of small satellites, providing full hardware redundancy for all

actuators is difficult. In order to overcome these limitations, this thesis investigates the methodologies required to design and incorporate a fault tolerant control (FTC) system that performs its functions autonomously despite failures. An efficient design framework that accepts the inevitability of failures and counteracts the effect of failures through functional redundancy is proposed for autonomous fault recovery of small satellites.

1.1 Rationale Behind Fault Tolerant Control Design

Anomalies categorized by spacecraft subsystems show that Guidance, Navigation, and Control (GN&C) subsystems have higher number of anomalies that result in a mission critical failure when compared to other subsystems [Robertson & Stoneking 2003, Hall 2003]. A mission critical failure is defined as a premature loss of a spacecraft or loss of its ability to perform its primary mission during its design life. Two examples where minor actuator faults have lead to complete loss of spacecraft are stated below:

1. NASA's Earth orbiting Lewis Spacecraft was launched on August 23, 1997, for measuring changes in Earth's land surfaces. Contact with the spacecraft was lost on August 26; it then reentered the atmosphere and was destroyed on September 28 [NASA 1998]. The investigation board report stated that the spacecraft failed mainly due to a technical flaw in the attitude control system design causing excessive thruster firings that lead to the shutdown of all thrusters, leaving the spacecraft in an uncontrolled attitude draining most of its battery charge [NASA 2007].
2. The US Department of Defense developed the NAVSTAR GPS constellations that employed 24 satellites in orbit around the Earth to provide weather and navigation capabilities for military. All satellites were 3-axis stabilized, nadir pointing, using reaction wheels. One spacecraft, GPS BII-07, suffered a reaction wheel failure that lead to 3-axis stabilization failure and total loss of spacecraft [Robertson & Stoneking 2003].

Tables 1.1 and 1.2 summarize various on-orbit failures of thruster assemblies and momentum/reaction wheels. More than half a century into the Space Age, actuators on-board spacecraft are still prone to failures. One question that can be drawn from the above examples is that - *“While some degree of random failure is inevitable, could something have*

been done to minimize the consequences of failure or, at least, their severity (in terms of economic losses, control dexterity, etc.)?”

Given the fact that only limited time and information may be available, the nature and location of actuator faults could be detected and diagnosed in many cases. This provides an opportunity to reconfigure the control system so that sufficient degree of attitude and orbit control dexterity is introduced to ensure overall spacecraft stability. A cost effective way to obtain increased reliability and safety in automated systems is to introduce FTC. The basic implementation strategy of FTC involves the design of an ‘intelligent’ software that monitors behavior of components such that local faults are prevented from developing into failures that can lead to total mission loss. Many FTC algorithms have been developed in practice and applied to real spacecraft.

1. Far Ultraviolet Spectroscopic Explorer (FUSE) satellite was at the peak of its scientific productivity when hardware problems caused the loss of two of its four reaction wheels required for attitude control. The pitch and yaw wheels despun due to excessive friction between the rotors and wheel housings [Kruk *et al.* 2002b]. Engineers reprogrammed the control software by developing a new control law, integrating the Magnetic Torquer Bars in the control loop along with the remaining two reaction wheels, and fine pointing capability was reestablished [Roberts *et al.* 2004].
2. After one year of perfect operation in space, controllers at the Surrey Space Centre observed a sudden change to the attitude dynamics of the CERISE microsatellite as it tumbled rapidly after collision with a piece of space debris in its 700 km polar Earth orbit. The ground engineers analyzed the collision dynamics and reprogrammed the on-board computers with novel magnetic control algorithms to re-stabilize the microsatellite and regain full operational mission capability [Sweeting *et al.* 2004].

With increasing emphasis placed on reliability and safety, examples described above clearly motivate the need for development of robust FTC algorithms capable of overcoming actuator faults to prevent mission failure. AOCS are becoming more and more sophisticated with increasingly complex system configurations. Controlling these systems under a wide variety of operating conditions autonomously is a challenging task.

Table 1.1: Summary of on-orbit failures of thruster assemblies.

Spacecraft	Cause of Anomaly	Impact	Reference
Galaxy 8i	During September 2000, three of four xenon ion thrusters failed.	Shortened life	[Robertson & Stoneking 2003]
Iridium 27	During September 1997, thruster anomaly depleted operational fuel.	Total loss	[Robertson & Stoneking 2003]
Nozomi	During December 1998, thruster valve was stuck partially open and the propulsion system consumed more fuel than expected during Earth swingby.	Mission interruption	[Robertson & Stoneking 2003]
JCSat-1B	During January 2005, the spacecraft experienced attitude loss during maneuver due to thruster anomaly.	Mission Interruption	[Crosby 2009]
EchoStar VI	During April 2001, the spacecraft was hit by one or more micrometeorites, in its attitude control system causing a propellant leak in one of the thrusters.	Mission Interruption	[Tafazoli 2005]

Table 1.2: Summary of on-orbit failures of momentum/reaction wheels.

Spacecraft	Cause of Anomaly	Impact	Reference
Radarsat-1	During September 1999, the primary pitch momentum wheel failed due to excessive friction and temperature.	Mission degradation	[Kim & Deraspe 2003]
TOPEX	During October 2005, the satellite could not perform attitude maneuvers due to the failure of pitch reaction wheel	Total loss	[sat nd 2009]
EchoStar V	During July 2001, one of the three momentum wheels onboard the ACS failed.	Mission interruption	[Tafazoli 2005]
GOES-9	During July 1998, a momentum wheel onboard was drawing high current resulting in hot operating conditions.	Total loss	[Tafazoli 2005]
GPS BI-05	Wheel no. 2 and 3 stopped completely with full motor voltage applied.	Total loss	[Tafazoli 2005]

1.2 Ryerson University Small Satellite Program

Micro and small satellite designs have revolutionized space engineering techniques to complement the interests of both academic institutions and industry partners. Pressure on financial budgets, coupled with rapid advancement of micro-technology, has catalyzed the development of small specialized satellites that are faster and cheaper to produce despite the limitations they place on the mission [Ludwig 1967]. Anticipating further advances in miniaturization, the *Space Systems Dynamics and Control* (SSDC) laboratory at *Ryerson University*, established in September 2005 under the supervision of *Dr. K.D. Kumar*, focuses primarily on the design and development of small satellites to pursue an active space initiative. The overall objective is to advance research on miniature satellite design with the ultimate goal of developing formations of autonomous small satellites to realize space missions - complementing the conventional large satellites that perform large-scale space science missions.

The *RyeSat* program includes the design and development of the following miniature satellites: (1) 350 gm can-sized satellite (*RyeCanSat*), (2) 1 kg pico-sized satellite (*RyePicoSat*), and (3) 100 gm femto-sized satellite (*RyeFemSat*). The design of *RyeCanSat* has been completed and it has undergone flight testing using a balloon and a rocket to an altitude of 3000 ft [Alger & Kumar 2008]. *RyePicoSat* is an effort to bring knowledge gained thus far from the *RyeCanSat* into a modular university satellite, allowing for the continuous improvement of individual subsystems while retaining the ability to utilize older space-qualified components. *RyePicoSat* is proposed for *Ryerson Pico-satellite Formation Flying Experiment* missions.

The primary objective of this thesis is to augment the *RyeSat* AOCS design by developing FTC algorithms that provides autonomous recovery from actuator faults. We approach this goal by systematically categorizing *RyeSat* based on actuator configurations as follows:

1. *Redundant Actuator Configuration*: For high performance space missions, the total number of actuators used may be greater than the number of states to be precisely controlled. Control redundancy is typically preferred to ensure optimality with respect to control effort. Also, the spacecraft attitude and orbit can be precisely con-

trolled even if some of the actuators fail, as long as the number of active actuators are greater than or equal to the number of states to be controlled.

2. *Underactuated Configuration*: Failure of more than one actuator can make the spacecraft underactuated. These spacecraft are characterized by the fact that they have fewer actuators than the degrees of freedom to be controlled. The objective is to utilize the dynamic coupling between the directly actuated states and unactuated states to develop a control algorithm that counteract the effects of actuator failure.

Consider the following class of systems having a state model nonlinear in the state vector x and linear in the control vector u ,

$$\dot{x} = f(x, t) + B(x, t)u \quad (1.1)$$

where $x \in \mathbb{R}^n$ is the state vector, $f(x, t) \in \mathbb{R}^n$ represents the nonlinearity of the system, $B(x, t) \in \mathbb{R}^{n \times m}$ is the input matrix, and $u \in \mathbb{R}^m$ is the control vector. The dynamical system described by Eq. (1.1) can be classified based on actuator configuration as follows:

- Redundant actuation: If $m > p$, the number of control inputs regulating the system in Eq. (1.1) is more than the number of degrees of freedom to be controlled (p).
- Underactuated: If $m < p$, then for the system in Eq. (1.1) with p degrees of freedom, only m states are actuated, and $p - m$ degrees of freedom are unactuated.

The system given by Eq. (1.1) represents a nonlinear plant model that is *affine* in the control input vector u , that is, characterized by u appearing linearly in the state equation.

Based on actuator configurations and affine nature of the control input, we classify the RyeSat AOCS design goals as follows:

1. *Orbit Control*. The translational dynamics of two RyeSat (point masses) are examined in a leader-follower formation configuration. First objective is to develop a FTC algorithm for demonstrating high precision orbit maintenance and formation reconfiguration in the presence of actuator faults. Next, the RyeSat formation is examined in an underactuated configuration to control the relative positions between spacecraft using reduced inputs.

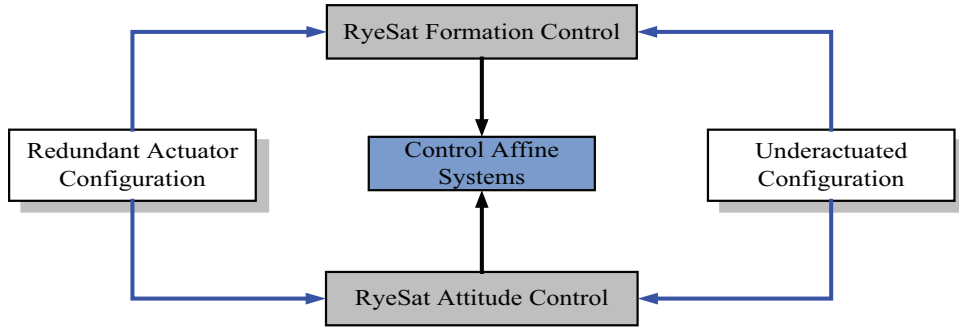


Figure 1.1: Classification of RyeSat AOCS framework based on actuator configuration.

2. *Attitude Control.* The rotational dynamics of RyeSat (rigid body) are examined to develop a fault tolerant attitude control algorithm to demonstrate rapid attitude acquisition, tracking, and pointing capabilities using a redundant reaction wheel configuration. The spacecraft is also evaluated in an underactuated configuration where the attitude control objectives have to be achieved using less than three control inputs.

The inter-link between formation control and attitude control based on underactuated and redundant actuator configurations are shown using a schematic diagram in Fig. 1.1. The problem of controlling spacecraft characterized by models that are non-affine in the control input is a difficult one. Consider the following class of systems having a state model nonlinear in the state vector x and nonlinear in the control vector u ,

$$\dot{x} = f(x, t) + Bg[u(t)] \quad (1.2)$$

where $x \in \mathbb{R}^n$ is the state vector, $f(x, t) \in \mathbb{R}^n$ represents the nonlinearity of the system, $B \in \mathbb{R}^{n \times m}$ is the input matrix, $u \in \mathbb{R}^m$ is the control vector, and $g[u(t)]$ is the nonlinear control input function. The main difficulty in determining the control input for this case arises from the fact that $u(t)$ appears in Eq. (1.2) in a nonlinear fashion.

Scope of this thesis also includes investigating the attitude control problem of RyeSat driven by nonlinear actuators. Within this classification of non-affine control models the main contributions are: (i) a novel attitude control methodology using a single thruster is proposed, and (ii) fault tolerant control of RyeSat in tethered configuration is investigated. Using a single thruster for attitude control by changing the thruster gimbal angles constitutes a non-affine system in underactuated configuration. The tethered RyeSat controlled

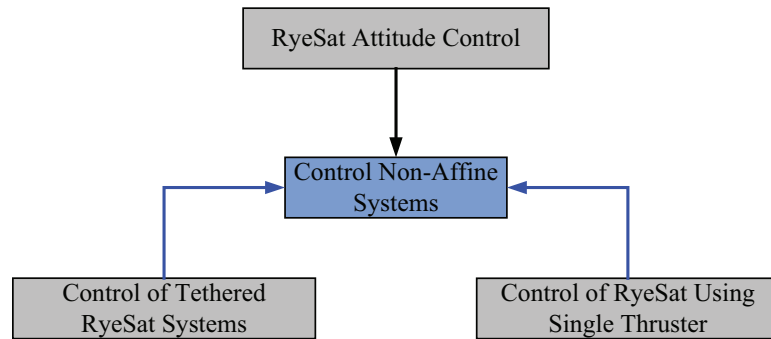


Figure 1.2: Classification of RyeSat AOCS framework based on non-affine control models.

using tether attachment points is a non-affine system in redundant actuator configuration. This classification is shown in Fig. 1.2. Finally, the classifications outlined in Figs. 1.1 and 1.2 can be combined to provide a schematic of RyeSat AOCS design framework from the perspective of this dissertation. The overall framework relating the system interconnections to actuator configurations and control models (affine and non-affine) is shown in Fig. 1.3.

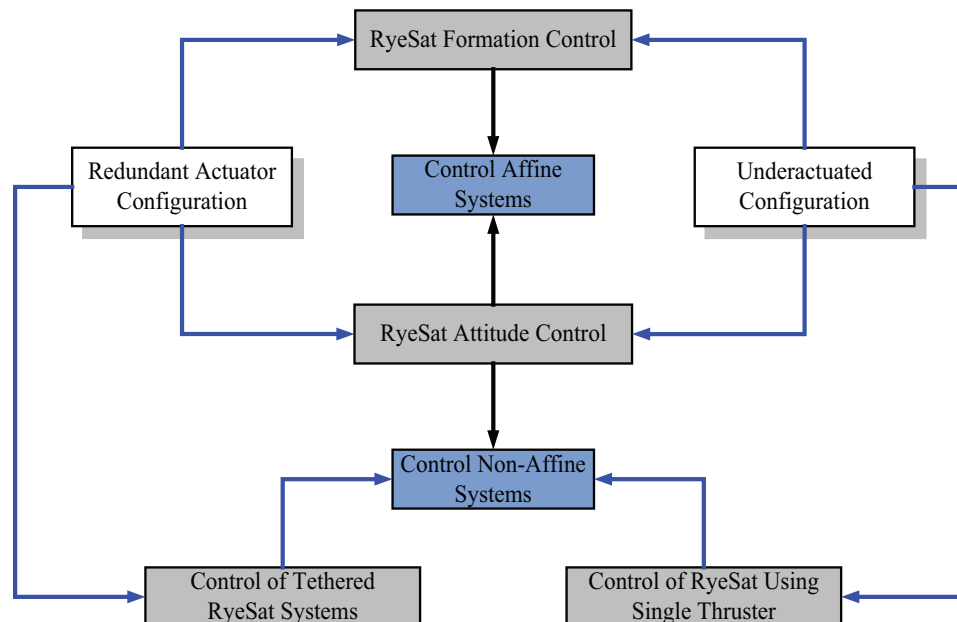


Figure 1.3: Schematic of RyeSat AOCS design framework.

1.3 Literature Review

Recent advances in micro and nanotechnology have succeeded in changing the focus of aerospace industry toward smaller, lower-cost spacecraft design [Rycroft & Crosby 2001]. Scientific payloads onboard a spacecraft for Earth observation and space monitoring rely on the AOCS to orient the spacecraft towards a prescribed direction with high accuracy. As a consequence, AOCS actuator failure still represents one of the most serious threats to spacecraft operations. Control reconfiguration in the event of actuator faults depends entirely on the mode of spacecraft operation, namely, (i) orbit control, and (ii) attitude control. This section places the objectives of this thesis in perspective with state-of-the-art control techniques available in the current literature for spacecraft formation control using thrusters, and spacecraft attitude control using reaction wheels, thrusters, and tethers.

1.3.1 Spacecraft Formation Control

Spacecraft formation flying (SFF) has been identified as an enabling technology for many future space missions [Neeck *et al.* 2005]. The functionality of a single, complex spacecraft can be distributed between a cluster of smaller, closely flying spacecraft. Formation flying typically involves active, real-time, closed-loop control of multiple, cooperating satellites in autonomous formation [Folta *et al.* 2002]. Thus, unlike station-keeping, where a satellite's position is controlled relative to a desired orbit, formation-keeping involves the control of one or more satellites relative to another satellite. Over the past decade, several theoretical investigations pertaining to accurate SFF relative motion models, formation trajectory generation, and formation control have been reported in the literature.

Dynamics and Modeling

The design of control methodologies for SFF relies heavily on the dynamics of relative motion of satellites within a cluster. Several investigations have considered linearized relative motion equations in a Cartesian coordinate frame, called the Hill's equations [Hill 1878] or the Clohessy-Wiltshire (CW) equations [Clohessy & Wiltshire 1960]. The Hill's equations have also been extended to elliptic Keplerian orbits discarding orbital perturbations. These models are called the Lawden equations [Lawden 1954] or Tschauner-Hempel equa-

tions [Tschauner 1967]. Other approaches for modeling spacecraft formations are orbit element differences [Schaub *et al.* 1999] and Theona theory [Golikov 2003].

To design formation flying architectures for LEO it is important to consider relative effects caused by nonlinearity of the model, eccentricity effects, and the disturbance forces (Earth's gravitational field, atmospheric drag, and solar radiation pressure). For LEO, the most significant perturbation arises from the second zonal harmonic (J_2) of the Earth's non-spherical geopotential [Chobotv 2002]. Ignoring these perturbations leads to formation designs that require more frequent corrections, and thus more fuel [Schaub & Junkins 2003].

Several analytical and numerical solutions to achieve relative orbit periodicity can be found in the current literature. Spacecraft formation initialization for eccentric reference orbits [Inalhan *et al.* 2002] and conditions accommodating corrections due to nonlinearity as well as eccentricity [Vaddi *et al.* 2003, Gurfil 2005, Xing *et al.* 2007] result in naturally periodic relative orbits. Schaub and Alfriend [Schaub & Alfriend 2001] developed J_2 invariant relative orbits for formation flying using differences in mean orbit elements. Coupled linearized differential equations with constant coefficients capturing the effects of J_2 potential was presented by Schweighart and Sedwick [Schweighart & Sedwick 2002]. Third-order analytical solutions to describe nonlinear periodic motions in Hill's frame has been considered in [Richardson & Mitchell 2003]. An iterative shooting approach (numerical) based on the Newton method has been utilized to formulate "almost" periodic [Damaren 2007] and quasi-periodic [Eyer & Damaren 2009] closed relative trajectories for SFF under the influence of $J_2 - J_6$ gravitational perturbations.

Controller Design - Fully Actuated

Several control algorithms based on traditional linear and nonlinear control methods have been utilized for precise tracking of spacecraft formations. Control schemes related to linear feedback theory are not within the scope of this thesis and readers are referred to [Kristiansen & Nicklasson 2009] and [Scharf *et al.* 2004] for a consolidated literature review on various linear and nonlinear control techniques applied to formation control. Within the nonlinear control framework, several techniques such as robust control [Hu & Ng 2007, Xu *et al.* 2007], Lyapunov based nonlinear feedback control [Vaddi & Vadali 2003, Yan *et al.* 2000, Vignal & Pernicka 2006], sliding mode control (SMC) [Yeh *et al.* 2002,

Massey & Shtessel 2005, Liu *et al.* 2006], state-dependant Riccati equation (SDRE) control [Stansbery & Cloutier 2000, Won & Ahn 2003], and adaptive control [Hadaegh *et al.* 1998, de Queiroz *et al.* 2000, Wong *et al.* 2002, Pongyithum *et al.* 2005] have been proposed to deal with system nonlinearities, model uncertainties, and external disturbances.

As yet, only very few research papers account for unexpected actuator faults [Ren & Beard 2004, Lim & Bang 2009]. Precise control of relative positions and velocities of several spacecraft in formation is a challenging task when considering actuator failures that can destabilize the formation geometry. For autonomous coordinated control during formation flying, robust performance and fault tolerance of the controllers are key issues that need to be addressed.

Controller Design - Underactuated

SFF can be evaluated as an underactuated system if the configuration of thrusters (characterized by the failure of one or more pair of thrusters) cannot provide three independent control thrusts in the radial, along-track, and cross-track directions, respectively. Vadali *et al.* [Vadali *et al.* 2008] have shown that a 50% reduction in along-track control acceleration can be achieved without the use of radial thrust, for circular reference orbits. Spacecraft formation flying using no radial thrust has been examined previously based on linearized Hill's equations. The feasibility of using only along track input in the form of differential drag between two spacecraft as the means for controlling their relative positions was examined in [Leonard *et al.* 1989]. This method was improved by [Bevilacqua & Romano 2008] by proposing a two-phase control method using differential drag for rendezvous maneuvers. LQR with no radial axis inputs using thrusters was implemented by [Starin *et al.* 2001a]. A novel proportional linear controller using only along track thrust has been developed to achieve bounded relative position errors [Kumar *et al.* 2007].

Theoretical proofs that are important for investigating the underlying system dynamics and establishing closed-loop stability conditions has not been developed in the current literature. If the relative orbit chosen is large enough to create substantial errors between the linear and nonlinear relative equations of motion, linear control algorithms guarantees only local stability. External perturbations will produce a differential force along the uncontrolled axis which cannot be compensated using linear control algorithms.

1.3.2 Spacecraft Attitude Control

The low-cost microsatellite paradigm requires the design of attitude control systems capable of providing rapid attitude acquisition, tracking, and pointing capabilities, while the equations that govern large-angle maneuvers are highly coupled and nonlinear. Scientific payloads onboard a spacecraft for Earth observation and space monitoring rely on the attitude control system to be oriented towards a prescribed direction with high accuracy.

Controller Design - Fully Actuated

Precise attitude control in the presence of environmental disturbances, uncertain nature of spacecraft dynamical systems, and actuator saturation have attracted considerable research interest in the existing literature. Several control methodologies have been proposed, such as nonlinear feedback control [Wen & Kreutz-Delgado 1991, Xing & Parvez 2001], variable structure control (VSC) [Vadali 1986, Crassidis & Landis Markley 1996], adaptive VSC [Boskovic *et al.* 2004, Wallsgrove & Akella 2005], inverse optimal control [Bharadwaj *et al.* 1998, Krstic & Tsiotras 1999, Luo *et al.* 2005], and robust control [Ahmed *et al.* 1998, Li *et al.* 2010].

With respect to attitude actuator failures, control reconfiguration techniques existing in the current literature rely on fault detection and isolation (FDI). Several attitude control algorithms that implement a retrofit FDI component have been proposed for counteracting faults in thrusters [Bošković *et al.* 1999, Chen & Saif 2007] and reaction wheels [Tudoroiu & Khorasani 2007, Jin *et al.* 2008]. FDI approaches that require system redesign are fairly complex and depends strongly on the efficacy of the fault detection algorithm. Also, explicit failure identification requires substantial onboard computational resources. An alternative approach to reconfigurable ACS design is based on adaptive control theory where the controller parameters are constantly updated based on adaptive estimates of the altered dynamics after failure [Tandale & Valasek 2006]. An adaptive approach to attitude tracking control of spacecraft was presented by Cai *et al.* [Cai *et al.* 2008] to account for various thruster faults. Jiang *et al.* [Jiang *et al.* 2010] proposed an adaptive FTC scheme for attitude tracking of flexible spacecraft to counteract the effects of reaction wheel failures.

Although various nonlinear and adaptive control schemes have been proposed for fault-tolerant attitude control of spacecraft, none of the literature discussed above have experi-

mentally validated the performance of the algorithms on a reaction wheel assembly (RWA) or thrusters. It is important to include high fidelity mathematical models of actuators to understand the effects of actuator parameters on overall system performance.

Controller Design - Underactuated

Real-time FDI algorithms and passive FTC approaches for spacecraft attitude control are modeled based on the assumption that the spacecraft is equipped with redundant actuators. Despite the failure of actuators, adaptive control techniques can be used to generate three independent control torques using the remaining functional actuators. Therefore, it is still possible to efficiently track the attitude of the spacecraft using a reconfigurable control methodology. However, the problem becomes more challenging if the control system can deliver torque components about two axes only due to failure of one or more actuators.

Assuming that the failure can be detected, 3-axis stabilization is still possible by reconfiguring to a control algorithm that utilizes only two torque components. Researchers have treated this problem in the Earth Centered Inertial (ECI) frame of reference. In this case, Brockett's theorem [Brockett 1984] must be addressed and control methods that can avoid Brockett's condition is necessary. If the problem is treated in the ECI frame, the spacecraft undergoes attitude motion without considering its orbital motion around the Earth. Therefore, the angular velocity components would converge to zero if the spacecraft is 3-axis stabilized. Several control algorithms have been proposed for attitude control of rigid spacecraft using only two control torques.

The initial focus attributed only to the stabilization of angular velocities of a rigid spacecraft with less than three control torques [Brockett 1984, Aeyels 1985, Sontag & Sussmann 1988, Morin 1996, Shen & Tsiotras 1999]. The objective is to null the angular velocity vector of the spacecraft. Stabilization of the complete set of attitude system, i.e., dynamics combined with kinematics is a much more difficult problem, and it has been addressed in [Byrnes & Isidori 1991, Krishnan *et al.* 1994, Tsiotras *et al.* 1995, Coron & Keraï 1996, Morin & Samson 1997, Han & Pechev 2009]. The objective is to stabilize a spacecraft about a desired attitude using control torque components about two axes only. Readers can refer to [Tsiotras & Doumchenko 2000] for a complete literature survey of spacecraft attitude control methods using reduced inputs.

Most of the existing literature on spacecraft attitude control using reduced inputs do not consider the torque due to Earth's gravity and the effects of external disturbances and modeling uncertainties. The gravity gradient torque can significantly effect the motion of the spin axis of a non-symmetric spacecraft in a precessing LEO [Harding 1966]. For low-cost missions the possibility of handling actuator failures without the need for redundant elements is even more appealing; the actuator system remains minimal and, assuming that the failure can be detected, a sufficient degree of attitude dexterity may be available at the negligible cost of a control law reconfiguration, provided that the resulting maneuver accuracy is compatible with mission constraints.

1.3.3 Tethered Spacecraft Systems

Spacecraft often require reaction wheels, control moment gyros, and reaction control jets as means of actuators for the ACS, to meet 3-axis pointing requirements. The idea of utilizing lightweight deployable tether can alleviate the requirement for other attitude control system elements. The Smithsonian Astrophysical Observatory and the Italian space industry Alenia Spazio conducted a study to test the use of tethers as a backup concept for stabilizing the attitude of a large space station for NASA. They claimed that the main benefits of the system are: (1) simplicity, (2) relatively low cost, and (2) reusability [van Pelt 2009].

The dynamics and control aspects of single tether systems have been studied extensively by several researchers in the last two decades [Beletsky & Levin 1993]. The control of two tether systems has received little focus compared to that of single tether systems, mainly due to the added complexity of having two-reel mechanisms. However, the ability to provide superior control of the motion of the subsatellite using two tethers, coupled with the benefit of redundancy in case of tether severance suggests that a two tether system may present some significant advantages and unique mission opportunities.

An excellent review of the dynamics and control aspects of TSS is available in [Kumar 2006b]. A comprehensive review of the earlier work on tethered satellites was treated by Misra and Modi, focusing primarily on single-tether two-body systems [Misra & Modi 1983, Misra & Modi 1986]. In the presence of an offset between the tether attachment point and the mass center of the end satellite, termed the tether

offset, the satellite experiences additional moments, and its attitude motion becomes coupled to that of the tether librational motion [Modi 1990]. Several linear and nonlinear control algorithms have been developed for regulating tether attachment points to enable attitude control [Fan & Bainum 1988, Kline-Schoder & Powel 1993, Kumar & Nakajima 2000, Modi *et al.* 1991, Modi *et al.* 1992, Pradhan *et al.* 1999, Grassi & Cosmo 1996, Modi *et al.* 1998, Kumar & Kumar 2001]. The choice of tether offset has a significant effect on the system transient response [Bainum *et al.* 1985]. The effectiveness of offset control scheme was also validated by [Modi *et al.* 1990] through a ground-based experiment.

Several interesting space applications of tethers have been proposed and several missions have been flown [Cosmo & Lorenzini 1997]; some missions were successful and others were unsuccessful. The major successful missions include the Canadian Space Agency's observation of Electric-Field Distributions on the Ionospheric Plasma-A Unique Strategy (OEDIPUS) missions: OEDIPUS-A in 1989 [Tyc & Han 1995] and OEDIPUS-C in 1995 [Tyc *et al.* 1997], NASA's Small Expendable Deployer System (SEDS) missions: SEDS-1 in 1993 and SEDS-2 in 1994 [Smith 1995], NASA's Plasma Motor Generator (PMG) experiment in 1993 [Jost & Chlouber 1995], and the U.S. Naval Research Laboratory's tether physics and survivability (TiPS) in 1996 [Purdy *et al.* 1997].

Despite of the significant achievements, there are still many open problems of theoretical and practical importance to realize a reliable and efficient TSS. Some of the unsuccessful missions were the NASA and Italian Space Agency's (ASI) TSS-1 in 1992 [Tomlin *et al.* 1995] and NASA's Advanced Tether Experiment (ATEX) in 1998 [Zedd 1997]. The major causes of failure of these missions were found to be associated with tether deployment and tether breakage. Researchers have tried to solve these problems using high performance tether deployment system and multi-strand tethers; however, the problems of tether deployment and breakage still exist. Therefore, it is very important to emphasize the challenges associated with the attitude stabilization of a tether system when tether deployment suddenly stops and tether breakage occurs. The applications of fault-tolerant adaptive nonlinear control methodologies that circumvent the problem of tether severance has not been studied by researchers.

1.4 Fault-Tolerance in Spacecraft Systems

The basic premise of autonomous FTCS presented in this thesis is that it tolerates failures in actuators and enhances the reliability and life of the spacecraft by providing uninterrupted acceptable performance. For systems equipped with more actuators than the degrees of freedom to be controlled, it is important to design a control reconfiguration mechanism that can autonomously substitute the redundant actuators in place of faulty units. This prevents faulty actuators from further deteriorating the performance of the spacecraft.

1.4.1 Fault Classification

Actuator faults can be classified as, (1) *additive faults*, and (2) *multiplicative faults*, based on the way faults are modeled and added to the system (Figure 1.4). Additive faults are usually associated with reaction wheels used for attitude control. Changes in friction between stator and rotor due to aging, temperature etc. could lead to increased/decreased generated reaction torque when compared to the commanded value. Malfunctioning of the actuators may also continuously generate reaction torque (reaction wheel) or forces

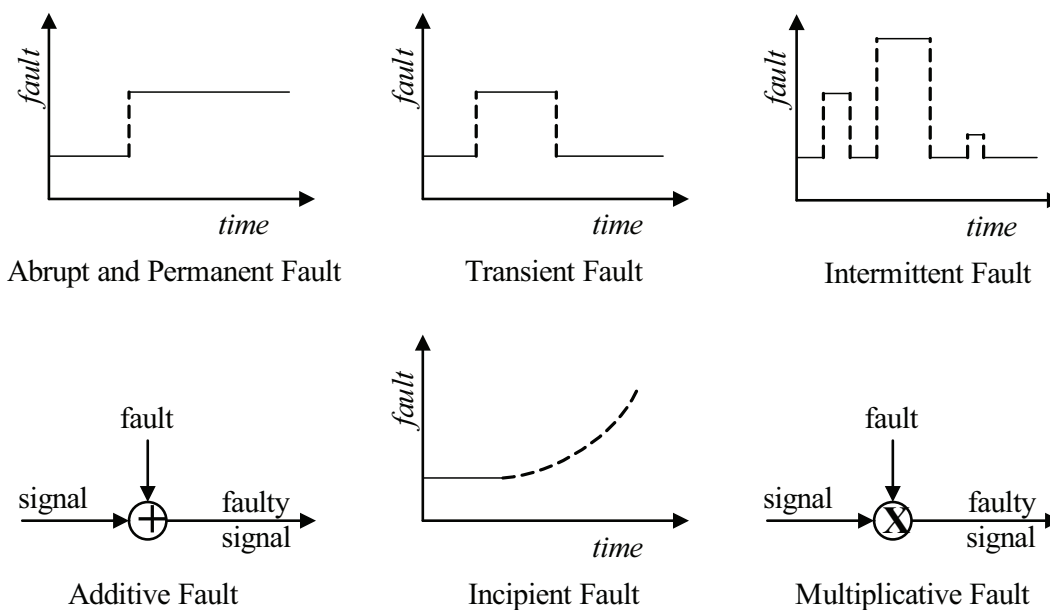


Figure 1.4: Fault classification based on representation and time characteristics.

(thrusters) due to stuck control surfaces. Such faults are modeled as an abrupt change of the nominal control action and therefore classified as multiplicative faults. Actuator degradation is also a class of multiplicative fault.

Faults are also classified based on fault forms or their time characteristics as, (1) *abrupt*, (2) *incipient*, and (3) *transient*. Abrupt faults occur instantaneously as a result of hardware damage. This leads to total failure of the actuator and such faults remains until the faulty unit is repaired or replaced. Incipient faults (drift-like, due to wear and tear of the motor) represent slow variations in the actuator performance, often as a result of aging. Tolerating incipient faults is crucial in AOCS problems where early reconfiguration of worn actuators is required. Finally, transient faults represent temporary malfunctions of an actuator. Repeated occurrences of transient faults is termed as intermittent faults.

1.4.2 Failure Modes in Reaction Wheels and Thrusters

The actuators considered in this thesis are mainly reaction wheels (attitude control) and thrusters (orbit control, attitude control). The nature of failures in reaction wheels and thrusters, and their effects on system performance are described in this subsection.

1.4.2.1 Reaction Wheel Failure Modes

A reaction wheel consists of a flywheel driven by an electric motor and the associated bearings and drive electronics. With regards to stabilizing the attitude of a spacecraft, reaction wheels are sensitive devices that are vulnerable to different sources of faults [Murugesan & Goel 1987].

1. *Failure to respond to control signals*: This type of failure causes the wheel to decelerate slowly or hold its speed, without any response to control signals due to faulty drive electronics, drive motor, and power supply.
2. *Decreased reaction torque*: The generated reaction torque could be less than the commanded value by the controller due to increased friction between stator and rotor, marginal failure of bearings, and decreased motor torque and current drive. These

factors effect the rate of change of the wheel speed and consequently decrease the generated reaction torque.

3. *Increased bias torque*: When the external disturbances are negated and the demanded reaction torque by the ACS is zero, the reaction wheel should hold its speed and generate no torque. Incipient faults can occur based on changes in friction due to aging, time-varying temperature etc., that may accelerate or decelerate the wheel, thereby generating a bias torque, even when the commanded torque is zero.
4. *Continuous generation of reaction torque*: Faults in the bus voltage and intermittent time-varying faults in the motor current might result in continuous increase or decrease in wheel speed, thereby generating reaction torque, independent of the commanded torque by the controller.

1.4.2.2 Thruster Failure Modes

A thruster consists of a flow control valve and a combustion chamber. When propellant passes through the combustion chamber, chemical reaction takes place generating thrust through the nozzle. Thrusters are used during various phases of a mission for spacecraft attitude control, orbit correction (station-keeping), and momentum dumping operations. To avoid single point failures, generally, two set of functionally redundant thrusters are used in spacecraft.

1. Stuck-open failure is a type of failure that is very common with thrusters where the flow control valve is stuck open causing large leakage and depletion of propellant. This leads to large constant thrust delivered by faulty thrusters causing rapid attitude/station-keeping error build-up and reducing the life of the mission.
2. Stuck-close fault occurs when the flow control valve remains closed and thereby the thruster does not generate thrust/torque when required. Intermittent occurrence of this fault can cause large deviations to the orbit of the spacecraft. Abrupt or permanent closure of the flow control valve requires transferring control authority to the redundant system via control reconfiguration algorithm.

All of the above mentioned failures in thrusters and reaction wheels can result in large attitude/station-keeping errors and/or attitude loss. If these faults are not negated using a control reconfiguration mechanism, the consequences can range from complicated reacquisition of spacecraft attitude/orbit to catastrophic ending of the mission.

1.4.3 Controller Reconfiguration

The proposed fault-tolerant architecture for spacecraft ACS to accommodate for actuator and faults is shown in Figure 1.5. The shaded region projects the main focus of this thesis. Our objective is to improvise the design of ‘Controller’ subcomponent to achieve fault-tolerance in a spacecraft control system. The nominal controller is redesigned by adding an adaptive retrofit component. There are two main steps in the proposed control flow: (1) The plant parameters are assumed to be unknown, and therefore the control parameters have to be provided by an adaptation law, Adaptive Parameter Estimation Scheme. (2) Adaptive Fault Tolerant Control Mechanism is used to adjust the estimated parameters in the control input computation. As a result, the adaptive control design provides new

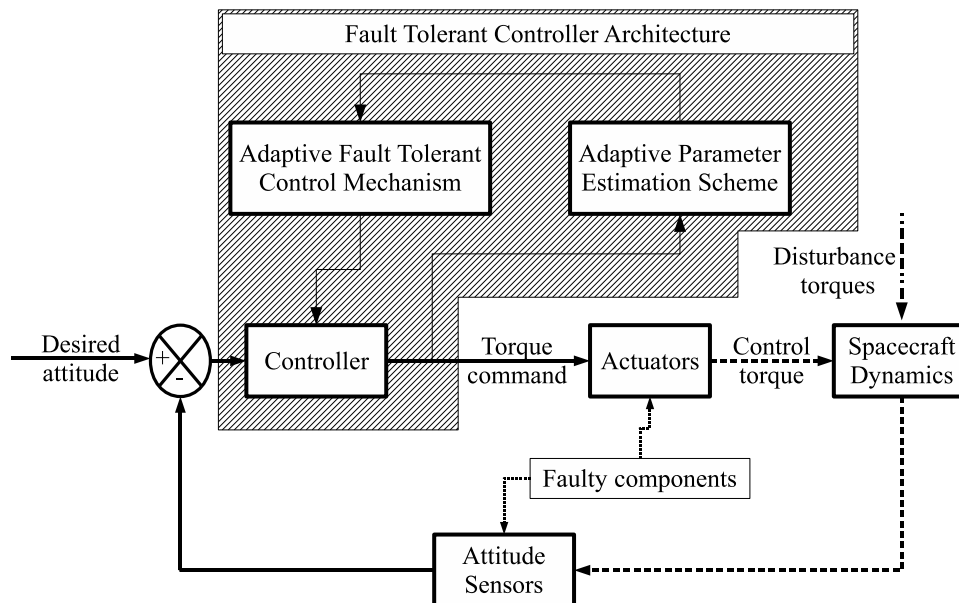


Figure 1.5: Schematic of the proposed fault tolerant attitude control system.

torque/force commands to compensate for actuator faults by autonomous reconfiguration of the control algorithm. The schematic of the FTCS for orbit control would be the same as Figure 1.5 with the input to controller being the trajectory tracking errors.

Based on the fault classification provided in Section 1.4.1, the actuator failures commonly encountered in spacecraft systems can be termed as: (1) *Lock-In-Place* (LIP), (2) partial *Loss of Effectiveness* (LOE), and (3) *Float*. In lock-in-place type failures, the actuator freezes at a certain condition and does not respond to subsequent commands. In this case, the remaining operating actuators must not only compensate for the lack of the desired control effort of the failed actuator, but must also cancel the undesired control effect produced if the actuator freezes at any position other than zero. Partial loss of effectiveness may occur due to physical damage of the control effector. Float-type failure occurs when the actuator contributes zero force/torque to the control authority.

A basic actuator fault structure that differentiates commanded control and applied control is shown in Figure 1.6. The preceding control failures can be modeled for each control by the following mathematical model:

$$u_{ai} = u_{ci} + \sigma[\bar{u}_i - u_{ci}] \quad (1.3)$$

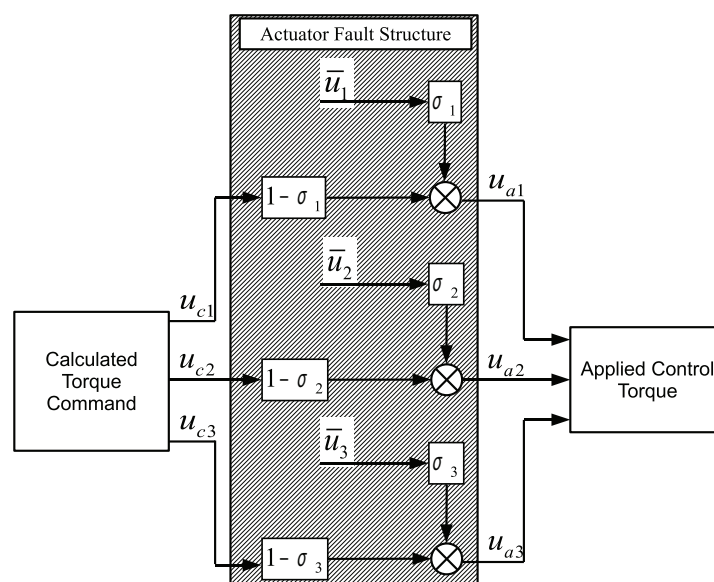


Figure 1.6: Schematic of a control system with actuator faults.

For a case in which the control is a vector, $\sigma = \text{diag}\{\sigma_1, \sigma_2, \sigma_3\}$ is the actuator failure indicator, $\bar{u}_i, i \in \{1, 2, 3\}$ represent uncertain actuator failures, $u_{ci}, i \in \{1, 2, 3\}$ is the desired control force/torque commanded by the controller, and $u_{ai}, i \in \{1, 2, 3\}$ is the control that can actually be applied by the actuators.

- No failure: In the absence of failure, $u_{ai} = u_{ci}$ and the values of σ and \bar{u}_i are represented as zero vector, respectively.
- Lock-in-Place fault: For LIP fault (stuck-open fault), the value of σ goes to 1 and \bar{u}_i going to the constant value at which the actuator has frozen leading to $u_{ai} = \bar{u}_i$.
- Loss of Effectiveness: In the case of LOE, if it is assumed that there is 50% degradation in the control actuation, σ takes a value of 0.5 and \bar{u}_i is represented as a zero vector.
- Float: Float type failures can also be accounted for, with $\sigma = 1$ and $\bar{u}_i = 0$.

By augmentation of the adaptive fault-tolerant control scheme with this control failure model (Figure 1.6), a framework is created that accommodates actuator failures and damage as changes in the parameters of the system.

1.5 Problem Statement

An overview of the fault tolerant spacecraft control discipline based on classification of faults, failure modes in reaction wheels and thrusters, and control law reconfiguration was presented in the previous section. Assessing this in perspective with the literature review presented in Section 1.3 gives a clear picture of the subsequent developments that have taken place in spacecraft attitude and formation control discipline. More interestingly, it is important to identify the scarcity of work essentially in autonomous FTC strategies for spacecraft AOCS that can be implemented during various phases of a mission. Our retrospect is on how passive control methods fit conceptually into the autonomous AOCS framework and how to improve pointing accuracy and establish precise orbital and attitude maneuvers even with the failure of control actuators onboard a spacecraft. Many significant challenges must be overcome before an autonomous FTCS for spacecraft can be realized. The problem statements for this dissertation can be classified as:

[**PROB1**] *Nonlinear spacecraft models.* The inherent nonlinearity in the attitude and formation dynamics of spacecraft is identified as one of the technological bridges to be crossed for successfully developing a fault tolerant controller. A linear representation of the mathematical model does not accurately describe the dynamic behavior of spacecraft for a wide range of operating conditions.

[**PROB2**] *Model uncertainties and external disturbances.* In space applications, controllers designed based on nonlinear spacecraft models can also be imprecise due to unknown values of some physical parameters, disturbance models, etc. The resulting mismatch between the model and the real system is referred to as model uncertainty. The problem of disturbance rejection is particularly pronounced for spacecraft that operate in the altitude ranges where their dynamics is affected by various environmental and non-environmental disturbances.

[**PROB3**] *Control input saturation.* Saturation is very critical for space systems because continued control operation in the presence of actuator saturation (wheel speed saturation, maximum thrust) can lead to substantial performance degradation and instability. For the case of tracking maneuvers, input saturation can contribute significantly to tracking errors along with parameter uncertainties and various sources of internal and external disturbances.

[**PROB4**] *Actuator faults.* Most actuator faults in the AOCS introduce constant or state-dependant disturbances into the overall closed-loop system causing the spacecraft dynamics to deviate largely from its nominal operational regime. Actuator failure can also force the remaining operational and redundant actuators to function with maximum control authority leading to control input saturation.

It should be noted that the challenges described above are correlated to each other and the development of a robust controller can be only accomplished if these problems are taken into account explicitly. If an actuator fault occurs, the controller's command will not be applied properly to the spacecraft. To avoid this situation, one needs to design a FTC algorithm capable of overcoming the above mentioned challenges with explicit consideration of actuator faults while developing any theoretical framework.

1.6 Research Objectives

In response to the problem statement described above, this dissertation focusses on the design of adaptive FTC algorithms for spacecraft with redundant actuators and robust control algorithms for spacecraft in an underactuated configuration. In addition, efficacy of the developed control methodologies are illustrated for RyeSat formation control, RyeSat attitude control, and control of tethered RyeSat configurations.

From practical viewpoint, our goal is to design a control system that can achieve high precision pointing, fast slewing, and large maneuvers in the presence of large disturbances, model uncertainties, and actuator faults. The following objectives are identified.

[OBJ1] Adaptive FTC for redundant actuator configurations: Develop a reconfigurable control strategy based on adaptive control theory, in which the adaptive control structure implicitly reconfigures the control algorithm using adaptive estimates of altered spacecraft dynamics after failure. Instead of using an explicit FDI algorithm, this methodology allows the controller to constantly update its parameters using an adaptation mechanism. The objective is to provide autonomous fault recovery using a reliable and const-effective control algorithm that accounts for modeling uncertainties, external disturbances, and actuator failures simultaneously.

[OBJ2] Robust control for underactuated configurations: For small spacecraft with high precision operational requirements, cost and weight penalties associated with actuator redundancy may be unacceptable. Hence, if the spacecraft becomes underactuated due to actuator failures, a cost reducing alternative is to design a robust control technique that can achieve control objectives using only the remaining healthy actuators. We utilize the nonlinear dynamic coupling between the directly actuated degrees of freedom and the unactuated degrees of freedom to develop a robust nonlinear control algorithm that can stabilize all degrees of freedom.

[OBJ3] Validation: Failure analysis should be conducted to determine the effect of actuator malfunction on the performance and flight-worthiness of the control system. We approach the validation of the proposed control algorithms from three perspectives:

conventional theoretical analysis, numerical simulation study, and real-time experimental testing. Analytical studies are performed using adequate nonlinear control theory to demonstrate AOCS performance and stability. Simulation studies are used as a design tool to demonstrate system performance, compliance with design requirements, and validate established theoretical framework. Finally, we utilize the reaction wheel hardware and spacecraft formation test-bed for real-time testing of the control algorithm. This ensures that the control profile demanded by the AOCS can actually be achieved using real hardware.

[OBJ4] Applications: Implementation and validation of the developed fault tolerant and robust control techniques using a closed-loop control experiment permits the verification of a system-level integration of the controller with actuators. To complement this effort, a number of application studies were conducted to assess the performance and usability of the proposed control algorithms. In particular, we focus on underactuated and redundant actuator configuration with emphasis on spacecraft formation and attitude control. For systems that are non-affine in control, an adaptive FTC algorithm is proposed to stabilize the attitude of a tethered RyeSat configuration and a robust control scheme is developed for RyeSat attitude stabilization using a single gimbaled-thruster.

Innovative small satellite designs have pioneered many advances in satellite technology. Recent years witnessed a substantial progress in the design of new sensing and actuation devices for spacecraft, thereby, increasing the demand for performance and capability of attitude sensors and actuators onboard nanosatellites. The development of practically viable control algorithms has not kept pace with new capabilities enabled by novel hardware designs and increased computational power for spacecraft.

Researchers have often sought to ‘fault-avoidance’ techniques such as enhancements in design and fabrication, and elaborate and intensive testing to improve the reliability of spacecraft ACOS. However, failures do occur in control actuators during their long operational life leading to malfunction of the entire control system. Therefore, it is important to design an autonomous FTC algorithm that operates satisfactorily not only in the absence but also in the presence of actuator failures.

1.7 Main Contributions

Autonomous fault tolerant adaptive control scheme for spacecraft systems equipped with redundant actuators and robust control of spacecraft systems in underactuated configuration, represent the two central themes of this thesis. Specifically, the following contributions are identified, and expanded based on objectives stated in Section 1.6.

1. **Fault-tolerant Control of Spacecraft Formations (OBJ1, OBJ3, Chap. 2)**

This dissertation presents a novel control scheme capable of achieving high precision station-keeping and formation geometry reconfiguration for multiple spacecraft in formation flying by explicit consideration of model uncertainties, external disturbances, and actuator faults simultaneously. In particular, we propose a fault-tolerant formation flying concept, identify the possible types of actuator faults, and derive a novel adaptive control scheme based on existing variable structure control theory. A high fidelity computer simulation model is developed to validate the proposed algorithm. Although there is a plethora of control designs available in the current literature for spacecraft formation control, the technique presented in this dissertation is the first to consider faults in thrusters and provide an autonomous fault recovery scheme.

2. **Control of Underactuated Spacecraft Formations (OBJ2, OBJ3, Chap. 3)**

Feasibility of achieving reliable formation control without the need for thrust in the radial or along-track direction is explored in this paper. For configurations associated with no radial axis input, the control laws available in the current literature are based on linearized relative motion dynamics and only work in a sufficiently small neighborhood of the origin. The configuration based on the exclusion of along-track force, not examined in the literature previously, is challenging because it fails the linear controllability test and hence requires the use of nonlinear control techniques. This dissertation introduces a new concept of formation control without the use of force in along-track direction and the stability of the underactuated configuration is proved using nonlinear control theory. We developed a comprehensive numerical simulation model and a hardware test bed to facilitate testing and validation of the proposed underactuated configuration and control algorithm.

3. **Fault-tolerant Attitude Control of Spacecraft (OBJ1, OBJ3, Chap. 4)**

Attitude control in the presence of environmental disturbances, model uncertainties, and actuator/sensor faults have attracted considerable research interest in the existing literature. Although various methodologies have been developed for fault tolerant attitude control of spacecraft, it is rare that the performance of the adaptive nonlinear algorithms are experimentally validated on a reaction wheel assembly (RWA).

The main contributions of Chapter 4 can be stated as follows. An adaptive FTC algorithm is proposed for precise 3-axis attitude control for miniature satellites using reaction wheels as attitude effectors. Two configurations of RWA are examined in this work, (1) three wheels in orthogonal configuration combined with one oblique wheel; and (2) four wheels in a pyramid configuration. When a reaction wheel failure or fault occurs, the control signals are autonomously redistributed to the remaining healthy wheels using an adaptive gain that is updated on-line based on the attitude tracking error. Experimental results are compared with numerical simulations to demonstrate the successful implementation of the proposed fault-tolerant algorithm.

4. **Attitude Control of Underactuated Spacecraft (OBJ2, OBJ3, Chap. 5)**

Spacecraft attitude stabilization in the local vertical and local horizontal frame (LVLH) using control torques supplied by gas jet actuators about only two of its principal axes is examined in this chapter. Based on this underactuated dynamics, we propose a time-invariant continuous feedback control scheme capable of achieving attitude stabilization for cases where there is no control available on either roll or yaw axis of the spacecraft. The results obtained forms the basis of developing an attitude control system for pico-satellites using a novel single-thruster based control strategy.

5. **RyeSat attitude control using a single thruster (OBJ2, OBJ3, Chap. 6)**

A single-thruster control concept, either by design or in a contingency, is challenging because the thruster exerts both force and torque on a satellite. Torques are generated using a thruster orientation mechanism with which the thrust vector can be tilted on a two axis gimbal. With recent renewed interest to return to the Moon, NASA has proposed a new series of Crew Exploration Vehicle capable of carrying as-

tronauts to the Moon. The control concept using a single-thruster can be conceived as a last-ditch emergency backup system, in the absence of nominal control capacity, to execute attitude maneuvers during de-orbit and descent phases (for descent to the lunar surface, or, attaining a heat-shield-forward attitude trajectory during atmospheric reentry). For low-cost missions using pico-satellites, the possibility of handling actuator failures without the need for redundant elements is even more appealing. The proposed control method is capable of achieving complete three-axis spacecraft attitude stabilization using a single thruster.

6. **Fault-tolerant Attitude Control of Tethered Spacecraft (OBJ1, Chap. 7)**

Based on the complexity of the model and various attractive potential applications in space, a Tethered Spacecraft System was chosen to analyze the advantages of offering a fault-tolerant attitude control framework. Several missions have already been flown to verify the TSS concept. Some of the unsuccessful missions were the NASA and Italian Space Agency's TSS-1 in 1992 and NASA's Advanced Tether Experiment (ATEX) in 1998. The major causes of failure of these missions were found to be associated with tether deployment and tether breakage. In this chapter, a novel fault-tolerant adaptive control scheme is proposed to control the attitude motion of a two-tether subsatellite system using coordinated movement of the tether attachment points. Specifically, we consider the case where tether deployment suddenly stops and one of the tethers is severed. An abrupt blockage of the tether attachment point and a fault in the actuator that can reverse the motion of the attachment point is also simulated to validate the effectiveness of the proposed control scheme when subjected to un-anticipated actuator faults. To date, the approach presented in this paper is the only control technique available in the literature that is capable of providing autonomous control for tethered satellite systems in the event of tether severance.

The approach for designing a fault tolerant spacecraft control system has undergone a fundamental shift in philosophy in the last five to eight years. Initially, the concept was to design a control law robust enough to guarantee system stability in the face of the full range of potential failures. Then, upon the event of a failure, the system would identify the fault, isolate the failure mode, estimate new system parameters, and select new control law

gains and/or control input distribution to regain some level of performance. The tuning of gains in control algorithms is not straightforward because the resulting closed-loop error dynamics are nonlinear; moreover, it may not be possible to find constant gains that yield desirable performance for all operating conditions. Therefore, the only means of obtaining a stabilizing control law with good performance is to use an algorithm that can constantly update its parameters.

The control methodology proposed in this thesis minimizes complexities in the control reconfiguration stage by employing a novel adaptive control retrofit scheme. Therefore, with the help of adaptive online parameter estimation, the method removes the toil of FDI, and thus, the time required to cope with faults is reduced. A robust adaptive control algorithm is designed where the uncertainties on constant or slowly-varying parameters due to actuator fault is reduced by parameter adaptation and other sources of uncertainties and disturbances are handled by inherent robustness of the controller.

1.8 Thesis Outline

We begin with the spacecraft formation flying problem in Chapter 2. A fault-tolerant adaptive control algorithm is developed to cope with thruster faults by considering cases of formation-keeping and formation reconfiguration. Chapter 3 presents the formation control problem in the underactuated configuration. Complete loss of control authority in along-track or radial direction is considered. Results obtained from implementing the proposed control algorithm on a hardware test-bed are also presented in this chapter. The numerical and experimental results of implementing the FTC scheme for attitude tracking of spacecraft using reaction wheels as actuators are detailed in Chapter 4. The underactuated configuration for spacecraft attitude control is addressed in Chapter 5 and the results of attitude stabilization using two control inputs are supplemented by introducing a novel single-thruster attitude control strategy for pico-satellites (Chapter 6). In Chapter 7 an approach is presented for control of two-tether satellite systems that encounter faults during tethered attachment point actuation and complete failure of one tether. We conclude with a summary of our accomplishments (Chapter 8) and suggestions for future work.

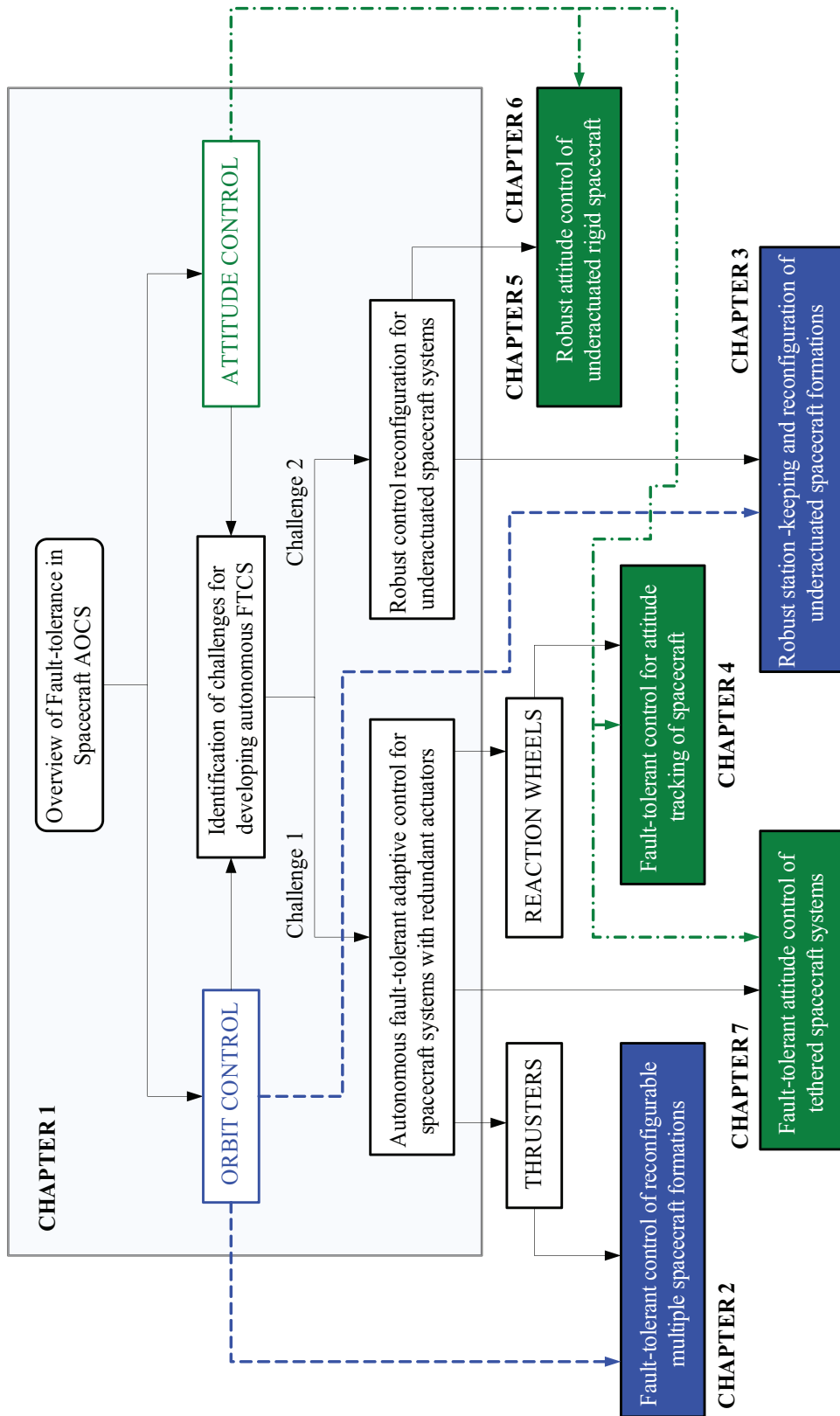


Figure 1.7: Thesis outline: The main chapters are represented by shaded boxes.

CHAPTER 2

Fault Tolerant Control of Spacecraft Formations

MULTIPLE spacecraft formation flying is one of the key technologies of current and future space missions. Due to limitations on launch vehicle allowance size, in concordance with the challenges associated with precision control of large space structures, flying a collection of spacecraft in formation would be the only viable approach to enable vast improvements in angular resolution for future space telescopes and interferometers. The main challenge is to control the relative positions of spacecraft in formation when the external disturbances from gravitational perturbation, atmospheric drag, solar radiation pressure, electromagnetic forces, and Earth's oblateness (differential J_2) cause drifts of both the relative positions of the spacecraft and the formation center. In this chapter, we address the nonlinear problem of formation flying in low Earth orbits and develop a control methodology that yields sub-millimeter formation-keeping. Our main focus is to counteract the effects of onboard thruster faults and failures by utilizing a reconfigurable approach to control algorithm design. To prevent thruster faults and environmental disturbances from causing the spacecraft in formation to drift apart, a closed-loop nonlinear control algorithm is developed based on sliding mode control that incorporates a novel adaptive parameter update scheme to enable autonomous fault recovery.

The chapter is organized as follows: Section 2.1 introduces the mathematical model of the spacecraft formation system. Adaptive FTC algorithms are formulated with detailed proof of closed-loop system stability in Section 2.2. For a detailed assessment of the system performance under the proposed control strategies and validation of the established theoretical framework, the results of numerical simulations incorporating different fault scenarios are presented in Section 2.3. Finally, some brief conclusions are provided in Section 2.4.

2.1 SFF Mathematical Model

The investigation is initiated by formulating the complete nonlinear equations of motion of the SFF system to develop a mathematical model that facilitates the design of nonlinear control methodologies. The proposed system comprises of a *leader spacecraft* in an elliptical planar trajectory with the Earth's center at one of its foci and a *follower spacecraft* moving in a desired relative trajectory about the leader spacecraft.

2.1.1 Cartesian Coordinate Frames

The coordinate frames used to represent the dynamics of the leader and follower spacecraft are shown in Fig. 2.1. An *Earth centered inertial* (ECI) frame is denoted by $\mathfrak{J} - XYZ$, has its origin located at the center of the Earth, with Z_I -axis passing through the celestial North pole, X_I -axis directed towards the vernal equinox, and Y_I -axis completes the right-handed triad. The orbital motion of the leader spacecraft is defined by $\vec{r}_l \in \mathbb{R}^3$, $\vec{r}_l \triangleq [r_l \ 0 \ 0]^T$, and true anomaly θ .

The motion of the follower spacecraft is described relative to the leader spacecraft using a relative local vertical local horizontal (LVLH) frame $\mathfrak{B} - xyz$ fixed at the center of the leader spacecraft with the x -axis pointing along the local vertical, the z -axis taken along normal to the orbital plane, and the y -axis representing the third axis of the right-handed $S - xyz$ frame. $\vec{\rho} \in \mathbb{R}^3$, $\vec{\rho} \triangleq [x \ y \ z]^T$, defines the relative position vector of the follower spacecraft from the origin of the leader spacecraft coordinate frame. Both, \vec{r}_l and \vec{r}_f are expressed in the LVLH frame. In this dissertation, the motion along x , y , and z will be referred to as *radial*, *along-track*, and *cross-track* motion, respectively. It is important to note that the leader position need not be necessarily occupied by a physical spacecraft, but can merely be used as an orbit reference point for all follower spacecraft. In a circular orbit, the y -axis is parallel to the leader spacecraft velocity vector, and the leader orbit frame rotates relative to the *ECI* frame with an angular velocity,

$$n = \sqrt{\frac{\mu_e}{r_l^3}} \quad (2.1)$$

where μ_e is the geocentric gravitational constant of the Earth and r_l is the distance from the frame origin to the center of the Earth. Two spacecraft in circular orbits with the same

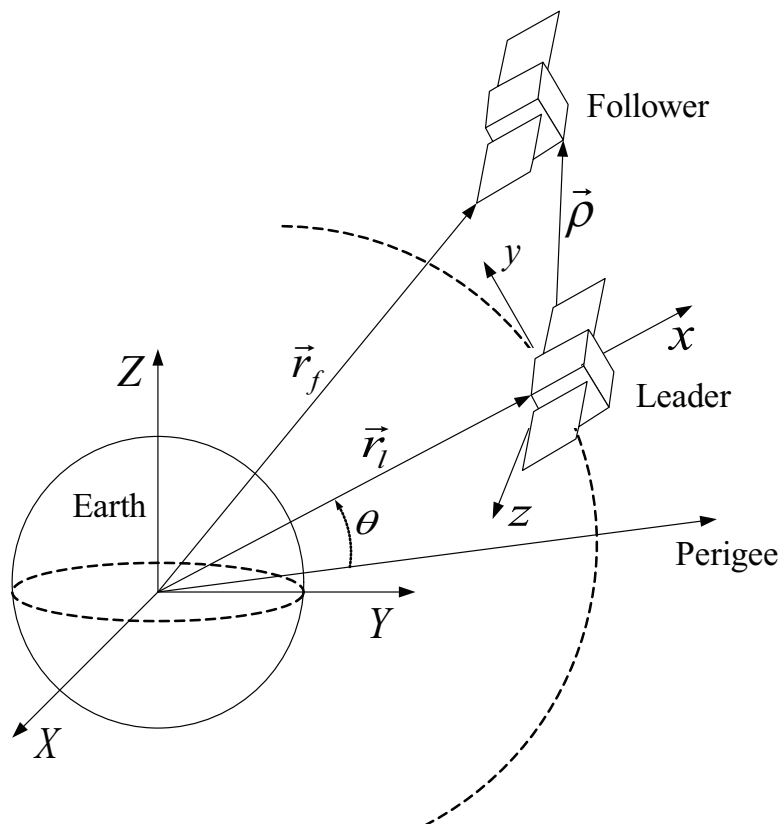


Figure 2.1: Geometry of orbit motion of leader and follower spacecraft.

altitude will have the same orbital velocity, and this velocity will be constant throughout the orbit in the absence of orbital perturbations. If they are separated in the along-track direction, the separation distance would remain constant since orbital velocities are equal. For the case of elliptical orbits, the spacecraft closer to the Earth will have higher orbital velocity. Therefore, the separation distance will contract and expand, depending on whether the formation is approaching the orbit apogee or perigee.

2.1.2 Coordinate Frame Rotations

The rotation from the ECI frame to the leader orbital frame (T_{IB}) is dependent on the orbital elements of the leader spacecraft orbit, and are expressed based on three rotations [Kristiansen & Nicklasson 2009]. The first rotation is about the inertial Z_I -axis with the right ascension of the ascending node of the orbit, Ω_l . The second rotation is about the

x -axis in the rotated frame with the orbit inclination, i_l . The final rotation accounts for the orbit perigee and the location of the spacecraft ($\omega_l + \theta$) about the new z -axis.

$$T_3(\Omega_l) = \begin{bmatrix} \cos(\Omega_l) & -\sin(\Omega_l) & 0 \\ \sin(\Omega_l) & \cos(\Omega_l) & 0 \\ 0 & 0 & 1 \end{bmatrix} \quad \text{and} \quad T_1(i_l) = \begin{bmatrix} 1 & 0 & 0 \\ 0 & \cos(i_l) & -\sin(i_l) \\ 0 & \sin(i_l) & \cos(i_l) \end{bmatrix}$$

$$T_3(\omega_l + \theta) = \begin{bmatrix} \cos(\omega_l + \theta) & -\sin(\omega_l + \theta) & 0 \\ \sin(\omega_l + \theta) & \cos(\omega_l + \theta) & 0 \\ 0 & 0 & 1 \end{bmatrix}$$

The rotation matrix to transform from the ECI frame to the leader frame is given by

$$T_{IB} = T_3(\Omega_l) \times T_1(i_l) \times T_3(\omega_l + \theta) \quad (2.2)$$

2.1.3 Equations of Motion

The orbital equations of motion for the leader spacecraft and the full nonlinear translational dynamics of the follower spacecraft relative to the leader spacecraft taking into account the thrust and disturbance forces can be written as [Schaub & Junkins 2003]:

$$\ddot{r}_l - r_l \dot{\theta}^2 + \frac{\mu_e}{r_l^2} = 0 \quad (2.3)$$

$$r_l \ddot{\theta} + 2\dot{\theta} \dot{r}_l = 0 \quad (2.4)$$

$$m_f \ddot{x} - 2m_f \dot{\theta} \dot{y} - m_f (\dot{\theta}^2 x + \ddot{\theta} y) + m_f \mu_e \left(\frac{r_l + x}{r_f^3} - \frac{1}{r_l^2} \right) = u_{fx} + F_{dx} \quad (2.5)$$

$$m_f \ddot{y} + 2m_f \dot{\theta} \dot{x} + m_f (\ddot{\theta} x - \dot{\theta}^2 y) + m_f \frac{\mu_e}{r_f^3} y = u_{fy} + F_{dy} \quad (2.6)$$

$$m_f \ddot{z} + m_f \frac{\mu_e}{r_f^3} z = u_{fz} + F_{dz} \quad (2.7)$$

where $r_f = [(r_l + x)^2 + y^2 + z^2]^{1/2}$ is the absolute position of the follower spacecraft, F_{dj} is the net relative perturbations acting on the SFF system, and u_{fj} are the components of the control input vector, for $j = x, y, z$. The equations of motion given by Eqs. (2.3)-(2.7) involves ten states, $X_a = [r_l, \dot{r}_l, \theta, \dot{\theta}, x, \dot{x}, y, \dot{y}, z, \dot{z}]^T$, and the combined effects of nonlinearity and eccentricity are accounted for, thus providing a generalized framework. This mathematical model for SFF is also referred to as the ‘‘true model’’ [Vaddi 2003].

2.1.4 Desired Formation Geometry

Formation flying guidance is defined as the generation of any reference trajectories used as a input for a formation member's relative state tracking control law [Scharf *et al.* 2004]. In the present investigation, two formation flying designs are considered. They are circular and projected circular formations. The circular formation is one in which the satellites maintain a constant distance from each other. The formation can be derived from Hill's equations analytically or geometrically [Sabol *et al.* 2001]. Spacecraft in projected circular formation maintains a fixed distance in the along-track/cross-track (y/z) plane. This characteristic has applications for ground observing Synthetic Aperture Radar (SAR) missions. Since most SAR applications target objects on the surface of the Earth, it is desirable to achieve a formation plane perpendicular to the radial vector in order to have a field of view that has its target on the Earth.

The desired or commanded states $(x_d, \dot{x}_d, y_d, \dot{y}_d, z_d, \dot{z}_d)$ are taken as the solution of the linearized form of the relative equations of motion when $F_{dj} = 0$, $j = x, y, z$. The following desired trajectories are considered:

1. *Circular Formation*: In this formation, the leader and the follower spacecraft maintain a constant separation from each other in three-dimensional space and the formation is mathematically defined as $x^2 + y^2 + z^2 = r_{dc}^2$. The relative motion in the radial/along-track (x/y) plane is fixed in eccentricity [Sabol *et al.* 2001]. The equations of desired circular trajectory are given as follows,

$$\begin{Bmatrix} x_d \\ y_d \\ z_d \end{Bmatrix} = \frac{r_{dc}}{2} \begin{Bmatrix} \sin(nt + \phi) \\ 2 \cos(nt + \phi) \\ \sqrt{3} \sin(nt + \phi) \end{Bmatrix} \quad (2.8)$$

2. *Projected Circular Formation*: In this formation, the leader and the follower spacecraft maintains a fixed relative distance when the formation is projected onto the along-track/cross-track ($y - z$) plane, and is mathematically defined as $y^2 + z^2 = r_{dpc}^2$.

$$\begin{Bmatrix} x_d \\ y_d \\ z_d \end{Bmatrix} = \frac{r_{dpc}}{2} \begin{Bmatrix} \sin(nt + \phi) \\ 2 \cos(nt + \phi) \\ 2 \sin(nt + \phi) \end{Bmatrix} \quad (2.9)$$

where r_{dc} and r_{dpc} are the circular and projected circular formation sizes (radius) respectively, ϕ is the in-plane phase angle between the leader and the follower spacecraft (the initial phase angle is defined, at the time of equator crossing of the leader spacecraft, in the local horizon $y - z$ plane), and n is the mean angular velocity and equals to $\sqrt{\mu_e/a_c^3}$ (μ_e is the gravitational parameter of the Earth; a_c is the semi-major axis of the leader spacecraft) [Yan *et al.* 2009]. In this chapter, we only deal with these two formation types, though the control algorithms developed are applicable to any formation types (in-plane and in-track) and multiple spacecraft configurations.

2.1.5 External Disturbances

The disturbances in Eqs. (2.5)-(2.7) are time-varying quantities attributed to gravitational field, solar radiation pressure, and third body perturbations. For spacecraft in LEO, the second zonal harmonic (J_2) of the oblate Earth's potential distribution is by far the most dominant perturbation. The disturbance accelerations due to J_2 are at least an order of magnitude larger than the other perturbations such as third-body gravitational effects, drag due to residual atmosphere, and solar radiation pressure [Sabol *et al.* 2001]. Earth's oblateness affects the formation geometry in two ways, 1) differential changes in the right ascension of the ascending node due to precession of the orbital plane, and 2) secular changes in the argument of perigee and mean anomaly due to rotation of the line of apsides in the orbital plane. Next, we show the steps involved in obtaining the relative acceleration components due to J_2 perturbation in the LVLH frame.

The leader (\vec{r}_l) and follower spacecraft (\vec{r}_f) positions in the LVLH frame are given by

$$\vec{r}_l = \begin{bmatrix} r_l & 0 & 0 \end{bmatrix}^T \quad \text{and} \quad \vec{r}_f = \begin{bmatrix} r_l + x & y & z \end{bmatrix}^T \quad (2.10)$$

and the transformation matrix, T_{IB} required to convert these positions from the relative frame to the Earth-centered inertial frame of reference is obtained by using the following rotation sequence

$$T_{IB} = T_3(\Omega_l) \times T_1(i_l) \times T_3(\omega_l + \theta) \quad (2.11)$$

Using the transformation matrix, T_{IB} , along with Eq. (2.10),

$$\vec{R}_l = T_{IB} \vec{r}_l \quad \text{and} \quad \vec{R}_f = T_{IB} \vec{r}_f \quad (2.12)$$

we obtain the positions of the leader spacecraft ($\vec{R}_l = [X_l, Y_l, Z_l]^T$) and follower spacecraft ($\vec{R}_f = [X_f, Y_f, Z_f]^T$) in the ECI frame. The perturbations due to J_2 in the ECI frame for the leader and follower spacecraft are given by [Schaub & Junkins 2003]

$$\vec{J}_{2l} = -\frac{3\mu_e J_2 R_e^2}{2\|\vec{R}_l\|^5} \begin{bmatrix} \left\{1 - \frac{5Z_l^2}{\|\vec{R}_l\|^2}\right\} X_l \\ \left\{1 - \frac{5Z_l^2}{\|\vec{R}_l\|^2}\right\} Y_l \\ \left\{3 - \frac{5Z_l^2}{\|\vec{R}_l\|^2}\right\} Z_l \end{bmatrix} \quad (2.13)$$

$$\vec{J}_{2f} = -\frac{3\mu_e J_2 R_e^2}{2\|\vec{R}_f\|^5} \begin{bmatrix} \left\{1 - \frac{5Z_f^2}{\|\vec{R}_f\|^2}\right\} X_f \\ \left\{1 - \frac{5Z_f^2}{\|\vec{R}_f\|^2}\right\} Y_f \\ \left\{3 - \frac{5Z_f^2}{\|\vec{R}_f\|^2}\right\} Z_f \end{bmatrix} \quad (2.14)$$

where μ_e is the Earth's gravitational parameter, R_e is the radius of the Earth, and J_2 is second zonal gravitational coefficient, $J_2 = 1.08263 \times 10^{-3}$. The full effects of differential J_2 can be added to the nonlinear relative mathematical model by transforming the disturbance forces from the Earth-centered inertial frame to the relative frame. Therefore, the external disturbance components in Eqs. (2.5)-(2.7) is given by

$$\vec{F}_d = T_{IB}^{-1}[\vec{J}_{2f} - \vec{J}_{2l}] \quad (2.15)$$

Figure 2.2 shows the nature of differential J_2 acceleration acting on the follower spacecraft in a projected circular formation ($r_{dpc} = 0.5$ km) around a leader spacecraft in a 500 km orbit with the following orbital parameters, $\Omega_l = 0^\circ$, $i_l = 45^\circ$, and $\omega_l = 0^\circ$.

Remark 2.1: We make the following assumptions, 1) the leader spacecraft remains in an unperturbed elliptical reference orbit, 2) all spacecraft in formation have the same ballistic coefficients and area-to-mass ratio and therefore the perturbing accelerations due to aerodynamic drag and solar radiation pressure have negligible effects on the relative translational dynamics, 3) mass of the follower spacecraft and the external disturbances are quantities unknown to the controller.

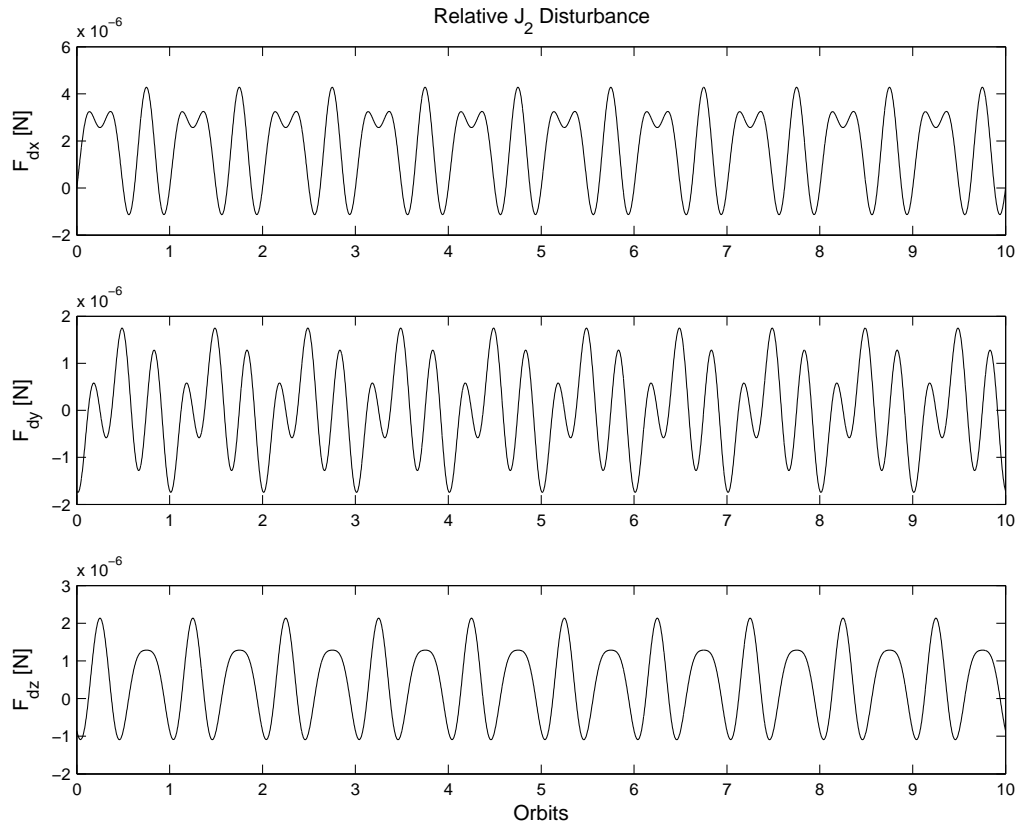


Figure 2.2: Relative J_2 disturbance ($r_p = 6878$ km and $R_d = 0.5$ km).

2.2 Design of Control Laws

In this section we present the theoretical basis for developing adaptive nonlinear control algorithms for the SFF mathematical model. First, the methods and analysis tools of Variable Structure Control (VSC) which is robust to nonlinear model errors are developed. The formulation of the nominal VSC algorithm is then improved using adaptive approximation in the presence of nonlinear model uncertainties. The main idea behind VSC approach is to design a high speed control algorithm that can drive the state trajectory of the nonlinear system onto a sliding or switching surface and maintain the system's state trajectory on the sliding surface. The property of remaining on the switching surface once intercepted is called a *sliding mode* where the behavior of the system is dominated by the lower-order dynamics and is inherently insensitive to external disturbances and model uncertainties.

External perturbations can deviate an uncontrolled spacecraft from its nominal orbit thereby dispersing the desired formation. Similarly, the formation spacecraft may not be placed in its desired orbit initially causing an offset in the relative position. These factors can increase the magnitude of the reaching phase to the sliding mode from the SFF control system's perspective. As the magnitude of the reaching phase grows larger, the effect of both external disturbances and internal parameter uncertainties also increases. Therefore, compared to linear hyperplane based sliding modes, terminal sliding mode (TSM) based on nonlinear switching surfaces offers superior properties such as fast, finite time convergence [Feng *et al.* 2002] making it very useful for high precision SFF control.

2.2.1 Basics of Variable Structure Control

VSC systems are a class of systems where the 'control law' is deliberately changed during the control process based on predefined rules which depend on the state of the system. For the purpose of illustration consider the following linear time-invariant system in state-space form (adapted from [Edwards & Spurgeon 1998]):

$$\begin{bmatrix} \dot{X}_1 \\ \dot{X}_2 \end{bmatrix} = \begin{bmatrix} 0 & 1 \\ 0 & 0 \end{bmatrix} \begin{bmatrix} X_1 \\ X_2 \end{bmatrix} + \begin{bmatrix} 0 \\ 1 \end{bmatrix} U \quad (2.16)$$

where $X \in \mathbb{R}^2 = [X_1, X_2]^T$ is the state vector, and U is a scalar control input. Next, define a linear sliding surface given by

$$S = X_2 + p X_1 \quad (2.17)$$

where p is a positive design scalar. Consider the VSC control law given by

$$U = -\eta \operatorname{sgn}(S) = \begin{cases} -\eta & \text{if } S > 0 \\ \eta & \text{if } S < 0 \end{cases} \quad (2.18)$$

where η is a positive design scalar that has a direct effect on the rate at which the sliding surface can be reached. The expression given by Eq. (2.18) is used to control the double integrator given by Eq. (2.16). The phase portrait of the closed-loop system obtained from using the control law given by Eq. (2.18) with $p = 1$ and $\eta = 2$ and different initial conditions is shown in Fig. 2.3. The inclined line ($S = X_2 + p X_1$) in Fig. 2.3 represents

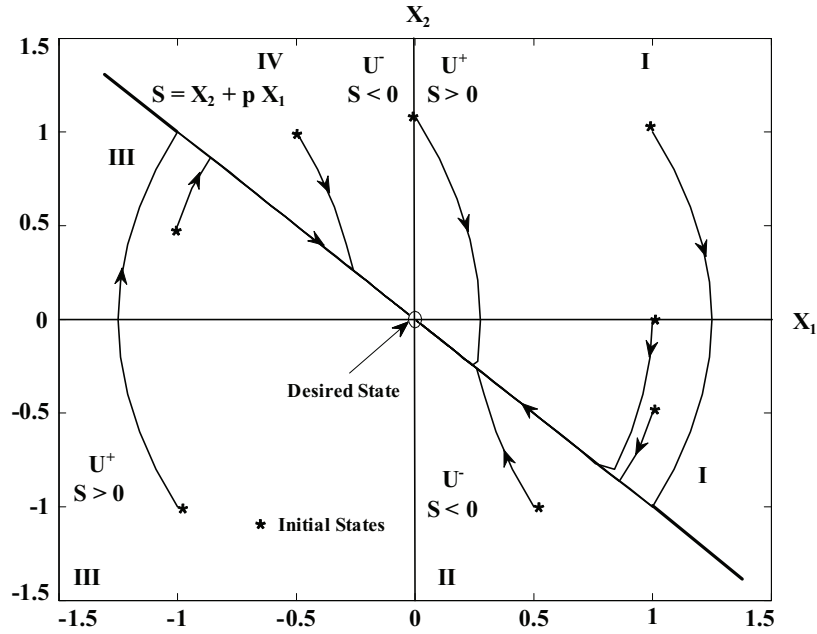


Figure 2.3: Phase portrait of the double integrator under VSC.

the set of points for which $S = 0$; in this case a straight line through the origin of gradient $-p$. This line divides the phase plane into four regions given by

$$\begin{aligned} \text{I} : X_1 > 0, S > 0 \quad \text{and} \quad \text{II} : X_1 > 0, S < 0 \\ \text{III} : X_1 < 0, S < 0 \quad \text{and} \quad \text{IV} : X_1 < 0, S > 0 \end{aligned} \quad (2.19)$$

For a given initial state, the control input U drives the system trajectory towards the line $S = 0$. For values of X_2 satisfying the inequality $p|X_2| < \eta$,

$$S \dot{S} = S[pX_2 - \eta \text{sgn}(S)] < |S|(p|X_2| - \eta) < 0$$

Therefore,

$$\lim_{S \rightarrow 0^+} \dot{S} < 0 \quad \text{and} \quad \lim_{S \rightarrow 0^-} \dot{S} > 0 \quad (2.20)$$

Consequently, when $p|X_2| < \eta$ the system trajectories on either side of the line $S = 0$ point towards the line. This is demonstrated in Fig. 2.3 which shows the phase portraits intercepting the line $S = 0$ from different initial conditions. The condition given by $S \dot{S} < 0$ is referred to as the *reachability condition*.

The trajectory of the system confined to the sliding surface, $S = 0$, satisfies the differential equation obtained from rearranging the terms in Eq. (2.17) for $S = 0$.

$$\dot{X}_1 = -p X_1 \quad (2.21)$$

This represents a first-order decay and the trajectories of the system will ‘slide’ along the line $S = 0$ to the origin. Such dynamical behavior is described as an *ideal sliding mode* and the line $S = X_2 + p X_1$ is termed the *sliding surface*. During sliding motion, lower-order dynamics dominate the behavior of the system independent of the control. Therefore, the control action only ensures that the sliding surface is reached and the conditions given by Eq. (2.20) are satisfied. The dynamic performance of the system is governed by the choice of the parameter p in the sliding surface.

The finite-time (t_r) convergence of the system trajectories to the sliding surface (*reaching time*) can be shown by recalling that

$$S \dot{S} \leq -\eta |S| \quad (2.22)$$

Dividing by $|S|$ and integrating both sides of Eq. (2.22) between 0 and t_r gives

$$\begin{aligned} \int_0^{t_r} \frac{S}{|S|} \dot{S} \, d\tau &\leq \int_0^{t_r} \eta \, d\tau \\ |S(t_r)| - |S(0)| &\leq -\eta t_r \end{aligned} \quad (2.23)$$

Since $|S(t_r)| = 0$, the reaching time is given by

$$t_r \leq \frac{|S(0)|}{\eta} \quad (2.24)$$

2.2.2 Control Problem

The control algorithms are designed based on a generalized framework. The eccentric nature of the leader spacecraft orbit is assumed to be unknown to the controller. We make the following modifications to Eqs. (2.5)-(2.7) assuming the leader spacecraft in a circular reference orbit, (1) $\ddot{\theta} = 0$, and (2) $\dot{\theta} = n = \sqrt{\mu_e/r_p^3}$, where r_p is the orbital radius of the leader spacecraft. Thus, Eqs. (2.3) and (2.4) are neglected for controller synthesis.

To facilitate the control design procedure, we re-formulate the relative dynamics of the SFF model [Eqs. (2.5)-(2.7)] in a state-dependent parameterized form as follows,

$$\begin{aligned}
\begin{bmatrix} \dot{x} \\ \dot{y} \\ \dot{z} \\ \ddot{x} \\ \ddot{y} \\ \ddot{z} \end{bmatrix} &= \begin{bmatrix} 0 & 0 & 0 & 1 & 0 & 0 \\ 0 & 0 & 0 & 0 & 1 & 0 \\ 0 & 0 & 0 & 0 & 0 & 1 \\ 3n^2 & 0 & 0 & 0 & 2n & 0 \\ 0 & 0 & 0 & -2n & 0 & 0 \\ 0 & 0 & -n^2 & 0 & 0 & 0 \end{bmatrix} \begin{bmatrix} x \\ y \\ z \\ \dot{x} \\ \dot{y} \\ \dot{z} \end{bmatrix} + \begin{bmatrix} 0 \\ 0 \\ 0 \\ \mu\left(\frac{1}{r_l^2} - \frac{(r_l+x)}{r_f^3}\right) - 2n^2x \\ n^2y - \frac{\mu y}{r_f^3} \\ n^2z - \frac{\mu z}{r_f^3} \end{bmatrix} \\
&+ \frac{1}{m_f} \begin{bmatrix} 0 & 0 & 0 \\ 0 & 0 & 0 \\ 0 & 0 & 0 \\ 1 & 0 & 0 \\ 0 & 1 & 0 \\ 0 & 0 & 1 \end{bmatrix} \left\{ \begin{bmatrix} u_{fx} \\ u_{fy} \\ u_{fz} \end{bmatrix} + \begin{bmatrix} F_{dx} \\ F_{dy} \\ F_{dz} \end{bmatrix} \right\} \quad (2.25)
\end{aligned}$$

or in a more general state space form as

$$\dot{X} = AX + E(X) + \frac{1}{m_f}B[U_f + F_d] \quad (2.26)$$

where $X \in \mathbb{R}^6 = [x, y, z, \dot{x}, \dot{y}, \dot{z}]^T$ is the state vector, $A \in \mathbb{R}^{6 \times 6}$ is the linear component of the relative equations of motion, $E \in \mathbb{R}^6$ represent the lumped nonlinearities, $B \in \mathbb{R}^{6 \times 3}$ is the input matrix, and $U_f \in \mathbb{R}^3 = [u_{fx}, u_{fy}, u_{fz}]^T$ is the vector of control inputs. The total control input is assumed to be subjected to saturation limit defined by

$$u_{fj} = \begin{cases} N & \text{if } u_{fj} > N \\ u_{fj} & \text{if } -N < u_{fj} < N \\ -N & \text{if } u_{fj} < -N \end{cases} \quad j = x, y, z \quad (2.27)$$

$F_d = [F_{dx}, F_{dy}, F_{dz}]^T$ is the vector of external disturbances with an unknown bound. Although the SFF dynamics described by Eqs. (2.5)-(2.7) considers external time-varying perturbations on the follower spacecraft (relative forces), for controller synthesis we assume that the perturbation is unknown. The upper bounds of the disturbances on $x, y,$

and z are not considered to be the same and we define

$$F_d(t) \in \mathcal{S}_f = \{F_d : |F_{dj}| \leq g_j \rightarrow G\} \quad (2.28)$$

where $G = [g_x, g_y, g_z]^T$. The property that $U_F > G$ holds to ensure that the control available from $U_f \in \mathcal{S}_u = \{u_{fj} : -N \leq u_{fj} \leq N, j = x, y, z\}$ is sufficient to reject any disturbance from \mathcal{S}_f . The disturbances, F_d , may also be constant.

Based on the mathematical model presented in the previous section, we define the relative state vector and the desired relative trajectory as $X(t), X_d(t) \in \mathbb{R}^6$, respectively. The performance measure is defined as the tracking error $e(t) \in \mathbb{R}^6$,

$$e(t) \triangleq X(t) - X_d(t) \quad (2.29)$$

Remark 2.2: As discussed earlier, the follower spacecraft mass, m_f , is assumed to be unknown, and the external perturbations are time-varying and periodic with an unknown upper bound, G . These unknown variations are estimated on-line by the adaptation laws that provide the estimated parameters to the controller. The parameter estimation errors are given by,

$$\begin{aligned} \tilde{m}_f(t) &= m_f - \hat{m}_f(t) \\ \tilde{G}(t) &= G - \hat{G}(t) \end{aligned} \quad (2.30)$$

where $\hat{m}_f(t) \in \mathbb{R}$ denotes the estimate of the follower spacecraft mass m_f and $\hat{G}(t) \in \mathbb{R}^3$ denotes the estimate of the external disturbance bound G . For the closed-loop system, the estimated parameters do not converge to their true values. The update laws are only introduced for robustness purposes.

Our objective is to develop a control algorithm for the SFF mathematical model, Eqs. (2.5)-(2.7), such that u_{fj} , $j = x, y, z$, belonging to \mathcal{S}_u , drives the relative states of the system to its desired relative trajectories as $t \rightarrow \infty$, so that the tracking errors converge to zero.

$$\lim_{t \rightarrow \infty} X(t) = X_d(t) \quad (2.31)$$

The desired trajectories for formation keeping considered in this study are, (1) Circular formation [Eq. (2.8)] with formation size r_{dc} , and (2) Projected circular formation [Eq. (2.9)] with formation size r_{dpc} .

2.2.3 Adaptive Sliding Mode Control

In this section, we present the design procedure to implement adaptive SMC for SFF control. Adaptive control deals with situations where some of the parameters are unknown or slowly time-varying. The basic idea is to estimate these unknown parameters online and then use the estimated ones in place of the unknown ones in the feedback control law.

2.2.3.1 Sliding Manifold

SMC design starts with building a sliding surface in the system state space. The motion of the system along the *sliding mode* is expected to meet the control requirements with desired robustness to bounded disturbances and parametric uncertainties. For the SFF control problem, we utilize the vector containing the trajectory tracking errors, Eq. (2.29), to design a sliding surface S given by,

$$S = C e(t) \quad (2.32)$$

The sliding surface S is a 3 dimensional manifold, $S \in \mathbb{R}^{3 \times 1}$ where $C \in \mathbb{R}^{3 \times 6}$ is a constant, strictly positive gain matrix, and $e(t) \in \mathbb{R}^{6 \times 1}$ is the error vector

$$e(t) = \begin{bmatrix} x - x_d & \dot{x} - \dot{x}_d & y - y_d & \dot{y} - \dot{y}_d & z - z_d & \dot{z} - \dot{z}_d \end{bmatrix}^T$$

$$C = \begin{bmatrix} C_1 & 1 & 0 & 0 & 0 & 0 \\ 0 & 0 & C_2 & 1 & 0 & 0 \\ 0 & 0 & 0 & 0 & C_3 & 1 \end{bmatrix} \quad (2.33)$$

where C_i is determined such that when the system is in sliding mode (dominated by lower-order dynamics), the closed-loop eigenvalues of the system are stable.

2.2.3.2 Controller Design

The objective is to alter the system dynamics along the sliding surface such that the trajectory of the system is steered onto the sliding manifold described by $S = 0$. Next, we derive the control laws based on Lyapounov's second method. After premultiplying Eq. (2.26) with m_F , it can be restated as

$$m_f \dot{X} = m_f AX + m_f E(X) + B[U_f + F_d] \quad (2.34)$$

To examine the convergence properties of the trajectory errors, consider a Lyapunov function candidate defined as follows:

$$V = \frac{1}{2}S^T m_f S + \frac{1}{2\gamma_1} \tilde{m}_f^2 + \frac{1}{2} \tilde{G}^T W^{-1} \tilde{G} \quad (2.35)$$

where γ_1 is a positive constant, and $W \in \mathbb{R}^{3 \times 3}$ is a constant, diagonal, positive-definite, adaptation gain matrix. Taking the derivative of V along its trajectory gives,

$$\begin{aligned} \dot{V} &= S^T m_f \dot{S} - \frac{1}{\gamma_1} \tilde{m}_f \dot{\tilde{m}}_f - \tilde{G}^T W^{-1} \dot{\tilde{G}} \\ &= S^T C m_f \dot{e} - \frac{1}{\gamma_1} \tilde{m}_f \dot{\tilde{m}}_f - \tilde{G}^T W^{-1} \dot{\tilde{G}} \\ &= S^T C \left[m_f \dot{X} - m_f \dot{X}_d \right] - \frac{1}{\gamma_1} \tilde{m}_f \dot{\tilde{m}}_f - \tilde{G}^T W^{-1} \dot{\tilde{G}} \end{aligned} \quad (2.36)$$

Substituting for $m_f \dot{X}$ from Eq. (2.34), we get

$$\dot{V} = S^T C \left[m_f [AX + E(X)] + B[U_f + F_d] - m_f \dot{X}_d \right] - \frac{1}{\gamma_1} \tilde{m}_f \dot{\tilde{m}}_f - \tilde{G}^T W^{-1} \dot{\tilde{G}} \quad (2.37)$$

As stated in the previous section in Eq. (2.28), the disturbances are assumed to be bounded and therefore we can define $\{\dot{V}_1 : \dot{V} < \dot{V}_1\}$ from Eq. (2.37) given by

$$\begin{aligned} \dot{V}_1 &= S^T C \left[m_f [AX + E(X)] + B U_f - m_f \dot{X}_d \right] + S^T C B |F_d| - \frac{1}{\gamma_1} \tilde{m}_f \dot{\tilde{m}}_f - \tilde{G}^T W^{-1} \dot{\tilde{G}} \\ &= S^T C \left[m_f [AX + E(X)] + B U_f - m_f \dot{X}_d \right] + S^T C B G \\ &\quad - \frac{1}{\gamma_1} \tilde{m}_f \dot{\tilde{m}}_f - \tilde{G}^T W^{-1} \dot{\tilde{G}} \end{aligned} \quad (2.38)$$

To replace m_f and G with its estimated values for the control algorithm, we add and subtract the following terms: (1) $\hat{m}_f AX$, (2) $\hat{m}_f E(X)$, (3) $\hat{m}_f \dot{X}_d$, and (4) $S^T C B \hat{G}$, and collect the common terms to re-formulate \dot{V}_1 in Eq. (2.38) as

$$\begin{aligned} \dot{V}_1 &= S^T C \left[\hat{m}_f [AX + E(X)] + B U_f + B \hat{G} - \hat{m}_f \dot{X}_d \right] + \tilde{m}_f S^T C \left[AX + E(X) - \dot{X}_d \right] \\ &\quad + S^T C B \tilde{G} - \frac{1}{\gamma_1} \tilde{m}_f \dot{\tilde{m}}_f - \tilde{G}^T W^{-1} \dot{\tilde{G}} \end{aligned} \quad (2.39)$$

Based on Eq. (2.39) the control law is defined as,

$$U_f = -(CB)^{-1} \left\{ \hat{m}_f C [AX + E(X) - \dot{X}_d] + CB \hat{G} + \eta \operatorname{sgn}(S) \right\} \quad (2.40)$$

where $\eta = \text{diag}\{\eta_x, \eta_y, \eta_z\}$ for all $\{\eta_i : \eta_i > 0\}$, and $\text{sgn}(S) = [\text{sgn}(S_x), \text{sgn}(S_y), \text{sgn}(S_z)]^T$. The adaptive laws for unknown mass and external disturbances are chosen as,

$$\dot{\hat{m}}_f = \gamma_1 S^T C [A(t)X + E(t) - \dot{X}_d] \quad \text{and} \quad \dot{\hat{G}} = W(CB)^T S \quad (2.41)$$

2.2.3.3 Stability Analysis

Here, we present the proof for closed-loop system stability to show that the control law defined by Eq. (2.40), and the adaptation laws given by Eq. (2.41) guarantees global asymptotic stabilization of the relative states of the spacecraft to any desired formation.

Lemma 2.1. Barbalat's lemma [Popov 1973]: *If $\Psi : R \rightarrow R$ is a uniformly continuous function for $t \geq 0$ and if $\lim_{t \rightarrow \infty} \int_0^t |\Psi(\tau)| d\tau$ exists and is finite, then $\lim_{t \rightarrow \infty} \Psi(t) = 0$.*

Theorem 2.1: *For the SFF mathematical model in Eq. (2.25) if, the sliding manifold is chosen as Eq. (2.32), the control law is defined as Eq. (2.40), and the parameter adaptation laws are defined as Eq. (2.41), then the system tracking error $e(t)$ will converge to zero as time approaches infinity.*

Proof: Consider the SFF equations of motion in the parameterized form as shown in Eq. (2.26) and multiplying the entire equation with B^T we get the following open-loop dynamics using the bounds of disturbances,

$$m_f B^T \dot{X} = m_f B^T A X + m_f B^T E(X) + U_f + G \quad (2.42)$$

Substituting the control law given by Eq. (2.40) in the open-loop dynamics we get,

$$\begin{aligned} m_f B^T \dot{X} &= m_f B^T A X + m_f B^T E(X) - \{\hat{m}_f C [A X + E(X) - \dot{X}_d] \\ &\quad + C B \hat{G} + \eta \text{sgn}(S)\} + G \end{aligned} \quad (2.43)$$

From Eq. (2.43), the following closed-loop error dynamics can be derived,

$$m_f \dot{S} = \tilde{m}_f C [A X + E(X) - \dot{X}_d] + \tilde{G} - \eta \text{sgn}(S) \quad (2.44)$$

Now consider the following Lyapunov function

$$V_1 = \frac{1}{2} S^T m_f S + \frac{1}{2\gamma_1} \tilde{m}_f^2 + \frac{1}{2} \tilde{G}^T W^{-1} \tilde{G} \quad (2.45)$$

Taking the first derivative along the trajectory of the system we get,

$$\dot{V}_1 = S^T m_f \dot{S} - \frac{1}{\gamma_1} \tilde{m}_f \dot{\tilde{m}}_f - \tilde{G}^T W^{-1} \dot{\tilde{G}} \quad (2.46)$$

Substituting Eq. (2.44) in Eq. (2.46) we get,

$$\begin{aligned} \dot{V}_1 &= S^T \left[\tilde{m}_f C [AX + E(X) - \dot{X}_d] + \tilde{G} - \eta \operatorname{sgn}(S) \right] - \frac{1}{\gamma_1} \tilde{m}_f \dot{\tilde{m}}_f - \tilde{G}^T W^{-1} \dot{\tilde{G}} \\ &= S^T [-\eta \operatorname{sgn}(S)] + \tilde{m}_f \left\{ S^T C [AX + E(X) - \dot{X}_d] - \frac{1}{\gamma_1} \dot{\tilde{m}}_f \right\} \\ &\quad + \tilde{G}^T [S - W^{-1} \dot{\tilde{G}}] \end{aligned} \quad (2.47)$$

Finally, by substituting Eq. (2.41) in Eq. (2.47) we conclude

$$\dot{V}_1 = S^T [-\eta \operatorname{sgn}(S)] \leq - \sum \eta_i |S_i| < 0 \quad \text{for } i = x, y, z \quad (2.48)$$

Since \dot{V}_1 is negative-definite and as stated before $\dot{V} < \dot{V}_1$, it is proven that \dot{V} is also negative-definite. Based on the inequality that $\sum |S_i| \geq \|S\|$ and defining $\lambda_{\min}(\eta) > 0$ as the minimum eigenvalue of the positive-definite matrix η , we can show that

$$\dot{V} \leq -\lambda_{\min}(\eta) \|S\| \quad (2.49)$$

Defining $|\Psi(t)| = \lambda_{\min}(\eta) \|S\| > 0$, and integrating both sides of Eq. (2.49) yields the following expression

$$V(0) \geq V(t) + \int_0^t |\Psi(\tau)| d\tau \geq \int_0^\infty |\Psi(\tau)| d\tau \quad (2.50)$$

From Eq. (2.50) we obtain that $S \in \mathcal{L}^\infty$. According to the proven condition from Eq. (2.48) we have $\dot{V} < \infty$ from which we can deduce the fact that $\dot{S} \in \mathcal{L}^\infty$. Taking the limit as $t \rightarrow \infty$ on both sides of Eq. (2.50) gives

$$\infty > V(0) \geq \lim_{t \rightarrow \infty} \int_0^t |\Psi(\tau)| d\tau \quad (2.51)$$

Now, using Barbalat's lemma (see Lemma 1) we obtain

$$\lim_{t \rightarrow \infty} |\Psi(\tau)| = \lim_{t \rightarrow \infty} \lambda_{\min}(\eta) \|S\| \rightarrow 0 \quad (2.52)$$

which implies that $S \rightarrow 0$ as $t \rightarrow \infty$. Since $V \in \mathcal{L}^\infty$, we can infer from Eq. (2.35) that $\tilde{m}_f, \tilde{G} \in \mathcal{L}^\infty$. Therefore, the adaptive control law described by Eqs. (2.40) and (2.41) ensures global asymptotic convergence of the position and velocity tracking errors, and all adaptive parameters associated with the closed-loop system are bounded. \square

Next, we prove that the SFF error trajectories can converge to the linear sliding surface S in finite-time. First, we introduce the following assumption,

$$L(\cdot) = \tilde{m}_f C [A(t)X + E - \dot{X}_d] + \tilde{G} \quad \text{and} \quad \|L\| \leq \bar{d} \quad (2.53)$$

Note that $L(\cdot)$ is the lumped term containing three parts: 1) system nonlinearities (depending on desired trajectories, spacecraft parameters, and nonlinear terms in equations of motion), 2) external disturbances (time-varying and state-dependent), and 3) parameter uncertainties. We assume that the term $L(\cdot)$ is bounded with an upper-bound of \bar{d} .

Theorem 2.2: *For the SFF mathematical model in Eq. (2.25), if the control law is defined as Eq. (2.40), then the trajectories, $e(t)$, of the closed-loop system will reach the sliding manifold, Eq. (2.32), $S = 0$ in finite-time.*

$$t_r \leq \frac{m_f \|S(0)\|}{\lambda_{\min}(\eta) - \bar{d}} \quad (2.54)$$

Proof: Consider the following candidate Lyapunov function,

$$V_f = \frac{1}{2} S^T m_f S \quad (2.55)$$

Taking the time derivative of Eq. (2.55) we get,

$$\dot{V}_f = S^T m_f \dot{S} \quad (2.56)$$

Substituting the closed-loop system given by Eq. (2.44) into Eq. (2.56) we obtain,

$$\dot{V}_f = S^T \left[\tilde{m}_f C [A(t)X + E - \dot{X}_d] + \tilde{G} - \eta \operatorname{sgn}(S) \right] \quad (2.57)$$

Based on the assumption given by Eq. (2.53) we obtain the following inequality,

$$\begin{aligned} \dot{V}_f &\leq S^T [\bar{d} - \eta \operatorname{sgn}(S)] \\ &\leq \bar{d} \|S\| - \lambda_{\min}(\eta) \|S\| \leq -[\lambda_{\min}(\eta) - \bar{d}] \|S\| \end{aligned} \quad (2.58)$$

By choosing $\eta > \bar{d}$ we prove that $\dot{V}_f < 0$. Also,

$$\dot{V}_f \leq - [\lambda_{\min}(\eta) - \bar{d}] \sqrt{\frac{2V_f}{m_f}} \quad (2.59)$$

Thus, we prove that the SFF error trajectories reach the sliding surface in finite-time. Integrating both sides of Eq. (2.59) from 0 to t_r we get,

$$\int_0^{t_r} \frac{dV_f}{\sqrt{V_f}} \leq - [\lambda_{\min}(\eta) - \bar{d}] \sqrt{\frac{2}{m_f}} \int_0^{t_r} dt \quad (2.60)$$

$$2 \left(\sqrt{V_f(t_r)} - \sqrt{V_f(0)} \right) \leq - [\lambda_{\min}(\eta) - \bar{d}] \sqrt{\frac{2}{m_f}} t_r \quad (2.61)$$

When the sliding surface is reached, $S(t_r) = 0$ and therefore, $V(t_r) = 0$. Using this property and the fact that $\sqrt{2V_f(0)/m_f} = \|S(0)\|$ in Eq. (2.61), we obtain

$$t_r \leq \frac{m_f \|S(0)\|}{\lambda_{\min}(\eta) - \bar{d}}$$

This completes the proof. □

2.2.4 Adaptive Nonsingular Terminal SMC

In this sub-section, an adaptive nonsingular terminal sliding mode control algorithm is designed for SFF. It is well known that the dynamic performance of a sliding mode controller relies heavily on the chosen *sliding manifold* or *switching surface*. We presented a conventional sliding mode controller based on linear sliding manifold in the previous sub-section. Nonlinear hyperplane based sliding modes offer a wide variety of design alternatives with fast and finite time convergence. Recently, a terminal sliding mode (TSM) control method was proposed and used in the control of rigid manipulators [Yuqiang *et al.* 1998].

The SMC schemes based on TSM were found to be very effective but singularity problems may occur if the initial conditions are not selected properly resulting in an infinite control law [Zhihong *et al.* 1994]. Based on the work presented by Feng *et al.* [Feng *et al.* 2002] we develop a nonsingular terminal sliding mode (NTSM) controller for SFF. The control algorithm is extended by adding a novel adaptive retrofit scheme to compensate for uncertainties in mass of the spacecraft, external disturbances, and actuator faults.

2.2.4.1 Design of Sliding Manifold

The objective is to improve the transient performance of the system substantially by designing nonlinear switching manifold. We reformulate the nonlinear SFF relative motion equations defined by Eq. (2.26) by multiplying with B^T , and the resulting equation can be represented in the following dynamical form

$$\begin{aligned} m_f \ddot{q} &= m_f M(q, \dot{q}) + U_f + F_d(t) \\ M(q, \dot{q}) &= B^T [AX + E(X)] \end{aligned} \quad (2.62)$$

where $q \in \mathbb{R}^3 = [x, y, z]^T$ is a vector of relative positions, and $M(q, \dot{q}) \in \mathbb{R}^3$ is a 3×1 vector containing the nonlinear terms. Let $q_d \in \mathbb{R}^3$ be the vector of desired positions for the follower spacecraft and $\dot{q}_d \in \mathbb{R}^3$ be the derivative of q_d . We now define, $\varepsilon(t) = q - q_d$, $\dot{\varepsilon}(t) = \dot{q} - \dot{q}_d$, and thus the error vector is described as follows:

$$e(t) = [\varepsilon, \dot{\varepsilon}]^T \quad (2.63)$$

The nonlinear sliding manifold is defined as

$$S = \varepsilon + C\dot{\varepsilon}^{p/q} \quad (2.64)$$

where $C \in \mathbb{R}^{3 \times 3}$ is a constant, diagonal, positive-definite, control design matrix. p and q are positive odd integers which satisfy the following condition

$$p > q \quad (2.65)$$

Remark 2.3: It is important to note that one of the vectors has fractional power in the nonlinear sliding surface given by Eq. (2.64). The vector $\dot{\varepsilon}^{p/q}$ is defined as

$$\dot{\varepsilon}^{p/q} = [(\dot{x} - \dot{x}_d)^{p/q}, (\dot{y} - \dot{y}_d)^{p/q}, (\dot{z} - \dot{z}_d)^{p/q}]^T$$

2.2.4.2 Controller Design

The design of a suitable control algorithm is the second phase of any VSC design procedure as mentioned earlier. Our objective is to derive a control law that can drive the the SFF error trajectories to the nonlinear switching surface defined in Eq. (2.64) and maintain

a sliding mode condition. In this section we derive the control law based on Lyapunov stability theorem. The candidate Lyapunov function is defined as follows:

$$V = \frac{1}{2}S^T m_f S + \frac{1}{2\gamma_1} \tilde{m}_f^2 + \frac{1}{2} \tilde{G}^T W^{-1} \tilde{G} \quad (2.66)$$

where γ_1 is a positive constant, and $W \in \mathbb{R}^{3 \times 3}$ is a constant, diagonal, positive-definite, adaptation gain matrix. Taking the derivative of V along its trajectory gives,

$$\begin{aligned} \dot{V} &= S^T m_f \dot{S} - \frac{1}{\gamma_1} \tilde{m}_f \dot{\tilde{m}}_f - \tilde{G}^T W^{-1} \dot{\tilde{G}} \\ &= S^T [m_f \dot{\varepsilon} + \frac{p}{q} C \dot{\varepsilon}^{p/q-1} m_f \ddot{\varepsilon}] - \frac{1}{\gamma_1} \tilde{m}_f \dot{\tilde{m}}_f - \tilde{G}^T W^{-1} \dot{\tilde{G}} \end{aligned} \quad (2.67)$$

Substituting for $m_f \ddot{q}$ from Eq. (2.62) into Eq. (2.67) we get

$$\begin{aligned} \dot{V} &= S^T [m_f \dot{\varepsilon} + \frac{p}{q} C \dot{\varepsilon}^{p/q-1} \{m_f M(q, \dot{q}) + U_f + F_d(t) - m_f \ddot{q}_d\}] - \frac{1}{\gamma_1} \tilde{m}_f \dot{\tilde{m}}_f - \tilde{G}^T W^{-1} \dot{\tilde{G}} \\ &= S^T [m_f \dot{\varepsilon} + \frac{p}{q} C \dot{\varepsilon}^{p/q-1} \{m_f M(q, \dot{q}) + U_f - m_f \ddot{q}_d\}] - \frac{1}{\gamma_1} \tilde{m}_f \dot{\tilde{m}}_f \\ &\quad + \frac{p}{q} S^T C \dot{\varepsilon}^{p/q-1} F_d(t) - \tilde{G}^T W^{-1} \dot{\tilde{G}} \end{aligned} \quad (2.68)$$

Since the disturbances are assumed to be bounded, we can define $\{\dot{V}_1 : \dot{V} < \dot{V}_1\}$ given by

$$\begin{aligned} \dot{V}_1 &= S^T [m_f \dot{\varepsilon} + \frac{p}{q} C \dot{\varepsilon}^{p/q-1} \{m_f M(q, \dot{q}) + U_f - m_f \ddot{q}_d\}] - \frac{1}{\gamma_1} \tilde{m}_f \dot{\tilde{m}}_f \\ &\quad + \frac{p}{q} S^T C \dot{\varepsilon}^{p/q-1} G - \tilde{G}^T W^{-1} \dot{\tilde{G}} \end{aligned} \quad (2.69)$$

Adding and subtracting, (1) $\hat{m}_f [\dot{\varepsilon} + (p/q) C M(q, \dot{q}) \dot{\varepsilon}^{(p/q-1)} - \ddot{q}_d]$, and (2) $(p/q) S^T C \dot{\varepsilon}^{(p/q-1)} \hat{G}$, we can replace the unknown terms in controller with the estimated parameters \hat{m}_f and \hat{G} .

The new form of \dot{V}_1 is as follows:

$$\begin{aligned} \dot{V}_1 &= S^T \left[\hat{m}_f \dot{\varepsilon} + \frac{p}{q} C \dot{\varepsilon}^{p/q-1} \left\{ \hat{m}_f M(q, \dot{q}) + U_f + \hat{G} - \hat{m}_f \ddot{q}_d \right\} \right] \\ &\quad + \tilde{m}_f S^T \left[\dot{\varepsilon} + \frac{p}{q} C \dot{\varepsilon}^{p/q-1} \{M(q, \dot{q}) - \ddot{q}_d\} \right] - \frac{1}{\gamma_1} \tilde{m}_f \dot{\tilde{m}}_f + \frac{p}{q} S^T C \dot{\varepsilon}^{p/q-1} \tilde{G} - \tilde{G}^T W^{-1} \dot{\tilde{G}} \end{aligned} \quad (2.70)$$

Based on Eq. (2.70) the control law is defined as,

$$U_f = -\hat{m}_f [M(q, \dot{q}) + \frac{q}{p} C^{-1} \dot{\varepsilon}^{2-p/q} - \ddot{q}_d] - \hat{G} - \eta \operatorname{sgn}(S) \quad (2.71)$$

where $\eta = \text{diag}\{\eta_x, \eta_y, \eta_z\}$ for all $\{\eta_i : \eta_i > 0\}$, and $\text{sgn}(S) = [\text{sgn}(S_x), \text{sgn}(S_y), \text{sgn}(S_z)]^T$. The adaptive laws for the unknown mass and external disturbances are chosen as,

$$\begin{aligned}\dot{\hat{m}}_f &= \gamma_1 S^T \left[\dot{\varepsilon} + \frac{p}{q} C \dot{\varepsilon}^{p/q-1} \{M(q, \dot{q}) - \ddot{q}_d\} \right] \\ \dot{\hat{G}} &= \frac{p}{q} W (C \dot{\varepsilon}^{p/q-1})^T S\end{aligned}\quad (2.72)$$

Remark 2.4: $\dot{\varepsilon}^{p/q-1}$ is a 3×3 diagonal matrix of the form

$$\dot{\varepsilon}^{(p/q-1)} = \begin{bmatrix} (\dot{x} - \dot{x}_d)^{(p/q-1)} & 0 & 0 \\ 0 & (\dot{y} - \dot{y}_d)^{(p/q-1)} & 0 \\ 0 & 0 & (\dot{z} - \dot{z}_d)^{(p/q-1)} \end{bmatrix}\quad (2.73)$$

Remark 2.5: Since p and q are positive odd integers, for the control law given by Eq. (2.71) to be non-singular, p and q must satisfy the inequality given by

$$1 < \frac{p}{q} < 2\quad (2.74)$$

2.2.4.3 Stability Analysis

In this section, we provide stability proof to show that the adaptive NTSM control law given by Eq. (2.71) guarantees global asymptotic stabilization of the tracking error.

Theorem 2.3: For the SFF model given by Eq. (2.62) if, the control laws are defined by Eqs. (2.71) and (2.72), then the error trajectories will converge to zero and the parameter estimation errors \tilde{m}_f and \tilde{G} will remain bounded as $t \rightarrow \infty$.

Proof: Now consider the following Lyapunov function

$$V = \frac{1}{2} S^T m_f S + \frac{1}{2\gamma_1} \tilde{m}_f^2 + \frac{1}{2} \tilde{G}^T W^{-1} \tilde{G}\quad (2.75)$$

Taking the first derivative of Eq. (2.75), substituting for $m_f \ddot{q}$ from Eq. (2.62), and following the steps described by Eqs. (2.67)-(2.69), we get

$$\begin{aligned}\dot{V}_1 &= S^T \left[\dot{\hat{m}}_f \dot{\varepsilon} + \frac{p}{q} C \dot{\varepsilon}^{p/q-1} \{ \hat{m}_f M(q, \dot{q}) + U_f + \hat{G} - \hat{m}_f \ddot{q}_d \} \right] \\ &\quad + \tilde{m}_f S^T \left[\dot{\varepsilon} + \frac{p}{q} C \dot{\varepsilon}^{p/q-1} \{ M(q, \dot{q}) - \ddot{q}_d \} \right] - \frac{1}{\gamma_1} \tilde{m}_f \dot{\hat{m}}_f \\ &\quad + \frac{p}{q} S^T C \dot{\varepsilon}^{p/q-1} \tilde{G} - \tilde{G}^T W^{-1} \dot{\hat{G}}\end{aligned}\quad (2.76)$$

Substituting the control law given by Eq. (2.71) and the parameter adaptation laws given by Eq. (2.72) in Eq. (2.76), and then canceling out the common terms we get,

$$\begin{aligned}\dot{V}_1 &= S^T \left[-\frac{p}{q} C \dot{\varepsilon}^{p/q-1} \eta \operatorname{sgn}(S) \right] \\ &\leq -\frac{p}{q} \sum C_i \dot{\varepsilon}_i^{p/q-1} \eta_i |S_i| \quad \text{for } i = x, y, z\end{aligned}\quad (2.77)$$

Applying the property given by Eq. (2.74) to Eq. (2.77), we obtain $\dot{V}_1 < 0$. Since \dot{V}_1 is negative-definite and as stated before $\dot{V} < \dot{V}_1$, it is proven that \dot{V} is also negative-definite. Therefore, V is a non-increasing Lyapunov function in the S -space. This implies that $V \in \mathcal{L}^\infty$ and we can establish that $S, \hat{m}_f, \hat{G} \in \mathcal{L}^\infty$. Therefore, the proposed NTSM control law ensures global asymptotic convergence of the SFF error trajectories to zero, and all adaptive estimation errors, \tilde{m}_f and \tilde{G} , are bounded as $t \rightarrow \infty$. \square

Although it is shown using Theorem 2.3 that $S \rightarrow 0$ as $t \rightarrow \infty$, we can utilize a different Lyapunov function to show that the SFF trajectories will reach $S = 0$ in finite-time, t_r . Based on the sliding manifold described by Eq. (2.64) we obtain,

$$m_f \dot{S} = m_f \dot{\varepsilon} + \frac{p}{q} C \dot{\varepsilon}^{\frac{p}{q}-1} (m_f M(q, \dot{q}) + U_f + F_d - m_f \ddot{q}_d) \quad (2.78)$$

Substituting for U_f from Eq. (2.71) into Eq. (2.78) yields

$$\begin{aligned}m_f \dot{S} &= m_f \dot{\varepsilon} + \frac{p}{q} C \dot{\varepsilon}^{\frac{p}{q}-1} \left\{ \begin{array}{l} m_f M(q, \dot{q}) + F_d - m_f \ddot{q}_d - \hat{G} - \eta \operatorname{sgn}(S) \\ -\hat{m}_f \left[M(q, \dot{q}) + \frac{q}{p} C^{-1} \dot{\varepsilon}^{2-\frac{p}{q}} - \ddot{q}_d \right] \end{array} \right\} \\ &= \frac{p}{q} C \dot{\varepsilon}^{\frac{p}{q}-1} \left[\tilde{m}_f M(q, \dot{q}) - \tilde{m}_f \ddot{q}_d + F_d - \hat{G} - \eta \operatorname{sgn}(S) + \tilde{m}_f \frac{q}{p} C^{-1} \dot{\varepsilon}^{2-\frac{p}{q}} \right]\end{aligned}$$

Carrying out further simplifications and collecting terms we obtain the following closed-loop error equation for the SFF system.

$$m_f \dot{S} = \frac{p}{q} C \dot{\varepsilon}^{\frac{p}{q}-1} \left\{ \tilde{m}_f \left[M(q, \dot{q}) + \frac{q}{p} C^{-1} \dot{\varepsilon}^{2-\frac{p}{q}} - \ddot{q}_d \right] + F_d - \hat{G} - \eta \operatorname{sgn}(S) \right\} \quad (2.79)$$

Since \tilde{m}_f and \tilde{G} are bounded, the following assumption is valid.

$$\left\| \tilde{m}_f \left[M(q, \dot{q}) + \frac{q}{p} C^{-1} \dot{\varepsilon}^{2-\frac{p}{q}} - \ddot{q}_d \right] \right\| + \|\tilde{G}\| \leq \Delta \quad (2.80)$$

Theorem 2.4: For the SFF mathematical model in Eq. (2.62), if the control law is defined as Eq. (2.71), then the trajectories, ε , of the closed-loop system will reach the nonlinear sliding manifold, Eq. (2.64), $S = 0$ in finite-time.

$$t_r \leq \frac{m_f \|S(0)\|}{k_s} \quad (2.81)$$

Proof: Consider the following candidate Lyapunov function,

$$V_f = \frac{1}{2} S^T m_f S \quad (2.82)$$

Taking the time derivative of Eq. (2.82) and substituting the closed-loop error system given by Eq. (2.79) we obtain,

$$\begin{aligned} \dot{V}_f &= \frac{p}{q} S^T C \varepsilon^{\frac{p}{q}-1} \left[\tilde{m}_f \left(M + \frac{q}{p} C^{-1} \varepsilon^{2-\frac{p}{q}} - \ddot{q} \right) + F_d - \hat{G} - \eta \operatorname{sgn}(S) \right] \\ &\leq \|S\| \|C \varepsilon^{\frac{p}{q}-1}\| \left[\left\| \tilde{m}_f \left[M(q, \dot{q}) + \frac{q}{p} C^{-1} \varepsilon^{2-\frac{p}{q}} - \ddot{q} \right] \right\| + \|\tilde{G}\| - \lambda_{\min}(\eta) \right] \\ &\leq -k_s \|S\| < 0 \quad \text{for } \|S\| \neq 0 \end{aligned} \quad (2.83)$$

where $k_s = \lambda_{\min}(\eta) - \Delta > 0$. Therefore, based on Lyapunov stability criterion, the NTSM manifold S in Eq. (2.64) converges to zero in finite-time

$$t_r \leq \frac{m_f \|S(0)\|}{k_s} \quad (2.84)$$

If $S = \varepsilon + C\dot{\varepsilon}^{p/q} = 0$ is reached, then, from Theorem 2.4 it can be obtained that the SFF error trajectories ε and $\dot{\varepsilon}$ will converge to zero in finite time. This completes the proof. \square

When the sliding mode $S = 0$ is reached the system dynamics is described by the following nonlinear differential equation

$$S = \varepsilon + C\dot{\varepsilon}^{p/q} = 0 \quad (2.85)$$

The finite time t_s taken for the system to travel from $\varepsilon(t_r) \neq 0$ to $\varepsilon(t_r + t_s) = 0$ can be derived as the solution to the first-order differential system in Eq. (2.85). This is given by

$$\begin{aligned} t_{si} &= -C^{q/p} \int_{\varepsilon_i(t_{ri})}^{\varepsilon_i(t_{ri}+t_{si})} \frac{d\varepsilon_i}{\varepsilon_i^{q/p}} \\ &= -C^{q/p} \frac{p}{p-q} \left[|\varepsilon_i(t_{ri} + t_{si})|^{1-q/p} - |\varepsilon_i(t_{ri})|^{1-q/p} \right] \\ &= C^{q/p} \frac{p}{p-q} |\varepsilon_i(t_{ri})|^{1-q/p} \end{aligned} \quad (2.86)$$

2.3 Performance Evaluation

To study the effectiveness and performance of the proposed formation control strategies, the detailed response is numerically simulated using the set of governing equations of motion [Eqs. (2.3)-(2.7)] in conjunction with the proposed control laws [Eqs. (2.40) and (2.71)]. The leader spacecraft is in an elliptic orbit with perigee altitude 500 km and an eccentricity of 0.2. The simulations were performed with the following parameters, $m_f = 10$ kg, $\Omega_l, \omega_l, i_l = 0^\circ$, and $\mu_e = 398600 \text{ km}^3\text{s}^{-2}$. The net disturbance force acting on the system is considered to be time-varying [Pongythithum *et al.* 2005] given by (in N),

$$\begin{bmatrix} F_{dx} \\ F_{dy} \\ F_{dz} \end{bmatrix} = 1.2 \times 10^{-3} \begin{bmatrix} 1 - 1.5 \sin(nt) \\ 0.5 \sin(2nt) \\ \sin(nt) \end{bmatrix} \quad (2.87)$$

The control gains used in all simulations for adaptive sliding mode control (ASMC) and adaptive nonsingular terminal sliding mode control (ANTSMC) are shown in Table 2.1. First, we present the effectiveness of the control strategies for a fault-free case of station-

Table 2.1: ASMC and ANTSMC parameters

Control Gains	ASMC	ANTSMC
$C_i, (i = 1, 2, 3)$	1	10^{-3}
$\{p, q\}$	--	{11, 9}
γ_1	0.08	0.08
$W_i, (i = 1, 2, 3)$	10^{-7}	10^{-7}
$\psi_i, (i = x, y, z)$	0.8	0.8
$\eta_i, (i = x, y, z)$	0.1	0.1
$N_i, (i = x, y, z)[mN]$	10	10

keeping and formation maneuvering. We then examine the effects of actuator degradation, actuator stuck fault, and short-term actuator failure on the performance of the proposed control strategies. Lastly, we illustrate some quantitative analysis on fuel consumption and steady-state stabilization errors.

2.3.1 Nominal Case

The desired relative motion considered for ideal formation-keeping is a projected circular formation, described by Eq. (2.9), with a 1 km formation radius. The phase angle (ϕ) between the leader and follower spacecraft is assumed to be 0 deg. The initial states for the numerical simulation are computed by substituting $t = 0$ in Eq. (2.9) and adding a 1 km position offset on x , y , and z . The initial velocity components for all states are calculated by taking the time derivative of Eq. (2.9) and substituting $t = 0$. The initial conditions for the parameter estimates are

$$\hat{m}_f(0) = 10 \quad \text{and} \quad \hat{G}(0) = [0, 0, 0]^T \quad (2.88)$$

Figure 2.4 shows relative position errors and thrust demand for formation-keeping when there is a 1 km position offset on all three relative states. The objective is to stabilize the

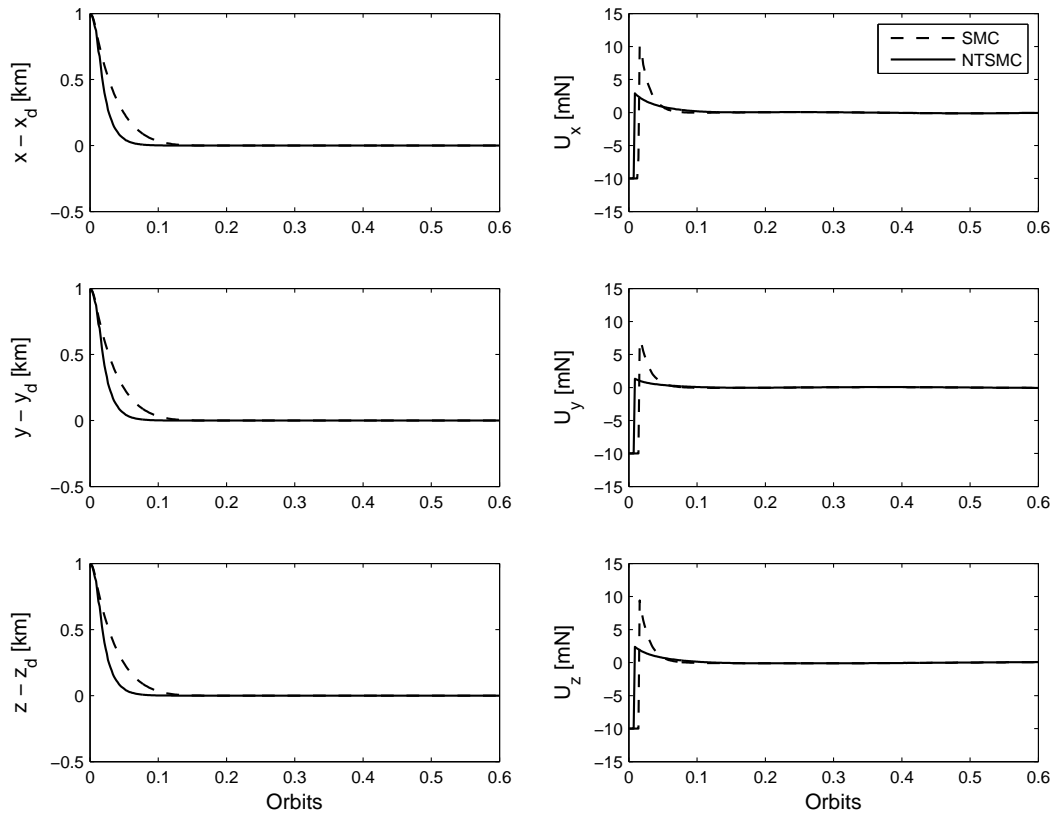


Figure 2.4: Relative position errors and thrust demand for formation keeping.

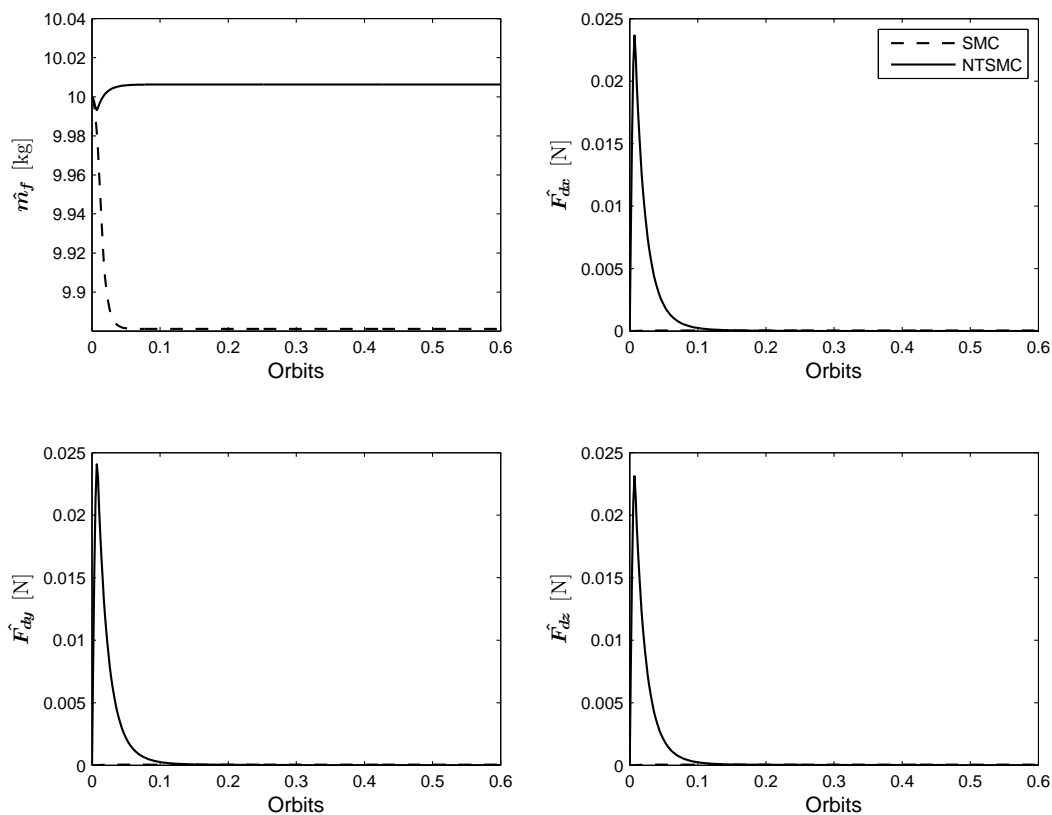


Figure 2.5: Adaptive parameter estimates for formation keeping.

formation when there is an initial misalignment, while positioning the follower spacecraft in orbit. The control forces are saturated at 10 mN. The advantage of using a nonlinear sliding surface can be seen in the error convergence plots in Fig. 2.4. Although a 1 km position offset is very high, it was used to examine the effects of control input saturation. ANTSMC requires less control input when compared to fuel consumed using ASMC and it can be seen that the control forces are saturated early in the transient period. The adaptive parameter estimates are shown in Fig. 2.5.

Next, we demonstrate the effectiveness of the proposed control strategies for multiple formation maneuvers. With the same initial conditions used for the formation keeping case, the follower spacecraft moves from a 1 to 10 km radius projected circular formation after two orbits and then after six orbits, the follower spacecraft maneuvers to a circular formation of 20 km radius. Figure 2.6 shows the relative position errors and thrust demand

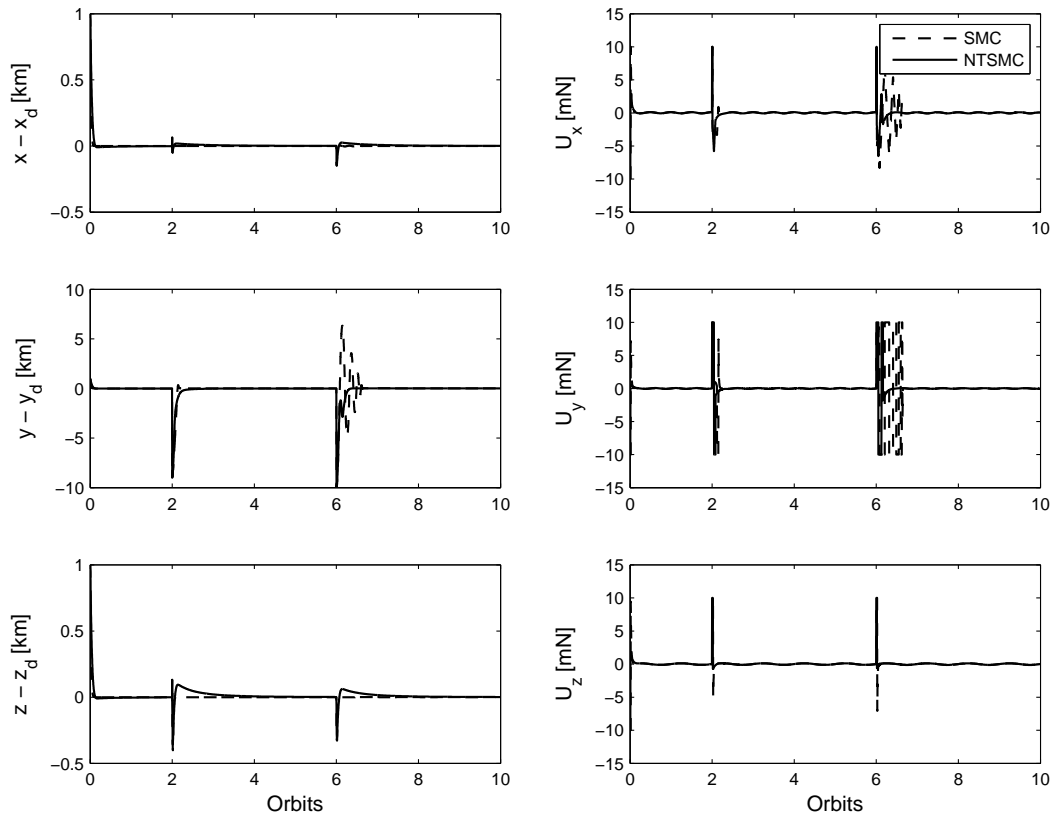


Figure 2.6: Tracking errors and thrust demand for formation reconfiguration.

for multiple formation maneuvers. It is clearly evident that U_y of ASMC saturates for a longer time after the second maneuver, which explains the bad performance of the controller in tracking the 20 km desired circular formation ($y - y_d$). This can also be observed in the 3D trajectory of the follower spacecraft, plotted in Fig. 2.7. ANTSMC ensures that the follower spacecraft maintains the desired geometry throughout the control process. Varying the control gains for ASMC can improve its performance, but it is important to keep the gains same (as shown in Table 2.1) for all simulation cases to establish a fair comparison between two control algorithms. Overall, the performance of both ASMC and ANTSMC, based on the formation maneuver criteria mentioned above, was very similar. The main differences were that, for the same maneuver sequence, the ANTSMC scheme was able to move the follower spacecraft with greater speed and more directly to the target reference orbit with less control saturation.

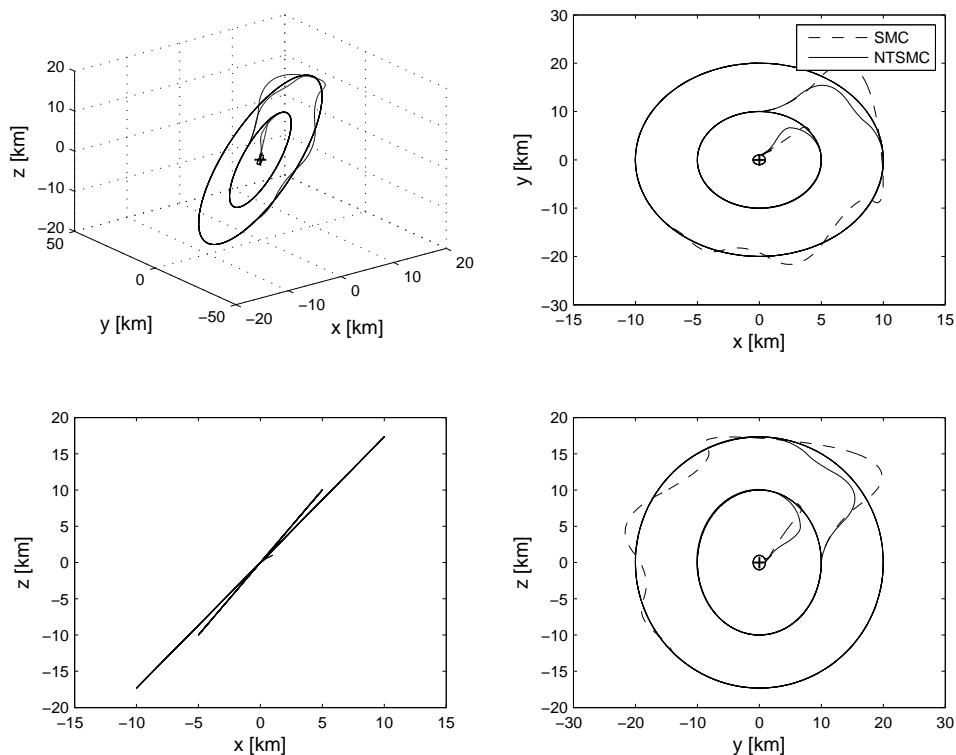


Figure 2.7: Three-dimensional trajectories of the entire formation maneuver.

2.3.2 Fault Case

In this section, we demonstrate the performance of the proposed control strategies when an abrupt actuator fault occurs. Our goal is to achieve the same formation objectives in the presence of actuator faults. We consider the following fault scenarios:

1. The first case considered is thruster degradation. In this case the effectiveness of the thrusters is decreased (LOE) after a certain time period, and it can be characterized by a decrease in actuator gain with respect to its nominal value given by, $u_{Fi} = \bar{k}u_{Fi}$, where $0 < \bar{k} < 1$, after failure.
2. We then assess the case for which all three thrusters are stuck at a particular position for a certain time period. This type of fault is called LIP and is given by $u_{Fi} = \bar{u}_{Fi}(t_f)$ where \bar{u}_{Fi} denotes the control input value at the time instant t_f of failure.
3. The third case presented is short-term failure of all three thrusters.

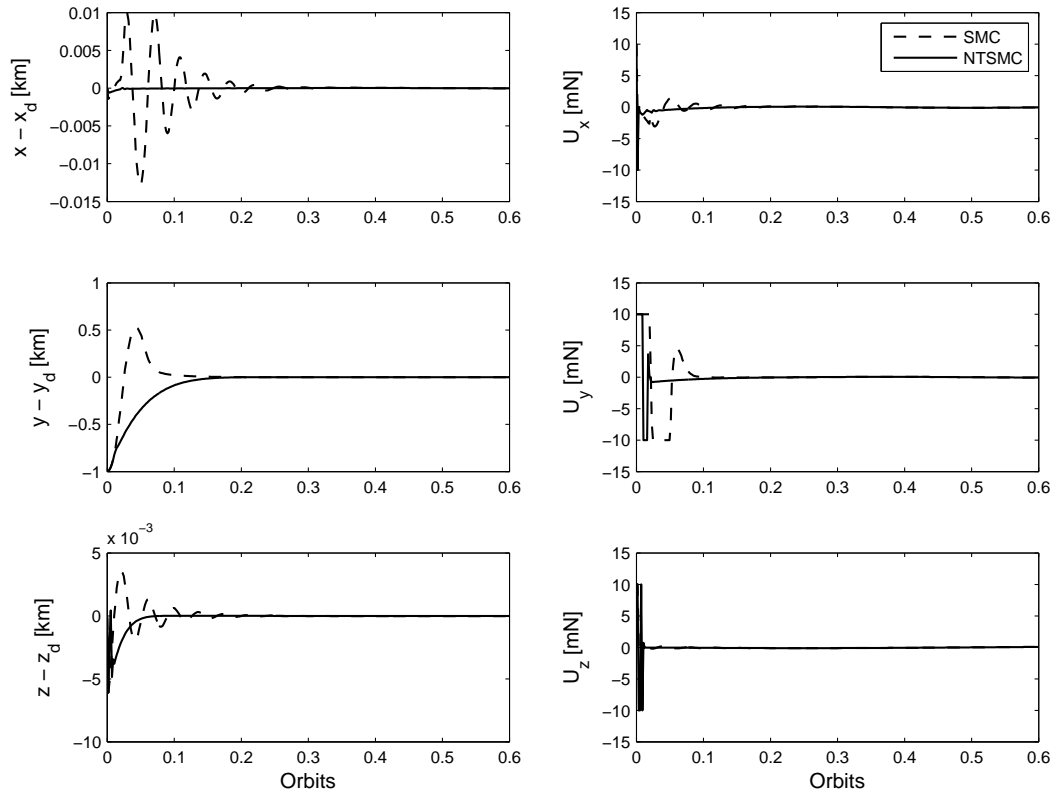


Figure 2.8: Relative position errors and thrust demand for formation keeping when thrusters degrade by 90% after 0.02 orbit.

For all the previously mentioned cases, the controller is never given any information of the faults, and therefore the proposed control algorithms accommodate the system faults without the process of fault detection and isolation.

Figure 2.8 shows the controlled position errors and control input required for formation-keeping when all three thrusters can only supply 10% of the actuation power after the time instant $t = 0.02$ orbit. The initial conditions for this case are given by, $X(0) = [0, 0, 0, 0, 0, 0]^T$. We consider the case where the leader spacecraft and the follower spacecraft are at the same location initially. It is seen that high control precision and smooth trajectory tracking are still obtained even when thrusters have encountered severe degradation. As evident in Fig. 2.8, the control inputs remain saturated for longer periods when compared with the case of no fault in Fig. 2.4. The degradation also has an effect on the error convergence of $(x - x_d)$ for the case of ASMC.

Performance of the proposed control algorithms to the LIP fault case is illustrated in Fig. 2.9 for the case of formation maneuvering from a 1 to 10 km projected circular formation after 2 orbits. All three control forces encounter an abrupt blockage between 1 and 2.2 orbits. Because the formation maneuver sequence starts after 2 orbits, the ASMC controller exhibits poor performance in tracking the desired trajectory. ANTSMC ensures that the errors accumulated during the fault period can be stabilized at a faster rate when compared with ASMC. This illustrates the fast convergence property of ANTSMC.

Figure 2.10 presents the relative position errors and control force for the case where all three thrusters fail between 0.5 and 1.5 orbits. This case can also be considered to simulate the scenario where the thrusters had to be switched off due to failure of the relative navigation sensors. With no control for an entire orbit, the follower spacecraft cannot track

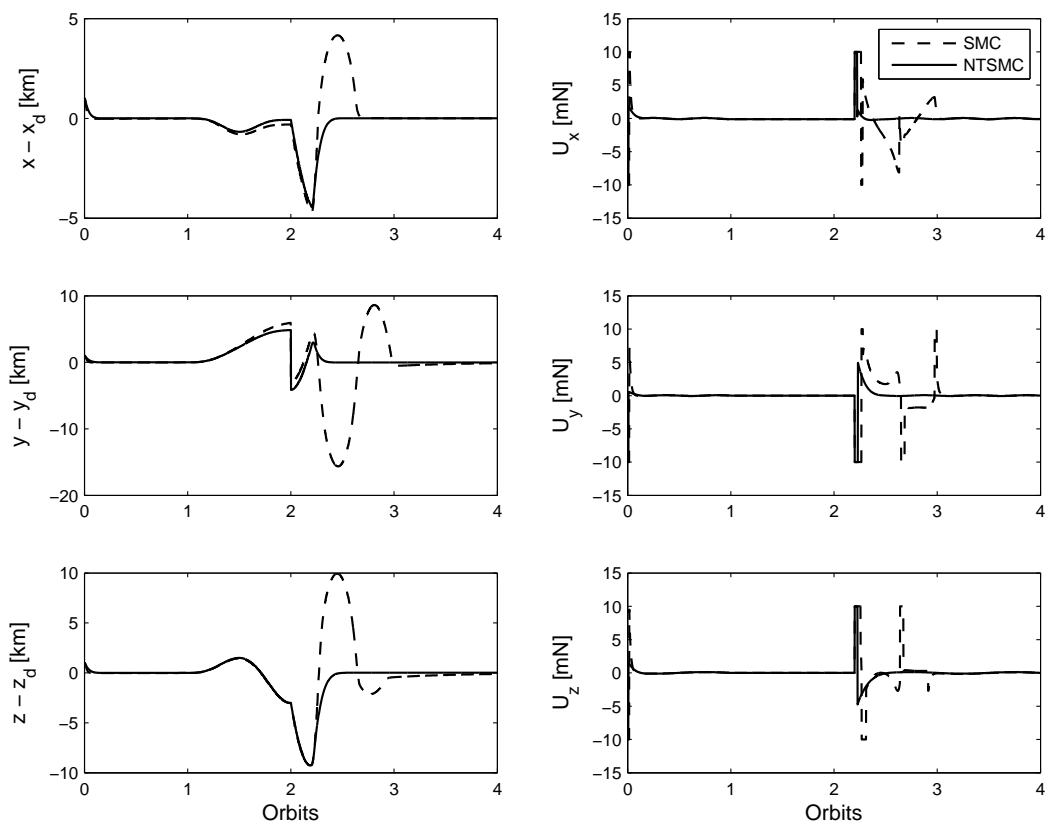


Figure 2.9: Relative position errors and thrust demand for formation maneuvering when thrusters 'jam' between 1 and 2 orbits.

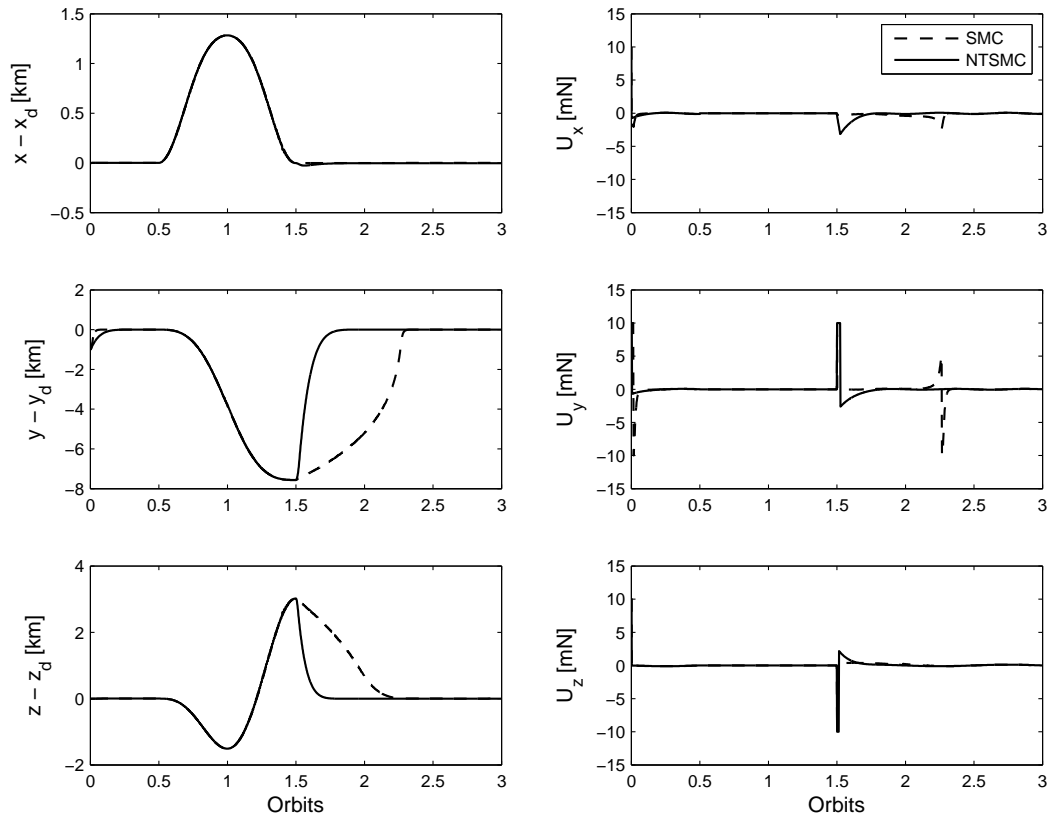


Figure 2.10: Relative position errors and thrust demand for formation keeping when thrusters 'fail' between 0.5 and 1.5 orbits.

its desired states satisfactorily whilst accumulating large errors. When the control input gets back into operation, within the same range of position errors, the adaptive NTSM controller dictates faster error convergence. It is seen that fairly good control performance is achieved under this severe scenario with limited thrust. In the case of ASMC, the system takes a longer time to settle to the desired formation.

2.3.3 Quantitative Analysis

Based on the performance analysis results detailed in this section, we compare the proposed control methodologies in terms of control precision and fuel consumption perspective. In assessing the effectiveness of the ASMC and NTSM controllers, the accuracy with which the formation can be maintained is an important criteria. Future missions of SFF for high-

resolution interferometry and stereographic imaging of the Earth demand high resolution and precision requirements for station-keeping. The maximum steady-state stabilization errors for all three directions for ASMC and NTSM techniques are compared in Table 2.2.

Table 2.2: Steady-state stabilization errors

Tracking error, km	Circular Reference Orbit		Elliptic Reference Orbit	
	Adaptive SMC	Adaptive NTSMC	Adaptive SMC	Adaptive NTSMC
$ e_x $	2.4×10^{-5}	5.6×10^{-8}	7.8×10^{-4}	1.5×10^{-7}
$ e_y $	1.1×10^{-5}	2.8×10^{-8}	4.2×10^{-4}	0.5×10^{-7}
$ e_z $	6.3×10^{-5}	3.5×10^{-8}	1.5×10^{-4}	1.3×10^{-7}

Table 2.3: Fuel-consumption per orbit

Fuel Consumption, m/s (per orbit)	Circular Reference Orbit		Elliptic Reference Orbit	
	Adaptive SMC	Adaptive NTSMC	Adaptive SMC	Adaptive NTSMC
ΔV_x	0.0409	0.0231	0.1382	0.1211
ΔV_y	0.1183	0.0374	0.1541	0.0734
ΔV_z	0.0555	0.0235	0.3050	0.2627

We considered an initial misalignment position offset of 100 m in all three directions and external disturbances for cases where the leader spacecraft is in a circular and elliptic reference orbit ($e = 0.2$). Both controllers are extensively tuned for fair comparison. The adaptive NTSM controller provides much better results when compared to any VSC based control algorithm present in current literature [Yeh *et al.* 2002, Lim *et al.* 2003, Massey & Shtessel 2005, Wang & Zhang 2007, Liu *et al.* 2006]. It is clearly evident from the values of largest steady-state errors that ASMC and NTSM control schemes satisfies the requirement of submillimeter precision in formation keeping.

The fuel consumption for all three thrusters are calculated for the same simulations described previously, and their respective ΔV requirements are shown in Table 2.3. The

ΔV is calculated based on the average budget obtained over a period of 10 orbits. The adaptive NTSM controller requires less fuel to correct for an initial position offset of 100m in 0.2 orbits when compared with the ASMC technique. For an elliptical orbit ($e = 0.2$), the corresponding fuel costs in terms of ΔV for both controllers are also shown in Table 2.3. Overall, it is very clear from the numerical simulation results that the proposed formation control scheme is mainly responsible for rejecting disturbances, maintaining formation stability, and commanding the formation.

2.4 Summary

In this chapter, we proposed two control strategies for efficient formation control using a novel adaptive framework. An adaptive nonsingular terminal sliding mode control scheme derived based on a nonlinear sliding manifold, and an adaptive sliding mode control algorithm formulated based on a conventional linear sliding manifold, was presented for a multiple spacecraft formation flying system comprising of a leader and a follower spacecraft. Uncertainties in the mass of the follower spacecraft and external disturbances with an unknown bound were employed to develop a novel adaptive parameter update scheme. The performance of the algorithms developed were through numerical simulation studies. The main objective was to develop a fault tolerant control scheme capable of providing submillimeter formation precision in the event of unexpected thruster faults.

The next chapter explores the feasibility of deploying only two pairs of thrusters in orthogonal directions to control multiple spacecraft formations. The dynamics of the SFF system examined in this chapter have the property that even if no control is exerted parallel to the radial direction or along-track direction, the resultant control configuration can ensure long-term formation-keeping and reconfiguration maneuvers. The advantages of this underactuated configuration is examined in Chapter 3. This is followed by experimental validation of the proposed technique on a hardware-in-loop (HIL) formation flying test-bed. Taking advantage of the nonlinear coupling in the radial and along-track equations of motion, an underactuated SFF configuration can be synthesized.

CHAPTER 3

Control of Underactuated Spacecraft Formations

FEASIBILITY of achieving reliable formation control without the need for thrust in the radial or along-track direction is explored in this chapter. Control algorithms developed in Chapter 2 were capable of achieving high precision formation maintenance and reconfiguration in the presence of time-varying uncertainties, disturbances, and thruster faults. These algorithms were developed based on the assumption that the formation geometry is maintained with a sufficient number of thrusters equal to, or larger than, the number of degrees of freedom to be controlled. Thus, the actuator configuration is still capable of providing control forces along three orthogonal directions despite the occurrence of thruster faults. In this chapter, we consider the case of complete failure of a pair of thrusters such that the AOCS onboard a follower spacecraft is no longer capable of providing control thrust in one of the three orthogonal directions.

We propose a nonlinear control scheme that requires either *radial* axis or *along-track* thrust, combined with force in the *cross-track* direction to control the motion of the follower spacecraft from any arbitrary initial condition to a closed stable relative orbit around the leader spacecraft. A design based on this framework must be precise, reliable, and simple enough to allow onboard implementation. Using fewer thrusters in an underactuated SFF configuration also offers reduced fuel expenditure. The benefits of the proposed controller are validated using numerical simulations to show that precise formation maintenance can be achieved in the presence of nonlinearities, variations in initial conditions, external disturbances, and control force saturation. Formation maintenance capability of the proposed algorithm is also validated on a hardware testbed using the *Satellite Airbed Formation Experiment* platform developed at Ryerson University.

The chapter is organized as follows: Nonlinear control algorithm based on sliding mode technique is formulated with detailed proof of stability for the closed-loop system in Section 3.1. For a detailed assessment of the system performance under the proposed control strategy, the results of numerical simulations incorporating different mission scenarios are presented in Section 3.2. The results of the HIL simulation using the SAFE system in underactuated configuration is presented in Section 3.3. Finally, the conclusions of the present study are stated in Section 3.4.

3.1 Design of Control Laws

The proposed system comprises of a *leader spacecraft* in an elliptical planar trajectory with the Earth's center at one of its foci and a *follower spacecraft* moving in a desired relative trajectory about the leader spacecraft (see Fig. 2.1). The mathematical model of the SFF system has been presented in Chapter 2, Section 2.1. These equations will not be reproduced in this chapter for brevity. Readers are requested to refer to equations of motion in Section 2.1 as prompted when developing control algorithms in this section. The control objective is to compute the thrust required to drive the follower spacecraft to a desired formation trajectory [Eqs. (2.8)-(2.9)] with respect to the leader spacecraft in the presence external perturbations. This task will be accomplished based on two important cases considered in this study, (1) No thrust along radial axis ($u_{fx} = 0$), and (2) No thrust available in the along-track direction ($u_{fy} = 0$). The desired trajectories for formation keeping considered in this study are, (1) Circular formation [Eq. (2.8)] with formation size r_{dc} , and (2) Projected circular formation [Eq. (2.9)] with formation size r_{dpc} . To implement a formation maneuver from one type of formation to another, we study a combination of both circular and projected circular formations with different formation sizes.

3.1.1 System Controllability

In order to check the controllability, we derive a linear system model from the given non-linear system equations of motion [Eqs. (2.5)-(2.7)] assuming the leader spacecraft in a circular orbit and taking first order perturbations for system variables x , y , and z . Thus,

the C-W equations follow their natural closed trajectory solutions (circular or projected circular formations) when the nonlinear model is linearized with respect to the leader spacecraft orbit. The state-space representation of the C-W equations is given by

$$\begin{bmatrix} \dot{x} \\ \dot{y} \\ \dot{z} \\ \ddot{x} \\ \ddot{y} \\ \ddot{z} \end{bmatrix} = \begin{bmatrix} 0 & 0 & 0 & 1 & 0 & 0 \\ 0 & 0 & 0 & 0 & 1 & 0 \\ 0 & 0 & 0 & 0 & 0 & 1 \\ 3n^2 & 0 & 0 & 0 & 2n & 0 \\ 0 & 0 & 0 & -2n & 0 & 0 \\ 0 & 0 & -n^2 & 0 & 0 & 0 \end{bmatrix} \begin{bmatrix} x \\ y \\ z \\ \dot{x} \\ \dot{y} \\ \dot{z} \end{bmatrix} + \begin{bmatrix} 0 & 0 & 0 \\ 0 & 0 & 0 \\ 0 & 0 & 0 \\ 1 & 0 & 0 \\ 0 & 1 & 0 \\ 0 & 0 & 1 \end{bmatrix} \begin{bmatrix} u_{fx} \\ u_{fy} \\ u_{fz} \end{bmatrix} \quad (3.1)$$

In general the above representation is expressed as $\dot{X} = AX + BU_F$, where $X \in \mathbb{R}^{6 \times 1}$ is the state vector, $A \in \mathbb{R}^{6 \times 6}$, $B \in \mathbb{R}^{6 \times 3}$, and $U_F \in \mathbb{R}^3 = [u_{fx}, u_{fy}, u_{fz}]^T$ is the vector of actual control inputs generated by the thrusters. As evident, the motion of the system in the orbital plane (radial/along-track or x/y) is decoupled from the out of plane motion (z). The cross-track component of the system has open-loop eigenvalues of $\lambda_{5,6} = \pm nj$ exhibiting a simple harmonic oscillator (Lyapunov stable but not asymptotically stable) [Starin *et al.* 2001b, Vassar & Sherwood 1985]. Therefore, under the influences of external perturbations and initial offset errors, a closed-loop control for the cross-track subsystem is necessary. The in-plane dynamics of the linear system can be represented in state-space form as follows:

$$\begin{bmatrix} \dot{x} \\ \dot{y} \\ \ddot{x} \\ \ddot{y} \end{bmatrix} = \begin{bmatrix} 0 & 0 & 1 & 0 \\ 0 & 0 & 0 & 1 \\ 3n^2 & 0 & 0 & 2n \\ 0 & 0 & -2n & 0 \end{bmatrix} \begin{bmatrix} x \\ y \\ \dot{x} \\ \dot{y} \end{bmatrix} + \begin{bmatrix} 0 & 0 \\ 0 & 0 \\ 1 & 0 \\ 0 & 1 \end{bmatrix} \begin{bmatrix} u_{fx} \\ u_{fy} \end{bmatrix} \quad (3.2)$$

The open-loop eigenvalues of the in-plane system are $\lambda_1 = 0$, $\lambda_2 = 0$, and $\lambda_{3,4} = \pm nj$. Utilizing the linear representation and assuming the system outputs to be x and y , the input-output transfer function based on control inputs u_{fx} and u_{fy} can be computed using $G(s) = Y(s)/U(s) = C(sI - A)^{-1}B$.

$$Y(s) = \frac{1}{s^2(s^2 + n^2)} \begin{bmatrix} s^2 & 2ns \\ -2ns & (s^2 - 3n^2) \end{bmatrix} U(s) \quad (3.3)$$

From the transfer function it is clearly evident that the associated modes are: (1) a pair of purely imaginary poles at the orbital frequency n , and (2) one double integrator. This implies that the system is conservative (imaginary modes), but unstable because of the double integrator. Therefore, the open-loop spacecraft relative translational dynamics are inherently unstable [Demourant & Chretien 2008]. Considering external disturbances and errors in initial conditions along with no control authority, the follower spacecraft will drift away from the leader spacecraft thereby dispersing the desired formation. With control available on both radial and along-track directions, the system in Eq. (3.2) is fully state controllable with rank = 4.

We now evaluate the controllability of the SFF system based on underactuated configuration candidates, no radial-axis or along-track input using the famous Kalman rank condition for controllability. Determining the controllability rank of the in-plane SFF linear system relative to the individual components of its input (radial or along-track) is very useful if one or more of the thrusters were to fail.

3.1.1.1 No radial axis control

The in-plane dynamics with control authority available only in the along-track direction can be expressed in standard state-space form as

$$\begin{bmatrix} \dot{x} \\ \dot{y} \\ \ddot{x} \\ \ddot{y} \end{bmatrix} = \begin{bmatrix} 0 & 0 & 1 & 0 \\ 0 & 0 & 0 & 1 \\ 3n^2 & 0 & 0 & 2n \\ 0 & 0 & -2n & 0 \end{bmatrix} \begin{bmatrix} x \\ y \\ \dot{x} \\ \dot{y} \end{bmatrix} + \begin{bmatrix} 0 \\ 0 \\ 0 \\ 1 \end{bmatrix} u_{fy} \quad (3.4)$$

where $X_a \in \mathbb{R}^{4 \times 1} = [x, y, \dot{x}, \dot{y}]^T$ is the state vector with $\bar{A}_a \in \mathbb{R}^{4 \times 4}$ and $\bar{B}_a \in \mathbb{R}^{4 \times 1} = [0, 0, 0, 1]^T$ denotes the underactuated in-plane system with thrust available only in the along-track direction. The controllability matrix for the LTI system in Eq. (3.4) can be computed using the formula $\mathfrak{C}_y = [B_a \ A_a B_a \ A_a^2 B_a \ A_a^3 B_a]$

$$\mathfrak{C}_y = \begin{bmatrix} 0 & 0 & 2n & 0 \\ 0 & 1 & 0 & -4n^2 \\ 0 & 2n & 0 & -2n^3 \\ 1 & 0 & -4n^2 & 0 \end{bmatrix} \quad (3.5)$$

The controllability matrix in Eq. (3.5) has full rank 4 and is nonsingular since $\det(\mathfrak{C}_y) = 12n^4$. The row and column vectors of \mathfrak{C}_y are linearly independent. Therefore, the entire state X_a is controllable using only along-track input if the radial thruster u_{fx} fails.

3.1.1.2 No control in the along-track direction

The state-space representation of the in-plane SFF dynamics given by Eq. (3.2) is modified to examine the case where only radial axis input ($u_{fy} = 0$) is considered to stabilize the system. The state vector, $X_a \in \mathbb{R}^{4 \times 1}$, and the system matrix, $\bar{A}_a \in \mathbb{R}^{4 \times 4}$, remain the same as in Eq. (3.4), but the new control matrix with no along-track input is given by $\bar{B}_b \in \mathbb{R}^{4 \times 1} = [0, 0, 1, 0]^T$. The resulting controllability matrix has the following form

$$\mathfrak{C}_x = \begin{bmatrix} 0 & 1 & 0 & -n^2 \\ 0 & 0 & -2n & 0 \\ 1 & 0 & -n^2 & 0 \\ 0 & -2n & 0 & 2n^3 \end{bmatrix} \quad (3.6)$$

Based on Eq. (3.6) it is clearly evident that the vectors of rows 1 and 4 of \mathfrak{C}_x are linearly dependent and $\det(\mathfrak{C}_x) = 4n^4 - 4n^4 = 0$, with $\text{rank } \mathfrak{C}_x = 3 < 4 = n$. Therefore, the in-plane SFF system is not completely state controllable with radial thruster (u_{fx}) alone if the along-track thruster (u_{fy}) were to fail. Before we conclude that the linear approximation is not stabilizable, it is important to determine the eigenvalue associated with the uncontrollable mode. Rearranging terms in Eq. (3.4) to represent the in-plane dynamics of the SFF system with only radial-axis input gives,

$$\begin{bmatrix} \dot{x} \\ \dot{y} \\ \ddot{y} \\ \dot{x} \end{bmatrix} = \begin{bmatrix} 0 & 0 & 0 & 1 \\ 0 & 0 & 1 & 0 \\ 0 & 0 & 0 & -2n \\ 3n^2 & 0 & 2n & 0 \end{bmatrix} \begin{bmatrix} x \\ y \\ \dot{y} \\ \dot{x} \end{bmatrix} + \begin{bmatrix} 0 \\ 0 \\ 0 \\ 1 \end{bmatrix} u_{fx} \quad (3.7)$$

Let $\bar{A}_b \in \mathbb{R}^{4 \times 4}$ and $\bar{B}_b \in \mathbb{R}^{4 \times 1} = [0, 0, 0, 1]^T$ be the representations for the state matrix and control matrix, respectively. Since the pair (A_b, B_b) is not completely state controllable, the nominal system in Eq. (3.7) can be decomposed into controllable and uncontrollable

parts using a transformation matrix, T [Zohdy *et al.* 1992]. The new state vector is given by $Z_b = T X_b$ and the open-loop system in the new coordinates has the form,

$$\dot{Z}_b = \bar{A}_b Z_b + \bar{B}_b u_{fx} \quad (3.8)$$

where

$$\bar{A}_b = T A_b T^{-1} = \begin{bmatrix} \bar{A}_{uc} & 0 \\ \bar{A}_{21} & \bar{A}_c \end{bmatrix} \quad \text{and} \quad \bar{B}_b = T B_b = \begin{bmatrix} 0 \\ \bar{B}_c \end{bmatrix} \quad (3.9)$$

The pair (\bar{A}_c, \bar{B}_c) are controllable and all the eigenvalues of \bar{A}_{uc} are uncontrollable. Based on Eq. (3.9), consider an orthogonal transformation matrix given by

$$T = \begin{bmatrix} 2n & 0 & 1 & 0 \\ 0 & 1 & 0 & 0 \\ 1 & 0 & -2n & 0 \\ 0 & 0 & 0 & -1 \end{bmatrix} \quad (3.10)$$

Since the rank of $\mathfrak{C}_x = 3 < 4 = n$, the system given by Eq. (3.7) has 3 controllable modes and 1 uncontrollable mode. Thus Eq. (3.8) can be written in the form:

$$\begin{bmatrix} \dot{z}_{b1} \\ \dots \\ \dot{z}_{b2} \\ \dot{z}_{b3} \\ \dot{z}_{b4} \end{bmatrix} = \begin{bmatrix} 0 & \vdots & 0 & 0 & 0 \\ \dots & \vdots & \dots & \dots & \dots \\ \frac{1}{4n^2+1} & \vdots & 0 & -\frac{2n}{4n^2+1} & 0 \\ 0 & \vdots & 0 & 0 & -4n^2+1 \\ -\frac{2n(1+3n^2)}{4n^2+1} & \vdots & 0 & \frac{n^2}{4n^2+1} & 0 \end{bmatrix} \begin{bmatrix} z_{b1} \\ \dots \\ z_{b2} \\ z_{b3} \\ z_{b4} \end{bmatrix} + \begin{bmatrix} 0 \\ \dots \\ 0 \\ 0 \\ -1 \end{bmatrix} u_{fx} \quad (3.11)$$

where the open-loop eigenvalues of \bar{A}_b are $\{0, 0, \pm j n\}$. Based on the definitions provided in Eq. (3.9), the uncontrollable mode is given by $\dot{z}_{b1} = 0$ and the eigenvalue associated with the uncontrollable mode is 0. Therefore, if the system is formulated with no along-track input, the linearized SFF dynamics possesses one uncontrollable critical mode. An eigenvalue is critical if it lies on the imaginary axis.

Two critical cases exists, when the linearization has an (1) uncontrollable zero eigenvalue, (2) an uncontrollable complex conjugate pair of purely imaginary eigenvalue. For critical cases, as noted by Isidori [Isidori 1995], the linear controllability analysis becomes inconclusive and a smooth stabilizing feedback designed using nonlinear considerations is

required to guarantee asymptotic stability. Critical cases have also been solved by linear methods and bifurcation theory for an adequate margin of stability [Fu & Abed 1993]. Most of these methods are associated with large gains and therefore nonlinear controllers with low gains are preferable to stabilize the system. Therefore, in this paper we synthesize a nonlinear control strategy with no control force in the along-track direction, capable of precise formation keeping and formation reconfiguration in the presence of time-varying and state-dependent external disturbances.

In the following sections, we present the design procedure to implement SMC for spacecraft formation control. The overall design can be divided into two main steps. Step 1 involves the construction of an exponentially stable sliding surface as a function of tracking errors to ensure that once the system is restricted to the defined manifold, the follower spacecraft precisely tracks the desired trajectory. Step 2 entails the derivation of feedback control algorithm that can drive the relative states to the sliding surface in finite time and maintain it in the manifold.

Before we develop a nonlinear control law for the underactuated SFF configuration, the equations of motion [taken from previous chapter Eq. (2.25)] are rewritten in state-space form as follows:

$$\begin{aligned}
\begin{bmatrix} \dot{x} \\ \dot{y} \\ \dot{z} \\ \ddot{x} \\ \ddot{y} \\ \ddot{z} \end{bmatrix} &= \begin{bmatrix} 0 & 0 & 0 & 1 & 0 & 0 \\ 0 & 0 & 0 & 0 & 1 & 0 \\ 0 & 0 & 0 & 0 & 0 & 1 \\ 3n^2 & 0 & 0 & 0 & 2n & 0 \\ 0 & 0 & 0 & -2n & 0 & 0 \\ 0 & 0 & -n^2 & 0 & 0 & 0 \end{bmatrix} \begin{bmatrix} x \\ y \\ z \\ \dot{x} \\ \dot{y} \\ \dot{z} \end{bmatrix} + \begin{bmatrix} 0 \\ 0 \\ 0 \\ \mu \left(\frac{1}{r_l^2} - \frac{(r_l + x)}{r_f^3} \right) - 2n^2 x \\ n^2 y - \frac{\mu y}{r_f^3} \\ n^2 z - \frac{\mu z}{r_f^3} \end{bmatrix} \\
&+ \begin{bmatrix} 0 & 0 & 0 \\ 0 & 0 & 0 \\ 0 & 0 & 0 \\ b_1 & 0 & 0 \\ 0 & b_2 & 0 \\ 0 & 0 & b_3 \end{bmatrix} \begin{bmatrix} u_{fx} \\ u_{fy} \\ u_{fz} \end{bmatrix} + \begin{bmatrix} 0 & 0 & 0 \\ 0 & 0 & 0 \\ 0 & 0 & 0 \\ 1 & 0 & 0 \\ 0 & 1 & 0 \\ 0 & 0 & 1 \end{bmatrix} \begin{bmatrix} F_{dx} \\ F_{dy} \\ F_{dz} \end{bmatrix} \quad (3.12)
\end{aligned}$$

The state vector $X \in \mathbb{R}^{6 \times 1} = [x, y, z, \dot{x}, \dot{y}, \dot{z}]^T$ can be split into two parts as $X = [x_1, x_2]^T$ where x_1 and x_2 represents the unactuated and actuated states, respectively. The unactuated states can be further transformed to $x_1 = [x_{10}, x_{11}]^T$, where $x_{10} \in \mathbb{R}^{3 \times 1} = [x, y, z]^T$. We now consider the two main cases of actuation failure to determine the state x_{11} :

Case I : ($u_{fx} = 0, b_1 = 0, b_2, b_3 = 1$) No control force available in the *radial* direction (x) and complete control authority available in the *along-track* (y) and *cross-track* (z) direction. For this case $x_{11} = \dot{x}$, $x_2 = [\dot{y}, \dot{z}]$, and $U \in \mathbb{R}^{2 \times 1} = [u_{fy}, u_{fz}]^T$.

$$A_{11} = \begin{bmatrix} 0 & 0 & 0 & 1 \\ 0 & 0 & 0 & 0 \\ 0 & 0 & 0 & 0 \\ 3n^2 & 0 & 0 & 0 \end{bmatrix}; A_{12} = \begin{bmatrix} 0 & 0 \\ 1 & 0 \\ 0 & 1 \\ 2n & 0 \end{bmatrix}; A_{21} = \begin{bmatrix} 0 & 0 & 0 & -2n \\ 0 & 0 & -n^2 & 0 \end{bmatrix}$$

$$E_1(X) = \begin{bmatrix} 0 \\ 0 \\ 0 \\ \mu\left(\frac{1}{r_i^2} - \frac{(r_l+x)}{r_f^3}\right) - 2n^2x \end{bmatrix}; E_2(X) = \begin{bmatrix} n^2y - \frac{\mu y}{r_f^3} \\ n^2z - \frac{\mu z}{r_f^3} \end{bmatrix}$$

Case II : ($u_{fy} = 0, b_2 = 0, b_1, b_3 = 1$) No control force available in the *along-track* direction (y) and complete control authority available in the *radial* (x) and *cross-track* (z) direction. For this case $x_{11} = \dot{y}$, $x_2 = [\dot{x}, \dot{z}]$, and $U \in \mathbb{R}^{2 \times 1} = [u_{fx}, u_{fz}]^T$.

$$A_{11} = \begin{bmatrix} 0 & 0 & 0 & 0 \\ 0 & 0 & 0 & 1 \\ 0 & 0 & 0 & 0 \\ 0 & 0 & 0 & 0 \end{bmatrix}; A_{12} = \begin{bmatrix} 1 & 0 \\ 0 & 0 \\ 0 & 1 \\ -2n & 0 \end{bmatrix}; A_{21} = \begin{bmatrix} 3n^2 & 0 & 0 & 2n \\ 0 & 0 & -n^2 & 0 \end{bmatrix}$$

$$E_1(X) = \begin{bmatrix} 0 \\ 0 \\ 0 \\ n^2y - \frac{\mu y}{r_f^3} \end{bmatrix}; E_2(X) = \begin{bmatrix} \mu\left(\frac{1}{r_i^2} - \frac{(r_l+x)}{r_f^3}\right) - 2n^2x \\ n^2z - \frac{\mu z}{r_f^3} \end{bmatrix}$$

3.1.2 Design of Sliding Manifold

The characteristics of underactuated systems pose numerous challenges to researchers, ranging from controller design to establishing stability margins. In particular, the non-linear dynamics of the SFF system [Eqs. (2.5)-(2.7)] clearly indicates the presence of unmatched disturbances (relative J_2 accelerations in x or y direction) if the control force in the radial (u_{fx}) or along-track (u_{fy}) direction were to fail. Hence, the sliding surface function for the underactuated SFF system should be designed such that not only the stability of the closed-loop system is guaranteed in the presence of unmatched perturbations, but also the desired dynamic behavior should be exhibited once the error trajectory of system is confined to the sliding surface. In terms of robustness, the conventional sliding surface design [Yeh *et al.* 2002, Lim *et al.* 2003, Massey & Shtessel 2005, Wang & Zhang 2007, Liu *et al.* 2006] has a major disadvantage because the sliding system is sensitive to unmatched uncertainties and disturbances due to unexpected actuator failure which will directly affect the dynamic performance.

3.1.2.1 Case I - Complete failure of radial axis thruster

The linearized HCW model [Eq. (3.1)] in the previous section can be represented in terms of new coordinates $x_1 \in \mathbb{R}^4$ and $x_2 \in \mathbb{R}^2$ as follows

$$\begin{bmatrix} \dot{x}_1 \\ \dot{x}_2 \end{bmatrix} = \begin{bmatrix} A_{11} & A_{12} \\ A_{21} & A_{22} \end{bmatrix} \begin{bmatrix} x_1 \\ x_2 \end{bmatrix} + \begin{bmatrix} 0 \\ B_2 \end{bmatrix} U \quad (3.13)$$

where x_1 and x_2 are as defined in Case I, and $B_2 \in \mathbb{R}^{2 \times 2} = I_{2 \times 2}$. Carrying out a similar transformation on the desired trajectory equations [Eqs. (2.8)-(2.9)] gives,

$$\begin{bmatrix} \dot{x}_1^d \\ \dot{x}_2^d \end{bmatrix} = \begin{bmatrix} A_{11}^d & A_{12}^d \\ A_{21}^d & A_{22}^d \end{bmatrix} \begin{bmatrix} x_1^d \\ x_2^d \end{bmatrix} \quad (3.14)$$

Based on Eq. (3.13) and Eq. (3.14), the error dynamics are given by,

$$\begin{aligned} \dot{e}_1 &= A_{11}e_1 + A_{12}e_2 + \bar{A}_{11}x_1^d + \bar{A}_{12}x_2^d \\ \dot{e}_2 &= A_{21}e_1 + A_{22}e_2 + B_2U + \bar{A}_{21}x_1^d + \bar{A}_{22}x_2^d \end{aligned} \quad (3.15)$$

where $\bar{A}_{ij} = A_{ij} + A_{ij}^d$ for $i, j = 1, 2$, and $e_i = x_i - x_i^d$. By exploiting the coupling between directly actuated and unactuated states, we define the sliding surface, S , as a function of the tracking errors and desired states.

$$S = \{e_1 \in \mathbb{R}^{4 \times 1}, e_2 \in \mathbb{R}^{2 \times 1} : e_2 + K e_1 = 0\} \quad (3.16)$$

where $K \in \mathbb{R}^{2 \times 4}$ is the weighting matrix. When the system reaches the sliding surface, $S = 0 \forall t > t_r$, where t_r is the reaching time after which sliding motion starts,

$$e_2 = -K e_1 \quad (3.17)$$

It is important to note that Eq. (3.17) holds only on the sliding surface and substituting this relation to the reduced order system in Eq. (3.15) gives

$$\dot{e}_1 = (A_{11} - A_{12}K)e_1 + \bar{A}_{11}x_1^d + \bar{A}_{12}x_2^d \quad (3.18)$$

During an ideal sliding mode behavior, e_2 can be considered as a control signal to stabilize e_1 . Therefore, the choice of sliding surface, S , clearly affects the dynamics of the reduced order system through the selection of weighting matrix K . The weighting matrix K prescribes a desired closed-loop behavior for the system [Eq. (3.18)] and can be determined using any *classical* approaches which provides a full state feedback control scheme for a system represented in state-space form. Since (A, B) is, by definition a controllable pair it follows directly that the matrix pair (A_{11}, A_{12}) is also controllable. To facilitate the stability analysis, we rewrite the sliding surface in the following form:

$$S = \{e \in \mathbb{R}^{6 \times 1} : \Lambda e = 0\} \quad (3.19)$$

$$\Lambda = [K \ I_{2 \times 2}] = \begin{bmatrix} K_{11} & K_{12} & K_{13} & K_{14} & 1 & 0 \\ K_{21} & K_{22} & K_{23} & K_{24} & 0 & 1 \end{bmatrix} \quad (3.20)$$

3.1.2.2 Case II - Complete failure of along-track thruster

Linear controllability analysis of the in-plane dynamics with no along-track input shows that the controllability matrix is rank deficient [Eq. (3.6)]. Also, the pair (A_{11}, A_{12}) is not completely state controllable if linear system for Case II is expressed in the form given by

Eq. (3.13). Therefore, a sliding surface designed based on the approach used for Case I can lead to unstable reduced order dynamics. Based on the error dynamics in Eq. (3.15) and the complete linear model [Eq. (3.1)], the reduced order system for Case II (excluding the desired trajectory terms - $\bar{A}_{11}x_1^d + \bar{A}_{12}x_2^d$) is given by

$$\begin{bmatrix} \dot{e}_x \\ \dot{e}_y \\ \dot{e}_z \\ \ddot{e}_y \end{bmatrix} = \begin{bmatrix} 0 & 0 & 0 & 0 \\ 0 & 0 & 0 & 1 \\ 0 & 0 & 0 & 0 \\ 0 & 0 & 0 & 0 \end{bmatrix} \begin{bmatrix} e_x \\ e_y \\ e_z \\ \dot{e}_y \end{bmatrix} + \begin{bmatrix} 1 & 0 \\ 0 & 0 \\ 0 & 1 \\ -2n & 0 \end{bmatrix} \begin{bmatrix} \dot{e}_x \\ \dot{e}_z \end{bmatrix} \quad (3.21)$$

The uncontrollable mode is extracted by representing the reduced order system with a new set of coordinates. In order to facilitate the analysis, linear change of coordinates for Eq. (3.21) can be obtained using the transformation matrix

$$T_1 = \begin{bmatrix} 2n & 0 & 0 & 1 \\ 0 & -1 & 0 & 0 \\ 0 & 0 & -1 & 0 \\ -1 & 0 & 0 & 2n \end{bmatrix} \quad (3.22)$$

By a change of basis using, (1) $z = T_1 e_1$, (2) $\bar{A} = T_1 A_{11} T_1^{-1}$, and (3) $\bar{B} = T_1 A_{12}$, Eq. (3.21) is transformed into the following lower order system

$$\begin{bmatrix} \dot{z}_1 \\ \dot{z}_2 \end{bmatrix} = \begin{bmatrix} \bar{A}_{uc} & 0 \\ \bar{A}_{21} & \bar{A}_c \end{bmatrix} \begin{bmatrix} z_1 \\ z_2 \end{bmatrix} + \begin{bmatrix} 0 \\ B_c \end{bmatrix} \begin{bmatrix} \dot{e}_x \\ \dot{e}_z \end{bmatrix} \quad (3.23)$$

where

$$\bar{A}_{uc} = 0; \quad \bar{A}_{21} = \begin{bmatrix} -1 \\ 0 \\ 0 \end{bmatrix}; \quad \bar{A}_c = \begin{bmatrix} 0 & 0 & -2n \\ 0 & 0 & 0 \\ 0 & 0 & 0 \end{bmatrix}; \quad B_c = \begin{bmatrix} 0 & 0 \\ 0 & -1 \\ -1 & 0 \end{bmatrix}$$

with (\bar{A}_c, B_c) a controllable pair. The uncontrollable mode is given by $\dot{z}_1 = 0$ which implies z_1 is a constant. Based on the transformation matrix given by Eq. (3.22), $z_1 = \dot{e}_y + 2n e_x$. Our objective is to develop a sliding surface that can eliminate the effect of this uncontrollable mode. Hence, using the properties of linear state-space theory, there exists

a linear feedback control with the gain matrix $K \in \mathbb{R}^{2 \times 3}$ such that $A_c - B_c K$ is Hurwitz.

$$e_2 = -K z_2 = -K \hat{T}_1 e_1 \quad (3.24)$$

where $\hat{T}_1 = T_1(2 : 4, :)$. This result can be utilized to define a sliding surface based on the pair (A_c, B_c) which is stable as opposed to a manifold designed based on (A_{11}, A_{12}) . The time-invariant switching function for Case II with a robust component added to alleviate the effect of matched part of the reduced order system and the uncontrollable mode is defined as,

$$S = \{e_1 \in \mathbb{R}^{4 \times 1}, e_2 \in \mathbb{R}^{2 \times 1} : e_2 + K \hat{T}_1 e_1 = 0\} \quad (3.25)$$

Therefore, asymptotic stabilization of the tracking errors can be guaranteed if the weighting matrix K is appropriately chosen to suppress the influence of the uncontrollable mode. Sufficiently fast error decay when sliding can be ensured by placing the closed-loop eigenvalues of $(A_c - B_c K)$ in the far left-hand half of the complex plane. The error dynamics are represented in the exact same manner as Eq. (3.15) with $e_1 = [e_x, e_y, e_z, \dot{e}_y]^T$ and $e_2 = [\dot{e}_x, \dot{e}_z]^T$. To facilitate the stability analysis, we rewrite the sliding surface in the following form:

$$S = \{e \in \mathbb{R}^{6 \times 1} : \Gamma e = 0\} \quad (3.26)$$

$$\Gamma = [K \hat{T}_1 \ I_{2 \times 2}] = \begin{bmatrix} -K_{13} & -K_{11} & -K_{12} & 2nK_{13} & 1 & 0 \\ -K_{23} & -K_{21} & -K_{22} & 2nK_{23} & 0 & 1 \end{bmatrix} \quad (3.27)$$

3.1.3 Nonlinear Control Formulation

The design of a suitable control algorithm that can steer the system trajectories to the sliding manifold is the second phase of any VSC design procedure. Our objective is to improve the transient performance of the system by employing a continuous, nonlinear control algorithm that can reduce the reaching phase and maintain the closed-loop trajectory on the sliding surface. The effects of both matched and unmatched uncertainties are pertinent when the motion is not constrained to the sliding surface.

$$\begin{bmatrix} \dot{x}_1 \\ \dot{x}_2 \end{bmatrix} = \begin{bmatrix} A_{11} & A_{12} \\ A_{21} & A_{22} \end{bmatrix} \begin{bmatrix} x_1 \\ x_2 \end{bmatrix} + \begin{bmatrix} E_1(X) \\ E_2(X) \end{bmatrix} + \begin{bmatrix} 0_{4 \times 2} \\ I_{2 \times 2} \end{bmatrix} U_f + \begin{bmatrix} F_{d1} \\ F_{d2} \end{bmatrix} \quad (3.28)$$

To generalize the control design procedure for cases I and II, the nonlinear equations of motion can be represented by Eq. (3.28) in terms of transformed coordinates [based on the classification outlined in Section 3.1.1 after Eq. (3.12)], where $E_1(X)$ and $E_2(X)$ are the nonlinear terms decomposed from $E(X)$ in Eq. (3.12), $U_f \in \mathbb{R}^{2 \times 1} = [u_{fi}, u_{fz}]^T$ is the vector of control inputs, and $F_{d1} \in \mathbb{R}^{4 \times 1} = [0, 0, 0, F_{di}]^T$, $F_{d2} \in \mathbb{R}^{2 \times 1} = [F_{dj}, F_{dz}]^T$, $\forall i, j = x$ or y (depending on Case I or Case II), are the differential perturbations.

One of the major challenges in trajectory tracking for multiple spacecraft in formation stems from the presence of uncertainties and differential perturbations. With no control force available in the radial or along-track direction, achieving precise formation-keeping and reconfiguration of desired formation geometry becomes a difficult task in the presence of uncertain and perturbing terms in the formation dynamics. A simple approach to extract the core information of uncertainties and perturbations is to utilize the estimate of its upper-bound in the controller design. This technique has been widely used for spacecraft attitude tracking control in the presence of time-varying disturbances [Singh 1987, Cai *et al.* 2008]. We assume that the desired reference trajectory, X_d , and the nonlinear component, $E(X)$, in the equations of motion are bounded as

$$\begin{aligned} \|X_d\| &\leq \rho_1 \\ \|E(X)\| &\leq \rho_2 \|X\| \end{aligned} \quad (3.29)$$

where $\rho_1 > 0$, and ρ_2 is the Lipschitz constant of the nonlinear vector field associated with $E(X)$. Vaddi [Vaddi 2003] showed that the Lipschitz constant can be determined by computing the ratio $\frac{\|E(X)\|}{\|X\|}$ for a particular region of interest (varying formation disc size 1 km – 150 km) and choosing its maximum value. As stated earlier, differential perturbations due to solar radiation pressure and aerodynamic drag can be neglected in this study since we assume that all spacecraft in formation have the same ballistic coefficients and area-to-mass ratio. Other types of uncertainties such as relative J_2 (modeled in Section 2.1.5), magnetic forces, luni-solar perturbations, dynamics of thrusters, perturbations due to thruster misalignment, etc. are assumed to be included in the following chosen uncertainty bound (with scalar constants $\rho_3, \rho_4 > 0$).

$$\|F_d\| \leq \rho_3 \|X\| + \rho_4 \quad (3.30)$$

We now develop the control scheme to ensure that the sliding manifold is reached and sliding on the manifold occurs. Based on the sliding manifolds given by Eqs. (3.19) and (3.26), the general structure of the surfaces are identical for cases I and II, and therefore the formulation of control scheme will be the same. Then, considering Eq. (3.19), we have

$$\dot{S} = \Lambda \dot{e} = U_f + \Lambda A X + \Lambda[E(X) + D F_d] - \Lambda \dot{X}_d \quad (3.31)$$

Due to the form of the aforementioned uncertainties given by Eqs. (3.29) and (3.30), a second order polynomial function that bounds the lumped term containing nonlinearities and disturbances in the system can be expressed as follows:

$$\begin{aligned} \gamma(t, X, X_d) &= \Lambda[E(X) + D F_d - \dot{X}_d] \\ \|\gamma(t, X, X_d)\| &\leq [(\rho_3 + \rho_2)\|X\| + (\rho_4 + \rho_1)] \|\Lambda\| \leq \rho \Phi \\ \Phi &= 1 + \|X\| \end{aligned} \quad (3.32)$$

Carrying out some algebraic manipulations based on Eqs. (3.31) and (3.32), the nonlinear control law capable of precise formation-keeping and reconfiguration is given by

$$U_f = - \left[\eta \frac{\varphi_2 S}{\|S\| + \delta} + \Lambda A X \right] \quad (3.33)$$

where δ is a small positive scalar specifying the boundary layer thickness that will eliminate chatter if appropriately chosen so that the unmodeled high frequency dynamics are not excited [Edwards & Spurgeon 1998]. This choice has no effect on the closed-loop trajectories, except when sliding along the sliding surface S_u , in which case the deadband will strongly influence the high frequency chatter in the control input. The scalar function ρ depends on the magnitude of the disturbances and uncertainties,

$$\eta = \frac{\varphi_1}{\varphi_2} (\varphi_3 + \varphi_4) \quad \forall \quad [0 \leq \varphi_2 < 1 \quad \text{and} \quad \varphi_1, \varphi_3, \varphi_4 \geq 0] \quad (3.34)$$

for some positive constants φ_1 , φ_2 , φ_3 , and φ_4 . The steps involved in adequately determining these nonnegative constants are detailed in the next section. It is also important to note that Eq. (3.32) is true regardless of any external disturbance, types of formation, and other uncertainties that arise due to changing spacecraft parameters or operating conditions. In this dissertation, $\|\cdot\|$ denotes the Euclidean norm for vectors and the induced spectral norm for matrices.

3.1.4 Stability Analysis

In this sub-section we present stability conditions for the SFF system in underactuated configuration, focussing primarily on robustness against disturbances. First, we show that the control law, Eq. (3.33), is capable of driving the closed-loop trajectory of the system towards a boundary layer on the sliding surface in finite time (Hitting Phase). Once the sliding surface is reached, the system enters into the sliding regime. We show that the sliding mode is robust to unmatched disturbances and uncertainties that mainly affects the unactuated states (Sliding Phase).

Theorem 3.1: *For the underactuated spacecraft formation flying mathematical model in Eq. (3.28) if, the sliding manifold is chosen as Eq. (3.19) or Eq. (3.26), the control law is defined as Eq. (3.33), and the bounds on the external disturbances and uncertainties on the system is assumed as given by Eq. (3.32) then the system reaches the sliding surface in finite time for a sufficiently small $\delta > 0$.*

Proof: Consider the Lyapunov function

$$V(S) = \frac{1}{2} S^T S \quad (3.35)$$

Taking the first derivative of $V(S)$ along the trajectory of the closed-loop system,

$$\dot{V}(S) = S^T \left[\Lambda (\dot{X} - \dot{X}_d) \right] \quad (3.36)$$

Substituting the SFF model, Eq. (3.28), and the control law given by Eq. (3.33), we get

$$\begin{aligned} \dot{V}(S) &= S^T \left[\Lambda (A X + E(X) + D F_d) + U_f - \Lambda \dot{X}_d \right] \\ &= S^T \left[-\eta \frac{\varphi_2 S}{\|S\| + \delta} + \gamma(t, X, X_d) \right] \end{aligned} \quad (3.37)$$

Based on Eq. (3.32) and setting $\varphi_3 = \rho \Phi$, the first derivative of $V(S)$ can be expressed as

$$\begin{aligned} \dot{V}(S) &\leq \|S\| \left[-\eta \frac{\varphi_2 \|S\|}{\|S\| + \delta} + \|\gamma(t, X, X_d)\| \right] \\ &\leq \|S\| \left[-\eta \frac{\varphi_2 \|S\|}{\|S\| + \delta} + \varphi_3 \right] \end{aligned} \quad (3.38)$$

Expressing φ_3 in terms of η , φ_1 , φ_2 , and φ_4 from Eq. (3.34) and substituting in Eq. (3.38),

$$\begin{aligned}\dot{V}(S) &\leq -\|S\| \left[\eta \varphi_2 \frac{\|S\|}{\|S\| + \delta} - \frac{\eta \varphi_2}{\varphi_1} + \varphi_4 \right] \\ &\leq -\varphi_4 \|S\| - \eta \varphi_2 \|S\| \left[\frac{\|S\|}{\|S\| + \delta} - \frac{1}{\varphi_1} \right]\end{aligned}\quad (3.39)$$

It is readily obtained from Eq. (3.39) that, if:

$$\begin{aligned}\frac{\|S\|}{\|S\| + \delta} - \frac{1}{\varphi_1} &\geq 0 \\ \|S\| &\geq \frac{\delta}{\varphi_1 - 1}\end{aligned}\quad (3.40)$$

then $\dot{V}(S) < 0$. The condition in Eq. (3.40) is only satisfied if

$$V(S) > \frac{1}{2} \left(\frac{\delta}{\varphi_1 - 1} \right)^2 = \varepsilon_1 \quad (3.41)$$

From Eq. (3.38), where $\frac{\|S\|}{\|S\| + \delta} \leq 1$ ($\forall \delta \geq 0$), we derive conditions for selecting gains

$$\begin{aligned}\eta \varphi_2 - \varphi_3 &> 0 \\ \varphi_1 &> \frac{\varphi_3}{\varphi_3 + \varphi_4}\end{aligned}\quad (3.42)$$

Using this fact it can be shown that $\dot{V}(S) \leq -\varepsilon_2 \sqrt{2V(S)}$ for some $\varepsilon_2 > 0$. This implies that the sliding boundary layer is reached in finite time. For the case where a small (δ) is chosen, then every solution will eventually enter the set $\mathfrak{R} = \{S : V(S) \leq \varepsilon_1\}$ and will be globally uniformly ultimately bounded with respect to the ellipsoid ε_1 . Thus, we have shown that the continuous control input given by Eq. (3.33) forces the solutions of the system towards a boundary layer surrounding the sliding surface S in the state space, and the system remains in it thereafter. \square

During sliding phase, the system is completely insensitive to disturbances and uncertainties acting within the channels implicit in the control inputs (matched perturbations). However, the sliding surface is sensitive to unmatched uncertainties and disturbances which will effect the dynamic performance of the closed-loop error system. Therefore, it is important to evaluate the properties of the system once the closed-loop error dynamics are constrained to S . To this end, we first introduce Shyu's stability criterion[Shyu *et al.* 1998] of the reduced-order system with unmatched uncertainties in Lemma 1.

Lemma 3.1: *Consider the following reduced order system with uncertainty*

$$\dot{x}_1 = (A_{11} - A_{12}K)x_1 + \bar{f}(x_1) \quad (3.43)$$

where $\bar{f}(x_1)$ is the unmatched uncertainty. Then, if $\bar{f}(x_1)$ satisfies the uniform Lipschitz condition $\|\bar{f}(x_1^1) - \bar{f}(x_1^2)\| \leq b\|x_1^1 - x_1^2\|$ where $0 \leq b \leq 0.5\lambda_{\min}(\bar{Q})/\|\bar{P}\|$ with $\bar{P}, \bar{Q} \in \mathbb{R}^{(n-m) \times (n-m)}$ which are symmetric, positive-definite matrices satisfying the Lyapunov equation $(A_{11} - A_{12}K)^T \bar{P} + \bar{P}(A_{11} - A_{12}K) = -\bar{Q}$, then the uncertain system, Eq. (3.43), on the sliding surface is asymptotically stable.

The nonlinear error dynamics of relative motion between a leader spacecraft in circular reference orbit and a follower are repeated here for the reader's convenience.

$$\begin{aligned} \dot{e}_1 &= A_{11}e_1 + A_{12}e_2 + \bar{f}_{ru}(X) \\ \dot{e}_2 &= A_{21}e_1 + A_{22}e_2 + B_2U + \bar{f}_{rm}(X) \end{aligned} \quad (3.44)$$

where $\bar{f}_{ru}(X) \in \mathbb{R}^4$ and $\bar{f}_{rm}(X) \in \mathbb{R}^2$ are the lumped terms containing the unmatched ($E_1(X)$, F_{d1} , $\bar{A}_{11}x_1^d$, and $\bar{A}_{12}x_2^d$) and matched components ($E_2(X)$, F_{d2} , $\bar{A}_{21}x_1^d$, and $\bar{A}_{22}x_2^d$) of uncertainties in the system, respectively. When in sliding mode the system is insensitive to the matched uncertainty, $\bar{f}_{rm}(X)$. The unmatched uncertainties are assumed to be *unknown* but bounded and satisfies, $\|\bar{f}_{ru}(X)\| \leq w_1 + w_2\|X\|$. During the sliding motion we know that $e_2 = -K e_1$ [from Eq. (3.16)], and therefore

$$\begin{aligned} e = X - X_d &= \begin{bmatrix} e_1 \\ e_2 \end{bmatrix} = \begin{bmatrix} e_1 \\ -K e_1 \end{bmatrix} \Rightarrow X = \begin{bmatrix} 1 \\ -K \end{bmatrix} e_1 + X_d \\ \|X\| &\leq \sqrt{1 + \|K\|^2} \|e_1\| + \|X_d\| \end{aligned} \quad (3.45)$$

Consequently the bound on the unmatched uncertainty can be written as

$$\|\bar{f}_{ru}(X)\| \leq \varphi_2 + \bar{w}_2\|e_1\| \quad (3.46)$$

where $\varphi_2 = \rho_1$ [from Eq. (3.29)] and $\bar{w}_2 = w_2\sqrt{1 + \|K\|^2}$. The equation representing the error dynamics confined to the sliding surface is obtained by substituting $S = 0$ in Eq. (3.44), giving the following closed-loop equation

$$\dot{e}_1 = (A_{11} - A_{12}K)e_1 + \bar{f}_{ru}(X) \quad (3.47)$$

In the following theorem, based on the sliding surface defined by Eq. (3.16), a stability criterion for the reduced order system [Eq. (3.47)] is presented. Several cases of asymptotic stabilization of the reduced order system in the presence of unmatched uncertainties, where the vector fields have a special form, have been studied in the literature. We utilize the procedure outlined in the book by Edwards and Spurgeon [Edwards & Spurgeon 1998] and Shyu's stability criterion (see Lemma 3.1) to present Theorem 3.2.

Theorem 3.2: *For the motion constrained to the sliding surface, the trajectory of the reduced-order system [Eq. (3.47)] starting from any initial condition will enter a compact set \mathfrak{S} containing the origin in finite time and the tracking error e_1 will be uniformly ultimately bounded with respect to the ellipsoid*

$$\mathfrak{S} = \left\{ e_1 \in \mathbb{R}^4 : \|e_1\| \leq \frac{2\varphi_2}{\xi - 2\bar{w}_1} \right\} \quad (3.48)$$

Then, the reduced-order system is globally asymptotically stable if $\xi > 2\bar{w}_1$, with $\xi \triangleq \lambda_{\min}(\bar{Q})/\lambda_{\max}(\bar{P})$, where $\bar{P}, \bar{Q} \in \mathbb{R}^{4 \times 4}$ are positive-definite matrices satisfying the Lyapunov equation

$$(A_{11} - A_{12}K)^T \bar{P} + \bar{P}(A_{11} - A_{12}K) = -\bar{Q} \quad (3.49)$$

Proof: Consider the Lyapunov function

$$V(e_1) = e_1^T \bar{P} e_1 \quad (3.50)$$

The first derivative of $V(e_1)$ along the motion of Eq. (3.47) is given by

$$\begin{aligned} \dot{V}(e_1) &= e_1^T \bar{P} \dot{e}_1 + \dot{e}_1^T \bar{P} e_1 \\ &= e_1^T \bar{P} [(A_{11} - A_{12}K)e_1 + \bar{f}_{ru}(X)] + [(A_{11} - A_{12}K)e_1 + \bar{f}_{ru}(X)]^T \bar{P} e_1 \\ &= e_1^T [\bar{P}(A_{11} - A_{12}K) + (A_{11} - A_{12}K)^T \bar{P}] e_1 + 2e_1^T \bar{P} \bar{f}_{ru}(X) \\ &\leq -e_1^T \bar{Q} e_1 + 2\|\bar{P} e_1\| \|\bar{f}_{ru}(X)\| \end{aligned} \quad (3.51)$$

Using the Rayleigh principle we know that

$$\lambda_{\min}(\bar{Q})\|e_1\|^2 \leq e_1^T \bar{Q} e_1 \leq \lambda_{\max}(\bar{Q})\|e_1\|^2 \quad (3.52)$$

In particular, if $\lambda_{\min}(\bar{Q}) \geq 0$ then it follows that $e_1^T \bar{Q} e_1 \geq 0$ for all e_1 . Using Eq. (3.52) and Eq. (3.46), Eq. (3.51) can be expressed as

$$\begin{aligned} \dot{V}(e_1) &\leq -\lambda_{\min}(Q)\|e_1\|^2 + 2\lambda_{\max}(\bar{P})\|e_1\| \|\bar{f}_{ru}(X)\| \\ &\leq -\lambda_{\max}(\bar{P}) [\xi\|e_1\| - 2\|\bar{f}_{ru}(X)\|] \|e_1\| \\ &\leq -\lambda_{\max}(\bar{P}) [\xi\|e_1\| - 2\bar{w}_1\|e_1\| - 2\varphi_2] \|e_1\| \end{aligned} \quad (3.53)$$

Therefore, it is clearly evident from Eq. (3.53) that $\dot{V}(e_1) < 0$ when e_1 is outside of the set

$$\mathfrak{S} = \left\{ e_1 \in \mathbb{R}^4 : \|e_1\| \leq \frac{2\varphi_2}{\xi - 2\bar{w}_1} \right\} \quad (3.54)$$

Analytical estimate of $\lambda_{\min}(Q)$ is not needed for numerical simulations because the proposed control law is independent of this parameter. When norm of the unactuated states, $\|e_1\| > \frac{2\varphi_2}{\xi - 2\bar{w}_1}$, then $\dot{V}(e_1)$ decreases; but once the states (e_1) enters the set \mathfrak{S} they cannot go out of it and hence the unactuated states will be confined to the set \mathfrak{S} . For every $e_1(t_0) \in \mathfrak{S}$ then $e_1(t) \in \mathfrak{S}$ for all $t \geq t_0$. Since $\dot{V}(e_1) < 0$, it also follows that if $e_1(t_0) \notin \mathfrak{S}$ then the trajectory will reach \mathfrak{S} in finite time t_r [Spurgeon & Davies 1993]. The system is therefore uniformly ultimately bounded with respect to the ellipsoid \mathfrak{S} . \square

3.2 Performance Evaluation

To study the effectiveness and performance of the proposed formation control strategies, the detailed response is numerically simulated using the set of governing equations of motion [Eqs. (2.5)-(2.7)] in conjunction with the proposed control law [Eq. (3.33)]. The SFF system parameters and the orbital parameters for the leader spacecraft used in the numerical simulations are shown in Table 3.1. For all numerical examples presented in this section, the net disturbance force, $F_d(t)$, acting on the system is considered to be differential J_2 based on the formulation presented in Section 2.1.5. The leader spacecraft is assumed to be in an unperturbed circular reference orbit and the differential force on the follower is calculated relative to the leader spacecraft orbit. The control gains ($K \varphi_i$) and the boundary layer (δ) used in all simulations for Cases I and II are shown in Table 3.2.

The desired relative motion considered for ideal formation keeping is a projected circular formation described by Eq. (2.9), with $r_{dpc} = 1$ km formation radius. The in-plane phase

Table 3.1: Leader spacecraft orbital parameters

Parameters	Values
μ_e (km ³ s ⁻²)	398600
r_p (km)	6878
Ω_l (deg)	0
i_l (deg)	45
ω_l (deg)	0

Table 3.2: Controller parameters for underactuated SFF

Control Gains	Case I	Case II
$[\varphi_1, \varphi_2, \varphi_3, \varphi_4]$	[2.0, 4.0, 1.0, 0.5]	[1.5, 1.5, 0.5, 0.2]
$[K_{11}, K_{12}, K_{13}, K_{14}]$	[4, -2, 0, 18]	[-0.0013, 0, 0.0028, ...]
$[K_{21}, K_{22}, K_{23}, K_{24}]$	[0, 0, 2, 0]	[0, 0.0013, 0, ...]
δ	10^{-5}	10^{-5}

angle (ϕ) between the leader and follower spacecraft is assumed to be zero degree. The initial relative positions for the numerical simulation are computed by substituting $t = 0$ in Eq. (2.9). The initial velocity components for all states are calculated by taking the time derivative of Eq. (2.9) and substituting $t = 0$. The initial state vector is:

$$X(0) = [0, r_{dpc}, 0, 0.5 n r_{dpc}, 0, n r_{dpc}]^T \quad (3.55)$$

Figure 3.1 shows the uncontrolled response for projected circular formation initial conditions with no external perturbations. The radial and cross-track errors remain bounded over 30 orbits, while the along-track error has a secular drift, increasing at a rate of 3.08 m per orbit. We now illustrate the efficacy of the proposed control schemes in eliminating this secular drift and achieving precision tracking performance. The results presented are: (1) Controlled performance demonstrating formation-keeping with perfect initial conditions, (2) Effects of initial condition errors and performance during formation maneuvers, and (3) Quantitative analysis on fuel consumption and steady-state stabilization errors.

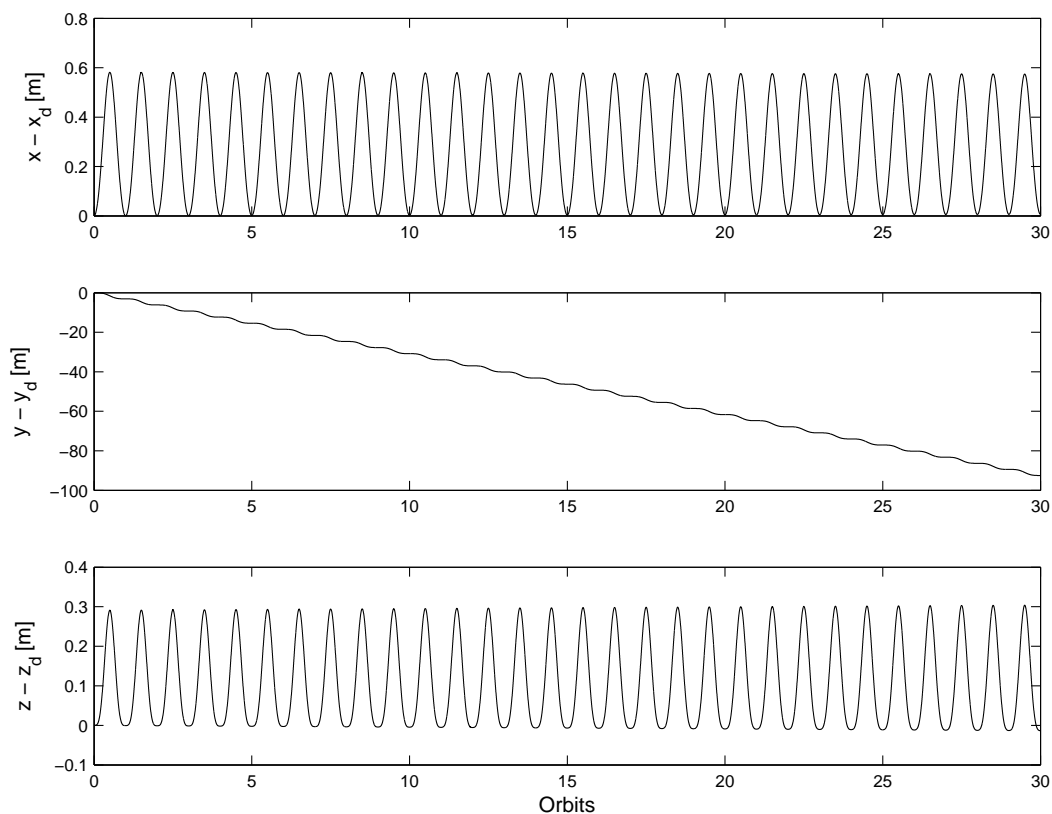


Figure 3.1: Deviation of the relative position errors with no control (no J_2).

3.2.1 Ideal Formation-keeping

Figure 3.2 shows relative position errors and thrust demand for formation keeping with no control available in the radial direction (Case I). No external disturbance is considered. The application of the proposed control scheme for this underactuated configuration results in a bounded along-track error with its maximum absolute value of 5 mm. The steady state error on the unactuated radial-axis is bounded by $|x - x_d| = 2$ mm. Near perfect tracking is achieved in the cross-track direction. The effect of relative J_2 perturbations on the system response is shown in Fig. 3.3 for case I. With no control force available in the radial-direction, the proposed control scheme successfully transforms an unstable formation (without control input) into a stable one with bounded in-plane relative position errors of $|x - x_d|_{max} < 0.03$ m, and $|y - y_d|_{max} < 0.05$ m. When control force is only available in the radial and cross-track directions (Case II), the proposed control scheme yields similar

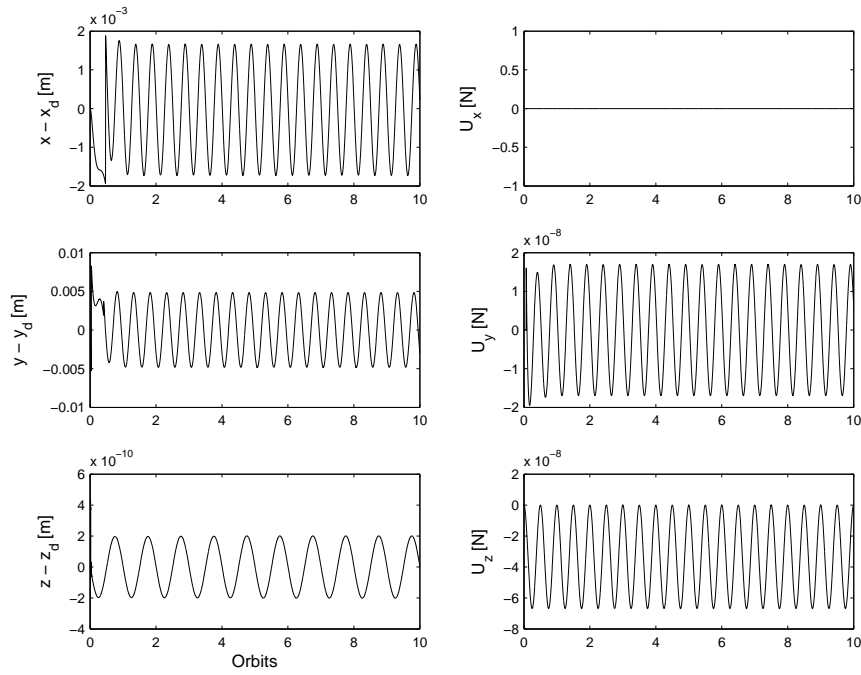


Figure 3.2: Controlled response for Case I (no external disturbances).

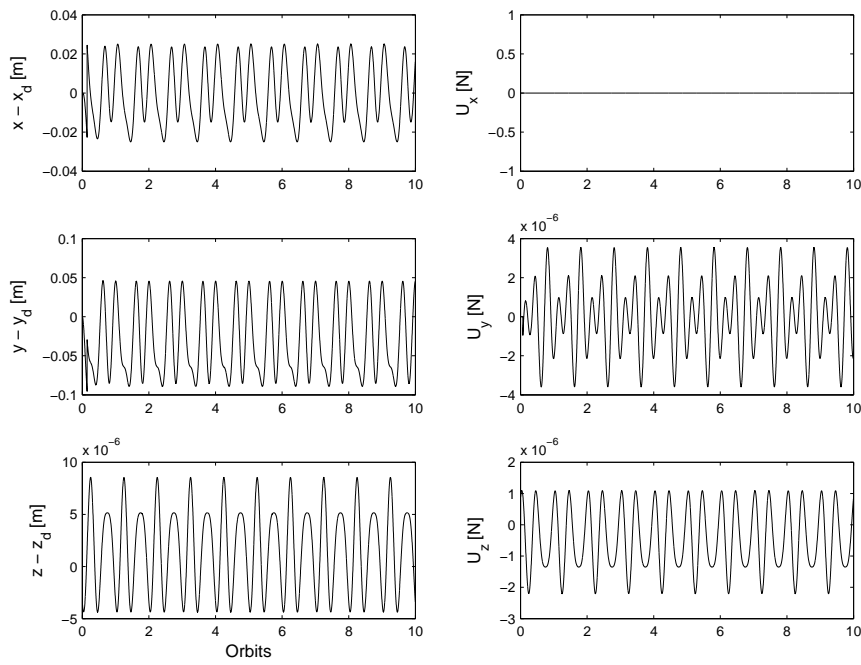


Figure 3.3: Controlled response for Case I (with relative J_2 disturbance).

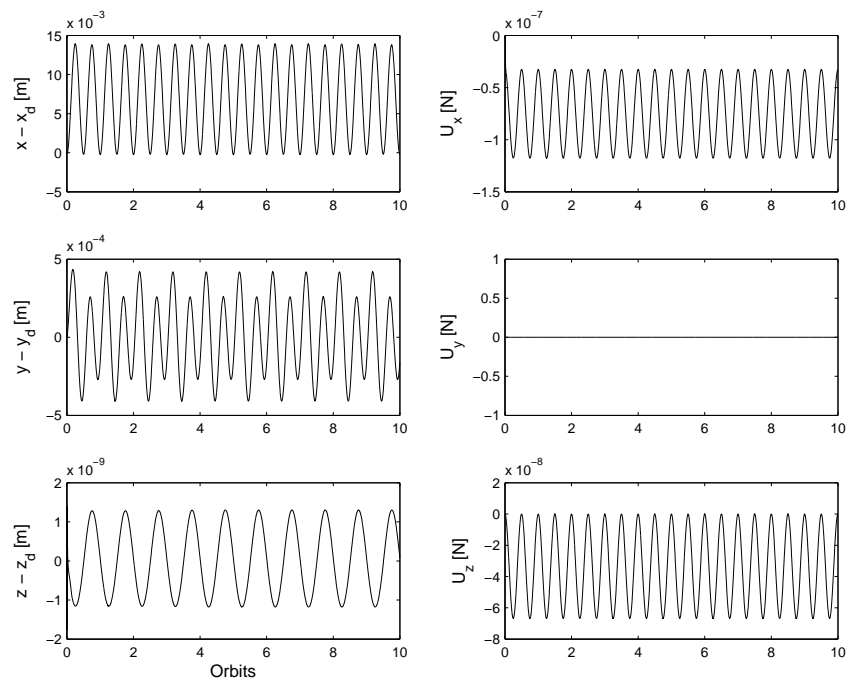


Figure 3.4: Controlled response for Case II (no external disturbances).

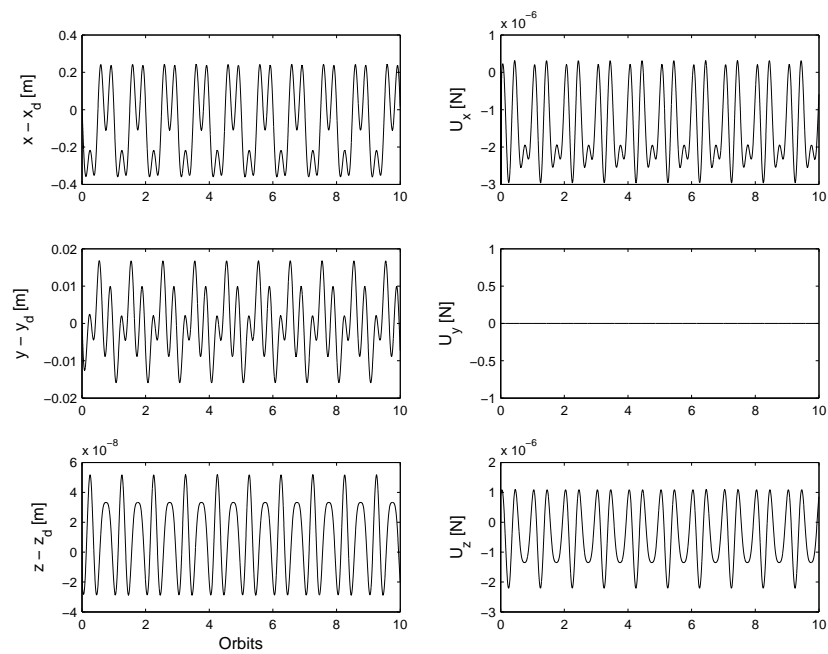


Figure 3.5: Controlled response for Case II (with relative J_2 disturbance).

results as discussed above. Figure 3.4 shows the controlled response of the system with no control available in the along-track direction. Although the linear approximation of this case states that the system is not completely state controllable, the proposed nonlinear control scheme efficiently tracks the desired trajectories. Performance of the control law in the presence of relative J_2 perturbations is shown in Fig. 3.5.

3.2.2 Initial Errors and Formation Reconfiguration

The performance evaluation discussed thus far mainly addresses the formation-keeping objectives to compensate for differential perturbations based on varying orbiting conditions. It is also important to examine the effectiveness of the proposed control scheme to perform orbital corrections. First, we consider the system response in the presence of errors in the initial state conditions for a projected circular formation. Autonomous control algorithms must be capable of correcting initial condition misalignment problems since there is no guarantee that the spacecraft in formation are initially placed exactly into the desired orbit. For an illustration, we assume that there is a 1 km initial offset in the radial, along-track, and cross-track positions.

Figure 3.6 shows the relative position errors and thrust demand for formation-keeping (Case I) when there is a position offset on all three relative states. With no control force available in the radial direction, it can be seen that the output forces in the along-track direction saturates early in the dynamic transient period.

For case II, we assume that there is no position offset in the radial direction and initial error of 1 km in the along-track and cross-track directions. The thrust constraint is reduced to 1 mN for this case. The relative position errors and the required control input forces are shown in Fig. 3.7. Radial and cross-track thrusts saturate during the initial short time period due to large initial errors. The time taken for formation stabilization also increases as we limit the control force to 1 mN.

Next, we demonstrate the effectiveness of the proposed control strategies for multiple formation maneuvers. With the same initial conditions as given by Eq. (3.55), the follower spacecraft moves from a 0.5 km to a 1.5 km (radius) projected circular formation after 5 orbits. Three-dimensional trajectories of the entire formation maneuver without radial axis

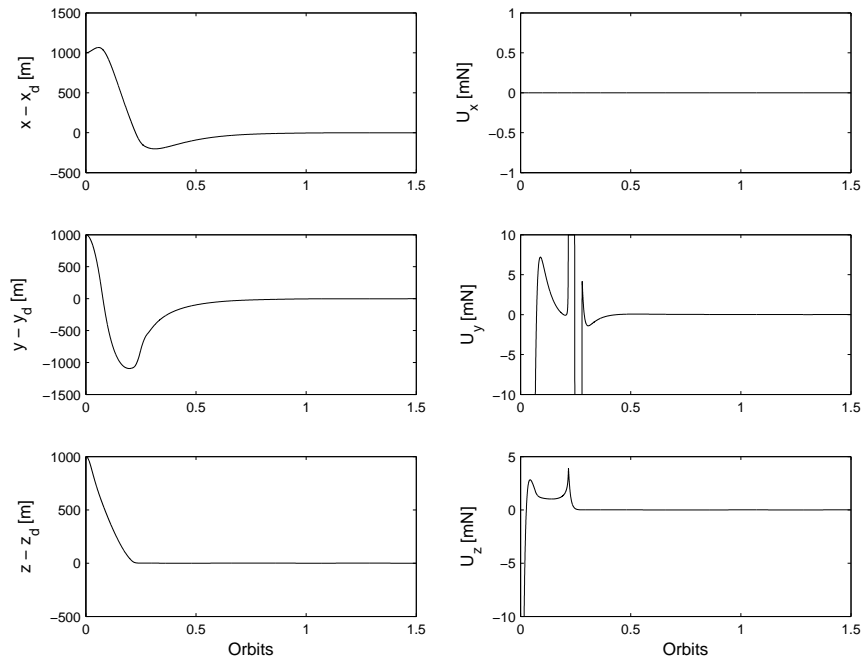


Figure 3.6: Case I with relative J_2 disturbance and initial offset errors.

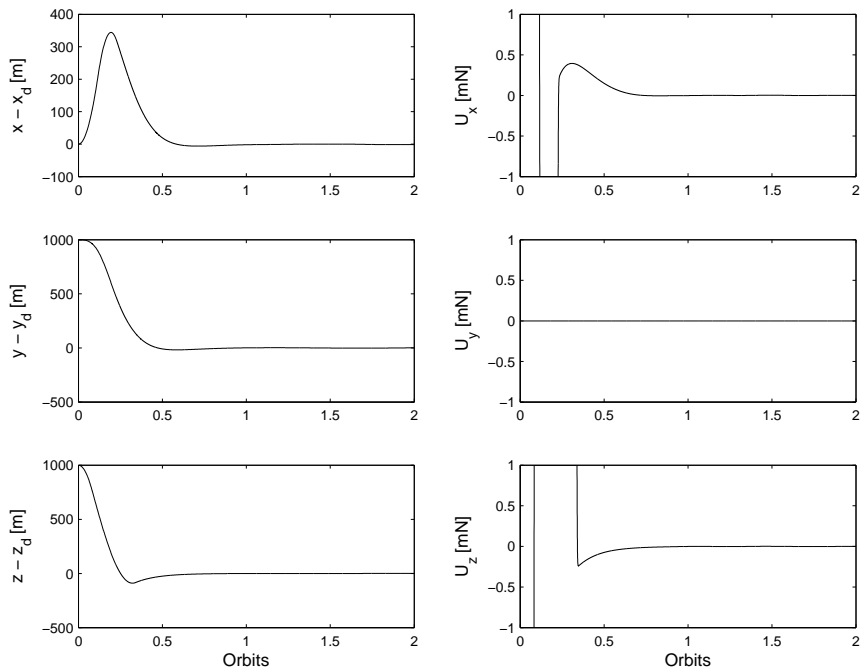


Figure 3.7: Case II with relative J_2 disturbance and initial offset errors.

input (Case I) and no along-track control force (Case II) are shown in Figs. 3.8 and 3.9, respectively. We also illustrate a scenario where the desired geometry is changed from a 0.5 km projected circular formation to a 2 km circular formation. The trajectories of the relative states in three-dimensional space are projected on to the (y, z) plane and shown in Figs. 3.10 and 3.11 for cases I and II, respectively. The simulation of extreme cases of initial errors and formation reconfiguration clearly indicate the proposed control scheme is indeed robust to changing operating conditions and ensures precise formation acquisition during reconfiguration maneuvers. It is also important to note that all these scenarios were simulated with the same control gains presented in Table 3.2. Hence, only one global control algorithm is required to execute the different tasks considered in this study.

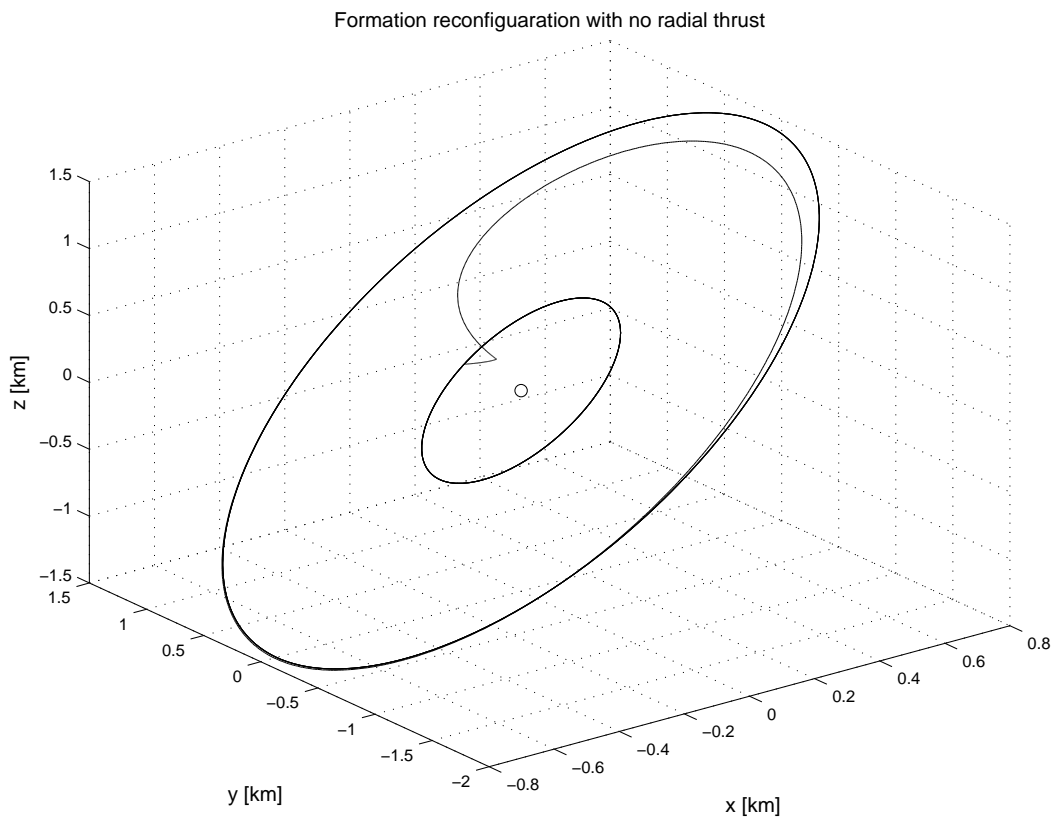


Figure 3.8: Case I - Formation reconfiguration from $R_d = 0.5\text{km}$ to $R_d = 1.5\text{km}$.

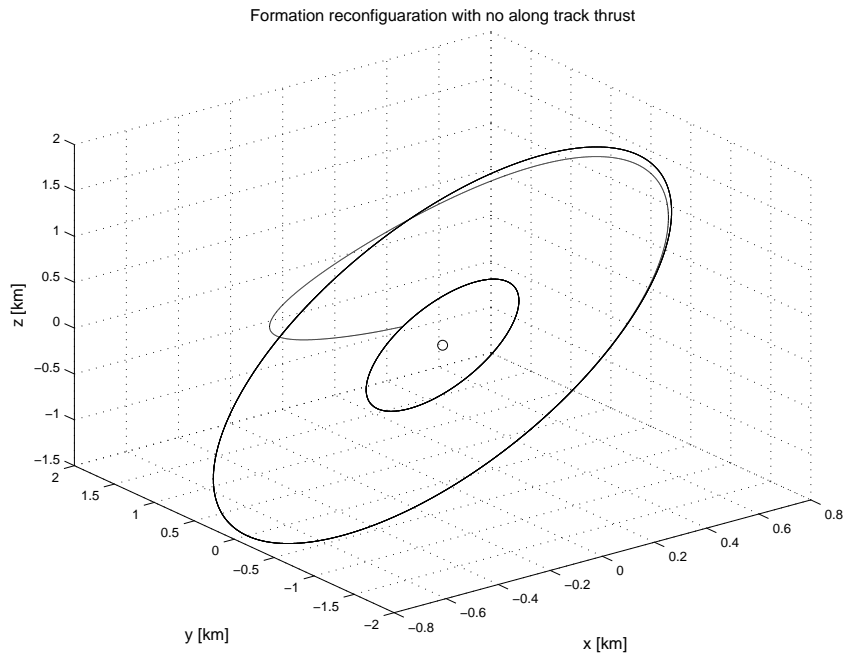


Figure 3.9: Case II - Formation reconfiguration from $R_d = 0.5\text{km}$ to $R_d = 1.5\text{km}$.

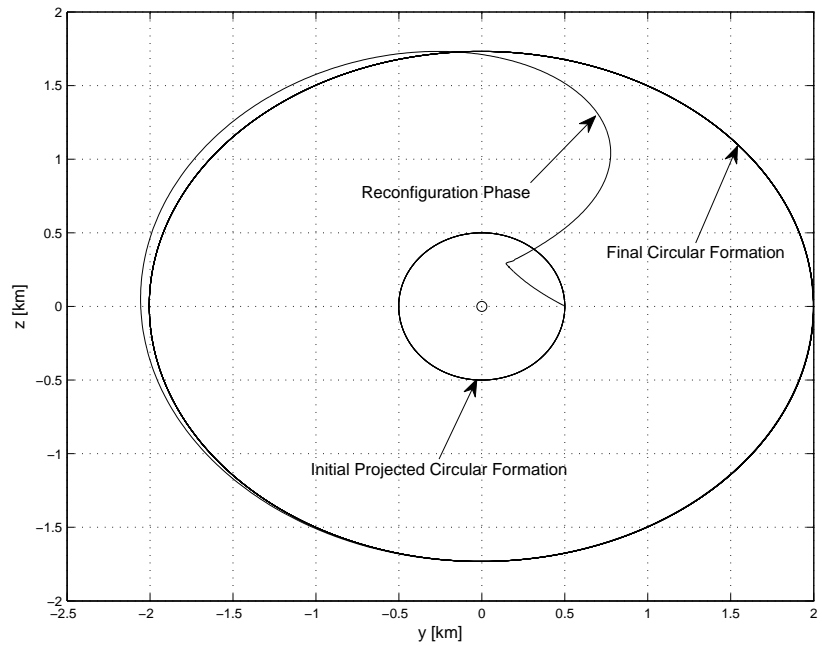


Figure 3.10: Case I - Projected circular to circular formation.

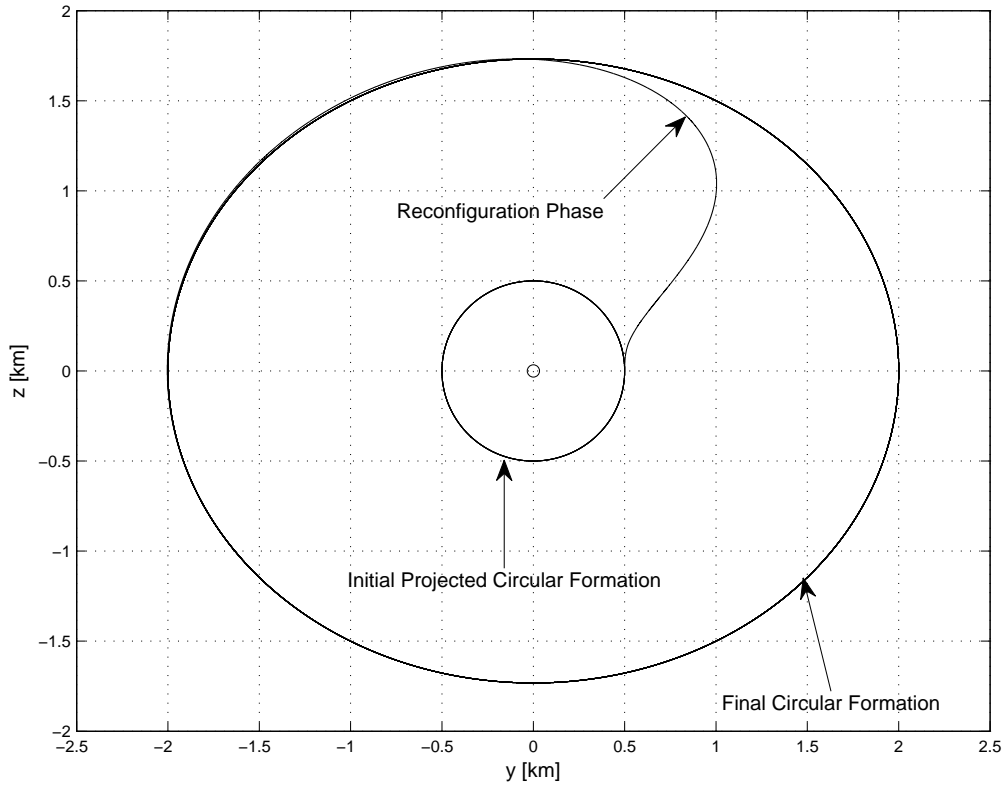


Figure 3.11: Case II - Projected circular to circular formation.

3.2.3 Quantitative Analysis

Based on the simulation results presented above, we examine the control precision and fuel consumption properties of the proposed control scheme. We simulate the following scenario where, (1) the desired reference orbit is a projected circular formation with $r_{dpc} = 1$ km, (2) the leader spacecraft is in an unperturbed circular reference orbit, and (3) the follower spacecraft is positioned correctly into the desired orbit [Eq. (3.55)]. In assessing the effectiveness the proposed control scheme, the accuracy with which the formation can be maintained is an important criteria. Future missions of SFF for high-resolution interferometry and stereographic imaging demand high resolution and precision requirements for station-keeping. The maximum steady-state stabilization errors for all three directions for cases I and II are compared in Table 3.3. The proposed control scheme is capable of accomplishing sub-millimeter tracking precision when no external disturbances are considered,

Table 3.3: Formation-keeping steady-state errors

Errors, m	No Disturbance		Differential J_2	
	Case I	Case II	Case I	Case II
$ e_x _{max}$	1.8×10^{-3}	7.2×10^{-3}	2.2×10^{-2}	2.0×10^{-1}
$ e_y _{max}$	5.0×10^{-3}	5.0×10^{-4}	5.0×10^{-2}	1.8×10^{-2}
$ e_z _{max}$	2.0×10^{-10}	1.2×10^{-9}	8.0×10^{-6}	5.0×10^{-8}

while the tracking capability reduces to the order of 10^{-2} m in the presence of differential J_2 perturbations. Among cases I and II, there is no great variation in performance based on the maximum steady-state errors. By eliminating either radial axis input or along-track input, precision formation maintenance can be achieved.

The fuel consumption for cases I and II are calculated for the same scenario described above, and their respective ΔV requirements are shown in Table 3.4. The ΔV is calculated based on the average budget obtained over a period of 10 orbits. For the case of no disturbance, eliminating radial-axis input (Case I) seems to be beneficial in terms of fuel cost when compared to eliminating along-track input (Case II). In the presence of differential J_2 perturbations, cases I and II provide similar results as seen in Table 3.4. We also calculate the cost required for formation keeping as the result of the integral

$$J = \int_0^{\tau} (u_{fx}^2 + u_{fy}^2 + u_{fz}^2) d\tau \quad (3.56)$$

where $\tau = 10$ is the number of orbits of the leader spacecraft. Figure 3.12 shows the comparison of fuel cost (no external disturbances) over a period of 10 leader orbits for the

Table 3.4: Fuel consumption comparison

Fuel Cost m/s (per orbit)	No Disturbance		Differential J_2	
	Case I	Case II	Case I	Case II
ΔV_x	...	4.3×10^{-4}	...	8.6×10^{-3}
ΔV_y	6.1×10^{-5}	...	8.5×10^{-3}	...
ΔV_z	1.9×10^{-4}	1.9×10^{-4}	5.5×10^{-3}	5.5×10^{-3}

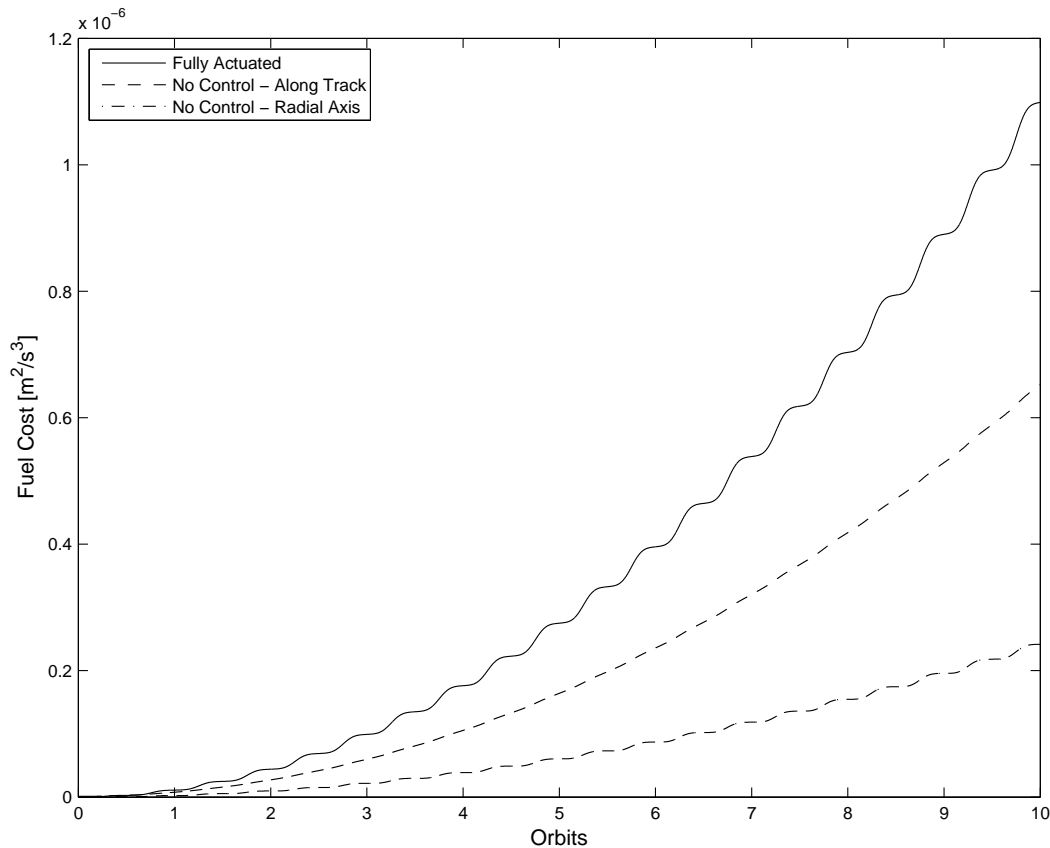


Figure 3.12: Comparison of fuel consumption (disturbance free case).

proposed control scheme (cases I and II) along with the results obtained for using a fully actuated system (control force available in radial, along-track, and cross-track directions). The control gains for the fully actuated case are chosen such that similar performance in terms steady-state errors are obtained in comparison to cases I and II. As shown in Fig. 3.12, the formation-maintenance cost for case I is lower than that for case II. Eliminating control force in any one of the orthogonal in-plane directions (either radial or along-track) reduces the formation-maintenance cost when compared to using control forces in all three orthogonal directions.

Figure 3.13 shows the fuel cost comparison when differential perturbations due to J_2 are taken into account. With no control authority in the radial direction, the formation-maintenance cost is slightly better when compared to the fully actuated case. In the presence of external disturbances, eliminating control force in the along-track direction

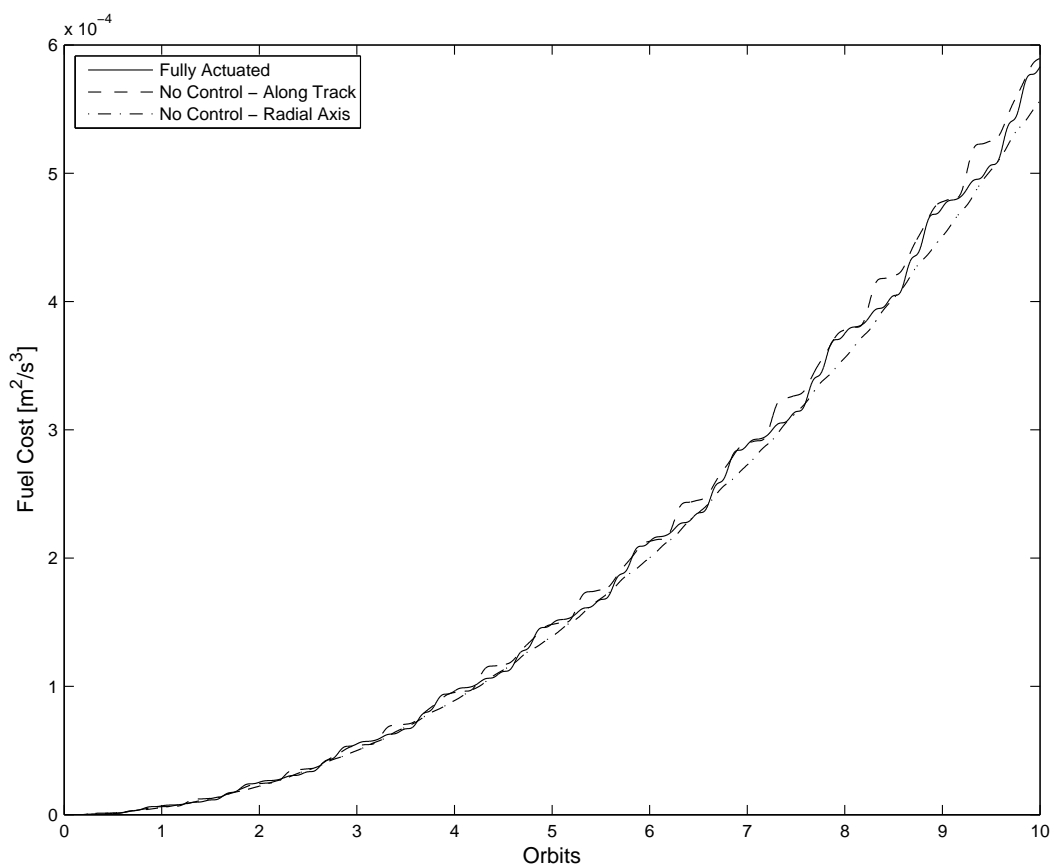


Figure 3.13: Comparison of fuel consumption (with relative J_2 disturbance).

does not provide any superior performance over the fully actuated case in terms of fuel consumption. Based on the comparison of control precision and fuel requirements, it is clearly evident that the proposed control scheme is very efficient in precisely tracking the desired formation with minimal fuel expenditure. The proposed control scheme can be used as a replacement option during the failure of thrusters in the radial or along-track direction. Also, the underactuated configurations proposed in this study can be used to account for fuel savings during station-keeping and formation reconfiguration maneuvers.

Advanced formation control algorithms are critical for realizing robust and autonomous precision formations. These algorithms must maintain precision control performance, provide autonomous recovery from thruster faults, and tailor the formation to science objectives through formation reconfigurations.

3.3 Hardware-in-the-Loop Simulation

Formation testbeds are essential for designing formation architectures and validating the performance of closed-loop control algorithms to achieve various formation objectives. The laboratory equipment used to test the proposed concept of underactuated SFF is called the *Satellite Airbed Formation Experiment* (SAFE) platform. This is developed to provide a design environment that can investigate the feasibility of formation control solutions presented in this chapter under given hardware limitations.

3.3.1 SAFE Overview

The SAFE platform replicates a frictionless environment using a two dimensional (2-D) glass table. This allows for simulated effects of microgravity while in a $1g$ environment. For friction exclusion, air-bearings are used. Air is transmitted through porous material of the air-bearings, under application of pressure, to create an air layer between the glass table and the spacecraft. The glass table provides three degrees of freedom: two translational and one rotational. The underactuated SFF concept is validated via Hardware-in-the-Loop (HIL) simulation, with the SAFE platform floating above the glass surface, commanded by the proposed control algorithm in MATLAB.

The major components that constitute the HIL test setup are as follows: 1) Satellite Airbed Formation Experiment (SAFE) platform, 2) Pneumatic actuation system, 3) Vision based position determination system, 4) Wireless communication unit, 5) Matlab/Simulink

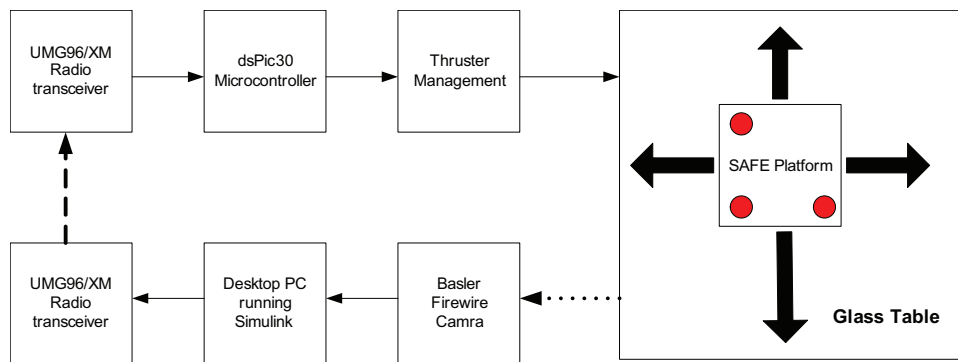


Figure 3.14: Block diagram representation of the SAFE test-bed.

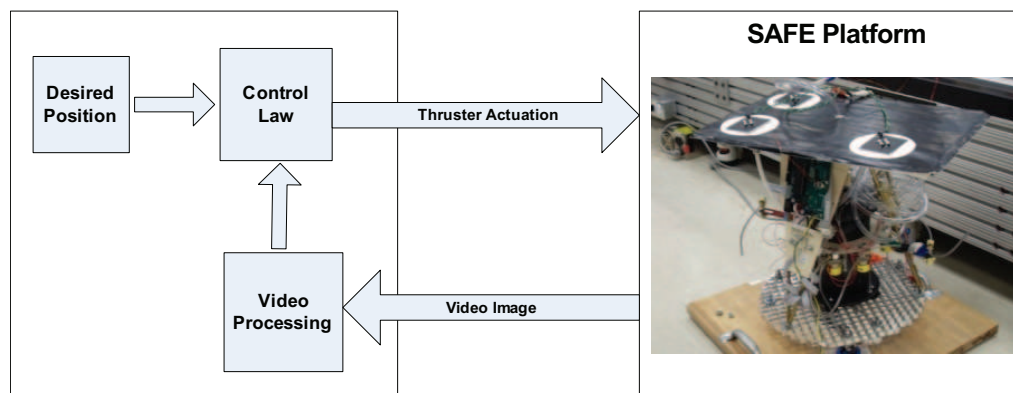


Figure 3.15: Block diagram representation of MATLAB and SAFE interface.

processing the control algorithm. Position and orientation of the SAFE platform is determined using the image tracking system and passed to the control algorithm for estimating the required thrust. Figures 3.14 and 3.15 shows the block diagram of the HIL setup. Table 3.5 gives the details of the key subsystems and its corresponding model used in the test setup. The glass table has a dimension of $3\text{m} \times 2\text{m}$, dsPIC30 is a 16-bit microcontroller from Microchip and the Basler Firewire-400 camera has a resolution of 25mm.

Table 3.5: SAFE Subsystem

Subsystem	Model
Radio transceiver	UMG96XM
Microcontroller	dsPIC30
Pneumatic valve	Clippard
Vision System	Basler Firewire Camera

3.3.2 SAFE System and Mathematical Model

The system architecture and various subsystems of the SAFE platform are described in this section. Three air bearings mounted at the bottom of the SAFE platform minimize its contact with the glass table and help it to float on the glass table. Eight pneumatic thrusters attached on the sides of the platform provide smooth translational motion along

the glass table. These thrusters are controlled by electronic solenoid valves and can only be in either of the two states: ON or OFF. The platform is configured to be controlled in a 'push' configuration, i.e., the thrusters can push the platform to the desired position on the glass table. Figures 3.16 and 3.17 illustrates the configuration of the thrusters and the positioning of the thrusters on the SAFE platform respectively. The red arrows indicate the direction of thrust.

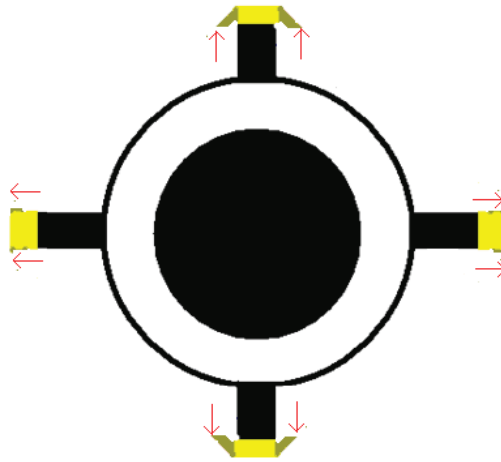


Figure 3.16: Configuration of thrusters on the SAFE platform.

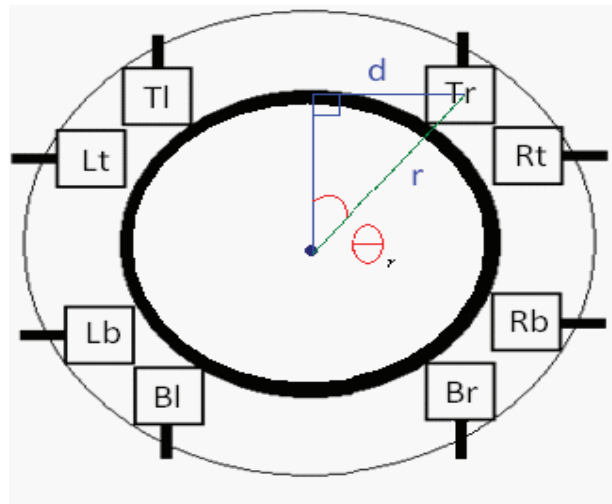


Figure 3.17: Positioning of thrusters on the SAFE platform.

The system also includes a 0.91 L storage tank on the SAFE platform. The wireless radio unit onboard the SAFE platform provides the means for communication between the computer executing the Simulink system model and the microcontroller controlled pneumatic actuation system operating the valves of the thrusters. LEDs are mounted on top of the platform to allow the vision system to continuously track the position of the platform. The vision system mounted on an elevated position above the glass table is hardwired to the computer. The measured position is then used in the control law to compute the sequence of actuation required to maintain the desired trajectory.

3.3.2.1 Equations of Motion

The relative system equations of motion are derived under the assumption that the leader satellite is a virtual point in the center of the glass table. The follower satellite is moving in a relative trajectory about the leader satellite. Its motion is described by the reference frame $S - xy$, Fig. 3.18. $S - XY$ is the inertial reference frame. To derive the equations

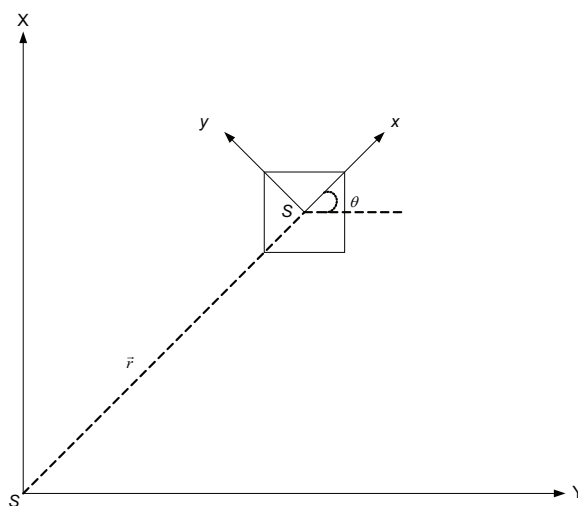


Figure 3.18: Reference frames for SAFE platform.

of motion in the body frame $S - xy$, the position vector of the SAFE platform with respect to $S - XY$ frame expressed in $S - xy$ frame can be written as follows:

$$\vec{r}_{xy} = x \hat{i} + y \hat{j} \quad (3.57)$$

Differentiating with respect to time leads to

$$\dot{\vec{r}}_{xy} = \dot{x} \hat{i} + x \dot{\hat{i}} + \dot{y} \hat{j} + y \dot{\hat{j}} \quad (3.58)$$

Substituting for $\dot{\hat{i}} = \vec{\omega} \times \hat{i}$ and $\dot{\hat{j}} = \vec{\omega} \times \hat{j}$ in Eq. (3.58), we have

$$\dot{\vec{r}}_{xy} = \left(\dot{x} \hat{i} + \dot{y} \hat{j} \right) + \vec{\omega} \times \left(x \hat{i} + y \hat{j} \right) \quad (3.59)$$

where ω is the angular velocity vector if the $S - xy$ frame. Eq. (3.59) represents the inertial velocity of the SAFE platform from a given position and velocity in the $S - xy$ frame. Next we derive an expression for inertial acceleration. Differentiating Eq. (3.59) gives,

$$\ddot{\vec{r}}_{xy} = (\ddot{x} \hat{i} + \ddot{y} \hat{j}) + 2(\vec{\omega} \times \dot{\vec{r}}_{xy}) + \vec{\omega} \times (\vec{\omega} \times \vec{r}_{xy}) + \dot{\vec{\omega}} \times \vec{r}_{xy} \quad (3.60)$$

The term $2(\vec{\omega} \times \dot{\vec{r}}_{xy})$ is called *coriolis acceleration* and the term $\vec{\omega} \times (\vec{\omega} \times \vec{r}_{xy})$ is known as *centripetal acceleration*. Taking $\vec{\omega} = \dot{\theta} \hat{k}$ and $\dot{\vec{\omega}} = \ddot{\theta} \hat{k}$, the acceleration is given by

$$\ddot{\vec{r}} = \left[\ddot{x} - 2\dot{\theta}\dot{y} - \dot{\theta}^2 x + \ddot{\theta}y \right] \hat{i} + \left[\ddot{y} + 2\dot{\theta}\dot{x} + \dot{\theta}^2 y + \ddot{\theta}x \right] \hat{j} \quad (3.61)$$

Based on Newton's 2nd law, the relative translational equations of motion are given by

$$\ddot{x} - 2\dot{\theta}\dot{y} - \dot{\theta}^2 x - \ddot{\theta}y = f_x/m_s \quad (3.62)$$

$$\ddot{y} + 2\dot{\theta}\dot{x} - \dot{\theta}^2 y + \ddot{\theta}x = f_y/m_s \quad (3.63)$$

where f_x, f_y are the control forces, and m_s is the mass of the spacecraft. In the following section, we formulate controllers for the fully actuated and underactuated configurations.

3.3.2.2 Design of Control Laws

Next, the control algorithm developed in Section 3.1 is reformulated to incorporate the mathematical model of the SAFE platform and to manage the switching of the thrusters. The vision system provides the inertial positions X, Y and θ . The inertial position error can then be written as $\tilde{X} = X - X_d$ and $\tilde{Y} = Y - Y_d$, where X_d and Y_d are the desired states. By choosing the desired states to be a particular position in the coordinate axes, we can simulate the formation acquisition procedure where the follower spacecraft is required to acquire a specific orbit with respect to the leader spacecraft.

Tracking errors, \tilde{X} and \tilde{Y} are expressed in the body frame using the following relation:

$$\tilde{x} = \tilde{X} \cos \theta + \tilde{Y} \sin \theta \quad \text{and} \quad \tilde{y} = -\tilde{X} \sin \theta + \tilde{Y} \cos \theta \quad (3.64)$$

Fully Actuated Configuration

The first step in developing a feedback control algorithm based on VSC theory entails the design of a sliding manifold. A two-layer linear sliding surface based on tracking errors for the SAFE satellite in fully actuated configuration is defined as follows:

$$S_x = \dot{\tilde{x}} + c_1 \tilde{x} \quad \text{and} \quad S_y = \dot{\tilde{y}} + c_2 \tilde{y} \quad (3.65)$$

The control law is given by

$$f_x = \begin{cases} U_{eqx} - \eta_x \text{sgn} S_x & \text{if } |S_x| > \delta \\ 0 & \text{if } |S_x| < \delta \end{cases} \quad (3.66)$$

$$f_y = \begin{cases} U_{eqy} - \eta_y \text{sgn} S_y & \text{if } |S_y| > \delta \\ 0 & \text{if } |S_y| < \delta \end{cases} \quad (3.67)$$

where U_{eqx} and U_{eqy} are the equivalent control terms that are obtained by solving $\dot{S}_x = 0$ and $\dot{S}_y = 0$, respectively, for the control terms. The thrusters are activated based on a tracking error dead-band defined by δ .

Underactuated Configuration

The sliding manifold for the underactuated configuration is developed based on the reduced order dynamics. We linearize the nonlinear translational dynamics [Eqs. (3.62) and (3.63)] based on the assumption that the spacecraft is rotating about its center of mass at a constant rate ($\ddot{\theta} = 0$). The linearized equations of motion in state-space form with control authority available only in the along-track direction (y) is given by

$$\begin{bmatrix} \dot{x}_1 \\ \dot{x}_2 \end{bmatrix} = \begin{bmatrix} A_{11} & A_{12} \\ A_{21} & A_{22} \end{bmatrix} \begin{bmatrix} x_1 \\ x_2 \end{bmatrix} + \begin{bmatrix} 0_{3 \times 1} \\ 1 \end{bmatrix} f_y \quad (3.68)$$

where $x_1 \in \mathbb{R}^3 = [x, y, \dot{x}]^T$ represent the unactuated states and $x_2 = \dot{y}$ is the actuated

state. The elements of the A matrix are obtained from Eqs. (3.62) and (3.63) with $\ddot{\theta} = 0$:

$$A_{11} = \begin{bmatrix} 0 & 0 & 1 \\ 0 & 0 & 0 \\ \dot{\theta}^2 & 0 & 0 \end{bmatrix}; \quad A_{12} = \begin{bmatrix} 0 \\ 1 \\ 2\dot{\theta} \end{bmatrix}; \quad A_{21} = \begin{bmatrix} 0 & \dot{\theta}^2 & -2\dot{\theta} \end{bmatrix}; \quad A_{22} = 0 \quad (3.69)$$

Based on the reduced order error dynamics, $\dot{\tilde{x}}_1 = A_{11}\tilde{x}_1 + A_{12}\tilde{x}_2$, the sliding manifold that couples the actuated and unactuated states is chosen as:

$$S_{xy} = \tilde{x}_2 + P\tilde{x}_1 \quad (3.70)$$

where $P \in \mathbb{R}^{1 \times 3}$ is chosen such that during sliding motion, $S_{xy} = 0$, the reduced order error dynamics is stable. Solving for $S_{xy} = 0$ gives $\tilde{x}_2 = -P\tilde{x}_1$ that yields the error dynamics

$$\dot{\tilde{x}}_1 = (A_{11} - A_{12}P)\tilde{x}_1 \quad (3.71)$$

Thus, the choice of surface S_{xy} from Eq. (3.70) clearly affects the dynamics in Eq. (3.71) through the design of P in Eq. (3.70). For $\dot{\theta} = 0.0033$ rad/s and $P = [0.005 \quad -0.001 \quad 1.470]$, the closed-loop eigenvalues of $[A_{11} - A_{12}P]$ are:

$$\lambda_{1,2} = -0.0037 \pm 0.0015i \quad \text{and} \quad \lambda_3 = -0.0010 \quad (3.72)$$

indicating a stable dynamics that governs the sliding motion. Next, the control algorithm that ensures the sliding manifold is reached and motion on S_{xy} is maintained, is given by

$$f_y = \begin{cases} U_{eq} - \eta_{xy} \text{sgn} S_{xy} & \text{if } |S_{xy}| > \delta \\ 0 & \text{if } |S_{xy}| < \delta \end{cases} \quad (3.73)$$

where η_{xy} is a positive scalar. The control law ensures that the sliding manifold is reached and whilst sliding, the system behaves as a reduced order motion which does not depend on the control signal f_y .

Thruster Firing Scheme

The thrusters are fired according to the following sequence (Fig. 3.17): when f_x is positive, the thrusters Lt, Lb, are switched ON and Rt and Rb are switched OFF. While f_x is negative Lt, Lb are switched OFF and Rt and Rb are switched ON. Similarly when f_y is positive the thrusters Bl, Br, are switched ON and Tl and Tr are switched OFF, and while f_y is negative Bl, Br, are switched OFF and Tl and Tr are switched ON.

3.3.3 Experimental Results

The results obtained from the HIL simulations on the SAFE platform are described in this section. The following controller parameters were chosen: $c_1 = 0.1$, $c_2 = 0.2$, $\eta_x = 1$, $\eta_y = 2$, $\eta_{xy} = 5$, and $P = [0.0051, -0.0014, 1.4702]$. The performance of the HIL system was first

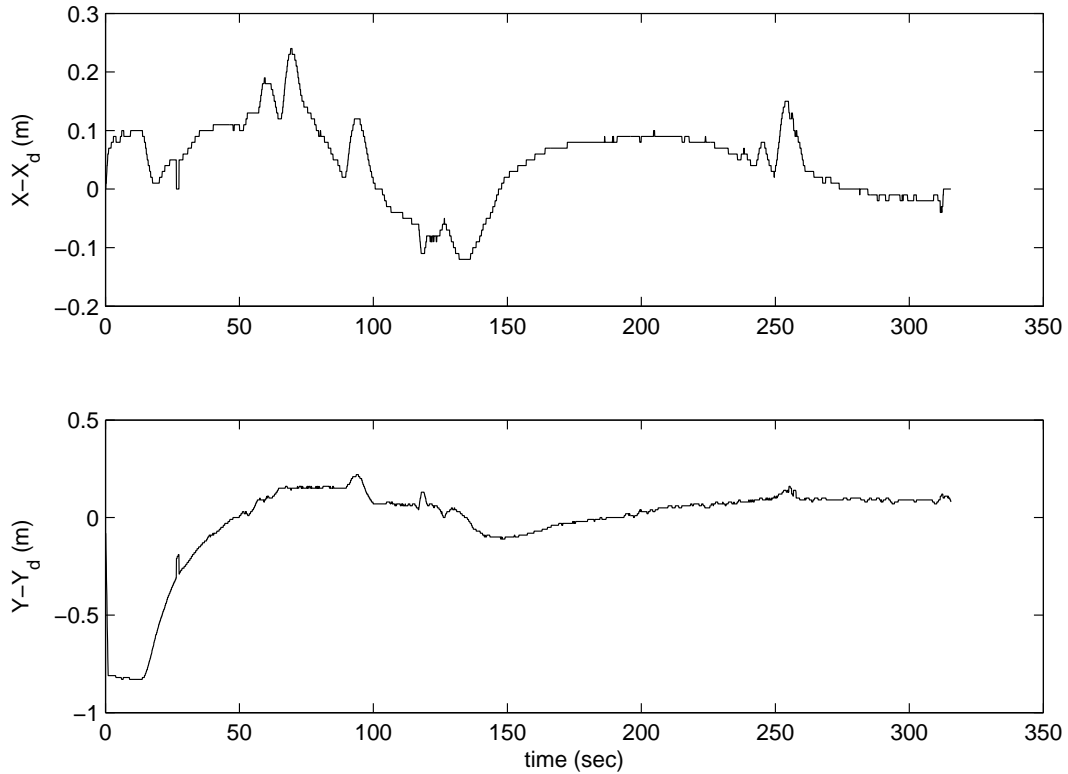


Figure 3.19: Tracking errors - Fully actuated configuration ($X_d = 0, Y_d = 0$).

evaluated in the fully actuated configuration. The methodology to control the thrusters is based on control laws given by Eqs. (3.66) and (3.67). Here the SAFE platform was placed at an arbitrary initial location, $(0.06, -0.08)$ and commanded to traverse towards a desired location $(0, 0)$ and maintain its position. Figure 3.19 shows the X and Y trajectory tracking errors that was traced by the platform on the glass table. The disturbances observed on the system performance can be attributed to the external disturbances due to the tether being used as an air supply mechanism.

Next, the performance of the system in the underactuated configuration is examined. Without radial axis thrust ($f_x = 0$) and using thrust only in the along-track direction, the control scheme given by Eq. (3.73) is used to control the translational dynamics of the SAFE platform. An arbitrary initial position $(0.06, -0.08)$ is chosen and the spacecraft is commanded to move to the desired location, $(0, 0)$. Figure 3.20 shows the X and Y trajectory tracking errors that was traced by the platform on the glass table. From Figs. 3.19 and 3.20, it can be seen that the platform moves to and maintains its position at the desired location with reasonable accuracy (± 0.1 m).

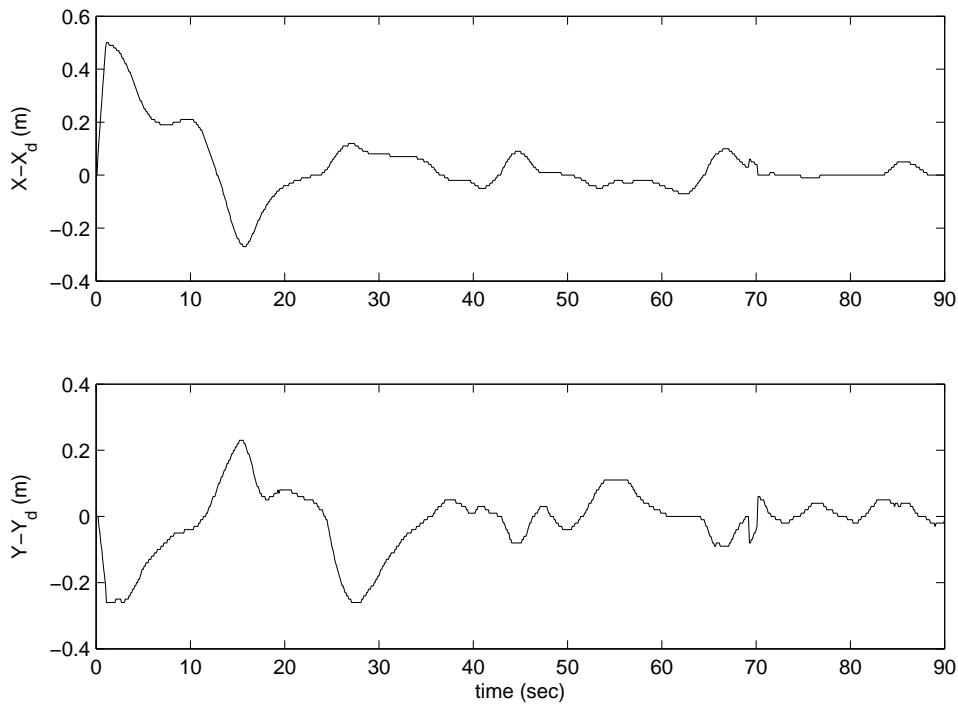


Figure 3.20: Tracking errors - Underactuated configuration ($X_d = 0, Y_d = 0$).

The experimental results presented in this section clearly demonstrates the efficacy of the proposed control algorithm for achieving precision spacecraft positioning in underactuated configuration. The fully actuated system stabilizes to the desired location with less error as compared to the underactuated system.

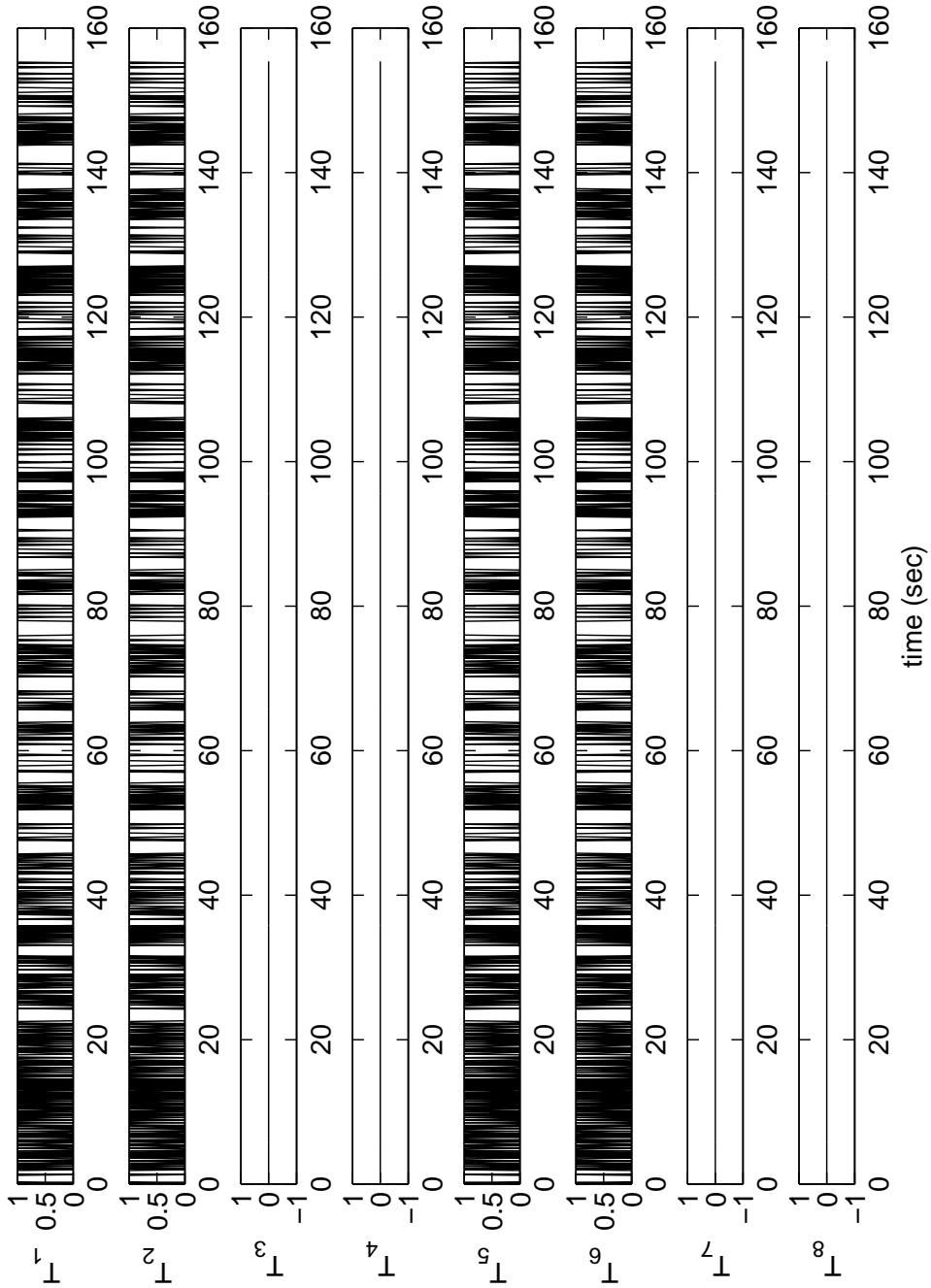


Figure 3.21: Thruster profiles - Underactuated configuration ($X_d = 0.4$, $Y_d = 0.6$).

3.4 Summary

In this chapter, we developed a nonlinear control strategy capable of precision formation control to study two configurations of reduced inputs, where no control force is available in the (1) radial direction, or (2) along-track direction. In particular, the second case, not examined in the literature previously, is challenging because it fails the linear controllability test and hence requires the use of nonlinear control techniques. External disturbances due to differential J_2 is effectively attenuated using the proposed technique and the nonlinearities due to system dynamics are not required in the controller design. Quantitative analysis of the simulation results show that eliminating the radial axis thrust reduces the fuel cost for formation maintenance.

The underactuated configuration (no control authority in the radial direction) was demonstrated using a HIL simulation performed on a formation testbed simulating formation acquisition. The theoretical and experimental results presented in this chapter clearly indicate that the proposed control scheme represents a practical design approach for multiple spacecraft formations to deal with the problem of formation maintenance and reconfiguration maneuvers for the case where the radial or along-track thrusters fail. In chapters 2 and 3, the spacecraft were assumed to be point masses and hence the attitude motion was neglected. In the next chapter, we treat the spacecraft as a rigid body and examine the effects of actuator faults on the performance of the attitude control system of the spacecraft. In Chapter 5, we implement the control strategy proposed in this chapter for attitude control in underactuated configuration.

Fault Tolerant Attitude Control of Spacecraft

SPACECRAFT mission success is highly dependent on the performance and robustness of the attitude control system. Scientific payloads onboard a spacecraft for Earth observation and space monitoring rely on the attitude control system to be oriented towards a prescribed direction with high accuracy to increase the operational envelope and efficiency of miniature spacecraft. Actuation methods used to control the orientation of a spacecraft fall into three main categories [Schaub & Lappas 2009]: 1) reaction control thrusters, 2) internal momentum exchange devices like reaction wheels and control moment gyros, and 3) external environmental influences such as the gravity gradient, atmospheric, solar radiation pressure, or magnetic torques. With increasing demands in the context of agile mission scenarios and stringent physical size constraints, the development of low-cost customizable attitude actuators for small spacecraft is a difficult task.

Attitude control systems (ACS) are required to provide the spacecraft with attitude maneuver, tracking, and pointing capabilities. Loss of critical control actuators like reaction wheels can lead to spacecraft pointing control accuracy degradation and for some cases, the spacecraft may completely lose its stabilization capability. The ability of the spacecraft to attain sufficient degree of attitude dexterity after losing two reaction wheels has been practically demonstrated for several missions like TOPEX [Lam *et al.* 2001], and FUSE [Kruk *et al.* 2002a]. Three-axis stabilization using two remaining reaction wheels was accomplished by integrating other torque generating actuators like reaction control thrusters and magnetic torquer bars (MTB). Thruster assisted approach is not desirable because they consume a lot of propellant while MTBs are only applicable for spacecraft in LEO. In this chapter, we present an adaptive fault-tolerant control algorithm capable of

providing highly accurate 3-axis attitude tracking for miniature spacecraft using reaction wheels as actuators. The aim is to develop a comprehensive computer simulation model and a hardware test-bed to facilitate testing and validation of the proposed fault-tolerant control algorithm. A high-fidelity numerical model of the spacecraft is integrated with a reaction wheel assembly developed for pico-satellites using a hardware-in-the-loop test-bed interfaced via MATLAB.

The chapter is organized as follows: Section 4.1 introduces the nonlinear mathematical model of the spacecraft. The proposed fault-tolerant control algorithm is formulated in Section 4.2 along with detailed proof of stability for the closed-loop system in the presence of fading actuation and complete wheel failure. The hardware model and configuration of the reaction wheels are presented in Section 4.3. The numerical simulation results incorporating different fault scenarios are presented in Section 4.4. The HIL simulation results are detailed in Section 4.6. Finally, the conclusions of the present study are stated in Section 4.6.

4.1 Spacecraft Mathematical Model

The investigation is initiated by formulating the complete nonlinear equations of motion of the rigid spacecraft to develop a mathematical model that facilitates the design of nonlinear control methodologies. Our focus is on testing and validating the proposed fault-tolerant control algorithm for spacecraft ACS with reaction wheels as actuators. The proposed system consists of a *rigid body spacecraft* in a circular orbit around the Earth (Figure 4.1).

4.1.1 Coordinate Frames

The coordinate frames used to represent the dynamics of the spacecraft are shown in Figure 4.1. An *Earth centered inertial* (ECI) frame is denoted by $\mathfrak{J} - X_I Y_I Z_I$, has its origin located at the center of the Earth, with Z_I -axis passing through the celestial North pole, X_I -axis directed towards the vernal equinox, and Y_I -axis completes the right-handed triad. Next, we define a local vertical local horizontal (LVLH) orbital reference frame $\mathfrak{L} - x_o y_o z_o$ fixed at the center of the spacecraft with the x_o -axis along the direction of motion, the y_o -axis opposite to the direction of the angular velocity (normal to the orbit

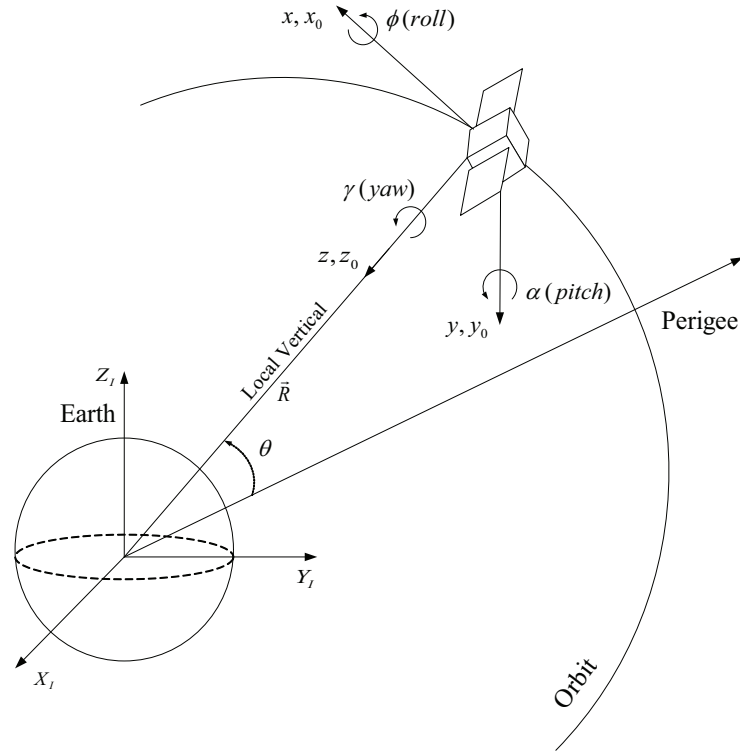


Figure 4.1: Geometry of orbit motion of rigid spacecraft.

plane), and the z_o -axis pointing towards the Earth. The nodal line represents the reference line in orbit for the measurement of the true anomaly (eccentric orbit) or reference angle θ (circular orbit). The corresponding principal body-fixed coordinate axes of the spacecraft are denoted by $\mathfrak{B} - xyz$ with its origin located at the center of mass of the spacecraft. The notation [Fragopoulos & Innocenti 2004] used for representing the relative velocity vector, \mathbf{v} , of frame \mathfrak{L} relative to frame \mathfrak{J} , expressed in the coordinates of \mathfrak{B} is: \mathbf{v}_{LI}^B . The cross-product of vectors $a \times b$ is defined as $[a^\times]b$ where $[a^\times]$ is a skew-symmetric operator.

4.1.2 Spacecraft Dynamics

Consider a rigid spacecraft with a 4-wheel cluster installed to provide internal torques. The rotational equations of motion for the spacecraft actuated by reaction wheels are given by [Tsiotras *et al.* 2001]

$$\dot{H}_{BI}^B + \omega_{BI}^B \times H_{BI}^B = \tau_e \quad (4.1)$$

where ω_{BI}^B is the angular velocity of the spacecraft relative to the inertial frame \mathfrak{I} , expressed in the \mathfrak{B} frame, and $\tau_e \in \mathbb{R}^{3 \times 1}$ represents the external torque acting on the system. H_{BI}^B is the total angular momentum of the spacecraft relative to \mathfrak{I} and expressed in \mathfrak{B} , given by

$$H_{BI}^B = J\omega_{BI}^B + AH_w \quad (4.2)$$

where \mathbf{A} is the 3×4 project matrix whose columns represent the influence of each reaction wheel on the angular acceleration of the spacecraft. We define a matrix $J = J_s - AJ_w A^T$, where $J_s \in \mathbb{R}^{3 \times 3}$ is the moment of inertia of the spacecraft, including the wheels, and $J_w \in \mathbb{R}^{4 \times 4} = \text{diag}([J_{w1}, J_{w2}, J_{w3}, J_{w4}])$ denotes the axial moment of inertia of the reaction wheels. The axial angular momentum of the reaction wheels, H_w , can be expressed as

$$H_w = J_w(\Omega + A^T \omega_{BI}^B) \quad (4.3)$$

where $\Omega \in \mathbb{R}^{4 \times 1}$ denotes the axial angular velocity of the reaction wheels.

Combining Eqs. (4.1)-(4.3), the attitude dynamics of a rigid spacecraft controlled by reaction wheels can in general be described the following nonlinear differential equation:

$$J\dot{\omega}_{BI}^B = -\omega_{BI}^B \times (J_s \omega_{BI}^B + AJ_w \Omega) + A\tau_{rw} + \tau_e \quad (4.4)$$

The torques generated by the reaction wheels (τ_{rw}) are given by

$$\tau_{rw} = \dot{H}_w = J_w(\dot{\Omega} + A^T \dot{\omega}_{BI}^B) \quad (4.5)$$

During validation of the control algorithms using computer simulations, the angular velocity of the reaction wheels are obtained by numerically integrating Eq. (4.5). For HIL simulations, each wheel module is equipped with a tachometer that measures the wheel speed which is differentiated to compute the torque applied to the spacecraft.

4.1.3 Attitude Kinematics

The spacecraft attitude kinematic equations relate the time derivatives of the attitude coordinates to the angular velocity vector. Euler angles, Cayley-Rodrigues parameters, modified Rodrigues parameters, and quaternion (also called Euler parameters) are some of

the parameterization methods available in the literature to represent the kinematic equations of motion of the spacecraft. In this study, we adopt the unit quaternion [Wie 1998] to describe the attitude of the spacecraft. The unit quaternion \bar{q} is defined by

$$\bar{q} = \begin{bmatrix} \bar{e} \sin(\Phi/2) \\ \cos(\Phi/2) \end{bmatrix} = \begin{bmatrix} q_v \\ q_4 \end{bmatrix} \quad (4.6)$$

where Φ denotes the principal angle, and $\bar{e} = [e_1, e_2, e_3]^T$ denotes the principal axis associated with Euler's Theorem ($e_1^2 + e_2^2 + e_3^2 = 1$). $q_4 \in \mathbb{R}$ and $q_v \in \mathbb{R}^{3 \times 1} = [q_1, q_2, q_3]^T$ denote the Euler parameters that represent the orientation of the spacecraft body frame, \mathfrak{B} , with respect to the orbital frame, \mathfrak{L} , and satisfy the constraint $q_v^T q_v + q_4 = 1$. The nonlinear differential equations governing the kinematics of the spacecraft in terms of Euler parameters can be expressed as

$$\begin{bmatrix} \dot{q}_v \\ \dot{q}_4 \end{bmatrix} = \frac{1}{2} \begin{bmatrix} q_4 I + [q_v^\times] \\ -q_v^T \end{bmatrix} \omega_{BL}^B \quad (4.7)$$

where $I \in \mathbb{R}^{3 \times 3}$ represents the identity matrix, and $[q_v^\times]$ denotes a skew-symmetric matrix which is given by

$$[q_v^\times] = \begin{bmatrix} 0 & -q_3 & q_2 \\ q_3 & 0 & -q_1 \\ -q_2 & q_1 & 0 \end{bmatrix} \quad (4.8)$$

The angular velocity of the body-fixed reference frame, \mathfrak{B} , with respect to the inertial frame, \mathfrak{I} , can be expressed as

$$\omega_{BI}^B = \omega_{BL}^B + \omega_{LI}^B \quad (4.9)$$

The direction cosine matrix C_L^B that describes the orientation of the spacecraft body-fixed frame, \mathfrak{B} , with respect to the LVLH reference frame, \mathfrak{L} defined in terms of Euler parameters is given by

$$C_L^B = (q_4^2 - q_v^T q_v)I + 2q_v q_v^T - 2q_4 [q_v^\times] \quad (4.10)$$

The orbital angular velocity expressed in the \mathfrak{B} frame, ω_{LI}^B , can be obtained by rotating the angular velocity in \mathfrak{L} using the transformation matrix C_L^B as follows:

$$\omega_{LI}^B = C_L^B \begin{bmatrix} 0 & -\omega_0 & 0 \end{bmatrix}^T \quad (4.11)$$

where $\omega_0 = \dot{\theta}$ is the magnitude of orbital angular velocity of the LVLH frame. For a circular orbit, $\dot{\theta} = \sqrt{\mu_e/R_c^3}$, where μ represents the gravitational parameter of the Earth, and R_c defines the distance of the spacecraft measured from the center of the Earth.

4.1.4 External Disturbances

The external torques (τ_e) are assumed to include gravity gradient torque (τ_g) and other disturbance torques (τ_d) acting on the spacecraft, $\tau_e = \tau_g + \tau_d$. The gravity gradient torque is given by [Schaub & Junkins 2003]

$$\tau_g = 3\omega_0^2 [\hat{c}_3^\times] J_s \hat{c}_3, \quad \hat{c}_3 = C_L^B [0 \ 0 \ 1]^T \quad (4.12)$$

The disturbance torque considered in this study is of the form [Cai *et al.* 2008]

$$\tau_d = \left(\frac{1}{2} + \|\omega_{BL}^B\|^2 \right) \begin{bmatrix} \sin(0.8t) \\ \cos(0.5t) \\ \cos(0.3t) \end{bmatrix} \quad (4.13)$$

4.1.5 Attitude Tracking

In the case of tracking a desired rotational motion, the target attitude of the spacecraft in the desired reference frame \mathfrak{B}_δ with respect to the LVLH frame \mathfrak{L} is described by the orientation $(q_{dv}, q_{d4}) \in \mathbb{R}^3 \times \mathbb{R}$ that satisfies the constraint $q_{dv}^T q_{dv} + q_{d4}^2 = 1$. Let $\omega_d \in \mathbb{R}^3$ denote the angular velocity of \mathfrak{B}_δ with respect to \mathfrak{L} , expressed in the frame \mathfrak{B}_δ . We assume that there exists known, finite constants, $c_1 > 0$ and $c_2 > 0$ such that $\|\omega_d\| \leq c_1$ and $\|\dot{\omega}_d\| \leq c_2$ for all $t \geq 0$. To address the attitude tracking problem, we define the quaternion tracking error $(q_e, q_{4e}) \in \mathbb{R}^3 \times \mathbb{R}$ as the relative orientation between the body-fixed frame \mathfrak{B} and the desired reference frame \mathfrak{B}_δ , which is computed as

$$\begin{aligned} q_e &= q_{d4} q_v - q_4 q_{dv} + [q_v^\times] q_{dv} \\ q_{4e} &= q_{d4} q_4 + q_{dv}^T q_v \end{aligned} \quad (4.14)$$

where $q_e^T q_e + q_{4e}^2 = 1$. The corresponding rotation matrix $C_e = C(q_e, q_{4e}) \in SO(3)$ is given by

$$C_e = (q_{4e}^2 - q_e^T q_e) I + 2q_e q_e^T - 2q_{4e} [q_e^\times] \quad (4.15)$$

where $C_e^T C_e = 1$, $\|C_e\| = 1$, $\det(C_e) = 1$, and $\dot{C}_e = -[\omega_e^\times]C_e$. Next, we define the relative angular velocity $\omega_e \in \mathbb{R}^3$ of \mathfrak{B} with respect to \mathfrak{B}_d as follows:

$$\omega_e = \omega_{BL}^B - C_e \omega_d \quad (4.16)$$

To derive the error dynamics, we first represent the attitude dynamics in Eq. (4.4) in terms of the relative motion of \mathfrak{B} in \mathfrak{L} . Taking the first derivative of Eq. (4.9) and using the fact that $\dot{C}_L^B = -[\omega_{BL}^B]^\times C_L^B$ we obtain

$$\dot{\omega}_{BI}^B = \dot{\omega}_{BL}^B + \dot{\omega}_{LI}^B = \dot{\omega}_{BL}^B - \omega_{BL}^B \times \omega_{LI}^B \quad (4.17)$$

From Eqs. (4.4), (4.7), (4.14), (4.16), and (4.17), the equations that govern the relative attitude error dynamics and kinematics are given by

$$J\dot{\omega}_e = J[(\omega_{BL}^B \times \omega_{LI}^B) + [\omega_e^\times]C_e \omega_d - C_e \dot{\omega}_d] - \omega_{BI}^B \times (J_s \omega_{BI}^B + A J_w \Omega) + A \tau_{rw} + \tau_e \quad (4.18)$$

$$\dot{q}_e = \frac{1}{2}(q_{4e} I + [q_e^\times])\omega_e \quad (4.19)$$

$$\dot{q}_{4e} = -\frac{1}{2}q_e^T \omega_e \quad (4.20)$$

4.1.6 Actuator Dynamics

Reaction wheels are widely used to perform precise spacecraft attitude maneuvers because they allow continuous and smooth control. They are capable of changing its internal angular momentum vector as each wheel spins about a body-fixed axis with variable spin speed. The angular momentum generated by the reaction wheel is transferred to the spacecraft system and momentum generated by spacecraft rotation affects the reaction wheel system [Schaub & Junkins 2003]. Torques are produced on the spacecraft by accelerating or decelerating the reaction wheels.

Conventional feedback control algorithms for spacecraft attitude control are mostly designed for control torque and the actuator dynamics of the reaction wheel are often neglected. However, in real applications, it is important to integrate the characteristics and actuator dynamics of the reaction wheels into the ACS dynamics. The control torque produced on the spacecraft is dependent on the characteristics of the input voltage that, in turn, control the actuator dynamics of the reaction wheels.

Each reaction wheel considered in this study consists of a rotating flywheel, suspended on ball bearings, and is driven by an electrical brushless direct current (DC) motor which can provide an electric torque. The motor torque delivered by a DC-motor is directly proportional to the armature current (*ampere*), $i_a \in \mathbb{R}^{4 \times 1}$, and can be written as [Bialke 1998]

$$\tau_m = K_t i_a \quad (4.21)$$

where $K_t \in \mathbb{R}^{4 \times 4} = \text{diag}([k_{t1}, k_{t2}, k_{t3}, k_{t4}])$ is the motor torque constant. For a constant flux, the induced voltage in the armature (back-EMF), $e_b \in \mathbb{R}^{4 \times 1}$, is directly proportional to the angular velocity of the rotor shaft. The rotor shaft of the motor will have the same angular velocity and acceleration as the reaction wheel. Thus, based on Faraday's law of inductance, the back-EMF is given by

$$e_b = K_b \Omega \quad (4.22)$$

where $K_b \in \mathbb{R}^{4 \times 4} = \text{diag}([k_{b1}, k_{b2}, k_{b3}, k_{b4}])$ is the back-EMF constant. Using Krichoff's voltage law, we obtain the differential equation for the armature of the DC-motor circuit:

$$L_a \frac{di_a}{dt} + R_a i_a + K_b \Omega = e_a \quad (4.23)$$

where $L_a \in \mathbb{R}^{4 \times 4} = \text{diag}([l_{a1}, l_{a2}, l_{a3}, l_{a4}])$ is the armature inductance (*henry*), $R_a \in \mathbb{R}^{4 \times 4} = \text{diag}([r_{a1}, r_{a2}, r_{a3}, r_{a4}])$ is the armature resistance (*ohm*), and $e_a \in \mathbb{R}^{4 \times 1}$ is the applied armature voltage (*volt*). The values of inductance in the armature circuit of the reaction wheels considered in this study are very small and therefore neglected in the dynamic model of the DC-motor. Thus, Eq. (4.23) can be simplified to obtain the following linear equation

$$i_a = R_a^{-1}(e_a - K_b \Omega) \quad (4.24)$$

The friction in a reaction wheel can be mathematically broken down into viscous friction and Coulomb friction. The viscous friction varies with speed and the Coulomb friction is a constant with polarity dependence on wheel direction of rotation [Bialke 1998]. A simplified model of the friction torque as the sum of Coulomb and viscous terms is given by

$$\tau_f = N_c \text{sgn}(s) + f s \quad (4.25)$$

where $N_c = 7.06 \times 10^{-4}$ Nm is the Coulomb friction coefficient, $f = 1.21 \times 10^{-6}$ Nm/rpm is the viscous friction coefficient, and s is the wheel speed in revolutions per minute (*rpm*). Net torque from reaction wheels is the motor torque, τ_m , less any frictional losses, τ_f :

$$\tau_{net} = \tau_m - \tau_f \quad (4.26)$$

Based on Newton's third law, the reaction torque (τ_{rw}) applied to the spacecraft is equal and opposite to the net torque, τ_{net} , which accelerates or decelerates the flywheel. Using Eqs. (4.5), (4.21), and (4.24)-(4.26), we obtain

$$\tau_{rw} = -\tau_{net} = \tau_f - \tau_m = N_c \text{sgn}(s) + fs - K_t R_a^{-1}(e_a - K_b \Omega) \quad (4.27)$$

Let the torque demanded by the spacecraft be denoted as u_r . The input voltage required to control the actuator dynamics of the reaction wheel can be obtained from Eq. (4.27) as

$$e_a = K_b \Omega - R_a K_t^{-1}(u_r - \tau_f) \quad (4.28)$$

Our control objective is achieve high precision attitude tracking maneuvers in the presence of external disturbances, parameter uncertainties, and unknown reaction wheel faults. A fault-tolerant attitude tracking control scheme is proposed in this study that can render the closed-loop system asymptotically stable with the attitude orientation and angular velocity tracking errors converging to a small neighborhood of the origin.

4.2 Fault-Tolerant Attitude Tracking Control Law

In this section we present the theoretical basis for developing adaptive fault-tolerant control algorithms for the spacecraft mathematical model. First, the methods and analysis tools of Variable Structure Control (VSC) are developed that are robust to nonlinear modeling errors. The formulation of the nominal VSC law is then improved using adaptive approximation in the presence of nonlinear model uncertainty. The concept behind VSC approach is to design a high speed control algorithm that can drive the state trajectory of the nonlinear system onto a sliding or switching surface and maintain the system's state trajectory on the sliding surface.

4.2.1 Design of Sliding Manifold

The sliding manifold for the spacecraft system should be designed such that not only the stability of the closed-loop system is guaranteed in the presence of perturbations, but also the desired dynamic behavior should be exhibited once the error trajectory of system is confined to the sliding surface. A linear sliding surface based on the angular velocity errors and the quaternion attitude parameter errors is defined as follows:

$$\sigma = \omega_e + \beta \operatorname{sgn}(q_{4e}) q_e \quad (4.29)$$

where $\beta > 0$ is the sliding gain chosen by the designer and $\operatorname{sgn}(q_{4e})$ is given by

$$\operatorname{sgn}(q_{4e}) = \begin{cases} 1 & \text{for } q_{4e} \geq 0 \\ -1 & \text{for } q_{4e} < 0 \end{cases} \quad (4.30)$$

Once the error trajectory has reached the sliding surface, the system is forced to remain in sliding mode. Thus, the convergence of the angular velocity errors and the quaternion errors can be determined by solving $\sigma = 0$.

$$\begin{aligned} \sigma &= \omega_e + \beta \operatorname{sgn}(q_{4e}) q_e = 0 \\ \omega_e &= -\beta \operatorname{sgn}(q_{4e}) q_e \end{aligned} \quad (4.31)$$

Next, we verify the Lyapunov stability of kinematic subsystem Eqs. (4.19)-(4.20) when the system is confined to the sliding manifold [Eq. (4.31)]. We define a candidate Lyapunov function as follows:

$$V(q) = [q_{4e} - \operatorname{sgn}(q_{4e})]^2 + q_e^T q_e \quad (4.32)$$

Taking the time derivative of the Lyapunov function and substituting the relative attitude error kinematics from Eqs. (4.19)-(4.20) yields

$$\begin{aligned} \dot{V}(q) &= 2[q_{4e} - \operatorname{sgn}(q_{4e})]\dot{q}_{4e} + 2q_e^T \dot{q}_e \\ &= [q_{4e} - \operatorname{sgn}(q_{4e})](-q_e^T \omega_e) + q_e^T (q_{4e} \mathbf{I} + [q_e^\times]) \omega_e \end{aligned} \quad (4.33)$$

Substituting Eq. (4.31) into Eq. (4.33), we get

$$\begin{aligned} \dot{V}(q) &= [q_{4e} - \operatorname{sgn}(q_{4e})][\beta \operatorname{sgn}(q_{4e}) q_e^T q_e] + q_e^T (q_{4e} \mathbf{I} + [q_e^\times])[-\beta \operatorname{sgn}(q_{4e}) q_e] \\ &= -\beta q_e^T q_e - \beta \operatorname{sgn}(q_{4e}) q_e^T [q_e^\times] q_e \end{aligned} \quad (4.34)$$

Using the property of skew-symmetric matrices, $[q_e^\times]q_e = [0, 0, 0]^T$, Eq. (4.34) can be written as

$$\dot{V}(q) = -\beta q_e^T q_e \quad (4.35)$$

Since $\beta > 0$, it is obtained that $\dot{V}(q) < 0$ for $q_e \neq 0$ such that q_e converges to zero. If $q_{4e} \geq 0$, we have $\lim_{t \rightarrow \infty} q_{4e}(t) = 1$ since for this case $\dot{q}_{4e} \geq 0$. If $q_{4e} \leq 0$, we have $\lim_{t \rightarrow \infty} q_{4e}(t) = -1$ since in this case $\dot{q}_{4e} \leq 0$. From Eq. (4.31), we can easily show that the angular velocity error $\omega_e \rightarrow 0$. Therefore, by designing the sliding manifold as given by Eq. (4.29), the stability of the system in sliding mode is guaranteed.

4.2.2 Control Law Formulation

The second phase of the design procedure is to develop a nonlinear control algorithm that can steer the trajectories of the system, Eqs. (4.18)-(4.20), to the sliding manifold given by Eq. (4.29). The algorithm should also be capable of maintaining the system states on the sliding manifold for all $t > t_r$, where t_r is the sliding surface reaching time. The main challenge is to control the attitude of the spacecraft in the presence of parameter uncertainties, external disturbance torques. Combining Eq. (4.29) with Eqs. (4.18)-(4.20), we have the following error model:

$$J\dot{\sigma} = A\tau_{rw} - A\Gamma\tau_{rw} + \Delta \quad (4.36)$$

where the matrix $\Gamma = \text{diag}([\gamma_1, \gamma_2, \gamma_3, \gamma_4])$ is comprised of scalar functions γ_i which satisfy $0 \leq \gamma_i \leq 1$. This matrix is called the reaction wheel effectiveness matrix where γ_i being the "health indicator" for the i -th reaction wheel. Several cases include, $\gamma_i = 0$ which states that the i -th reaction wheel is fully functional, $\gamma_i = 1$ implies that the i -th reaction wheel has saturated or totally failed, and $0 < \gamma_i < 1$ indicates the wheel speed degradation of the i -th reaction wheel.

$$\begin{aligned} \Delta = & J[(\omega_{BL}^B \times \omega_{LI}^B) + [\omega_e^\times]C_e\omega_d - C_e\dot{\omega}_d] - \omega_{BI}^B \times (J_s\omega_{BI}^B + AJ_w\Omega) \\ & + \frac{\beta}{2}\text{sgn}(q_{4e})(q_{4e}I + [q_e^\times]) + \tau_e \end{aligned} \quad (4.37)$$

Note that Δ is the lumped term containing two parts (adapted from [Cai *et al.* 2008]):
1) system nonlinearities based on desired attitude trajectory, physical parameters, and

nonlinear coupling terms, and 2) time-varying and state dependent external perturbation torques due to gravity gradient and other disturbance torques. In the event of reaction wheel failures/faults, achieving precision attitude control becomes a difficult task in the presence of system nonlinearities, and time varying external disturbances. In this study, we explore the nonregressor-based approach to dealing with the effect of Δ which was used in Cai et al. [Cai *et al.* 2008] for attitude tracking control considering thruster failures and thrust limits. This indirect approach assumes that Δ is bounded and its upper bound can be utilized to extract core information of the system nonlinearities, uncertainties, and disturbances in the control design. Therefore, we assume that Δ is unknown but bounded and satisfies the relation

$$\|\Delta\| < p_0 + p_1\|X\| = \eta \quad (4.38)$$

where p_0 and p_1 are known positive constants, and $X \in \mathbb{R}^6 = [q_v, \omega_{BL}^B]^T$.

The proposed attitude tracking scheme comprises of two components: 1) a robust control algorithm that can stabilize the attitude orientation and angular velocity tracking errors to a small set containing the origin, and 2) an adaptive component capable of handling uncertainties due to constant or slow-varying parameters, external disturbances, and actuator faults. The control algorithm and the adaptive law are given by

$$u_r = -\alpha A^T \sigma - (\rho + 1)\eta A^T \text{sgn}(\sigma) \quad (4.39)$$

$$\dot{\rho} = -b_1 \rho + b_2 \eta \|\sigma\| \quad (4.40)$$

where $\alpha, b_1, b_2 > 0$ are scalar constants, and $\text{sgn}(\sigma) = [\text{sgn}(\sigma_1), \text{sgn}(\sigma_2), \text{sgn}(\sigma_3)]^T$. In Eq. (4.39), $u_r \in \mathbb{R}^4$ is the torque required to control the spacecraft. This torque command is used to determine the input voltage required [Eq. (4.28)] to control the actuator dynamics of the wheel. Substituting the control algorithm, Eq. (4.39), into the error model given by Eq. (4.36), we get

$$J\dot{\sigma} = -\alpha \sigma - (\rho + 1)\eta \text{sgn}(\sigma) + \alpha A \Gamma A^T \sigma + (\rho + 1)\eta A \Gamma A^T \text{sgn}(\sigma) + \Delta \quad (4.41)$$

4.2.3 Stability Analysis

In this sub-section we present stability conditions for the proposed adaptive fault-tolerant control algorithm, focussing primarily on robustness against uncertainties, disturbances,

and reaction wheel faults. We show that the control law, Eq. (4.39), is capable of driving the closed-loop trajectory of the system towards the sliding surface. Once the sliding surface is reached, the system enters into the sliding regime. We show that the sliding mode is robust to external disturbances, system nonlinearities, and unknown reaction wheel faults. The stability conditions for the fading actuation and reaction wheel failure cases are shown within the same stability proof.

The actuator effectiveness matrix Γ is defined such that it includes both decrease in effectiveness and failure of reaction wheels. We consider a maximum of two wheel failure for the RWA in pyramid configuration (A2) and single wheel failure for RWA in standard 3-orthogonal and 1-oblique configuration. Let $0 \geq \lambda_{min} < 1$ be an unknown constant defining the minimum eigenvalue of $A\Gamma A^T$, which is always less than 1 as long as no more than two wheels lose complete power. We define the following parameter [Alwi *et al.* 2008]

$$\zeta = \frac{1}{1 - \lambda_{min}} \quad (4.42)$$

Theorem 4.1: *For the spacecraft attitude dynamics model governed by Eqs. (4.18)-(4.20) if, the sliding manifold is chosen as Eq. (4.29), the adaptive control scheme is defined by Eqs. (4.39)-(4.40), and the bounds on the external disturbances, uncertainties, and system nonlinearities are assumed to be governed by Eq. (4.38) then the closed-loop error trajectories will converge to a region*

$$B_1 \triangleq \left[\sigma : \|\sigma\| \leq \frac{\varepsilon^0}{\eta} \right]$$

Proof: Consider the positive definite, continuously differentiable candidate Lyapunov function defined as follows:

$$V(q_e, \sigma) = [q_{4e} - \text{sgn}(q_{4e})]^2 + q_e^T q_e + \frac{1}{8\alpha\beta} \sigma^T J \sigma + \frac{1 - \lambda_{min}}{8\alpha\beta b_2} (\rho - \zeta)^2 \quad (4.43)$$

Taking the first derivative of $V(q_e, \sigma)$ along the trajectory of the system yields,

$$\dot{V}(q_e, \sigma) = 2[q_{4e} - \text{sgn}(q_{4e})]\dot{q}_{4e} + 2q_e^T \dot{q}_e + \frac{1}{4\alpha\beta} \sigma^T J \dot{\sigma} + \frac{1 - \lambda_{min}}{4\alpha\beta b_2} (\rho - \zeta) \dot{\rho} \quad (4.44)$$

Substituting the relative attitude error kinematics from Eqs. (4.19)-(4.20) gives,

$$\begin{aligned}\dot{V}(q_e, \sigma) &= -[q_{4e} - \text{sgn}(q_{4e})](q_e^T \omega_e) + q_e^T (q_{4e} I + [q_e^\times]) \omega_e + \frac{1}{4\alpha\beta} \sigma^T J \dot{\sigma} \\ &\quad + \frac{1 - \lambda_{\min}}{4\alpha\beta b_2} (\rho - \zeta) \dot{\rho} \\ &= \text{sgn}(q_{4e}) q_e^T \omega_e + \frac{1}{4\alpha\beta} \sigma^T J \dot{\sigma} + \frac{1 - \lambda_{\min}}{4\alpha\beta b_2} (\rho - \zeta) \dot{\rho}\end{aligned}\quad (4.45)$$

Let

$$\dot{V}_1 = \frac{1}{4\alpha\beta} \sigma^T J \dot{\sigma} + \frac{1 - \lambda_{\min}}{4\alpha\beta b_2} (\rho - \zeta) \dot{\rho}\quad (4.46)$$

Now substituting Eqs. (4.40)-(4.41) into Eq. (4.46) we obtain

$$\begin{aligned}\dot{V}_1 &= \frac{1}{4\alpha\beta} \sigma^T [-\alpha\sigma - (\rho + 1)\eta \text{sgn}(\sigma) + \alpha A \Gamma A^T \sigma + (\rho + 1)\eta A \Gamma A^T \text{sgn}(\sigma) + \Delta] \\ &\quad + \frac{1 - \lambda_{\min}}{4\alpha\beta b_2} (\rho - \zeta) [-b_1 \rho + b_2 \eta \|\sigma\|] \\ &\leq -\frac{\sigma^T \sigma}{4\beta} - (1 - \lambda_{\min}) \frac{(\rho + 1)\eta}{4\alpha\beta} \|\sigma\| + \frac{\eta}{4\alpha\beta} \|\sigma\| \\ &\quad + \frac{1 - \lambda_{\min}}{4\alpha\beta b_2} (\rho - \zeta) [-b_1 \rho + b_2 \eta \|\sigma\|]\end{aligned}\quad (4.47)$$

Note that in Eq. (4.47) we use the fact that λ_{\min} is the minimum eigenvalue of $A \Gamma A^T$, $\sum_{i=1}^3 |\sigma_i| \geq \|\sigma\|$, and $\|\Delta\| \leq \eta$. Carrying out further simplifications and canceling terms in Eq. (4.47) we have

$$\dot{V}_1 \leq -\frac{\sigma^T \sigma}{4\beta} - (1 - \lambda_{\min}) \frac{\eta}{4\alpha\beta} \|\sigma\| + (1 - \lambda_{\min}) \frac{b_1}{4\alpha\beta b_2} (\rho \zeta - \rho^2)\quad (4.48)$$

It is well known that for any real number $a > 0$ and $b > 0$, $2ab \leq a^2 + b^2$. Hence we have

$$2\rho \frac{\zeta}{2} \leq \rho^2 + \left(\frac{\zeta}{2}\right)^2\quad (4.49)$$

Substituting Eq. (4.49) in Eq. (4.48), it can be readily obtained that

$$\dot{V}_1 \leq -\frac{\sigma^T \sigma}{4\beta} - (1 - \lambda_{\min}) \frac{\eta}{4\alpha\beta} \|\sigma\| + (1 - \lambda_{\min}) \frac{b_1}{16\alpha\beta b_2} \zeta^2\quad (4.50)$$

Using Eq. (4.50) in Eq. (4.45), we obtain

$$\dot{V}(q_e, \sigma) \leq \text{sgn}(q_{4e}) q_e^T \omega_e - \frac{\sigma^T \sigma}{4\beta} - (1 - \lambda_{\min}) \frac{\eta}{4\alpha\beta} \|\sigma\| + \frac{b_1(1 - \lambda_{\min})}{16\alpha\beta b_2} \zeta^2\quad (4.51)$$

Based on the sliding manifold, we have $w_e = \sigma - \beta \operatorname{sgn}(q_{4e})q_e$. Thus we obtain

$$\begin{aligned} \dot{V}(q_e, \sigma) &\leq \operatorname{sgn}(q_{4e})q_e^T \sigma - \beta q_e^T q_e - \frac{\sigma^T \sigma}{4\beta} - (1 - \lambda_{\min}) \frac{\eta}{4\alpha\beta} \|\sigma\| \\ &\quad + \frac{b_1(1 - \lambda_{\min})}{16\alpha\beta b_2} \zeta^2 \end{aligned} \quad (4.52)$$

The algebraic property introduced in Eq. (4.49) can also be utilized to establish the following inequality

$$\begin{aligned} 2\sqrt{\beta}\|q_e\| \frac{\|\sigma\|}{2\sqrt{\beta}} &\leq \beta\|q_e\|^2 + \frac{\|\sigma\|^2}{4\beta} \\ q_e^T \sigma &\leq \beta q_e^T q_e + \frac{\sigma^T \sigma}{4\beta} \end{aligned} \quad (4.53)$$

Substituting Eq. (4.53) in Eq. (4.52) and if $q_{4e} > 0$ we get

$$\begin{aligned} \dot{V}(q_e, \sigma) &\leq -(1 - \lambda_{\min}) \frac{\eta}{4\alpha\beta} \|\sigma\| + \frac{b_1(1 - \lambda_{\min})}{16\alpha\beta b_2} \zeta^2 \\ &\leq -\frac{(1 - \lambda_{\min})}{4\alpha\beta} \left[\eta\|\sigma\| - \frac{b_1\zeta^2}{4b_2} \right] \end{aligned} \quad (4.54)$$

Let $\varepsilon^0 = \frac{b_1\zeta^2}{4b_2}$. Therefore, it is seen from Eq. (4.54) that $\dot{V}(q_e, \sigma) < 0$ when σ is outside of the set

$$B_1 \triangleq \left[\sigma : \|\sigma\| \leq \frac{\varepsilon^0}{\eta} \right] \quad (4.55)$$

For the case $q_{4e} < 0$, substituting Eq. (4.53) in Eq. (4.52), we get

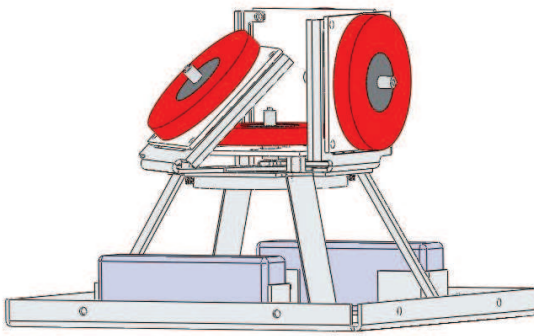
$$\dot{V}(q_e, \sigma) \leq -2\beta q_e^T q_e - \frac{\sigma^T \sigma}{2\beta} - \frac{(1 - \lambda_{\min})}{4\alpha\beta} \left[\eta\|\sigma\| - \frac{b_1\zeta^2}{4b_2} \right] \quad (4.56)$$

Therefore, the solution set defined by Eq. (4.55) is also valid for the case $q_{4e} < 0$. Based on the results obtained above, it can be concluded that an appropriate choice of the gains b_1 , b_2 , and η , close approximation to ideal sliding can be maintained even in the presence of actuator faults. Using Barbalat's lemma we can prove that all the states converge to zero as time approaches infinity. \square

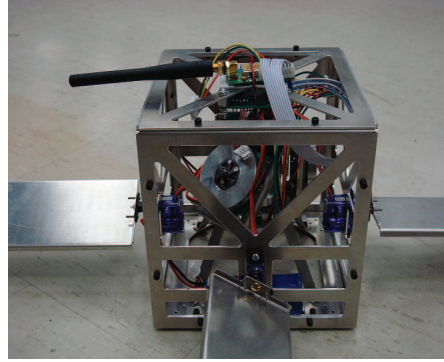
Remark 4.1: Two main factors induce multiplicative faults in reaction wheels: 1) viscous friction variations due to unexpected changes in temperature, and 2) unexpected changes in the motor torque values represented by changes in the motor torque constant, K_t . These factors affect the rate of change of the wheel speed and consequently decrease the generated reaction torque.

4.3 Reaction Wheel Experimental Testbed

Four reaction wheels are used in two configurations; 1) three orthogonal wheels and one skewed (Figure 4.2), and 2) pyramid configuration with the wheels at each corners of the pyramid (Figure 4.3). Each wheel board drives a brushless DC-motor and communicates over an I2C bus with the main controller. The control law will provide desired torques about the x , y , and z body axes, and the input voltage e_a required to control the actuator dynamics of the wheels are estimated using Eq. (4.28).



(a) Standard 4-wheel configuration



(b) RyePicoSat with reaction wheels

Figure 4.2: Schematic of traditional four wheel configuration.

The torques are distributed to each of the four wheels using the wheel distribution matrix A . For the cluster in Fig. 4.2, the axial angular momentum of the skewed wheel is at an angle of 45 degrees with the x , y , and z axes. Each of the wheels contributes to the body torques according to the relation given below:

$$\begin{bmatrix} \tau_x \\ \tau_y \\ \tau_z \end{bmatrix} = \begin{bmatrix} 1 & 0 & 0 & -\cos(\phi_2) \cos(\phi_1) \\ 0 & 1 & 0 & -\cos(\phi_2) \sin(\phi_1) \\ 0 & 0 & 1 & \sin(\phi_2) \end{bmatrix} \begin{bmatrix} \tau_{w1} \\ \tau_{w2} \\ \tau_{w3} \\ \tau_{w4} \end{bmatrix} \quad (4.57)$$

For the case of four reaction wheels mounted in pyramid configuration (Figure 4.3), it is possible to achieve three axis attitude stabilization and control using two remaining operational reaction wheels (if two wheels fail). Since all wheels are mounted in a skewed

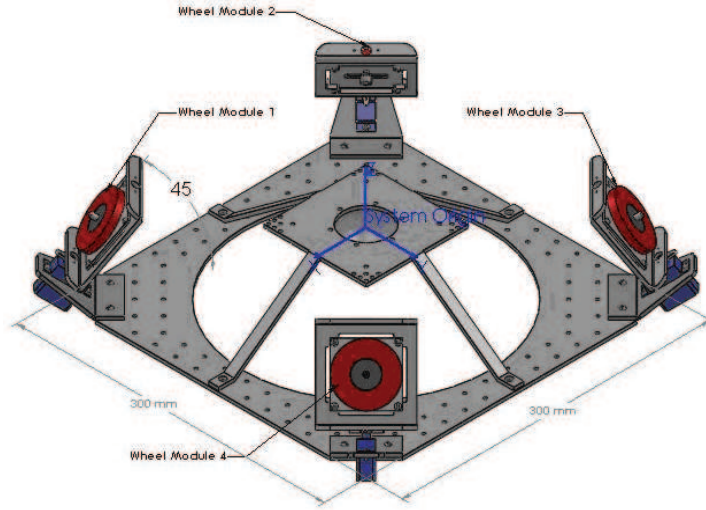


Figure 4.3: Schematic of four wheels in pyramid configuration.

configuration, the mapping matrix (A) from the RWA frame to the spacecraft body frame can be utilized to allow two remaining operational wheels to produce three control torques in the body frame. The contributions of each wheel torques to the body torques are obtained using the following relation:

$$\begin{bmatrix} \tau_x \\ \tau_y \\ \tau_z \end{bmatrix} = \begin{bmatrix} c\phi_1 s\phi_2 & -c\phi_1 s\phi_2 & -c\phi_1 s\phi_2 & c\phi_1 s\phi_2 \\ -c\phi_1 c\phi_2 & -c\phi_1 c\phi_2 & c\phi_1 c\phi_2 & c\phi_1 c\phi_2 \\ s\phi_1 & s\phi_1 & s\phi_1 & s\phi_1 \end{bmatrix} \begin{bmatrix} \tau_{w1} \\ \tau_{w2} \\ \tau_{w3} \\ \tau_{w4} \end{bmatrix} \quad (4.58)$$

The setup for the hardware-in-loop (HIL) simulation is shown in Figure 4.4. A high-fidelity mathematical model of the spacecraft is developed in Simulink and integrated with the fault-tolerant control algorithm block. The Simulink control algorithm block computes the desired control torques based on attitude errors, distributes the torques to the four wheels, and then converts the torques to voltages (e_a). The voltages are sent over a radio to the RWA hardware and are applied to the wheels. The wheel boards outputs wheel-speeds (Ω) back to Simulink through the radio and are then smoothed and passed to the mathematical model. The data from MATLAB must be converted from a double (8 byte) floating point number to a single (4 byte) floating point number and discretized at the sampling frequency before being sent to the hardware in order to match the formatting on-board the actuator.

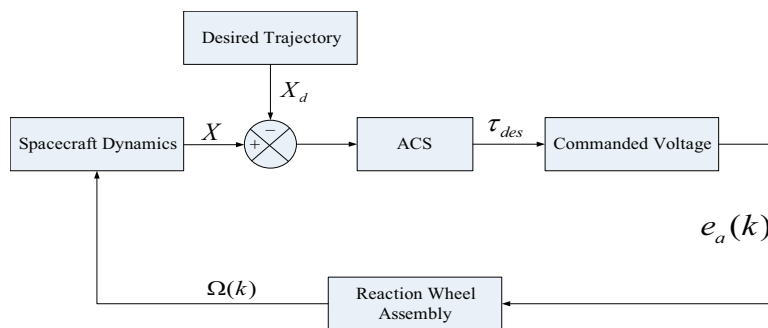


Figure 4.4: Schematic of HIL simulation.

When the hardware returns the data to MATLAB, it must then be converted back to the double floating point standard. Reaction wheel parameters are shown in Table 4.1.

Table 4.1: Reaction wheel parameters.

Wheel	K_b (V/rad/s)	K_t (N-m/A)	R_a (ohm)	Dead-zone (V)
1	0.0082	0.0082	0.6	± 1.10
2	0.0080	0.0080	0.6	± 1.15
3	0.0071	0.0071	0.6	± 1.20
4	0.0075	0.0075	0.6	± 1.15

4.4 Performance Analysis - Numerical Simulation

In this section, we illustrate the effectiveness of the proposed fault-tolerant control algorithm for the problem of attitude control of a rigid spacecraft. The detailed response of the system is numerically simulated using the set of governing equations of motion, Eqs. (4.4) and (4.7) in conjunction with the proposed control algorithm, Eqs. (4.39) and (4.40). The parameters of the spacecraft are shown in Table 4.2. The spacecraft is subjected to the following initial attitude disturbances:

$$q_{v0} = [0.4, 0.4, 0.4]^T \quad \text{and} \quad \omega_{BL}^B = [0, 0, 0]^T \quad (4.59)$$

Table 4.2: Spacecraft model parameters.

Parameters	Values
Orbit	
R_c (km)	6878
μ_e (km ³ s ⁻²)	398600
Size (m ³)	$0.1 \times 0.1 \times 0.1$
Moment of Inertia	
I_{xx} (kg m ²)	0.0015
I_{yy} (kg m ²)	0.0017
I_{zz} (kg m ²)	0.0020
Reaction Wheel	
Moment of inertia, J_{wi} , (kg m ²)	1×10^{-3}

The mapping matrix, A , that relates the reaction wheel control torques to spacecraft body-frame torques for (A1) and (A2) configurations are given by Eqs. (4.57) and (4.58). The constant gains for the control algorithm and adaptive update law, Eqs. (4.39) and (4.40), are chosen as $\alpha = 0.1$, $\beta = 0.6$, $b_1 = 0.5$, $b_2 = 2.5$, $p_1 = 1$, and $p_2 = 2$.

To systematically analyze the need for a fault-tolerant adaptive control algorithm for spacecraft attitude control, we compare the control scheme proposed in this chapter with a conventional proportional-derivative (PD) controller. The control allocation to remaining healthy wheels after wheel failure for PD control is also executed using the mapping matrix, A . The control input torque is formulated as

$$u_{r,PD} = A^T [\omega_{BI}^B \times (J_s \omega_{BI}^B + A J_w \Omega) - D \omega_e - K q_e] \quad (4.60)$$

where K and D are the proportional and derivative gain matrices, respectively. Substituting Eq. (4.60) into Eq. (4.18) with no fault condition and zero external disturbances, we have

$$J \dot{\omega}_e + D \omega_e + K q_e = 0 \quad (4.61)$$

This is similar to an ideal second-order dynamic system. Asymptotic stabilizability of the

spacecraft attitude and angular velocity errors is defined by choosing D and K such that:

$$D = 2\zeta \omega_n J \quad \text{and} \quad K = \omega_n^2 J \quad (4.62)$$

The settling time of the system response can be predetermined by prescribing appropriate values for damping ratio ζ and the natural frequency ω_n , $t_s = 4/(\zeta\omega_n)$. For all simulations considered in this study we choose $\zeta = 0.70$ and $\omega_n = 0.35$.

4.4.1 Case I - Three Wheels in Orthogonal Configuration

In this section, we demonstrate the attitude stabilization capability of the ACS using a three reaction wheel configuration that has each wheel aligned with the principal body-fixed coordinate axes of the spacecraft denoted by $\mathfrak{B} - xyz$. Numerical simulation results are presented to compare the proposed fault-tolerant control scheme given by Eqs. (4.39) and (4.40) with the conventional PD control algorithm given by Eq. (4.60). To establish a fair comparison framework, the controller parameters of both methodologies (proposed control law and PD) are selected such that their settling times were the same for the fault-free condition. The input voltage given by Eq. (4.28) is of the form $e_a \in \mathbb{R}^3 = [v_1, v_2, v_3]^T$. Similarly, the reaction wheels' angular speeds are given by $\Omega \in \mathbb{R}^3 = [\Omega_1, \Omega_2, \Omega_3]^T$. The torque mapping between the reaction wheel frame and spacecraft body axes is one-to-one with $A = I_{3 \times 3}$.

The following fault scenario is considered in the simulation:

$$\begin{aligned} v_1 &= 0.1 + v_1, \quad \text{for } 10 \leq t \leq 30 \text{ s} \\ \Omega_2 &= 0.5\Omega_2, \quad \text{for } t \geq 10 \text{ s} \end{aligned} \quad (4.63)$$

The fault case given by Eq. (4.63) represents a bias fault that occurs at the first wheel for 20 s after $t = 10$ s into the simulation, and the second wheel only supplies 50% of the actuation power at the time instant $t = 10$ s and, after. The comparison of attitude regulation capability of the ACS using the proposed method and PD control law are shown in Figs. 4.5 to 4.8 for the case of non-zero initial attitude [Eq. (4.59)], no attitude commands, in the presence of external disturbances ($\tau_e = \tau_g + \tau_d$), and faulty reaction wheels [Eq. (4.63)].

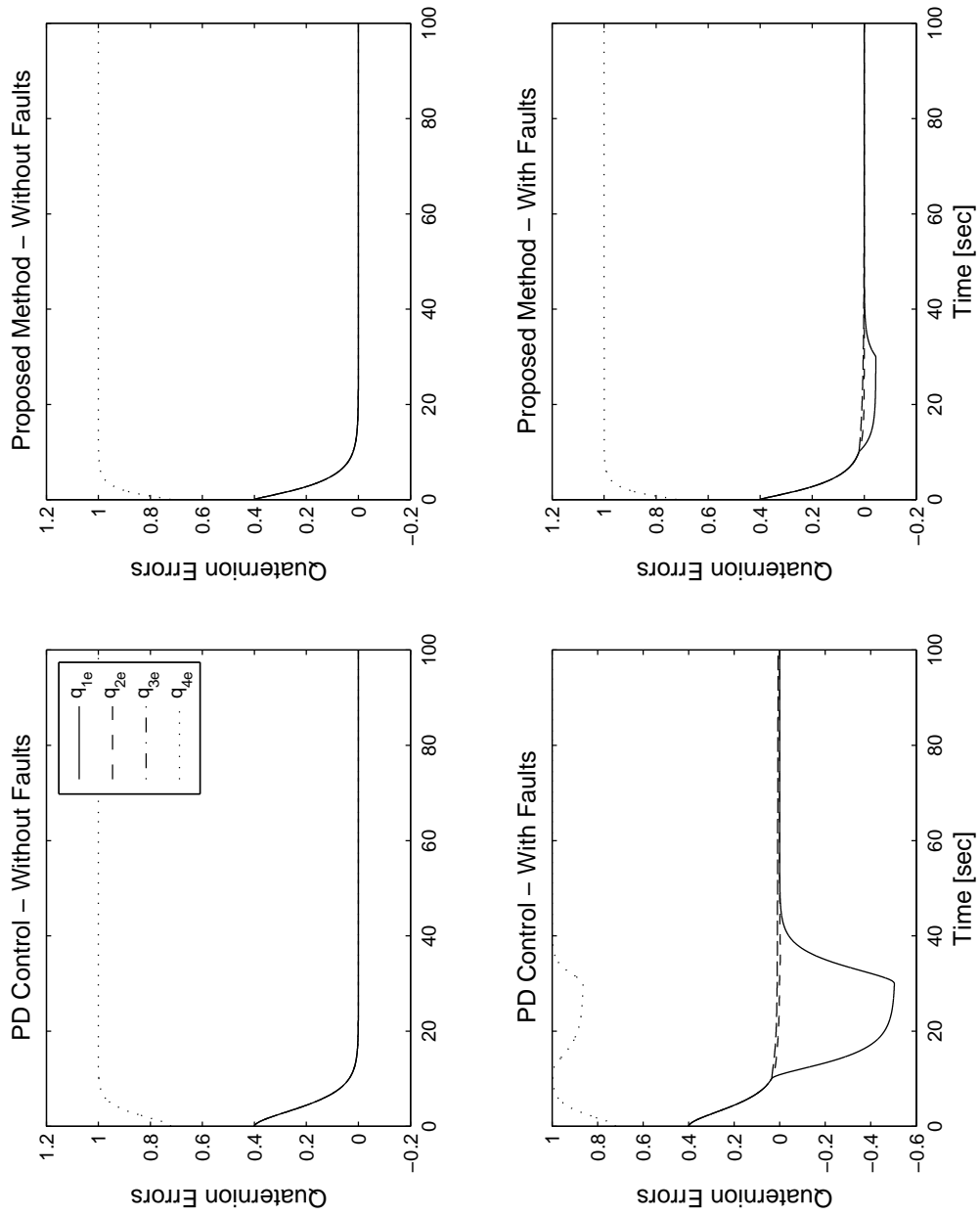


Figure 4.5: Attitude tracking errors for Case I.

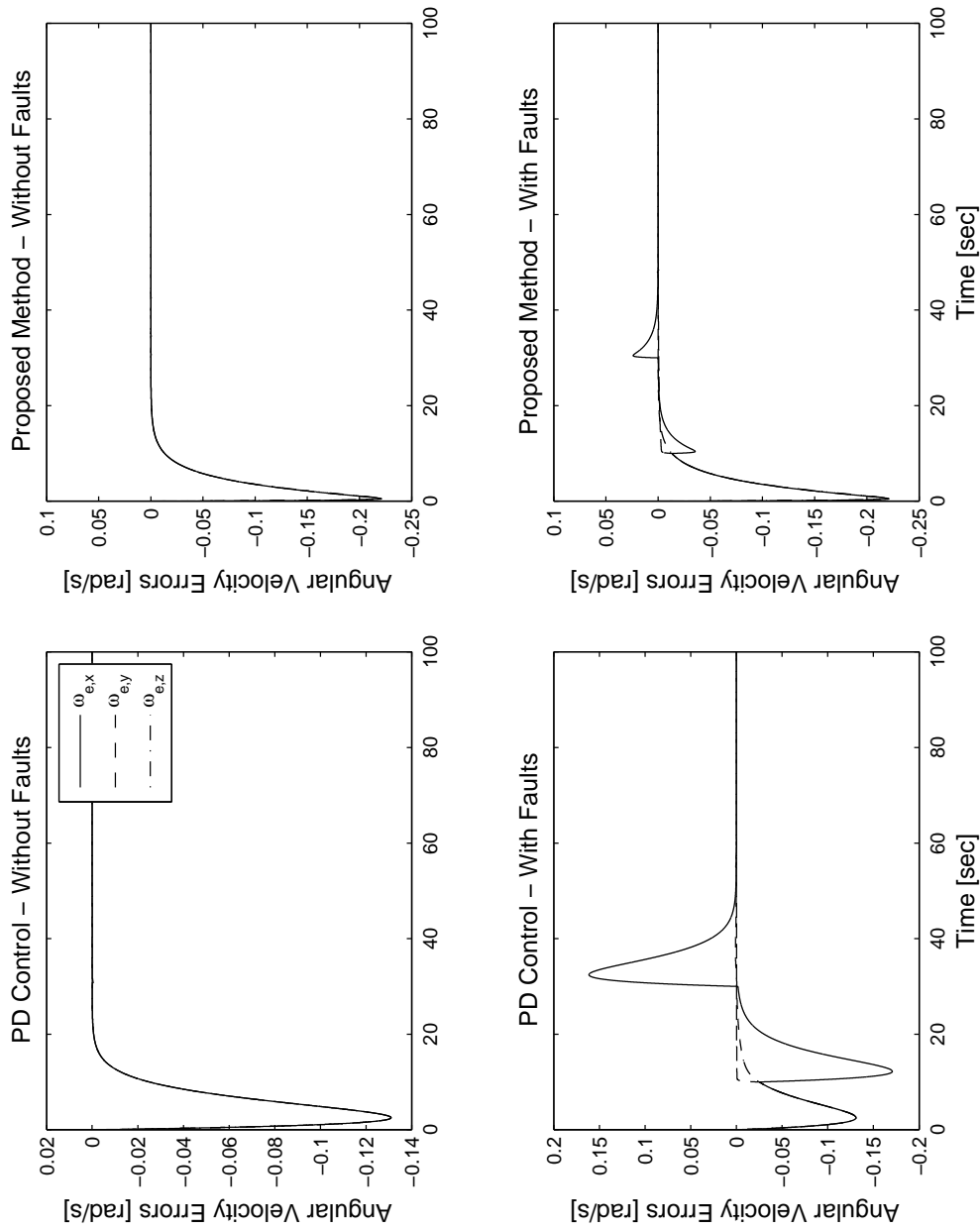


Figure 4.6: Angular velocity errors for Case I.

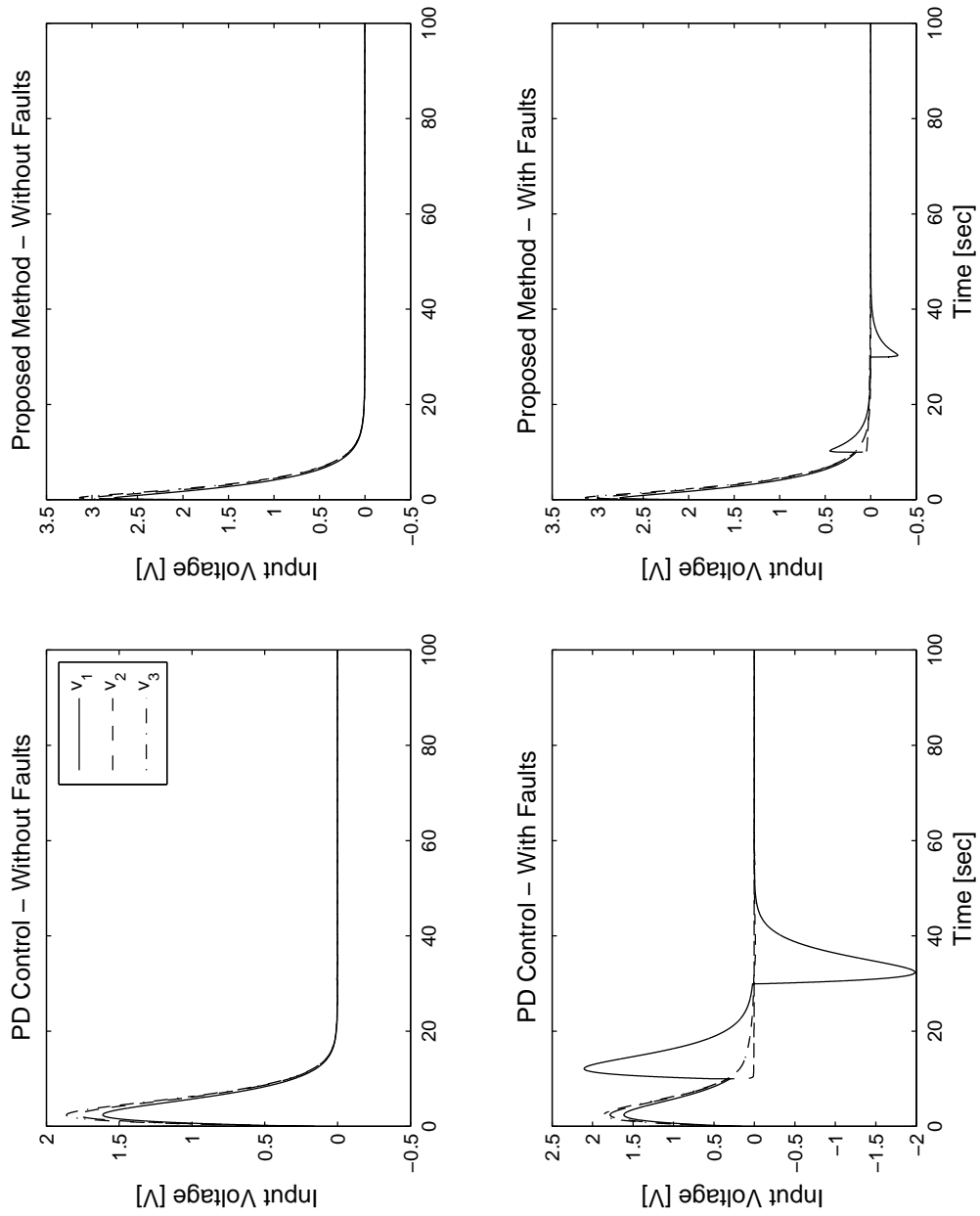


Figure 4.7: Reaction wheels' input voltage for Case I.

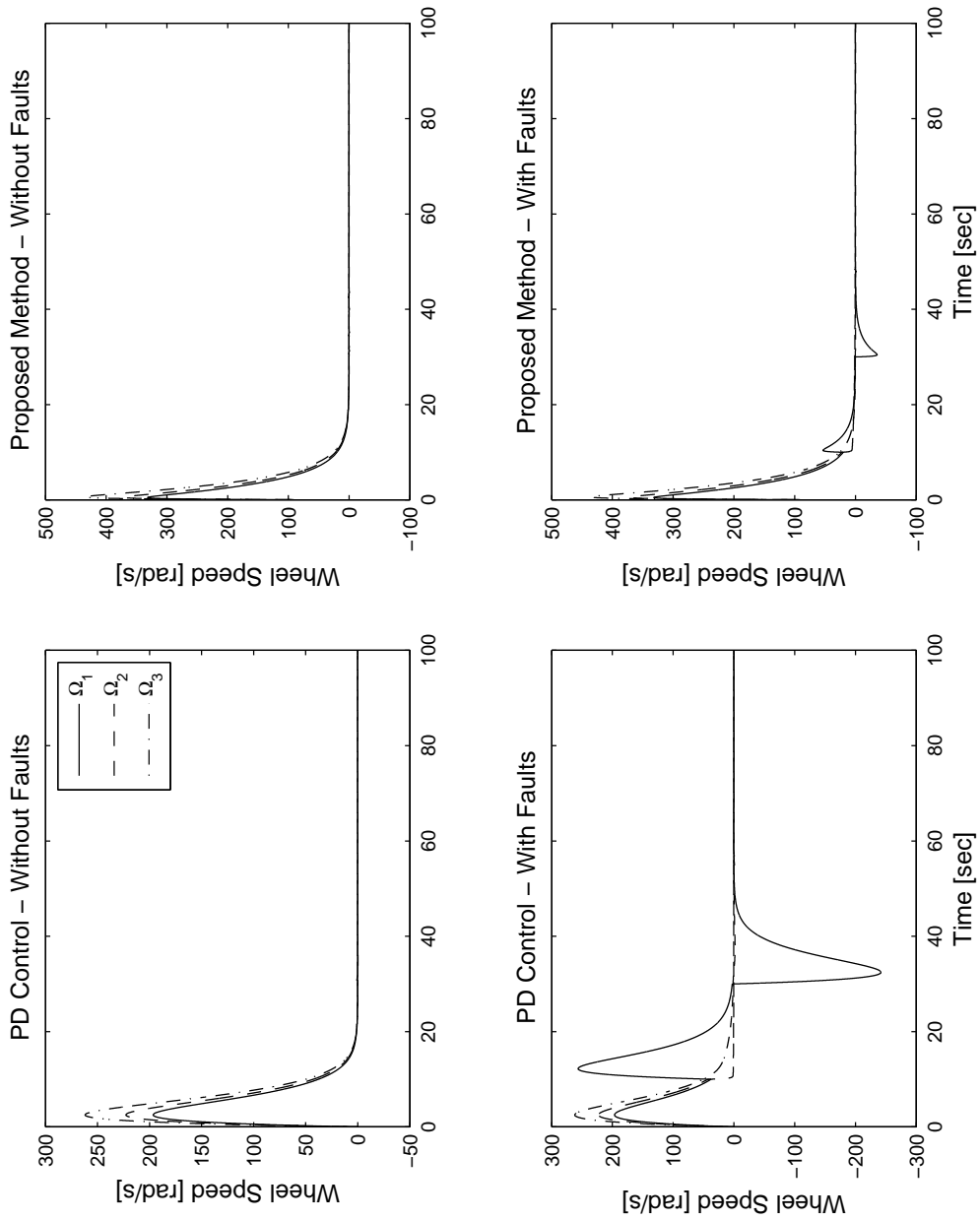


Figure 4.8: Reaction wheels' angular speed for Case I.

The evolution of the attitude quaternion errors can be seen in Fig. 4.5. For the fault-free case, the attitude quaternion errors asymptotically approach to zero starting from non-zero initial conditions. It can be seen that the settling time of the closed-loop ACS is about 16 s for the proposed method and PD control law. The results of the two methods become seemingly different in the presence of reaction wheel faults given by Eq. (4.63). A bias fault in the first wheel has a direct impact on the the quaternion error q_{1e} . During the faulty period q_{1e} overshoots to a value of about -0.6 using the PD control law. The fault tolerance capability of the proposed control method is evident in Fig. 4.5 as the adaptive reconfigurable scheme is able to suppress the effects of a bias fault on q_{1e} to about only -0.1 deviation in attitude error.

Figure 4.6 depicts the spacecraft angular velocity error. The variations in the angular rates during the transient period (for fault-free case) are due to spacecraft rotations until it reaches a stable attitude. However, for the fault scenario, we can see the impact of a bias fault on the response of $\omega_{e,x}$. The effect is more pronounced using a PD control law. This trend is also evident in the plots of input voltage and reaction wheels' angular speeds in Figs. 4.6 and 4.7, respectively. While the PD control resulted in poor performance, the proposed method did not show any deterioration of the desired performance in spite of unknown faults in reaction wheels.

4.4.2 Case II - Traditional Four Wheel Configuration

In this section, we demonstrate the attitude stabilization capability of the ACS using the traditional four reaction wheel set up. This redundant reaction wheel configuration has the first three reaction wheel spin axes aligned with the principal spacecraft body axes, while a fourth wheel is aligned diagonally with respect to the others as illustrated in Fig. 4.2a. Numerical simulation results are presented to compare the proposed fault-tolerant control scheme given by Eqs. (4.39) and (4.40) with the conventional PD control algorithm given by Eq. (4.60). The input voltage given by Eq. (4.28) is of the form $e_a \in \mathbb{R}^4 = [v_1, v_2, v_3, v_4]^T$. Similarly, the reaction wheels' angular speeds are given by $\Omega \in \mathbb{R}^4 = [\Omega_1, \Omega_2, \Omega_3, \Omega_4]^T$. The torque mapping between the reaction wheel frame and spacecraft body axes can be described by the following matrix:

$$A = \begin{bmatrix} 1 & 0 & 0 & -\cos(\phi_2)\cos(\phi_1) \\ 0 & 1 & 0 & -\cos(\phi_2)\sin(\phi_1) \\ 0 & 0 & 1 & \sin(\phi_2) \end{bmatrix} \quad (4.64)$$

where $\phi_1 = \phi_2 = 45$ deg. The following fault scenario is considered for the numerical simulations presented in this subsection:

$$\begin{aligned} v_1 &= 0.1 + v_1, & \text{for } 10 \leq t \leq 30 \text{ s} \\ v_3 &= 0, & \text{for } t \geq 10 \text{ s} \\ \Omega_2 &= 0.5\Omega_2, & \text{for } t \geq 10 \text{ s} \end{aligned} \quad (4.65)$$

The fault case given by Eq. (4.65) represents a bias fault that occurs at the first wheel for 20 s after $t = 10$ s into the simulation, the second wheel only supplies 50% of the actuation power at the time instant $t = 10$ s and, after, while wheel 3 has completely failed or is shut down after $t = 10$ s. This represents a severe case in which not only do some wheels lose partial power with varying input voltage levels, but one wheel has also completely failed after $t = 10$ s into the simulation.

The attitude response for large initial attitude errors [Eq. (4.59)] are compared for the fault case and fault-free scenario in Fig. 4.9. High control precision and good tracking can be observed for the proposed methodology and PD control in the fault-free case. In the presence of additive faults and single reaction wheel failure (third wheel fails completely), the pointing performance using PD control degrades drastically. The attitude errors stabilize asymptotically to zero when using the proposed fault-tolerant control scheme with minor degradation in tracking performance during the additive fault period (see Fig. 4.9). The failure of wheel-3 does not have any impact on the control performance under the proposed scheme while the attitude errors stabilize to non-zero values using the conventional PD control. This can be rectified by gain-adaptation within the PD control framework and the results observed in Fig. 4.9 suggests that a constant gain PD control scheme can lead to instability in the presence of reaction wheel failures. Similar trend is visible in the plots of the angular velocity errors depicted in Fig. 4.10. The proposed controller ensures effective tracking while the PD control scheme significantly degrades the performance after actuator faults have occurred.

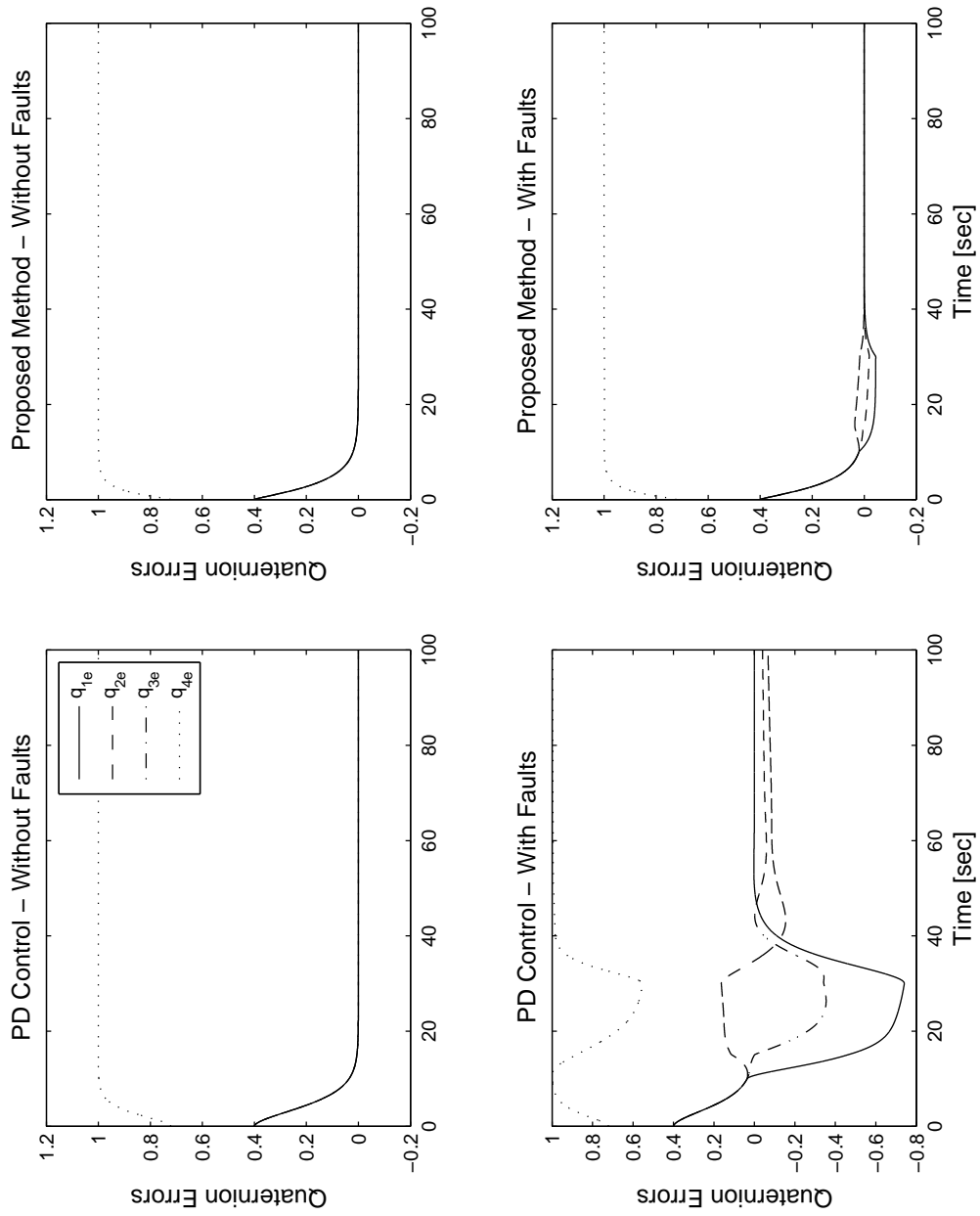


Figure 4.9: Attitude tracking errors for Case II.

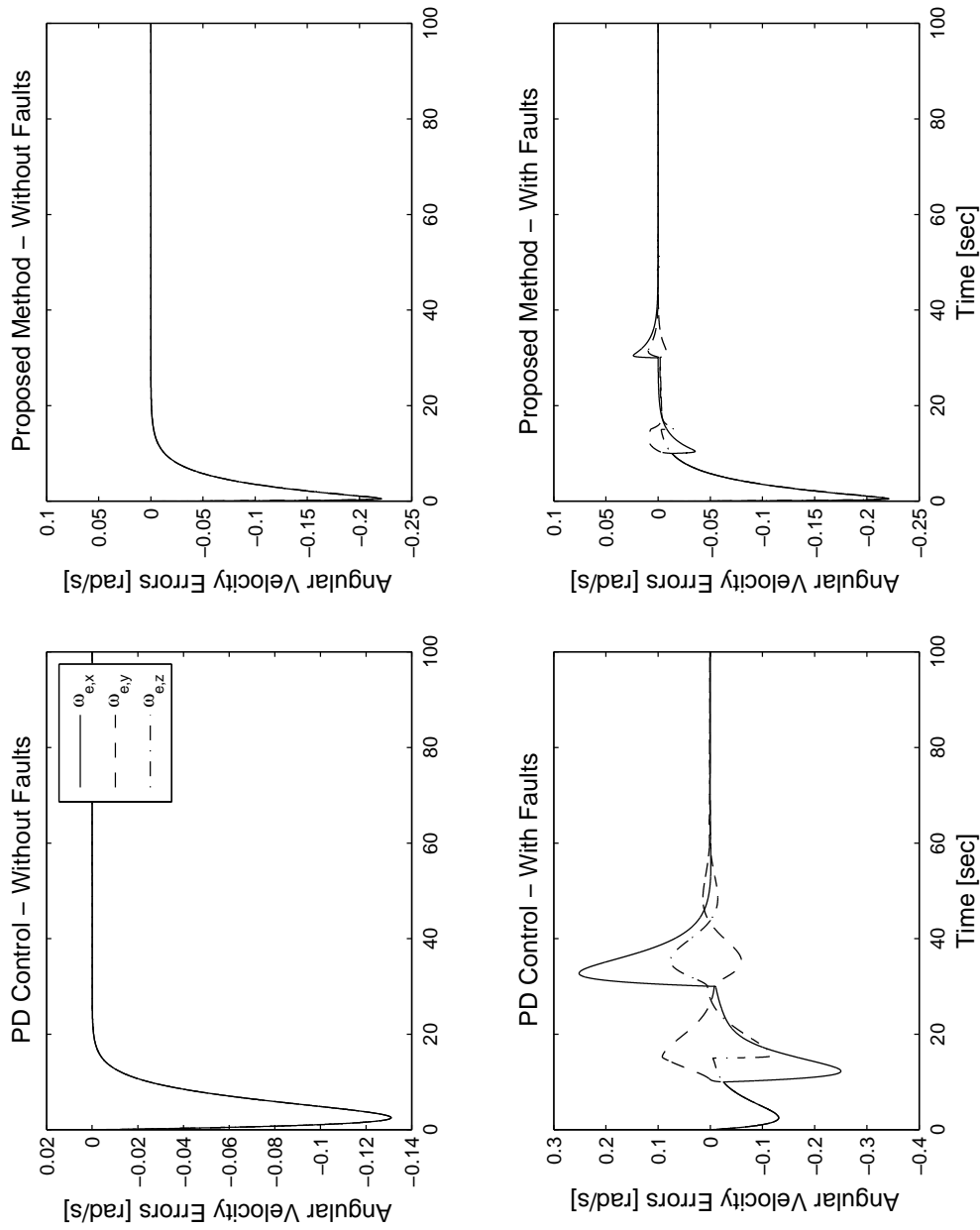


Figure 4.10: Angular velocity errors for Case II.

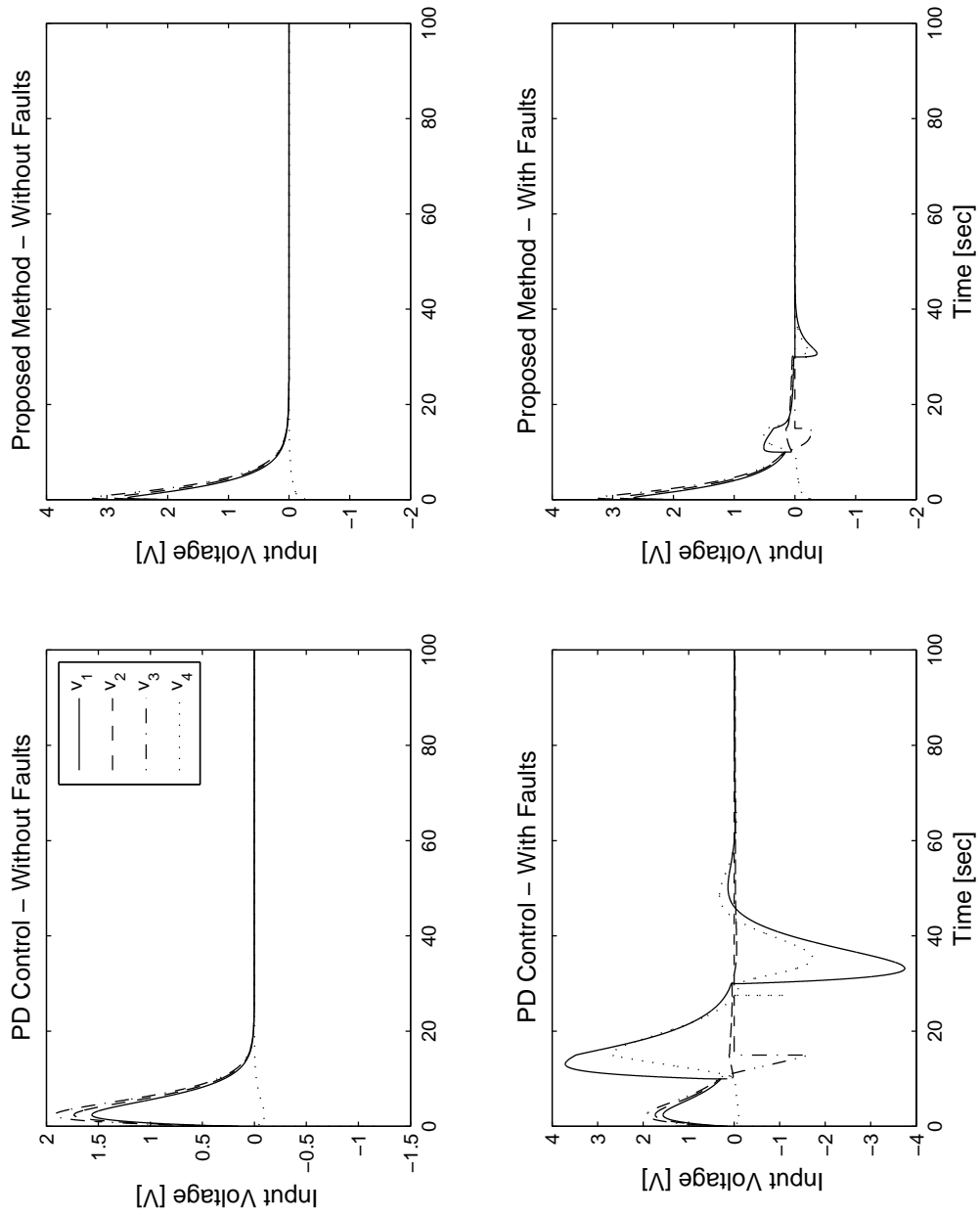


Figure 4.11: Reaction wheels' input voltage for Case II.

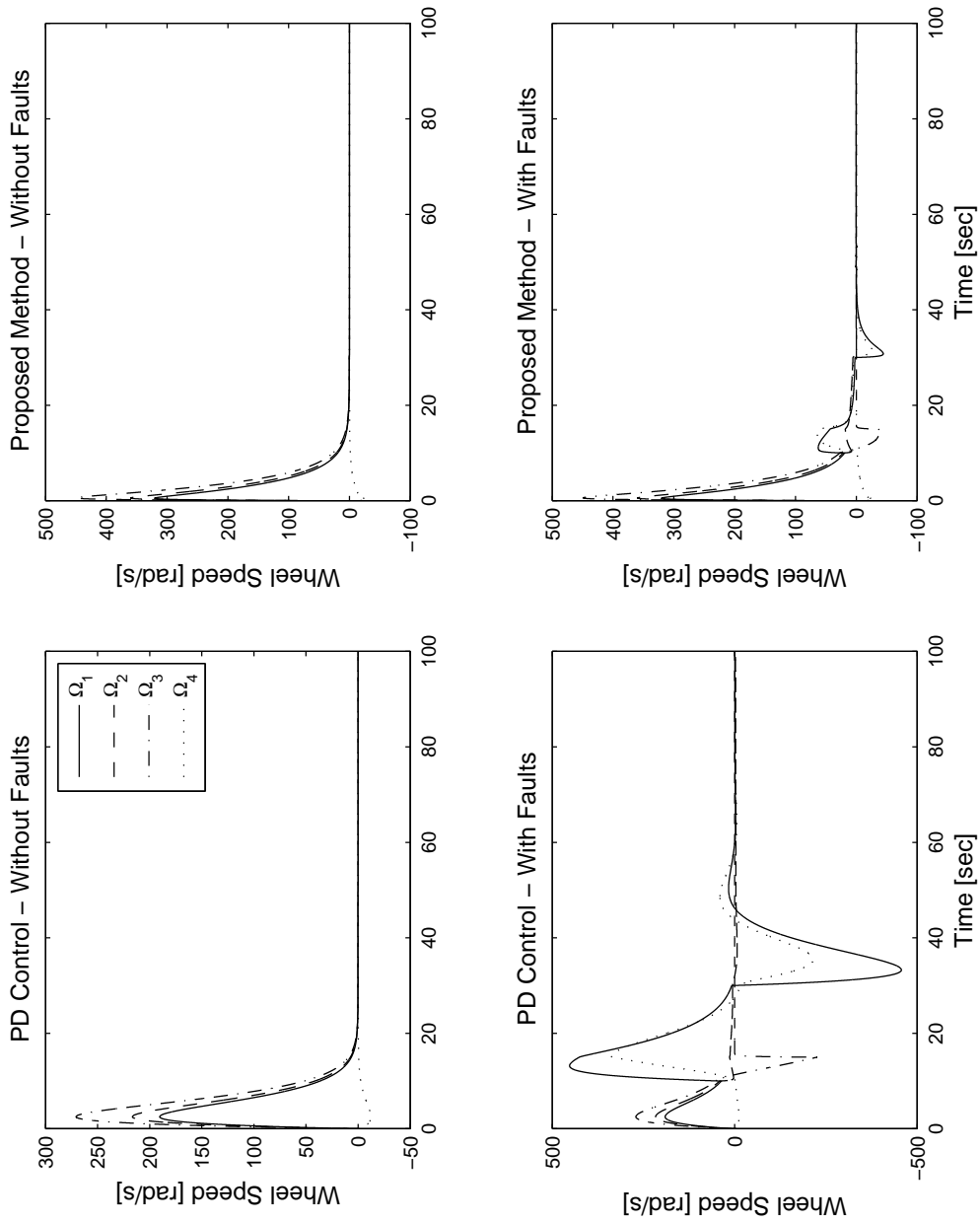


Figure 4.12: Reaction wheels' angular speed for Case II.

The reaction wheels' angular speed and motor input voltage levels required for the faulty and fault-free cases are compared in Figs. 4.11 and 4.12, respectively. Using PD control reduces the overall input voltage required for the fault-free case. However, PD control demands higher input voltage in the presence of actuator faults. This observation in Fig. 4.11 is consistent with the time history of attitude errors evident in Figs. 4.9 and 4.10. The proposed fault-tolerant solution reduces the input voltage required to actuate the reaction wheels even during the presence of reaction wheel faults and failure. The complete failure of wheel-3 can be seen in Figs. 4.11 and 4.12 with $v_3 = \Omega_3 = 0$.

Summarizing cases I and II (Sections 4.4.1 and 4.4.2), it is noted that the proposed fault-tolerant design method can significantly improve spacecraft attitude tracking performance over the conventional PD control scheme in the presence of unknown reaction wheel faults and single wheel failure. For the failure case, PD control is incapable of stabilizing the spacecraft attitude using fixed gains.

4.4.3 Case III - Four Wheels in Pyramid Configuration

In this section, we demonstrate the attitude stabilization capability of the ACS using a four reaction wheel assembly mounted in pyramid configuration (see Fig. 4.3). This redundant reaction wheel configuration has each reaction wheel aligned diagonally on four corners of the pyramid. In sections 4.4.1 and 4.4.2 we have already established that the conventional PD control results in poor attitude tracking performance when compared to the proposed fault tolerant control scheme for faulty actuators. Therefore, in this subsection we only examine the performance of the proposed control technique [Eqs. (4.39) and (4.40)] to maintain the spacecraft pointing accuracy subject to loss of two reaction wheels out of its four wheels assembly mounted in a pyramid configuration. The input voltage given by Eq. (4.28) is of the form $e_a \in \mathbb{R}^4 = [v_1, v_2, v_3, v_4]^T$. Similarly, the reaction wheels' angular speeds are given by $\Omega \in \mathbb{R}^4 = [\Omega_1, \Omega_2, \Omega_3, \Omega_4]^T$. The torque mapping between the reaction wheel frame and spacecraft body axes can be described by the following matrix:

$$A = \begin{bmatrix} c\phi_1 s\phi_2 & -c\phi_1 s\phi_2 & -c\phi_1 s\phi_2 & c\phi_1 s\phi_2 \\ -c\phi_1 c\phi_2 & -c\phi_1 c\phi_2 & c\phi_1 c\phi_2 & c\phi_1 c\phi_2 \\ s\phi_1 & s\phi_1 & s\phi_1 & s\phi_1 \end{bmatrix} \quad (4.66)$$

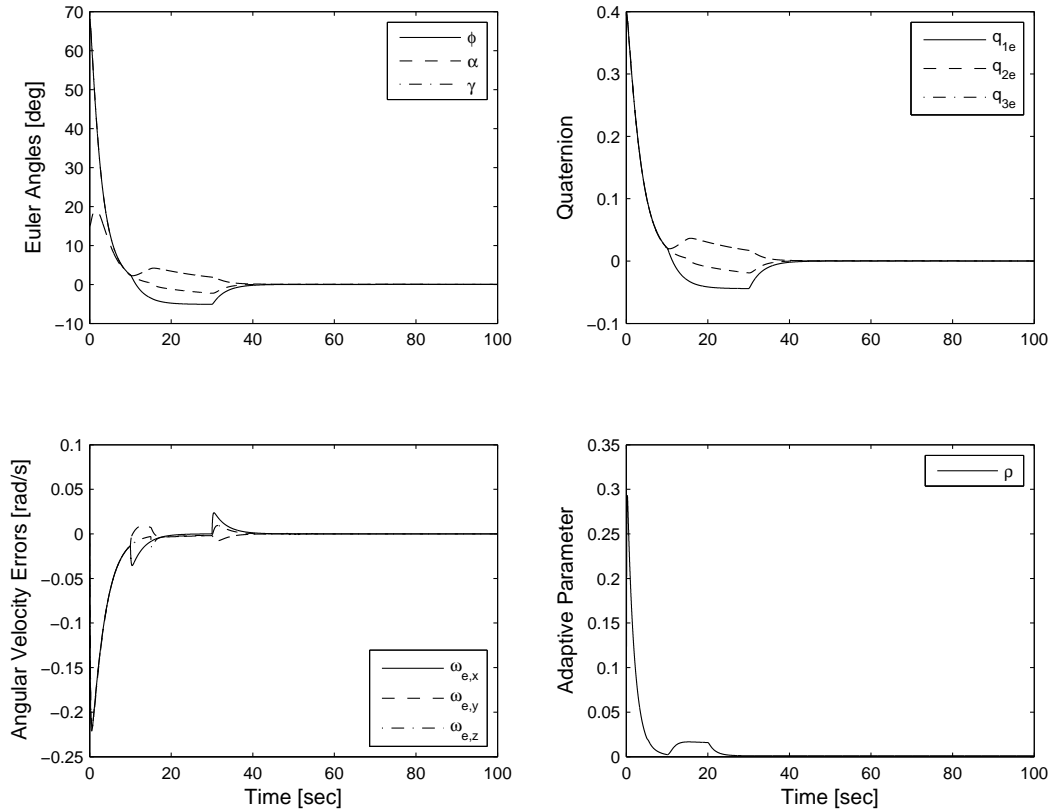


Figure 4.13: Angular velocity and attitude tracking errors for Case III.

where $\phi_1 = \phi_2 = 45$ deg. The following fault scenario is considered for the numerical simulations presented in this subsection:

$$\begin{aligned}
 v_2 &= 0.1 + v_2, & \text{for } 10 \leq t \leq 20 \text{ s} \\
 v_1 &= 0, & \text{for } t \geq 5 \text{ s} \\
 v_3 &= 0, & \text{for } t \geq 5 \text{ s}
 \end{aligned} \tag{4.67}$$

The fault case given by Eq. (4.67) represents a bias fault that occurs at the second wheel for 10 s after $t = 10$ s into the simulation, and wheels 1 and 3 have completely failed or are shut down after $t = 5$ s. The controller parameters as in the case of healthy reaction wheels is employed with $\alpha = 0.1$, $\beta = 0.6$, $b_1 = 0.5$, $b_2 = 2.5$, $p_1 = 1$, and $p_2 = 2$.

The evolution of the Euler angles, quaternion error vector, angular velocity errors, and the adaptive parameter ρ are shown in Fig. 4.13. It is clearly evident that the angular velocity and attitude tracking errors asymptotically approach to zero starting from non-

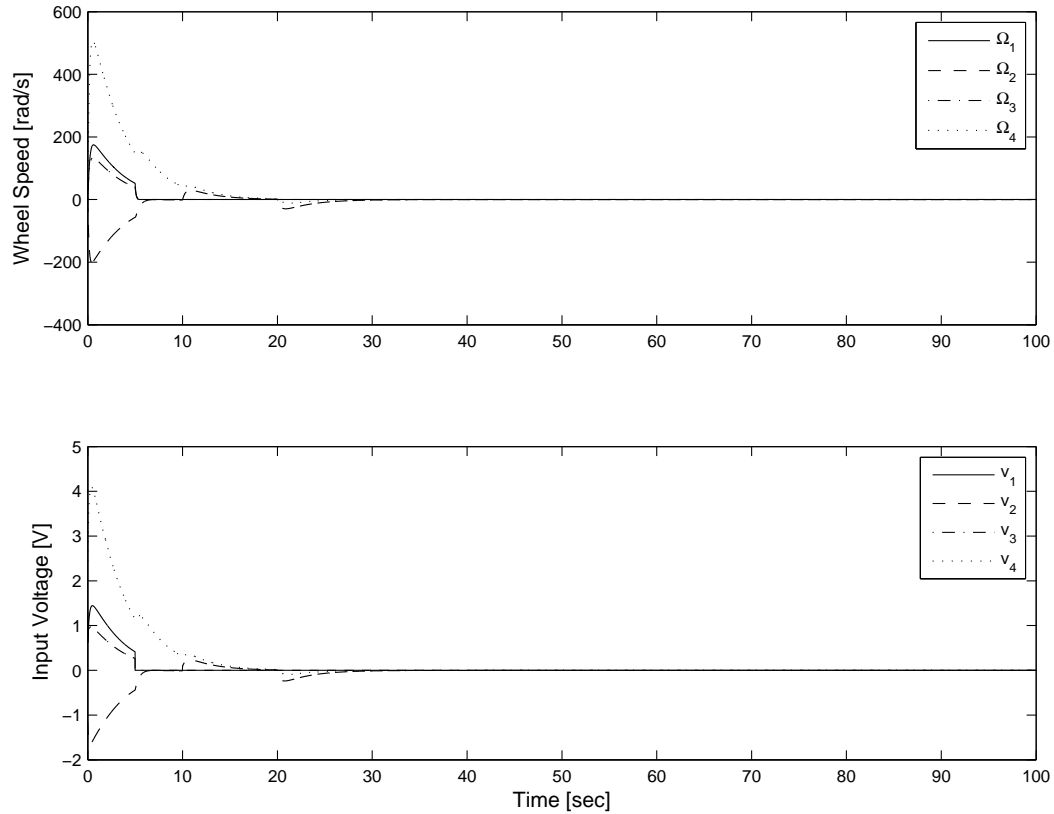


Figure 4.14: Reaction wheel parameters for Case III.

zero initial conditions. The effect of intermittent additive fault can be seen in the response of the adaptive parameter as the gain value begins to increase at the time instant of fault and counteracts the effects of the bias voltage fault on the attitude response. This clearly demonstrates the advantage of using a control strategy that can reconfigure its gains using an adaptive retrofit update law. During the first 5 seconds, with all four operational wheels, the spacecraft pointing performance is achieved quite well with no degradation. With the loss of reaction wheels 1 and 3 after 5 seconds, the pointing performance in roll (ϕ), pitch (α), and yaw (γ) axes suffer minor degradation. As the adaptive gain increases, the angular velocity and quaternion tracking errors are suppressed and the spacecraft reaches a stable attitude within 10 s after the fault. The failure of wheels 1 and 3 can be observed in the plot of reaction wheels' angular speed and input voltage depicted in Fig. 4.14.

4.5 Performance Evaluation - HIL Simulation

In this section, we present the hardware-in-the-loop (HIL) results of the proposed fault-tolerant control algorithm for the problem of attitude control of a rigid spacecraft. The detailed response of the spacecraft mathematical model is simulated in MATLAB using the set of governing equations of motion, Eqs. (4.4) and (4.7).

The angular velocity and attitude tracking errors are fed to the control block that augments the proposed control algorithm, Eq. (4.39), with an adaptive component, Eq. (4.40), to determine the control torque required to stabilize the spacecraft. The input voltage for the reaction wheel hardware is determined from the desired torque computed using the control algorithm, and is applied to the reaction wheels using a radio communication between MATLAB interface and the RWA hardware. The specifications of each reaction wheel are provided in Table 4.3.

Table 4.3: Reaction wheel specification sheet [Kumar & Misra 2009].

Parameter	Value
Operational speed range [rpm]	± 5000
Maximum stored momentum [mNms]	5.2
Maximum torque [mNm]	8.68
Control accuracy [deg]	0.1
Mass of wheel [g]	27.2
Mass of wheel module [g]	57
Power - steady state [W]	< 1.0
Power - maximum torque [W]	8
Operating voltage (module) [V]	3.5 – 5

The parameters of the spacecraft system are shown in Table 4.2. The spacecraft is subjected to the same initial attitude disturbances considered for cases in Section 4.4 [Eq. (4.59)]. The mapping matrix, A , that relates the reaction wheel control torques to spacecraft body-frame torques for (A1) and (A2) configurations are given by Eqs. (4.57) and (4.58). The constant gains for the control algorithm and adaptive update law, Eqs. (4.39)

and (4.40), are chosen as $\alpha = 0.1$, $\beta = 0.6$, $b_1 = 0.5$, $b_2 = 2.5$, $p_1 = 1$, and $p_2 = 2$ (same gains as considered in Section 4.4).

In the following subsections, HIL simulation results are presented for three configurations of RWA examining fault-free and faulty reaction wheel scenarios: 1) three wheels in orthogonal configuration, 2) standard four wheel configuration with three wheels orthogonally aligned with spacecraft body axes and one wheel skewed, and 3) four wheels in pyramid configuration. HIL results of the proposed fault-tolerant control strategy are presented for a fault-free condition first and then for a faulty condition.

4.5.1 Case I - Three Wheels in Orthogonal Configuration

Attitude stabilization capability of the ACS using a three reaction wheel hardware configuration that has each wheel aligned with the principal body-fixed axes of the spacecraft are presented in this section.

Simulations of a fault-free condition

The evolution of the Euler angles, applied control torques in spacecraft body-fixed coordinates, angular velocity errors, and the adaptive parameter ρ for the fault-free case can be seen in Fig. 4.15. The Euler angles asymptotically approaches to a stable boundary ± 0.5 deg starting from non-zero initial conditions. The settling time of the closed-loop ACS is about 15 s. When compared to the stabilization results for numerical simulations depicted in Fig. 4.5, we observe that perfect stabilization to zero equilibrium is not obtained using the RWA hardware.

The discrepancy in the stabilization results between the HIL and numerical simulations may be contributed to the mathematical modeling of the reaction wheel motor torque used in numerical simulations. Also, the reaction wheels operates at a nominal speed of 0 rad/s which causes the input voltages to drop within the deadzone (Table 4.1) once the spacecraft is stabilized close to the equilibrium. Hence, the required torque is very less compared to the transient phase. The time history of quaternion errors, reaction wheels' angular speed, input voltage, and reaction torque are shown in Fig. 4.16.

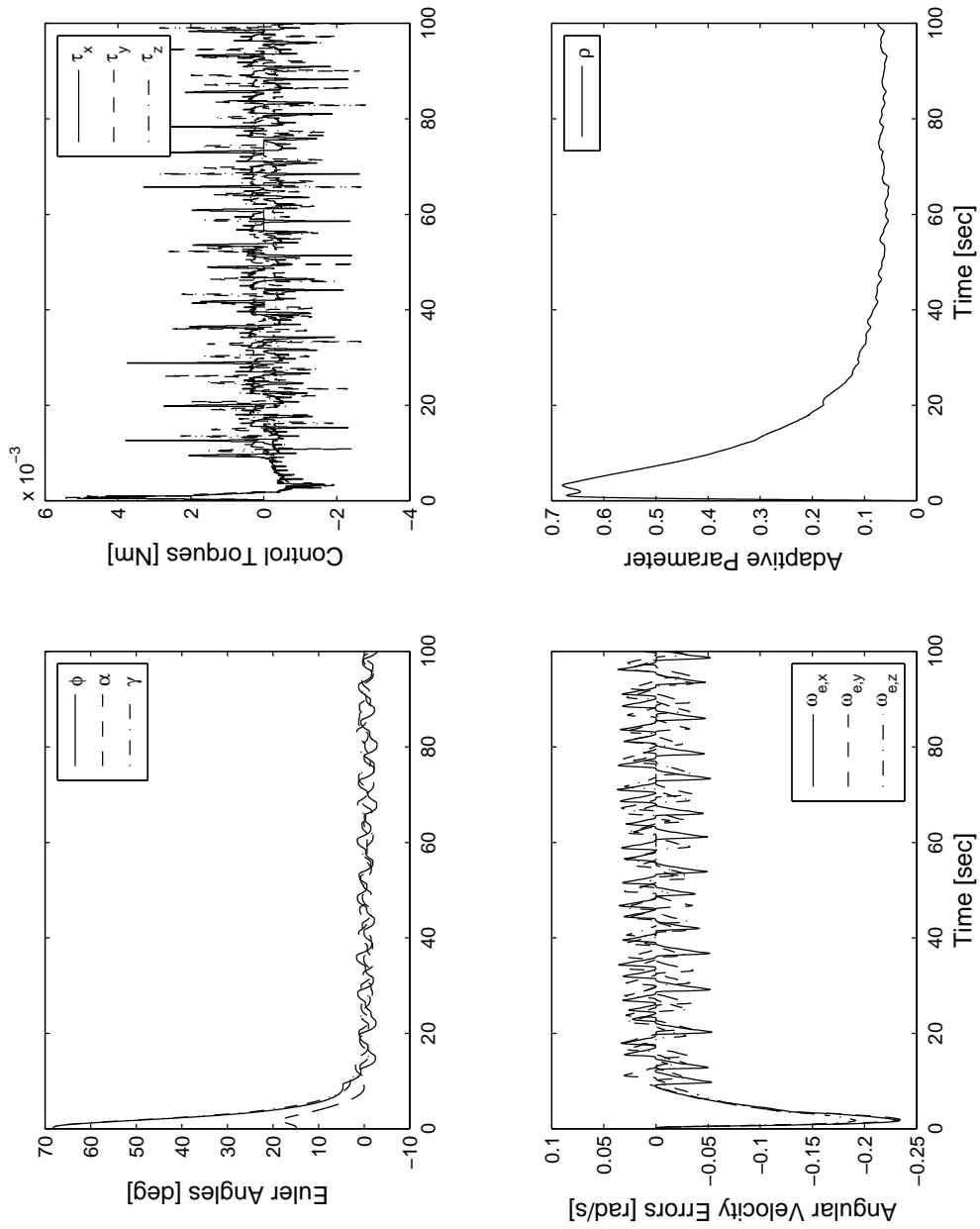


Figure 4.15: HIL simulation - Controlled performance for Case I: Fault-free conditions.

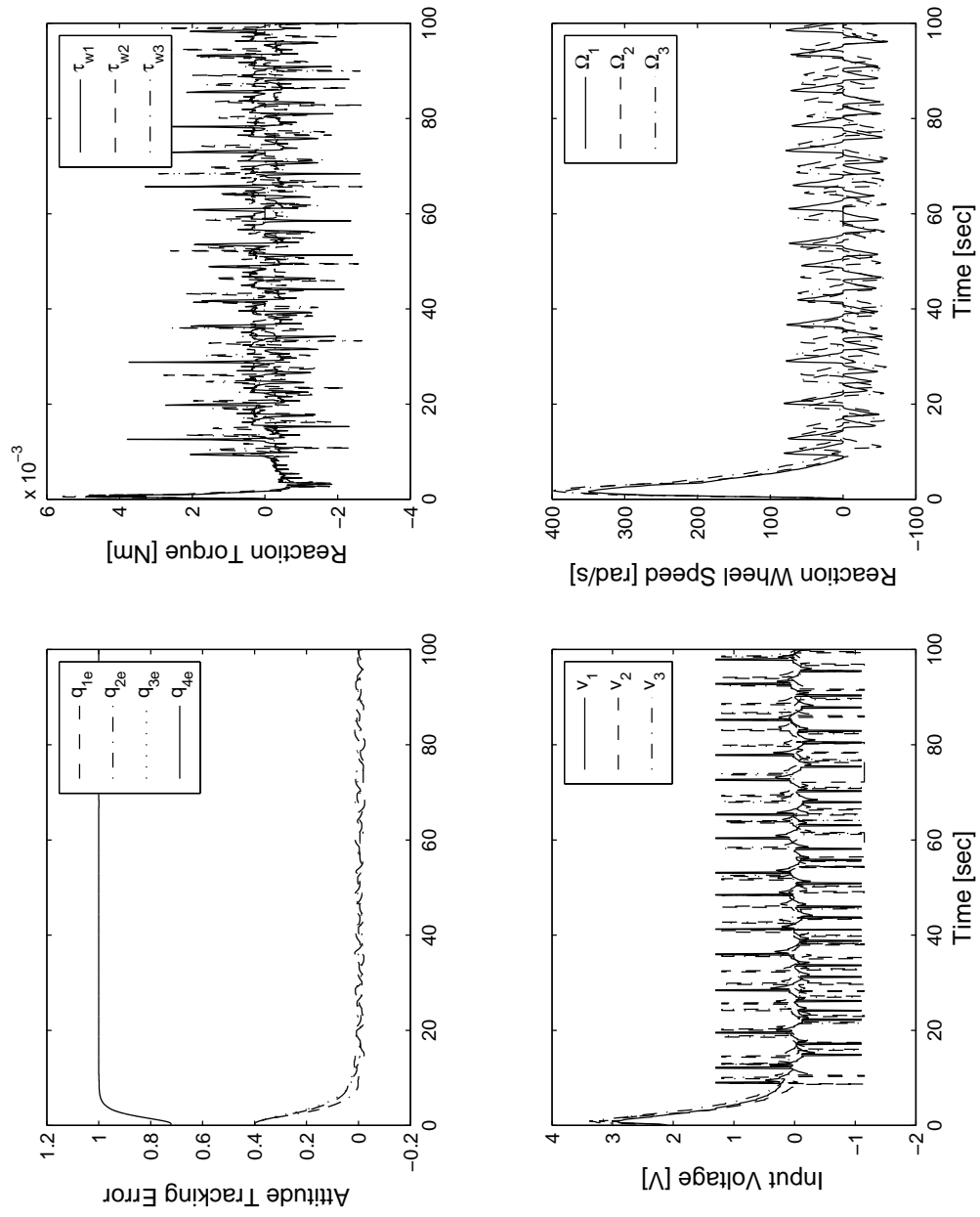


Figure 4.16: HIL simulation - Reaction wheel parameters for Case I: Fault-free conditions.

Simulations of a faulty condition

The asymptotic stability of the spacecraft attitude in response to a non-zero initial attitude, presence of environmental disturbances, and faulty reaction wheels is examined in this section. The following fault scenario is considered in the HIL simulation:

$$\begin{aligned} v_1 &= 0.1 + v_1, & \text{for } 10 \leq t \leq 30 \text{ s} \\ \Omega_2 &= 0.5\Omega_2, & \text{for } t \geq 10 \text{ s} \end{aligned} \quad (4.68)$$

The fault case given by Eq. (4.68) represents a bias fault that occurs at the first wheel for 20 s after $t = 10$ s into the simulation, and the second wheel only supplies 50% of the actuation power at the time instant $t = 10$ s and, after. The evolution of Euler angles, angular velocity errors, applied torque in spacecraft body-fixed axes, and the adaptive parameter for the faulty conditions in Eq. (4.68) are shown in Fig. 4.18. When compared to the fault-free case in Fig. 4.15, it is seen that high control precision and good tracking process are still obtained for a faulty case (Fig. 4.18).

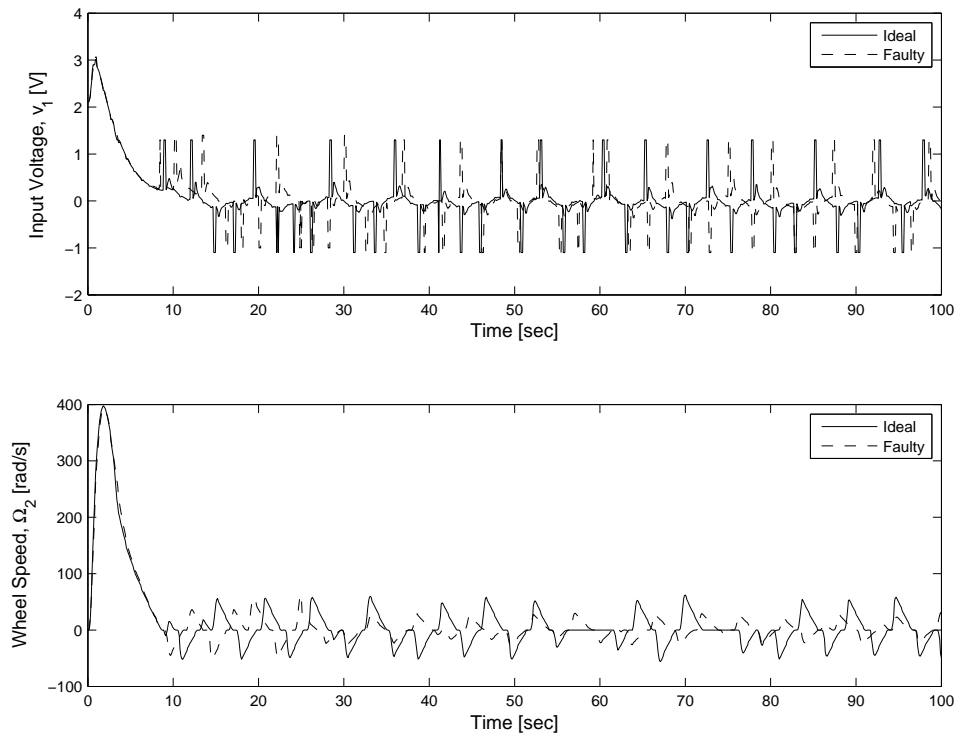


Figure 4.17: Difference between the generated faulty and ideal signals.

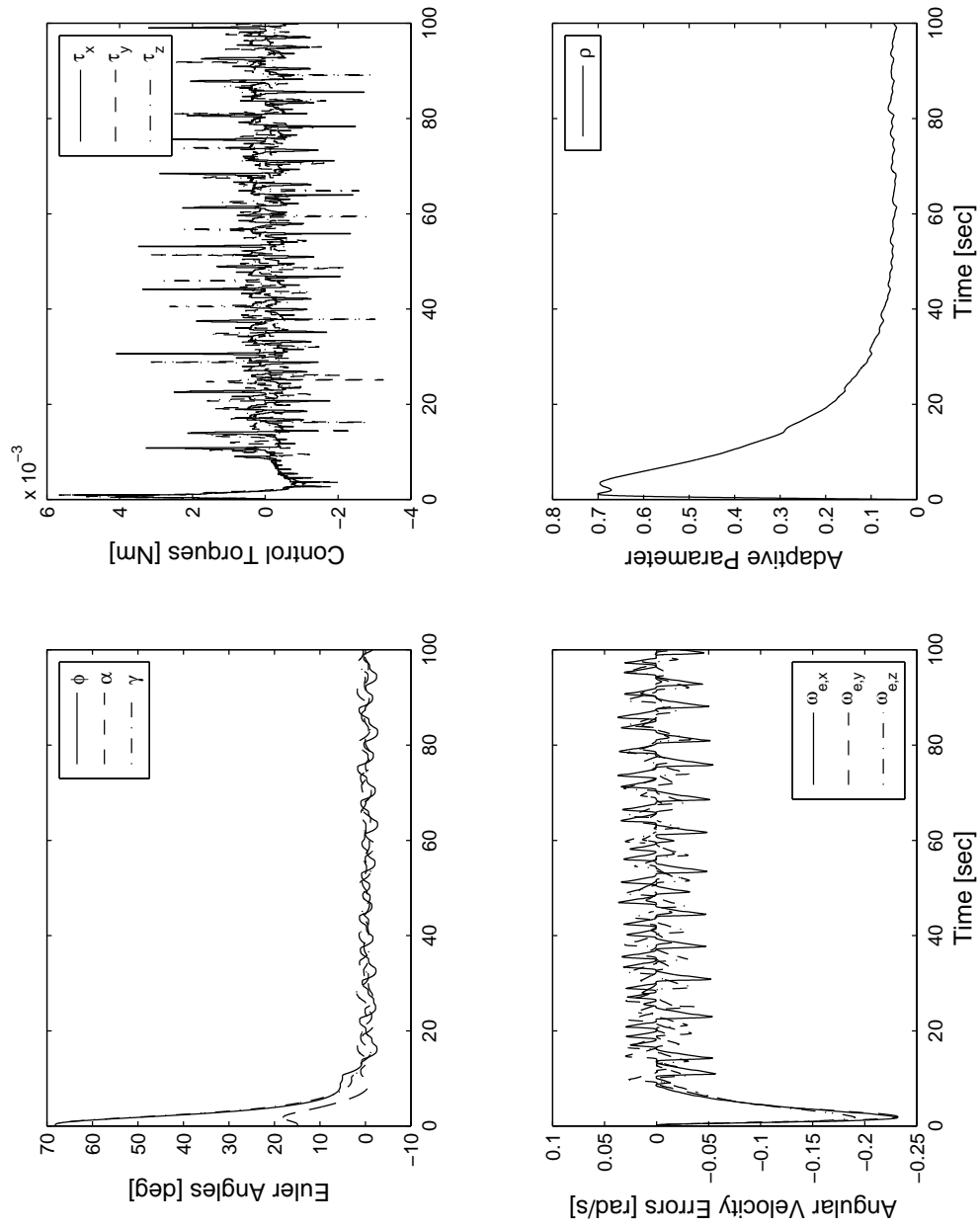


Figure 4.18: HIL simulation - Controlled performance for Case I: Faulty conditions.

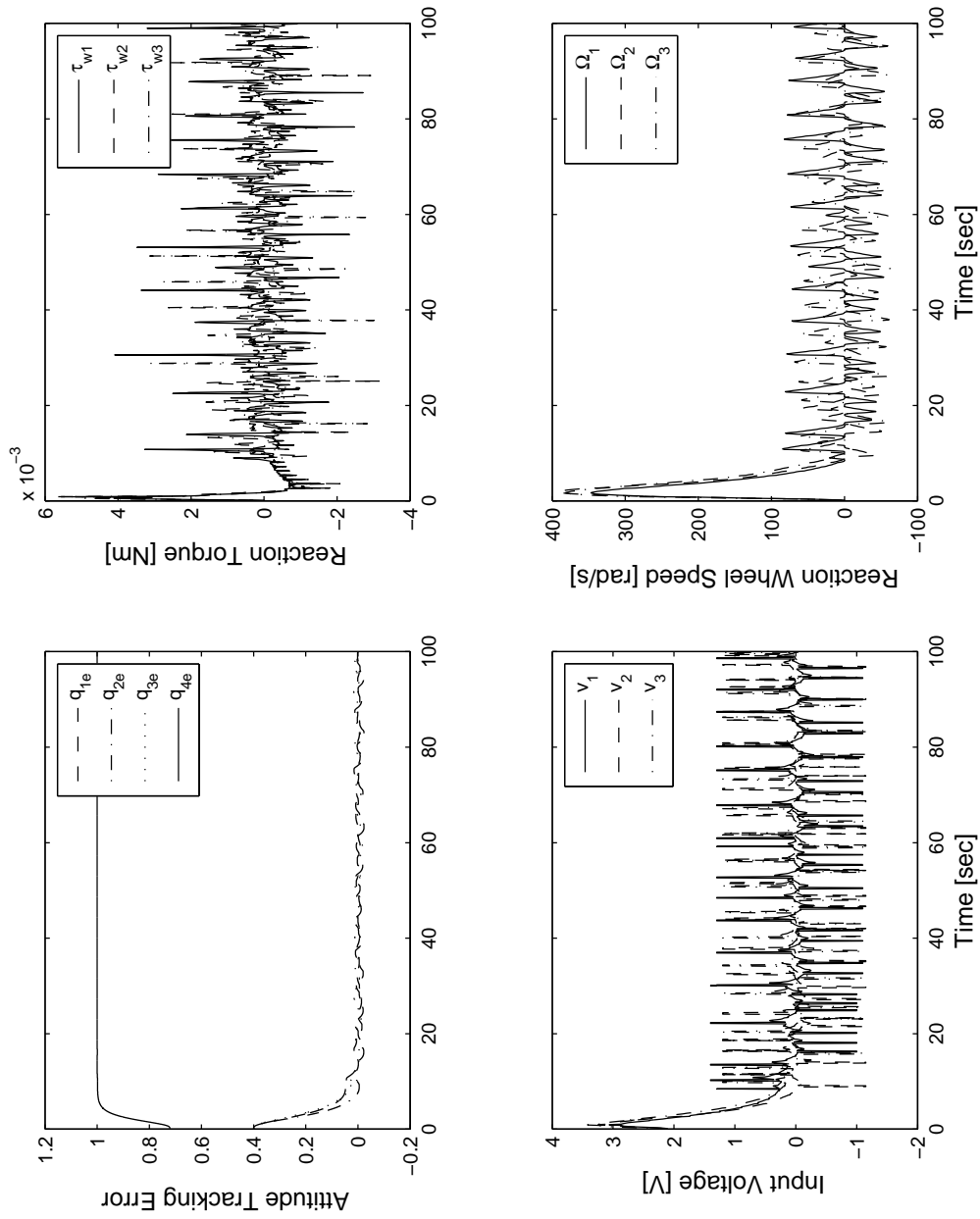


Figure 4.19: HIL simulation - Reaction wheel parameters for Case I: Faulty conditions.

Figure 4.19 shows the response curves of the attitude quaternion, the reaction torques generated by the wheel actuators, and the speeds and input voltage of the reaction wheels. To obtain a clear depiction of the faulty case, the differences in the control signals (input voltage) and the wheel speeds are shown in Fig. 4.17 with the faulty signals plotted over the ideal signals generated for the fault-free case. It is clearly evident that there is substantial degradation in the wheel speed Ω_2 after the fault has occurred at $t = 10$ s. Also, a phase offset in the input voltage signal v_1 for the faulty case can be observed in Fig. 4.17.

4.5.2 Case II - Traditional Four Wheel Configuration

In this section, we demonstrate the attitude stabilization capability of the ACS using the traditional four reaction wheel set up. This redundant reaction wheel configuration has the first three reaction wheel spin axes aligned with the principal spacecraft body axes, while a fourth wheel is aligned diagonally with respect to others as illustrated in Fig. 4.2a.

Simulations of a fault-free condition

The evolution of the Euler angles, applied control torques in spacecraft body-fixed coordinates, angular velocity errors, and the adaptive parameter ρ for the fault-free case can be seen in Fig. 4.20. The Euler angles asymptotically approaches to a stable boundary $\pm 0.5^\circ$ starting from non-zero initial conditions. The settling time of the closed-loop ACS is about 15 s. The time history of quaternion errors, reaction wheels' angular speed, and the input voltage are shown in Fig. 4.21.

Simulations of a faulty condition

The following fault scenario is considered in the HIL simulation:

$$\begin{aligned} v_1 &= 0.1 + v_1, & \text{for } 10 \leq t \leq 30 \text{ s} \\ v_3 &= 0, & \text{for } t \geq 10 \text{ s} \\ \Omega_2 &= 0.5\Omega_2, & \text{for } t \geq 10 \text{ s} \end{aligned} \tag{4.69}$$

Figure 4.22 shows the the performance of the proposed control scheme in stabilizing the attitude of the spacecraft in the presence of reaction wheel faults described by Eq. (4.69). The reaction wheels' angular speed and input voltages for this case are shown in Fig. 4.23. Failure of wheel-3 does not degrade the performance of the proposed control algorithm.

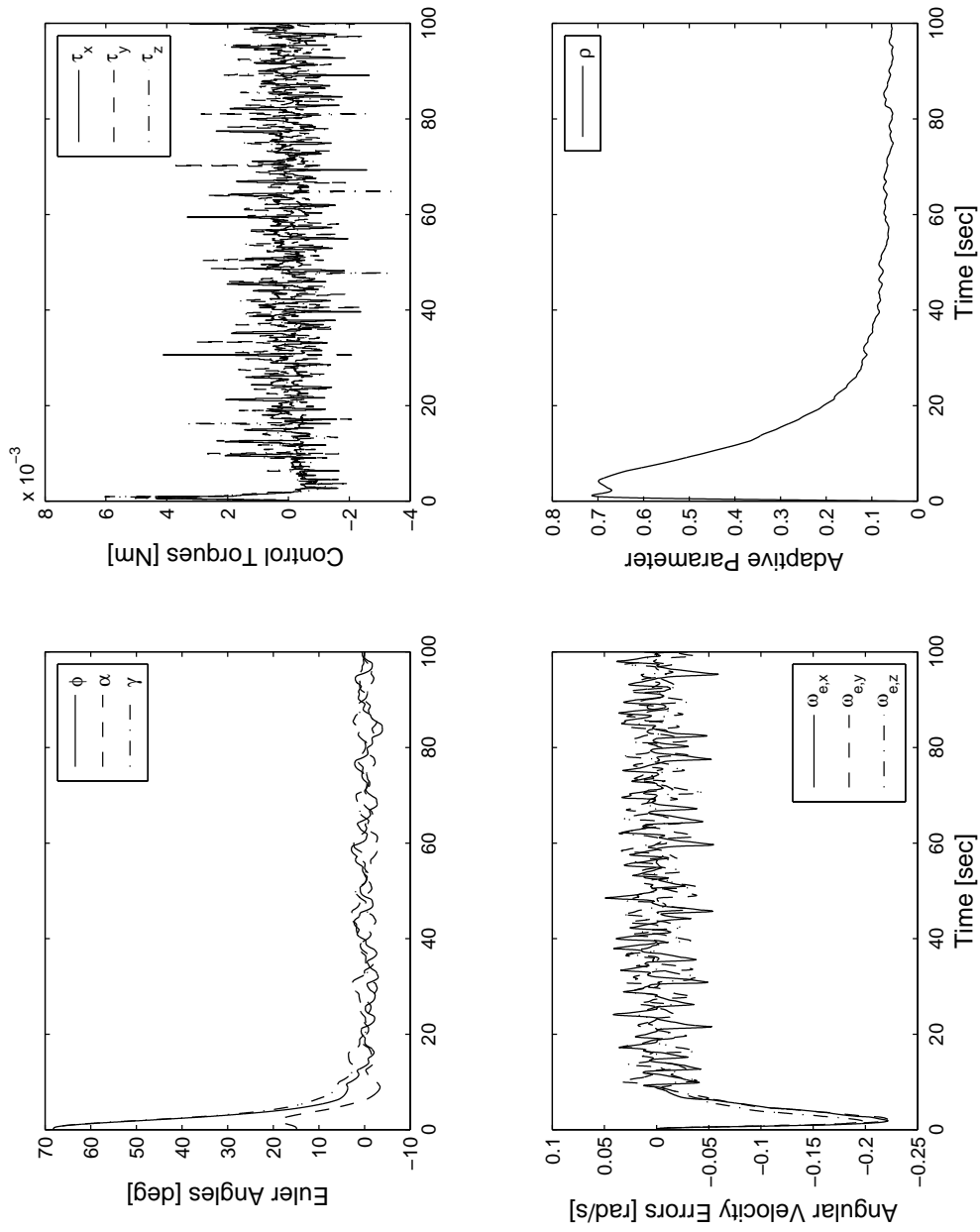


Figure 4.20: HIL simulation - Controlled performance for Case II: Fault-free conditions.

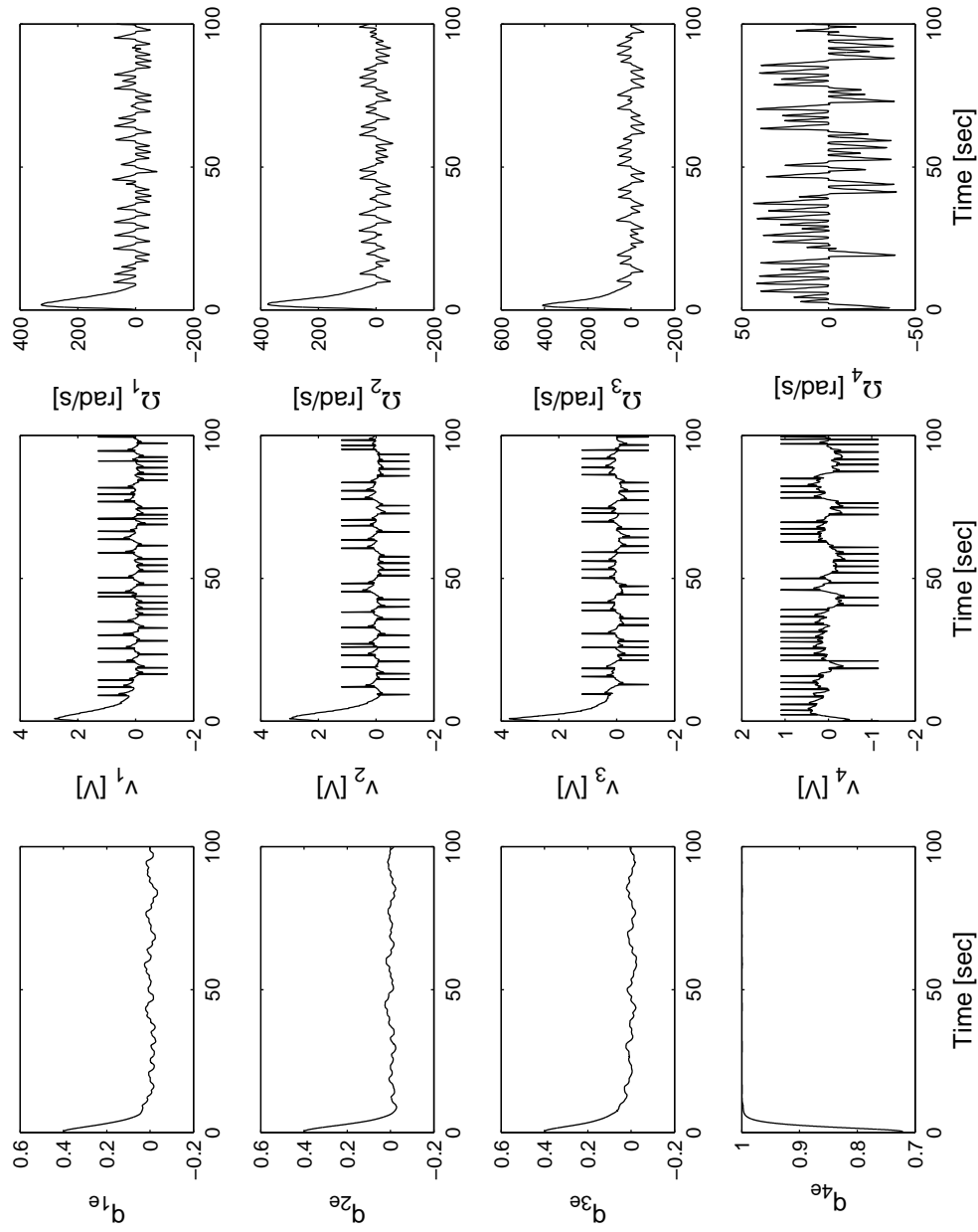


Figure 4.21: HIL simulation - Reaction wheel parameters for Case II: Fault-free conditions.

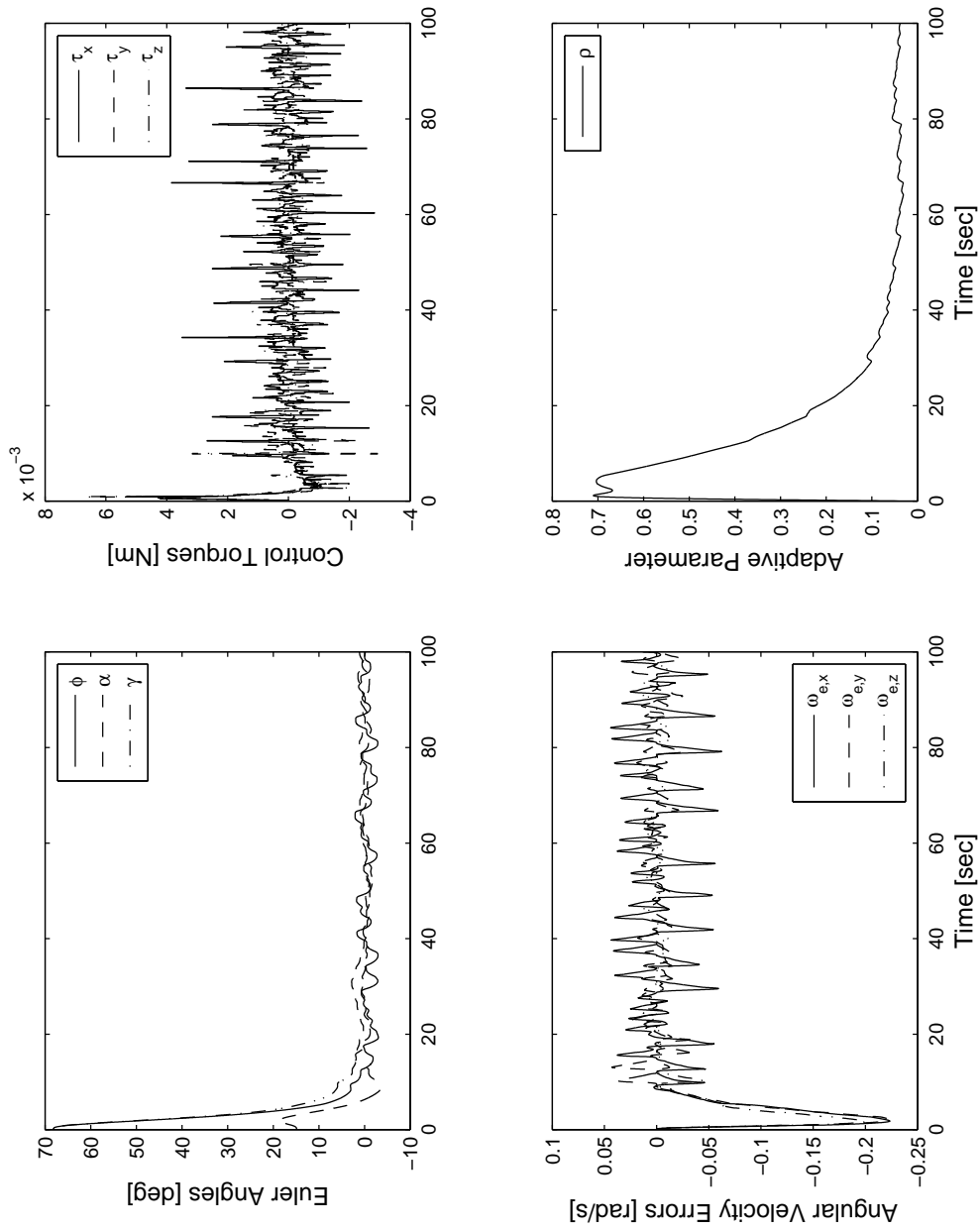


Figure 4.22: HIL simulation - Controlled performance for Case II: Faulty conditions.

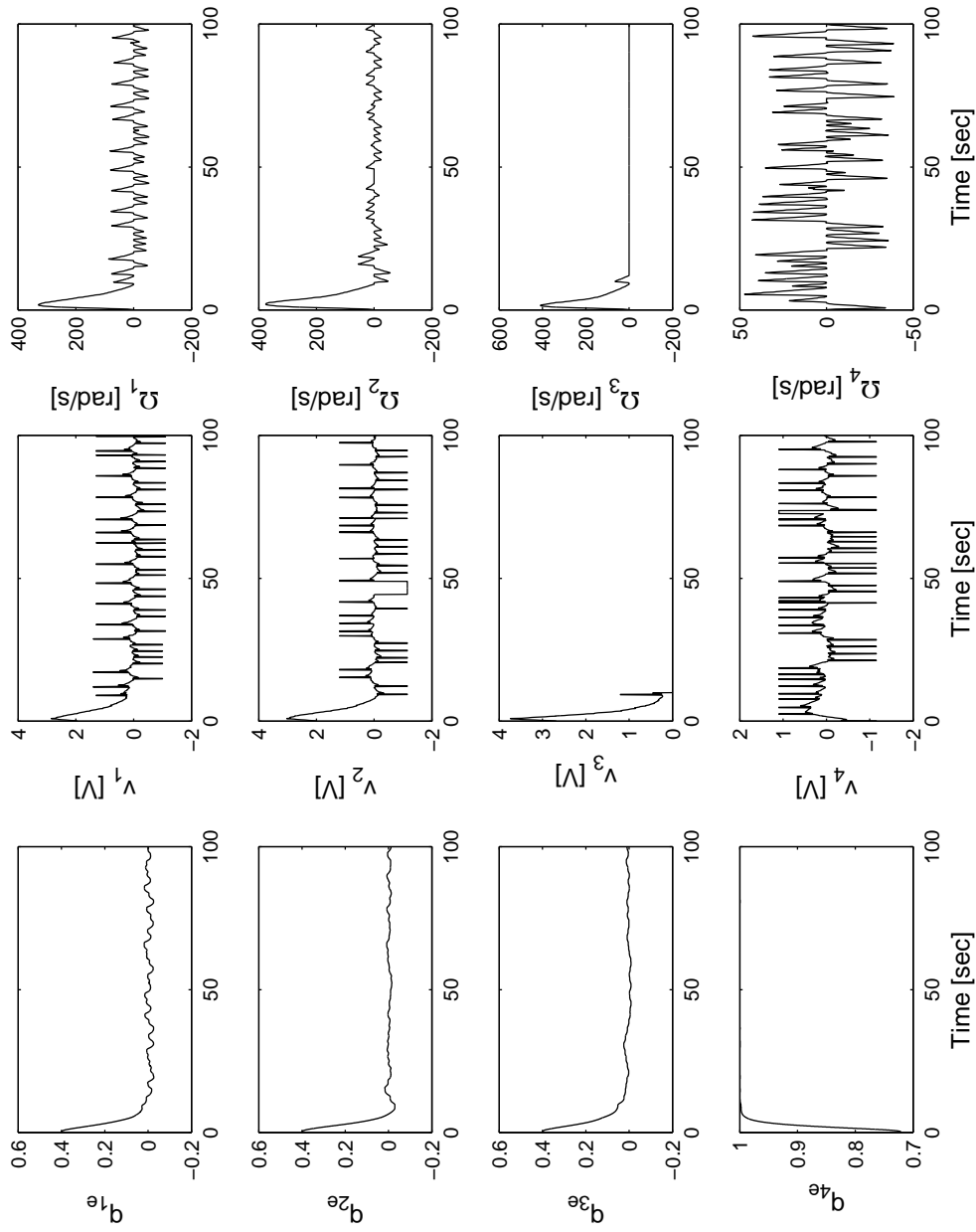


Figure 4.23: HIL simulation - Reaction wheel parameters for Case II: Faulty conditions.

4.5.3 Case III - Four Wheels in Pyramid Configuration

In this section, we illustrate the performance of the proposed technique using a four reaction wheel assembly mounted in pyramid configuration (Fig. 4.3).

Simulations of a fault-free condition

The evolution of the Euler angles, applied control torques in spacecraft body-fixed coordinates, angular velocity errors, and the adaptive parameter ρ for the fault-free case can be seen in Fig. 4.24. The Euler angles asymptotically approaches to a stable boundary $\pm 0.5^\circ$ starting from non-zero initial conditions. The settling time of the closed-loop ACS is about 15 s. The time history of quaternion errors, reaction wheels' angular speed, and the input voltage are shown in Fig. 4.25.

Simulations of a faulty condition

The following fault scenario is considered in the HIL simulation:

$$\begin{aligned} v_2 &= 0.1 + v_2, & \text{for } 10 \leq t \leq 20 \text{ s} \\ v_1 &= 0, & \text{for } t \geq 5 \text{ s} \\ v_3 &= 0, & \text{for } t \geq 5 \text{ s} \\ \Omega_4 &= 0.5\Omega_4, & \text{for } t \geq 10 \text{ s} \end{aligned} \tag{4.70}$$

Figure 4.26 shows the the performance of the proposed control scheme in stabilizing the attitude of the spacecraft in the presence of reaction wheel faults described by Eq. (4.70). The reaction wheels' angular speed and input voltages for this case are shown in Fig. 4.27. Failure of wheels 1 and 3 has no effect on the attitude response of the spacecraft. These preliminary results suggest that the proposed FTC approach is able to perform three axis stabilization with a reasonable pointing accuracy with only two reaction wheels.

The HIL simulation results presented in this section, all indicate that the proposed control methodology is robust and adaptive to external disturbances and faults in reaction wheels. It is important to note that, the reaction wheels used for the hardware simulations are not space qualified and have only recently been manufactured at Ryerson University. Our objective of this study was to test the control algorithm on an actual hardware to verify that the results predicted using the theoretical framework and numerical simulations are indeed attainable.

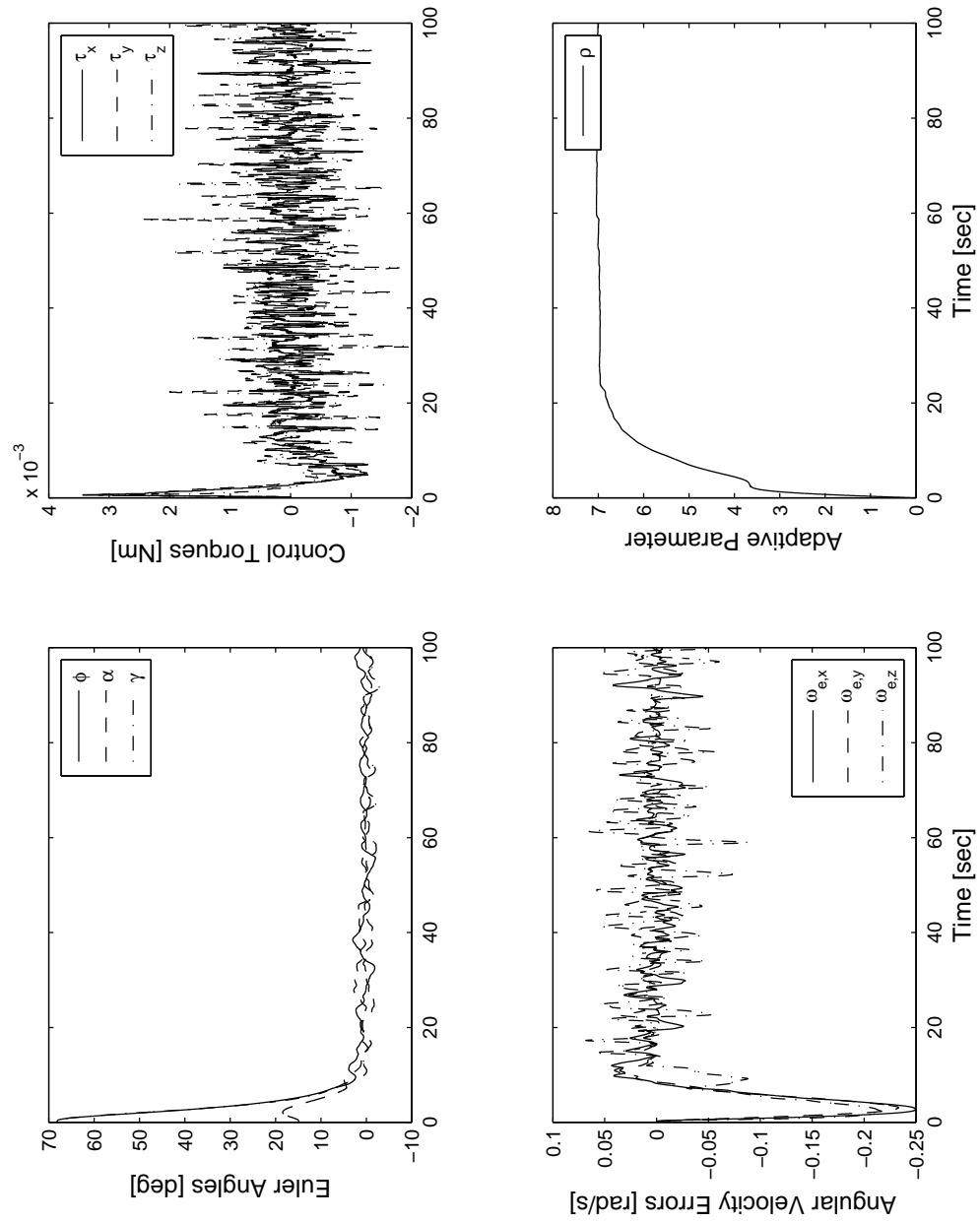


Figure 4.24: HIL simulation - Controlled performance for Case III: Fault-free conditions.

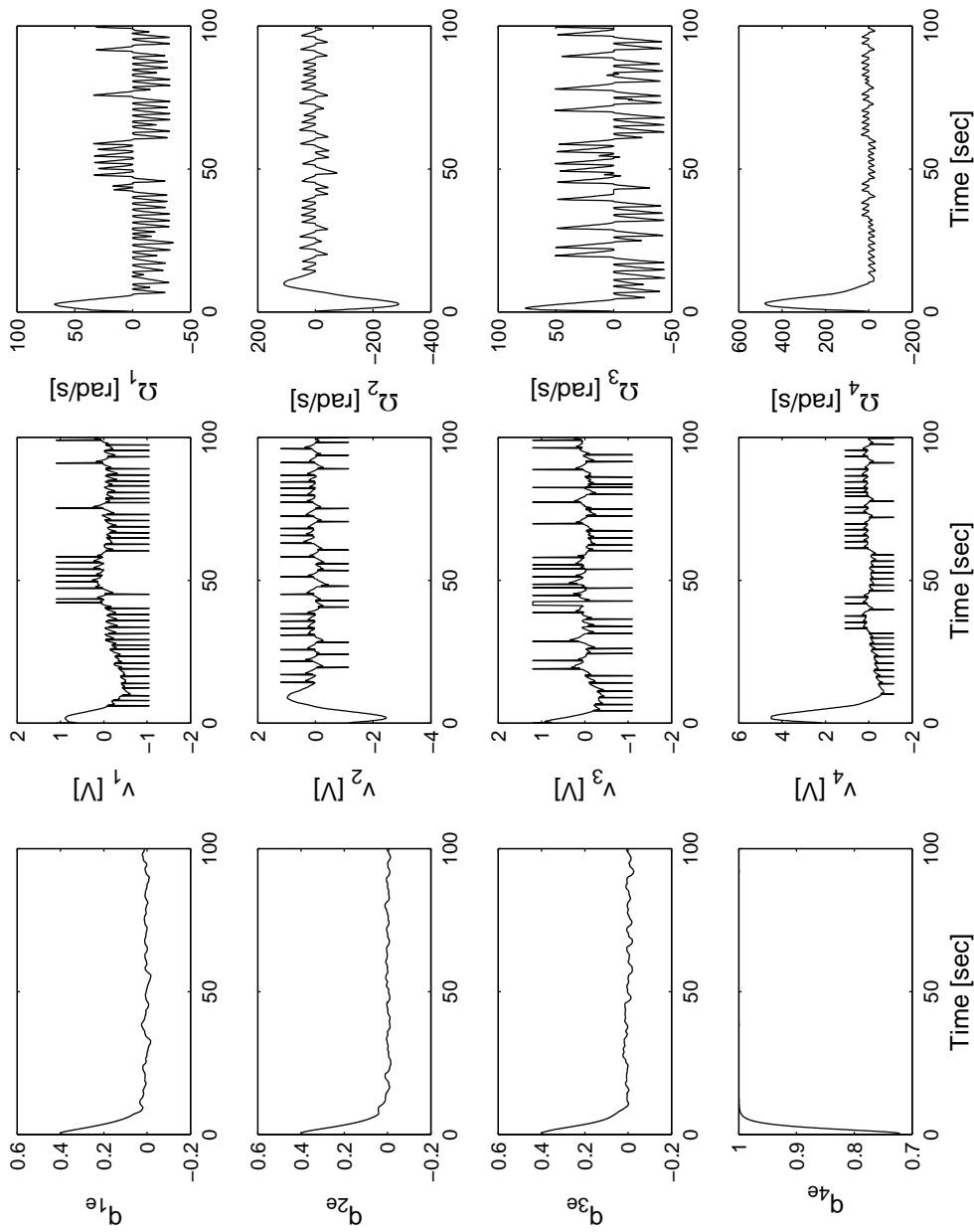


Figure 4.25: HIL simulation - Reaction wheel parameters for Case III: Fault-free conditions.

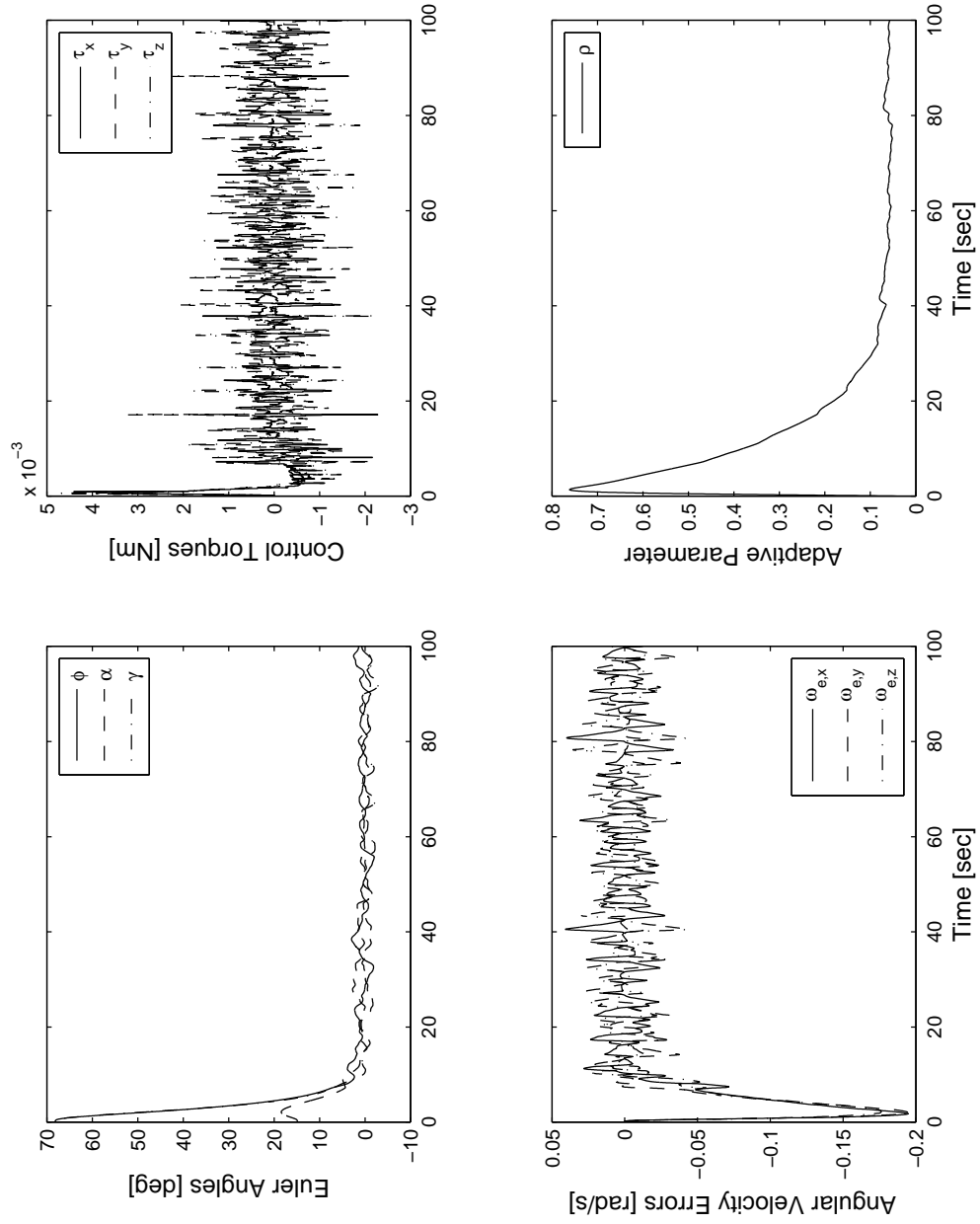


Figure 4.26: HIL simulation - Controlled performance for Case III: Faulty conditions.

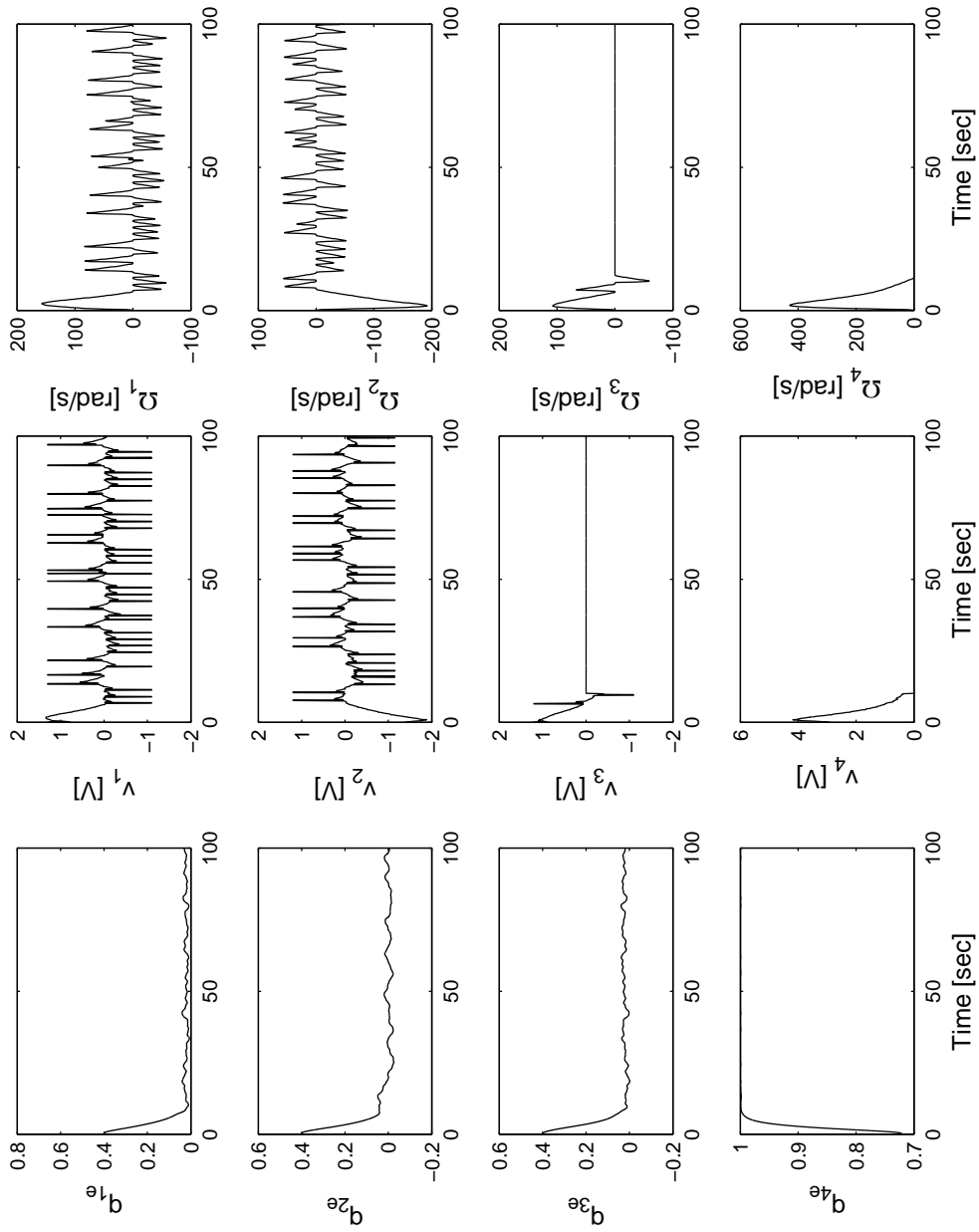


Figure 4.27: HIL simulation - Reaction wheel parameters for Case III: Faulty conditions.

4.6 Summary

In this chapter, we presented an adaptive fault-tolerant nonlinear control scheme for attitude tracking of a rigid spacecraft using reaction wheels. Although various nonlinear control algorithms have been published in the literature for rigid spacecraft attitude control, very few have addressed fault recovery, robustness, and adaptation using RWA hardware. We considered several scenarios of reaction wheel faults that can introduce constant or state-dependant disturbances into the overall closed-loop system causing the dynamics of the spacecraft to deviate largely from its nominal regime.

To verify and validate the effectiveness of the proposed control algorithm, a numerical model of the spacecraft attitude dynamics was developed which includes the mathematical models of environmental disturbances acting on the spacecraft in LEO. The domains of sliding mode and the estimates of domain of attraction along with the regions of asymptotic stability for the fault cases are analytically determined using nonlinear control theory. Overall, the results clearly establish the robustness of the proposed adaptive control methodologies in tracking the attitude of the spacecraft in the presence of actuator faults, model uncertainties, and time varying disturbances.

Attitude Control of Underactuated Spacecraft

AUTONOMOUS design approach for robust attitude control is of considerable importance to meet the increasing demands for low-cost, low-mass, and low-power consumption based attitude control system (ACS) design for spacecraft. Recent advances in spacecraft control systems have succeeded in developing attitude control algorithms capable of providing high precision pointing and optimal slew maneuvers. In the previous chapter, a novel fault-tolerant adaptive control algorithm was developed for autonomous recovery of spacecraft attitude in the event of actuator failures. Existing control techniques in the literature and the adaptive scheme presented in the Chapter 4 are developed based on the assumption that the spacecraft is actively controlled with a sufficient number of actuators equal to, or larger than, the number of degrees of freedom to be controlled. An underactuated spacecraft is a system with fewer independent control actuators than degrees of freedom to be controlled.

From a practical point of view, the need for control methodologies for underactuated spacecraft arises due to the following reasons: (1) To stabilize spacecraft systems which are underactuated by design. Including fewer actuators than typically required leads to lighter, less costly designs. (2) To stabilize a spacecraft that may become underactuated due to actuator failures. Rather than equipping the spacecraft with a redundant actuator, the software option is a cost-reducing alternative, since it only requires switching to a control law that utilizes the remaining actuators for 3-axis stabilization when an actuator failure is detected. This chapter presents a nonlinear control algorithm that can provide 3-axis attitude stabilization for a rigid spacecraft using control torques supplied by thrusters about only two of its principal axes.

The problem of attitude regulation of an underactuated rigid body considered in this study is in the local vertical and local horizontal frame (LVLH). The spacecraft's attitude is represented with respect to the rotating orbital reference frame to take into account the effect of spacecraft rotation around the Earth. In this case, the rigid body always rotates around the pitch axis, thus Brockett's condition is initially avoided. The main advantage of this approach is that it allows smooth time-invariant continuous feedback algorithms to be employed for 3-axis attitude using only two control inputs.

The chapter is organized as follows: Section 5.1 introduces the complete nonlinear mathematical model of the spacecraft orbiting the Earth. Control algorithms based on variable structure techniques are formulated with stability conditions for robustness against unmatched uncertainties and disturbances in Section 5.2. For a detailed assessment of the system performance under the proposed control strategy, the results of numerical simulations incorporating the effects of various system parameters are examined in Section 5.3. Finally, conclusions are stated in Section 5.4.

5.1 Spacecraft Mathematical Model

The investigation is initiated by formulating the complete nonlinear equations of motion of the underactuated rigid body spacecraft to develop a mathematical model that facilitates the design of nonlinear control methodologies. The proposed system consists of a *rigid body spacecraft* in an elliptical planar trajectory with the Earth's center at one of its foci.

5.1.1 Coordinate Frames

An *Earth centered inertial* (ECI) frame denoted by $\mathfrak{J} - X_I Y_I Z_I$ (Figure 5.1), has its origin located at the center of the Earth, with the Z_I -axis passing through the celestial North pole, the X_I -axis directed towards the vernal equinox, and the Y_I -axis completing the right-handed triad. Next, we define a local vertical local horizontal (LVLH) orbital reference frame $\mathfrak{L} - x_0 y_0 z_0$ with its origin always at the center of mass of the spacecraft. The nodal line represents the reference line in orbit for the measurement of the true anomaly (eccentric orbit) or angle θ (circular orbit). Here the x_0 -axis points along the local vertical,

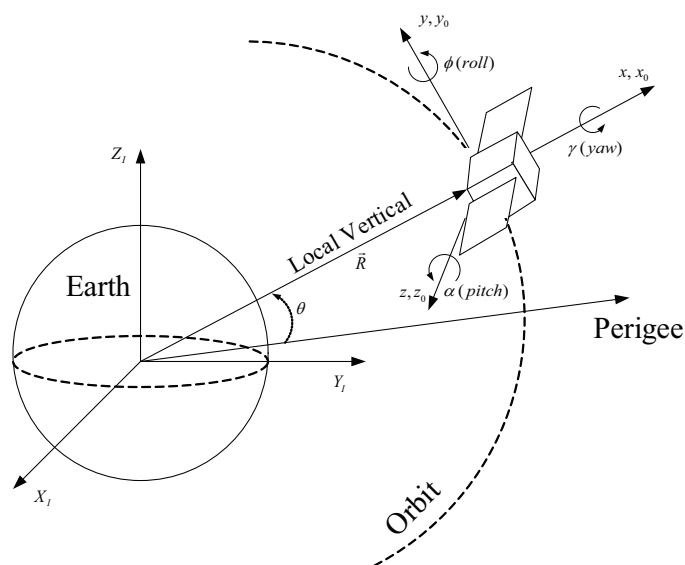


Figure 5.1: Geometry of orbit motion of rigid spacecraft.

the z_0 -axis is taken normal to the orbital plane, and the y_0 -axis along the orbit direction. The corresponding principal body-fixed coordinate axes of the spacecraft are denoted by $\mathfrak{B} - x y z$ with its origin located at the spacecraft center of mass.

The most commonly used sets of attitude parameters are the Euler angles (α, ϕ, γ) . They describe the attitude orientation of the body-fixed reference frame, $\mathfrak{B} - x y z$, relative to the LVLH reference frame, $\mathfrak{L} - x_0 y_0 z_0$, by a set of three successive rotations. The rotations may occur about any of the three orthogonal axes, but two successive rotations about the same axis is not possible. There are 12 sets of Euler angles for such successive rotations about the body-fixed axis.

The most commonly used rotation sequence is the $(3 - 2 - 1)$ set of Euler angles: α (pitch) about the z -axis (3), ϕ (roll) about the new y -axis (2), and finally γ (yaw) about the resulting x -axis (1). However, Euler angles exhibit singularities whenever the roll angle (ϕ) has a value of $\pm \frac{\pi}{2}$. The mathematical singularity is an *inherent* property of the Euler representation and does not reflect the physical limitations of the rigid spacecraft. The orientation of the body-fixed reference frame, $\mathfrak{B} - x y z$, with respect to the LVLH reference frame, $\mathfrak{L} - x_0 y_0 z_0$ using the $(3 - 2 - 1)$ rotation sequence is described by the direction cosine matrix $C^{B/L} = R_1(\gamma)R_2(\phi)R_3(\alpha) = R_x(\gamma)R_y(\phi)R_z(\alpha)$.

$$C^{B/L} = \begin{bmatrix} c\phi c\alpha & c\phi s\alpha & -s\phi \\ s\gamma s\phi c\alpha - c\gamma s\alpha & s\gamma s\phi s\alpha + c\gamma c\alpha & s\gamma c\phi \\ c\gamma s\phi c\alpha + s\gamma s\alpha & c\gamma s\phi s\alpha - s\gamma c\alpha & c\gamma c\phi \end{bmatrix} \quad (5.1)$$

where $c\phi = \cos \phi$ and $s\phi = \sin \phi$, $R_x(\gamma)$ denotes the rotation matrix for γ rotation about the x -axis, $R_y(\phi)$ denotes the rotation matrix for ϕ rotation about the y -axis, and $R_z(\alpha)$ denotes the rotation matrix for α rotation about the z -axis.

5.1.2 Spacecraft Angular Velocity

Let $\{\hat{i}, \hat{j}, \hat{k}\}$ and $\{\hat{i}_0, \hat{j}_0, \hat{k}_0\}$ be the sets of unit vectors associated with the reference frames $\mathfrak{B} - xyz$ and $\mathfrak{L} - x_0 y_0 z_0$, respectively. The transformation from the $\mathfrak{L} - x_0 y_0 z_0$ orbital frame to the body-fixed frame $\mathfrak{B} - xyz$ using $(3 - 2 - 1)$ rotation sequence is given by

$$\begin{bmatrix} \hat{i} \\ \hat{j} \\ \hat{k} \end{bmatrix} = \begin{bmatrix} c\phi c\alpha & c\phi s\alpha & -s\phi \\ s\gamma s\phi c\alpha - c\gamma s\alpha & s\gamma s\phi s\alpha + c\gamma c\alpha & s\gamma c\phi \\ c\gamma s\phi c\alpha + s\gamma s\alpha & c\gamma s\phi s\alpha - s\gamma c\alpha & c\gamma c\phi \end{bmatrix} \begin{bmatrix} \hat{i}_0 \\ \hat{j}_0 \\ \hat{k}_0 \end{bmatrix} \quad (5.2)$$

For a rigid spacecraft in an elliptical orbit around the Earth, the angular velocity of the body-fixed frame \mathfrak{B} relative to the ECI frame \mathfrak{J} is given by

$$\vec{\omega}^{B/I} = \vec{\omega}^{B/L} + \vec{\omega}^{L/I} \quad (5.3)$$

where $\vec{\omega}^{B/L}$ is the angular velocity of \mathfrak{B} relative to the orbital frame \mathfrak{L} , and $\vec{\omega}^{L/I}$ is the angular velocity of the orbital frame with respect to the ECI frame. From Fig. 5.1, the angular velocity of \mathfrak{L} relative to \mathfrak{J} is

$$\vec{\omega}^{L/I} = \dot{\theta} \hat{k}_0 \quad (5.4)$$

where $\dot{\theta}$ is the orbital rate of the spacecraft. For a circular orbit, $\dot{\theta} = \sqrt{\frac{\mu}{R_c^3}}$, where μ represents the gravitational parameter of the Earth, and R_c is the distance of the spacecraft from the center of the Earth. From Eq. (5.2) we have

$$\begin{bmatrix} \hat{i}_0 \\ \hat{j}_0 \\ \hat{k}_0 \end{bmatrix} = \begin{bmatrix} c\phi c\alpha & s\gamma s\phi c\alpha - c\gamma s\alpha & c\gamma s\phi c\alpha + s\gamma s\alpha \\ c\phi s\alpha & s\gamma s\phi s\alpha + c\gamma c\alpha & c\gamma s\phi s\alpha - s\gamma c\alpha \\ -s\phi & s\gamma c\phi & c\gamma c\phi \end{bmatrix} \begin{bmatrix} \hat{i} \\ \hat{j} \\ \hat{k} \end{bmatrix} \quad (5.5)$$

Substituting for \hat{k}_0 from Eq. (5.5) into Eq. (5.4) we get

$$\vec{\omega}^{L/I} = \dot{\theta} \begin{bmatrix} -\sin \phi \\ \sin \gamma \cos \phi \\ \cos \gamma \cos \phi \end{bmatrix} \quad (5.6)$$

The angular velocity of the spacecraft with respect to the orbital frame \mathcal{L} is given by

$$\begin{aligned} \vec{\omega}^{B/L} &= \omega_x^{BL} \hat{i} + \omega_y^{BL} \hat{j} + \omega_z^{BL} \hat{k} \\ &= \dot{\alpha} \hat{k}_0 + \dot{\phi} \hat{j}_1 + \dot{\gamma} \hat{i} \end{aligned} \quad (5.7)$$

where $\dot{\alpha}$ is about the k_0 axis in the frame $\mathcal{L} - x_0 y_0 z_0$, followed by $\dot{\phi}$ about the j_1 axis in the intermediate frame $\mathcal{S} - x_1 y_1 z_1$, and finally $\dot{\gamma}$ about the i axis in the frame $\mathcal{B} - x y z$. This can be rewritten as

$$\vec{\omega}^{B/O} = \begin{bmatrix} \hat{i} & \hat{j} & \hat{k} \end{bmatrix} \begin{bmatrix} \dot{\gamma} \\ 0 \\ 0 \end{bmatrix} + \begin{bmatrix} \hat{i}_1 & \hat{j}_1 & \hat{k}_1 \end{bmatrix} \begin{bmatrix} 0 \\ \dot{\phi} \\ 0 \end{bmatrix} + \begin{bmatrix} \hat{i}_0 & \hat{j}_0 & \hat{k}_0 \end{bmatrix} \begin{bmatrix} 0 \\ 0 \\ \dot{\alpha} \end{bmatrix} \quad (5.8)$$

The unit vectors are related to each other based on rotation matrices as follows

$$\begin{aligned} \begin{bmatrix} \hat{i}_1 & \hat{j}_1 & \hat{k}_1 \end{bmatrix}^T &= [R_x(\gamma)R_y(\phi)]^{-1} \begin{bmatrix} \hat{i} & \hat{j} & \hat{k} \end{bmatrix}^T \\ \begin{bmatrix} \hat{i}_0 & \hat{j}_0 & \hat{k}_0 \end{bmatrix}^T &= [R_x(\gamma)R_y(\phi)R_z(\alpha)]^{-1} \begin{bmatrix} \hat{i} & \hat{j} & \hat{k} \end{bmatrix}^T \end{aligned} \quad (5.9)$$

Using Eqs. (5.7)-(5.9) the angular velocity of the rigid spacecraft with respect to the orbital reference frame \mathcal{L} can be expressed as

$$\begin{aligned} \begin{bmatrix} \omega_x^{BL} \\ \omega_y^{BL} \\ \omega_z^{BL} \end{bmatrix} &= \begin{bmatrix} \dot{\gamma} \\ 0 \\ 0 \end{bmatrix} + R_x(\gamma)R_y(\phi) \begin{bmatrix} 0 \\ \dot{\phi} \\ 0 \end{bmatrix} + R_x(\gamma)R_y(\phi)R_z(\alpha) \begin{bmatrix} 0 \\ 0 \\ \dot{\alpha} \end{bmatrix} \\ &= \begin{bmatrix} 1 & 0 & -\sin \phi \\ 0 & \cos \gamma & \sin \gamma \cos \phi \\ 0 & -\sin \gamma & \cos \gamma \cos \phi \end{bmatrix} \begin{bmatrix} \dot{\gamma} \\ \dot{\phi} \\ \dot{\alpha} \end{bmatrix} \end{aligned} \quad (5.10)$$

Finally, using Eqs. (5.6) and (5.10) in Eq. (5.3) we get the angular velocity of the rigid spacecraft relative to the ECI frame \mathfrak{J} expressed in frame \mathfrak{B} as

$$\begin{bmatrix} \omega_x \\ \omega_y \\ \omega_z \end{bmatrix} = \begin{bmatrix} 1 & 0 & -\sin \phi \\ 0 & \cos \gamma & \sin \gamma \cos \phi \\ 0 & -\sin \gamma & \cos \gamma \cos \phi \end{bmatrix} \begin{bmatrix} \dot{\gamma} \\ \dot{\phi} \\ \dot{\alpha} \end{bmatrix} + \dot{\theta} \begin{bmatrix} -\sin \phi \\ \sin \gamma \cos \phi \\ \cos \gamma \cos \phi \end{bmatrix} \quad (5.11)$$

5.1.3 Equations of Motion

To apply the Lagrangian approach for the formulation of the system equations of motion, the expressions for the system kinetic energy (T) as well as the potential energy (U_p) are first obtained [Kumar 2006a]:

$$T = \frac{1}{2}m\dot{\vec{R}}^2 + \frac{1}{2}\vec{\omega}^T I \vec{\omega} \quad (5.12)$$

$$U_p = -\frac{\mu m}{R} - \frac{\mu}{2R^3} \text{tr}(I) + \frac{3\mu}{2R^3} C_1^T I C_1 \quad (5.13)$$

where I is the inertia tensor, $\text{tr}(I)$ is the trace of matrix I , $\vec{\omega}$ is the angular velocity vector, and $C_1 \in \mathbb{R}^3 = [C_{11}, C_{12}, C_{13}]^T$ is the direction cosine vector of the local vertical \vec{R} with respect to the spacecraft body fixed frame $S - xyz$. C_1 represents the first column of the direction cosine matrix defined in Eq. (5.1)

$$\begin{aligned} C_{11} &= \cos \alpha \cos \phi \\ C_{12} &= \cos \alpha \sin \phi \sin \gamma - \sin \alpha \cos \gamma \\ C_{13} &= \cos \alpha \sin \phi \cos \gamma - \sin \alpha \sin \gamma \end{aligned} \quad (5.14)$$

The Lagrangian equations of motion corresponding to the generalized coordinates ($q = \alpha, \phi, \gamma$) are obtained using the general relation

$$\frac{d}{dt} \left(\frac{\partial T}{\partial \dot{q}} \right) - \frac{\partial T}{\partial q} + \frac{\partial U_p}{\partial q} = Q_q \quad (5.15)$$

where Q_q is the generalized force corresponding to the generalized coordinate q . We substitute the generalized coordinates in the preceding Eq. (5.15) and express the derivative with respect to the true anomaly using the relations given below:

$$\dot{q} = \dot{\theta} q' = \frac{\sqrt{\mu a(1-e^2)}}{R^2} q' \quad (5.16)$$

$$\ddot{q} = \frac{\mu}{R^3} [(1 + e \cos \theta) q'' - 2q' e \sin \theta] \quad (5.17)$$

where the orbital radius R is replaced by the semi-major axis a and the eccentricity e , using the relation

$$R = \frac{a(1 - e^2)}{1 + e \cos \theta} = \frac{\mu^{1/3}(1 - e^2)}{\Omega^{2/3}(1 + e \cos \theta)} \quad (5.18)$$

The resulting governing nonlinear, coupled ordinary differential equations of motion of the system, after carrying out considerable algebraic manipulation and nondimensionalization, can be expressed in a general form as follows:

$$q'' = N(q)[F(q, q') + U_{fa}] \quad (5.19)$$

where $N(q) \in \mathbb{R}^{3 \times 3}$ and $F(q, q') \in \mathbb{R}^{3 \times 1}$ are matrices containing nonlinear functions, $q \in \mathbb{R}^3 = [\alpha, \phi, \gamma]^T$, and $U_{fa} \in \mathbb{R}^3 = [U_\alpha, U_\phi, U_\gamma]^T$ is the control torque. The variable of integration t (time) is changed to θ (true anomaly measured with respect to the orbit perigee) using Eqs. (5.16) and (5.17).

We define the following dimensionless parameters representing principal moment of inertia ratios of the rigid spacecraft,

$$k_1 = \frac{I_z - I_x}{I_y} \quad \text{and} \quad k_{xz} = \frac{I_x}{I_z} = \frac{1 - k_1}{1 - k_1 k_2} \quad (5.20)$$

$$k_2 = \frac{I_z - I_y}{I_x} \quad \text{and} \quad k_{yz} = \frac{I_y}{I_z} = \frac{1 - k_2}{1 - k_1 k_2} \quad (5.21)$$

The equations of motion derived from the Lagrangian relation are given by

$$\begin{bmatrix} \alpha'' \\ \phi'' \\ \gamma'' \end{bmatrix} = \begin{bmatrix} N_{11} & N_{12} & N_{13} \\ N_{21} & N_{22} & N_{23} \\ N_{31} & N_{32} & N_{33} \end{bmatrix} \left\{ \begin{bmatrix} F_\alpha \\ F_\phi \\ F_\gamma \end{bmatrix} + \begin{bmatrix} U_\alpha \\ U_\phi \\ U_\gamma \end{bmatrix} \right\} \quad (5.22)$$

where F_α , F_ϕ , and F_γ are the nonlinear terms given by

$$\begin{aligned} F_\alpha &= p_\alpha \cos \phi \cos \gamma + p_\phi \cos \phi \sin \gamma - p_\gamma \sin \gamma \\ F_\phi &= -p_\alpha \sin \gamma + p_\phi \cos \gamma \\ F_\gamma &= p_\gamma \end{aligned} \quad (5.23)$$

The coefficients p_α , p_ϕ , and p_γ in Eq. (5.23) are

$$\begin{aligned} p_\alpha &= [(1 - k_{xz} + k_{yz})(1 + \alpha')\phi' \sin \phi \cos \gamma] - (k_{xz} - k_{yz})(1 + \alpha')^2 \sin \phi \\ &\quad \cos \phi \sin \gamma + (1 + k_{xz} - k_{yz})[(1 + \alpha')\gamma' \cos \phi \sin \gamma + \phi'\gamma' \cos \gamma] \\ &\quad - 3(k_{xz} - k_{yz})(\cos \alpha \sin \phi \sin \gamma - \sin \alpha \cos \gamma) \cos \alpha \cos \phi \end{aligned}$$

$$\begin{aligned}
p_\phi &= [(1 - k_{xz} + k_{yz})(1 + \alpha')\gamma' \sin \phi \sin \gamma] - (1 - k_{xz})(1 + \alpha')^2 \sin \phi \\
&\quad \cos \phi \cos \gamma + (1 - k_{xz} - k_{yz})[(1 + \alpha')\gamma' \cos \phi \cos \gamma - \phi' \gamma' \sin \gamma] \\
&\quad + 3(1 - k_{xz})(\cos \alpha \sin \phi \cos \gamma + \sin \alpha \sin \gamma) \cos \alpha \cos \phi
\end{aligned}$$

$$\begin{aligned}
p_\gamma &= [k_{xz} - (1 - k_{yz}) \cos 2\gamma](1 + \alpha')\phi' \cos \phi - (1 - k_{yz})[(1 + \alpha')^2 \cos^2 \phi \\
&\quad - \phi'^2] \sin \gamma \cos \gamma + 3(1 - k_{yz})(\cos \alpha \sin \phi \cos \gamma + \sin \alpha \sin \gamma) \\
&\quad (\cos \alpha \sin \phi \sin \gamma - \sin \alpha \cos \gamma)
\end{aligned}$$

The elements of the matrix N in Eq. (5.22) are given by

$$\left[\begin{array}{ccc}
\frac{\sin^2 \gamma + k_{yz} \cos^2 \gamma}{k_{yz} \cos^2 \phi} & \frac{(1 - k_{yz}) \sin \gamma \cos \gamma}{k_{yz} \cos \phi} & \frac{\sin \phi (\sin^2 \gamma + k_{yz} \cos^2 \gamma)}{k_{yz} \cos^2 \phi} \\
\frac{(1 - k_{yz}) \sin \gamma \cos \gamma}{k_{yz} \cos \phi} & \frac{\cos^2 \gamma + k_{yz} \sin^2 \gamma}{k_{yz}} & \frac{(1 - k_{yz}) \sin \gamma \cos \gamma \sin \phi}{k_{yz} \cos \phi} \\
\frac{\sin \phi (\sin^2 \gamma + k_{yz} \cos^2 \gamma)}{k_{yz} \cos^2 \phi} & \frac{(1 - k_{yz}) \sin \gamma \cos \gamma \sin \phi}{k_{yz} \cos \phi} & \frac{\sin^2 \phi (\sin^2 \gamma + k_{yz} \cos^2 \gamma)}{k_{yz} \cos^2 \phi} + \frac{1}{k_{xz}}
\end{array} \right]$$

5.1.4 Underactuated Rigid Spacecraft Model

The nonlinear rigid spacecraft model given by Eq. (5.22) assumes that the spacecraft is actively controlled with a sufficient number of actuators equal to the degrees of freedom of the system. In this case, 3 pairs of gas jet thrusters are placed on each principal axis of the spacecraft. For $U \in \mathbb{R}^3 = [U_j]$, $j = \alpha, \phi, \gamma$, failure of the j -th axis actuation occurs when $U_j = 0$. Our objective is to devise a control law for 3-axis attitude stabilization under single-axis actuation failure (either yaw or roll).

Let the state vector of the system be $X \in \mathbb{R}^{6 \times 1} = [\alpha, \alpha', \phi, \phi', \gamma, \gamma']^T$. The state vector can be split into two parts as $X = [x_1, x_2]^T$ where x_1 and x_2 represents the unactuated and actuated states, respectively. The unactuated states can be further transformed to $x_1 = [x_{10}, x_{11}]^T$, where $x_{10} \in \mathbb{R}^{3 \times 1} = [\alpha, \phi, \gamma]^T$ always. Based on the axis of failure, the nonlinear equation of motion in Eq. (5.22) can be transformed to

$$\begin{bmatrix} x_{11}' \\ x_2' \end{bmatrix} = \begin{bmatrix} \bar{A}_{11} & \bar{A}_{12} \\ \bar{A}_{21} & \bar{A}_{22} \end{bmatrix} \left\{ \begin{bmatrix} F_1 \\ F_2 \end{bmatrix} + \begin{bmatrix} 0 \\ U_{ua} \end{bmatrix} + \begin{bmatrix} d_1 \\ d_2 \end{bmatrix} \right\} \quad (5.24)$$

We now consider the cases of actuation failure to specify state x_{11} as follows:

Case I : ($U_\phi = 0$) No control authority on *roll*-axis (ϕ) and full control actuation available on *pitch* (α) and *yaw* (γ) axes. For this case $x_{11} = \phi'$, $x_2 = [\alpha', \gamma']$, and $U_{ua} \in \mathbb{R}^{2 \times 1} = [U_\alpha, U_\gamma]^T$. Similarly, $F(q, q') = [F_1, F_2]^T$ where $F_1 = F_\phi$ and $F_2 = [F_\alpha, F_\gamma]^T$.

$$\bar{A}_{11} = N_{22}; \quad \bar{A}_{12} = \begin{bmatrix} N_{21} & N_{23} \end{bmatrix}; \quad \bar{A}_{21} = \bar{A}_{12}^T; \quad \bar{A}_{22} = \begin{bmatrix} N_{11} & N_{13} \\ N_{31} & N_{33} \end{bmatrix} \quad (5.25)$$

Case II : ($U_\gamma = 0$) No control authority on *yaw*-axis (γ) and full control actuation available on *pitch* (α) and *roll* (ϕ) axes. For this case $x_{11} = \gamma'$, $x_2 = [\alpha', \phi']$, and $U_{ua} \in \mathbb{R}^{2 \times 1} = [U_\alpha, U_\phi]^T$. Similarly, $F(q, q') = [F_1, F_2]^T$ where $F_1 = F_\gamma$ and $F_2 = [F_\alpha, F_\phi]^T$.

$$\bar{A}_{11} = N_{33}; \quad \bar{A}_{12} = \begin{bmatrix} N_{31} & N_{32} \end{bmatrix}; \quad \bar{A}_{21} = \bar{A}_{12}^T; \quad \bar{A}_{22} = \begin{bmatrix} N_{11} & N_{12} \\ N_{21} & N_{22} \end{bmatrix} \quad (5.26)$$

In both cases considered above, thrusters are body-fixed to the spacecraft to perform attitude maneuvers. A pair of thrusters are placed on the z -axis for pitch motion control, and depending on the considered axis of failure, either a pair of thrusters on y -axis for roll control or a pair of thrusters on x -axis for yaw control, are active.

5.2 Design of Control Laws

In this section we present the theoretical basis for developing nonlinear control algorithms for the rigid body spacecraft mathematical model. First, we develop a control law for a rigid spacecraft equipped with 3 pairs of thrusters that can provide torque about all three body-axes of the spacecraft. Then, we propose a control algorithm to stabilize the spacecraft attitude using control torques supplied by only two pairs of thrusters.

5.2.1 Proposed Control Law for Fully Actuated Spacecraft

We first consider the case where the spacecraft is fully actuated with complete control authority on its pitch, roll, and yaw axes. SMC design starts with building a sliding surface in the system state space. The motion of the system along the *sliding mode* is expected

to meet the control requirements with desired robustness to bounded disturbances and parametric uncertainties. For the fully actuated case, we utilize the vector containing the generalized coordinates ($q \in \mathbb{R}^{3 \times 1} = [\alpha, \phi, \gamma]^T$) and its first derivatives to design a linear sliding surface S_c given by,

$$S_c = q' + \Lambda q \quad (5.27)$$

The sliding surface S_c is a 3 dimensional manifold, $S_c \in \mathbb{R}^{3 \times 1}$, where $\Lambda \in \mathbb{R}^{3 \times 3}$ is a constant gain matrix,

$$\Lambda = \begin{bmatrix} \Lambda_\alpha & 0 & 0 \\ 0 & \Lambda_\phi & 0 \\ 0 & 0 & \Lambda_\gamma \end{bmatrix} \quad (5.28)$$

The basic idea is to alter the system dynamics along the sliding surface such that the trajectory of the system is steered onto the sliding manifold described by $S_c = 0$. Next, we derive the control laws based on Lyapounov stability theorem. The Lyapunov energy function can be defined as follows:

$$V = \frac{1}{2} S_c^T S_c \quad (5.29)$$

Taking the first derivative of V and substituting Eq. (5.19) gives,

$$\begin{aligned} V' &= S_c^T S_c' = S_c^T \{q'' + \Lambda q'\} \\ &= S_c^T \{N(q)[F(q, q') + U_{fa}] + \Lambda q'\} \end{aligned} \quad (5.30)$$

Let $N[F + U_{fa}] + \Lambda q' = -\eta_c \text{sat}(S_c)$, where $\eta_c \in \mathbb{R}^{3 \times 3} = \text{diag}\{\eta_{c\alpha}, \eta_{c\phi}, \eta_{c\gamma}\}$ for all $\{\eta_{ci} : \eta_{ci} > 0\}$, and $\text{sat}(S_c) = [\text{sat}(S_{c\alpha}), \text{sat}(S_{c\phi}), \text{sat}(S_{c\gamma})]^T$. The saturation function is used to suppress the control chatter. The control law for the fully actuated case can be defined as,

$$U_{fa} = -N(q)^{-1} \{\eta_c \text{sat}(S_c) + \Lambda q'\} - F(q, q') \quad (5.31)$$

The control law given by Eq. (5.31) can be substituted in Eq. (5.30) to get

$$\begin{aligned} V' &= S_c^T [-\eta_c \text{sat}(S_c)] \\ &\leq -\sum \eta_{ci} |S_{ci}| < 0 \quad \text{for } i = \alpha, \phi, \gamma \end{aligned} \quad (5.32)$$

This proves that V' is negative-definite. Therefore, V is a non-increasing Lyapunov function in the S -space. This implies that as $t \rightarrow \infty$, $V(t) = V_\infty$. Thus, we can establish that

$S_c \in \mathfrak{L}_\infty$. Based on the inequality that $\sum |S_{ci}| \geq \|S_c\|$ and defining $\lambda_{min}(\eta_c)$ as the minimum eigenvalue of the positive-definite matrix η_c ,

$$V' \leq \lambda_{min}(\eta_c)\|S_c\| \quad (5.33)$$

Integrating both sides of Eq. (5.34) yields

$$\begin{aligned} \int_0^\infty V'(t) dt &\leq - \int_0^\infty \lambda_{min}(\eta_c)\|S_c\| dt \\ V(t) &\leq V(0) - \int_0^\infty \lambda_{min}(\eta_c)\|S_c\| dt < \infty \end{aligned} \quad (5.34)$$

Therefore, from Eq. (5.34) we obtain that $S_c \in \mathfrak{L}_2$. According to the proven condition from Eq. (5.32) we have $V' < \infty$ from which we can deduce the fact that $S'_c \in \mathfrak{L}_\infty$. Now, using Barbalat's lemma [Slotine & Li 1991a] it can be shown that $S_c \rightarrow 0$ as $t \rightarrow \infty$. When the desired control torque in Eq. (5.31) is implemented the spacecraft trajectory converges to the sliding manifold ($S_c = 0$) and since the spacecraft attitude motion is stable on the sliding manifold, its trajectory converges to equilibrium ($q, q' \rightarrow 0$ as $t \rightarrow \infty$). Hence, for all initial conditions $q(0)$ and $q'(0)$, the control law in in Eq. (5.31) drives the system trajectories to the origin.

5.2.2 Sliding Mode Control for Underactuated Spacecraft

The conventional SMC law derived in the previous section assume that the spacecraft is actively controlled with a sufficient number of actuators equal to the degrees of freedom of the system. In terms of robustness, the conventional SMC law has a major disadvantage because the sliding system is sensitive to unmatched uncertainties and disturbances due to unexpected actuator failure which will directly affect the dynamic performance.

In this section we present some new results for 3-axis spacecraft attitude stabilization in the case of a single actuator failure. We develop a control algorithm which guarantees asymptotic stability of the zero equilibrium state of the Lagrange's equations under a maximum of one actuator failure. The design approach to be adopted involves a two stage process. The first stage requires the design of a sliding manifold S_u which guarantees the

desired dynamic behavior for the nominal system [Eq. (5.24)] in the presence of uncertainties and disturbances. The second stage is concerned with the development of a control strategy that can steer the system to the sliding surface and maintain it there.

5.2.2.1 Design of Sliding Manifold

To facilitate the design of a linear sliding surface and examine its properties, the nonlinear equations of motion of the spacecraft is linearized about its equilibrium state and represented in canonical form. From the Lagrange equations of motion described by Eq. (5.22), we get the equilibrium state vector $X_e = 0$, i.e., $(\alpha_e = \phi_e = \gamma_e = \alpha_e' = \phi_e' = \gamma_e' = 0)$. Considering first order approximation for the system state, we have the linearized equations of motion in state space form as follows [Wie 1998]:

$$X' = AX + BU \quad (5.35)$$

where $X \in \mathbb{R}^{6 \times 1} = [\alpha, \alpha', \phi, \phi', \gamma, \gamma']^T$, and the matrices $A \in \mathbb{R}^{6 \times 6}$, $B \in \mathbb{R}^{6 \times 3}$ are described in Eq. (5.36) with $k_1 = (I_z - I_x)/I_y$ and $k_2 = (I_z - I_y)/I_x$.

$$A = \begin{bmatrix} 0 & 1 & 0 & 0 & 0 & 0 \\ 3 \frac{k_2 - k_1}{1 - k_1 k_2} & 0 & 0 & 0 & 0 & 0 \\ 0 & 0 & 0 & 1 & 0 & 0 \\ 0 & 0 & -4k_1 & 0 & 0 & k_1 - 1 \\ 0 & 0 & 0 & 0 & 0 & 1 \\ 0 & 0 & 0 & 1 - k_2 & -k_2 & 0 \end{bmatrix}, \quad B = \begin{bmatrix} 0 & 0 & 0 \\ b_1 & 0 & 0 \\ 0 & 0 & 0 \\ 0 & b_2 & 0 \\ 0 & 0 & 0 \\ 0 & 0 & b_3 \end{bmatrix} \quad (5.36)$$

When all actuators are healthy, $b_1, b_2, b_3 = 1$, the controllability matrix $C = [B:AB:\dots:A^5B]$ is of rank 6. The matrix pair (A, B) defining the nominal linear system is also fully state controllable when $b_2 = 0$ (i.e. $b_1 = 1$ and $b_3 = 1$) or $b_3 = 0$ (i.e. $b_1 = 1$ and $b_2 = 1$). Therefore, the linear system is controllable even if the actuation on the *roll*-axis (ϕ) or the *yaw*-axis (γ) fails. If no actuation is available for the decoupled pitch dynamics ($b_1 = 0$), then the system is not fully state controllable. The linear system represented in terms of new coordinates $x_1 \in \mathbb{R}^4$ and $x_2 \in \mathbb{R}^2$, is given by

$$\begin{bmatrix} x_1' \\ x_2' \end{bmatrix} = \begin{bmatrix} A_{11} & A_{12} \\ A_{21} & A_{22} \end{bmatrix} \begin{bmatrix} x_1 \\ x_2 \end{bmatrix} + \begin{bmatrix} 0 \\ B_2 \end{bmatrix} U \quad (5.37)$$

This representation separates the actuated and unactuated states based on the failed axis (roll or yaw). By exploiting the coupling between the directly actuated and unactuated states, we define the sliding surface, S_u as a linear combination of the states.

$$S_u = \{x_1 \in \mathbb{R}^{4 \times 1}, x_2 \in \mathbb{R}^{2 \times 1} : \Lambda_1 x_1 + \Lambda_2 x_2 = 0\} \quad (5.38)$$

where $\Lambda_1 \in \mathbb{R}^{2 \times 4}$ and $\Lambda_2 \in \mathbb{R}^{2 \times 2}$ are weights on the states x_1 and x_2 respectively. When the system reaches the sliding surface, $S_u = 0 \forall t > t_r$, where t_r is the reaching time after which sliding motion starts,

$$x_2 = -\Lambda_2^{-1} \Lambda_1 x_1 \quad (5.39)$$

It is important to note that Eq. (5.39) holds only on the sliding surface and substituting this relation to the reduced order system in Eq. (5.37) gives

$$x_1' = (A_{11} - A_{12}K)x_1 \quad (5.40)$$

where $K = \Lambda_2^{-1} \Lambda_1 = [K_1 \ K_2]$ such that:

$$K_1 \in \mathbb{R}^{2 \times 3} = \begin{bmatrix} K_{11} & K_{12} & K_{13} \\ K_{21} & K_{22} & K_{23} \end{bmatrix} \quad \text{and} \quad K_2 \in \mathbb{R}^{2 \times 1} = \begin{bmatrix} K_{14} \\ K_{24} \end{bmatrix} \quad (5.41)$$

During an ideal sliding mode behavior, x_2 can be considered as a control signal to stabilize x_1 . Therefore, the choice of sliding surface clearly affects the dynamics of the reduced order system through the selection of weighting matrix K .

$$S_u = \{x_1 \in \mathbb{R}^{4 \times 1}, x_2 \in \mathbb{R}^{2 \times 1} : x_2 + Kx_1 = 0\} \quad (5.42)$$

Remark 5.1: The weighting matrix K prescribes a desired closed loop behavior of the system [Eq. (5.40)] and can be determined using any *classical* approaches that provides a state feedback controller for systems represented in state-space form. Since (A, B) is, by definition a controllable pair it follows directly that (A_{11}, A_{12}) is also controllable.

5.2.2.2 Nonlinear Control Formulation

The design of a suitable control algorithm that can steer the system trajectories to the sliding manifold is the second phase of any VSC design procedure. Our objective is to

improve the transient performance of the system by employing a continuous, nonlinear control algorithm that can reduce the reaching phase and maintain the attitude orientation of the spacecraft on the sliding surface. The effects of both matched and unmatched uncertainties are pertinent when the motion is not constrained to the sliding surface.

The developed control algorithm must be capable of achieving fast and accurate response in the presence of bounded disturbances and parametric uncertainties. With no control authority available in the roll or yaw axis, achieving precision attitude control becomes a difficult task in the presence of inherent model nonlinearities (depending on attitude trajectory and physical parameters), moment of inertia uncertainties, and external disturbances (changing with respect to operating conditions).

One approach is to introduce robustness against bounded uncertainties and disturbances by extracting its core information using a known upper-bound in the controller design. The external disturbance is related to gravity-gradient torque, solar radiation pressure, magnetic forces, and aerodynamic drag (all could be assumed bounded). Therefore, the lumped term containing the nonlinearities, uncertainties, and disturbances is given by

$$\xi(x_1, x_2) = [\bar{A}_{21} + K_2 \bar{A}_{11}] [F_1 + d_1] + [\bar{A}_{22} + K_2 \bar{A}_{12}] [F_2 + d_2] + K_1 x_{10}' \quad (5.43)$$

A feasible and practical control scheme should not be designed by including the term $\xi(x_1, x_2)$ directly. One way to account for this in the controller is to assume that the lumped disturbances are bounded and then use the upper bound in the control algorithm design.

$$\|\xi(q, q', q'')\| \leq \rho_1 + \rho_2 \|x_1\| + \rho_3 \|x_2\| = \varphi_3 \quad (5.44)$$

In order to ensure that the sliding manifold is reached and sliding on the manifold occurs, the continuous nonlinear control law is chosen as

$$U_{ua} = -(\bar{A}_{22} + K_2 \bar{A}_{12})^{-1} \left[\eta \frac{\varphi_2 S_u}{\|S_u\| + \delta} \right] \quad (5.45)$$

where δ is a small positive scalar specifying the boundary layer thickness that will eliminate chatter if appropriately chosen so that the unmodeled high frequency dynamics are not excited [Edwards & Spurgeon 1998]. This choice has no effect on the closed-loop trajectories, except when sliding along the sliding surface S_u , in which case details of the dead-band

will strongly influence the high frequency chatter in the control input. The scalar function η depends on the magnitude of the disturbances and uncertainties,

$$\eta = \frac{\varphi_1}{\varphi_2}(\varphi_3 + \varphi_4) \quad (5.46)$$

for some positive constants φ_1 , φ_2 , φ_3 , and φ_4 . The steps involved in adequately determining these nonnegative constants are detailed in the next section.

5.2.2.3 Stability Analysis

In this sub-section we present stability conditions for the spacecraft attitude motion focussing primarily on robustness against disturbances. First, we show that the control law, Eq. (5.45), is capable of driving the closed-loop trajectory of the system towards a boundary layer on the sliding surface in finite time. Once the sliding surface is reached, the system enters into the sliding regime. Then, we show that the sliding mode is robust to unmatched disturbances and uncertainties that mainly affects the unactuated states.

Theorem 5.1: *For the underactuated spacecraft mathematical model in Eq. (5.24) if, the sliding manifold is chosen as Eq. (5.42), the control law is defined as Eq. (5.45), and the bounds on the external disturbances, parameter uncertainties, and system nonlinearities are assumed to be governed by Eq. (5.44), then the closed-loop trajectories of the system will converge in finite time to a neighborhood area of the equilibrium set \mathfrak{F} .*

$$\mathfrak{F} \triangleq \left[S_u : \|S_u\| \leq \frac{\delta}{\varphi_1 - 1} \right] \quad (5.47)$$

Proof: Consider the Lyapunov function

$$V(S_u) = \frac{1}{2} S_u^T S_u \quad (5.48)$$

Taking the first derivative of $V(S_u)$ along the trajectory of the closed-loop system,

$$V'(S_u) = S_u^T S_u' = S_u^T [x_2' + K_1 x_{10}' + K_2 x_{11}'] \quad (5.49)$$

Substituting the mathematical model, Eq. (5.24), and the control law, Eq. (5.45), we get

$$\begin{aligned} V'(S_u) &= S_u^T [(\bar{A}_{21} + K_2 \bar{A}_{11}) (F_1 + d_1) + (\bar{A}_{22} + K_2 \bar{A}_{12}) (F_2 + d_2 + U_{ua}) + K_1 x_{10}'] \\ &= S_u^T \left[-\eta \frac{\varphi_2 S_u}{\|S_u\| + \delta} + \xi(x_1, x_2) \right] \end{aligned} \quad (5.50)$$

Using the property defined based on Eq. (5.44) and expressing φ_3 in terms of η , φ_1 , φ_2 , and φ_4 from Eq. (5.46), we get

$$\begin{aligned}
V'(S_u) &\leq \|S_u\| \left[-\eta \frac{\varphi_2 \|S_u\|}{\|S_u\| + \delta} + \|\xi\| \right] \\
&\leq \|S_u\| \left[-\eta \frac{\varphi_2 \|S_u\|}{\|S_u\| + \delta} + \varphi_3 \right] \\
&\leq \|S_u\| \left[-\eta \frac{\varphi_2 \|S_u\|}{\|S_u\| + \delta} - \frac{\eta \varphi_2}{\varphi_1} + \varphi_4 \right] \\
&\leq -\varphi_4 \|S_u\| - \eta \varphi_2 \|S_u\| \left[\frac{\|S_u\|}{\|S_u\| + \delta} - \frac{1}{\varphi_1} \right]
\end{aligned} \tag{5.51}$$

It is readily obtained from Eq. (5.51) that, if:

$$\begin{aligned}
\frac{\|S_u\|}{\|S_u\| + \delta} - \frac{1}{\varphi_1} &\geq 0 \\
\|S_u\| &\geq \frac{\delta}{\varphi_1 - 1}
\end{aligned} \tag{5.52}$$

then $V'(S_u) < 0$ when S_u is outside of the set

$$\mathfrak{F} \triangleq \left[S_u : \|S_u\| \leq \frac{\delta}{\varphi_1 - 1} \right] \tag{5.53}$$

The condition in Eq. (5.52) is only satisfied if

$$V(S_u) > \frac{1}{2} \left(\frac{\delta}{\varphi_1 - 1} \right)^2 = \varepsilon_1 \tag{5.54}$$

Based on the second line Eq. (5.51), where $\frac{\|S_u\|}{\|S_u\| + \delta} \leq 1$ ($\forall \delta \geq 0$), a condition for selecting the gain φ_3 in relation to φ_1 and φ_4 , can be derived such that:

$$\begin{aligned}
\eta \varphi_2 - \varphi_3 &> 0 \\
\varphi_1 &> \frac{\varphi_3}{\varphi_3 + \varphi_4}
\end{aligned} \tag{5.55}$$

Using this fact it can be shown that $V'(S_u) \leq -\varepsilon_2 \sqrt{2V(S_u)}$ for some $\varepsilon_2 > 0$. This implies that the sliding boundary layer is reached in finite time. For the case where a small (δ) is chosen, then every solution will eventually enter the set $\mathfrak{F} = \{S_u : V(S_u) \leq \varepsilon_1\}$. \square

The control law in Eq. (5.45) forces the solutions of the system towards a boundary layer on the sliding surface, S_u , where the behavior of the system is dominated by lower-order dynamics. Ideally, when in the sliding mode the system is completely insensitive to

disturbances and uncertainties acting within the channels implicit in the control inputs. However, the linear system in Eq. (5.37) clearly indicates that unmatched disturbances and uncertainties will affect the motion of unactuated states x_1 . Therefore, it is important to evaluate the properties of the spacecraft motion constrained to S_u . The linear system can be expressed in the general form as

$$\begin{aligned}x_1' &= A_{11}x_1 + A_{12}x_2 + D_1 \\x_2' &= A_{21}x_1 + A_{22}x_2 + B_2U + d_2\end{aligned}\tag{5.56}$$

where $x_1 \in \mathbb{R}^{4 \times 1}$ and $x_2 \in \mathbb{R}^{2 \times 1}$ are the actuated and unactuated states, respectively, $A_{11} \in \mathbb{R}^{4 \times 4}$, $A_{12} \in \mathbb{R}^{4 \times 2}$, $A_{21} \in \mathbb{R}^{2 \times 4}$, $A_{22} \in \mathbb{R}^{2 \times 2}$, $B_2 \in \mathbb{R}^{2 \times 2}$, $U \in \mathbb{R}^{2 \times 1}$ is the control input, $D_1 \in \mathbb{R}^{4 \times 1} = [0, 0, 0, d_1]^T$ and $d_2 \in \mathbb{R}^{2 \times 1} = [d_{21}, d_{22}]^T$ are the unmatched and matched components of nonlinear uncertainties and disturbances.

We now study the effect of unmatched component (D_1) of the disturbances when the dynamics of the system represents the dynamics of an ideal sliding mode. For convenience we set $\delta = 0$. To determine the spacecraft dynamics on the sliding surface, we can solve $S_u = 0$ for x_2 using Eq. (5.42) which yields $x_2 = -Kx_1$. We have shown in Theorem 5.1 that a control law exists such that the spacecraft motion can be constrained to S_u . This result can be substituted into Eq. (5.56) to obtain the following reduced order system

$$x_1' = (A_{11} - A_{12}K)x_1 + D_1\tag{5.57}$$

Let $A_c = A_{11} - A_{12}K$. We can ensure that A_c is a stable matrix with eigenvalues containing negative real parts by appropriately choosing K . For asymptotic stability we require that, if P and Q are positive definite matrices, then the solution to the Lyapunov equation [Eq. (5.58)] will exist because the matrix A_c is stable.

$$PA_c + A_c^T P = -Q\tag{5.58}$$

Theorem 5.2: *For the motion constrained to the sliding surface, the trajectory of the reduced order system [Eq. (5.57)] starting from any initial condition will enter a compact set containing the origin in finite time and the states will be uniformly ultimately bounded with respect to the ellipsoid*

$$\mathfrak{S} = \left\{ x_1 : \|x_1\| \leq 2 \frac{\sup_{D_1 \in \varepsilon_3} \|PD_1\|}{\lambda_{\min}(Q)} \right\}\tag{5.59}$$

Proof: Consider the Lyapunov function

$$V(x_1) = x_1^T P x_1 \quad (5.60)$$

The first derivative of $V(x_1)$ along the motion of Eq. (5.57) is given by

$$V'(x_1) = x_1^T (P A_c + A_c^T P) x_1 + 2x_1^T P D_1 = -x_1^T Q x_1 + 2x_1^T P D_1 \quad (5.61)$$

Using the Rayleigh principle we know that

$$\lambda_{\min}(Q) \|x_1\|^2 \leq x_1^T Q x_1 \leq \lambda_{\max} \|x_1\|^2 \quad (5.62)$$

In particular, if $\lambda_{\min}(Q) \geq 0$ then it follows that $x_1^T Q x_1 \geq 0$ for all x_1 . Based on these conditions, Eq. (5.61) can be expressed as

$$\begin{aligned} V'(x_1) &\leq -\lambda_{\min}(Q) \|x_1\|^2 + 2 \|x_1\| \cdot \|P D_1\| \\ &\leq -(\lambda_{\min}(Q) \|x_1\| - 2 \|P D_1\|) \|x_1\| \end{aligned} \quad (5.63)$$

It is clearly evident from Eq. (5.63) that $V'(x_1) < 0$ when x_1 is outside of the set

$$\mathfrak{S} \triangleq \left\{ x_1 : \|x_1\| \leq 2 \frac{\sup_{D_1 \in \varepsilon_3} \|P D_1\|}{\lambda_{\min}(Q)} \right\} \quad (5.64)$$

Analytical estimate of $\lambda_{\min}(Q)$ is not required for numerical simulations because the proposed control law is independent of this parameter. For every $x_1(t_0) \in \mathfrak{S}$ then $x_1(t) \in \mathfrak{S}$ for all $t \geq t_0$. Since $V'(x_1) < 0$, it also follows that if $x_1(t_0) \notin \mathfrak{S}$ then the trajectory will reach \mathfrak{S} in finite time t_r [Spurgeon & Davies 1993]. The system is therefore uniformly ultimately bounded with respect to the ellipsoid \mathfrak{S} . Explicit consideration of the actuated states (x_2) is not required because it is a well known fact that when in the sliding mode the system is totally insensitive to matched disturbances. This completes the proof. \square

Remark 5.2: The Euler angles γ , ϕ , and α are limited to the ranges $-\pi < \gamma < \pi$, $-\frac{\pi}{2} < \phi < \frac{\pi}{2}$, and $-\pi < \alpha < \pi$. Any initial condition that avoids singularities due to $\phi = \pm \frac{\pi}{2}$, Theorem 2 guarantees that a singularity is not subsequently encountered. Since $x_1 = [\alpha, \phi, \gamma, (\gamma' \text{ or } \phi')]^T$, it has been shown by condition in Eq. (5.63) that any initial condition that avoids the singularity in $\phi = \pm \frac{\pi}{2}$ will eventually converge to a neighborhood area of the equilibrium set \mathfrak{S} .

5.3 Performance Evaluation

To study the effectiveness and performance of the proposed nonlinear control strategies for underactuated spacecraft, the detailed response of the system is numerically simulated using the set of governing equations of motion [Eq. (5.24)] in conjunction with the proposed control law [Eq. (5.45)]. The integration is carried out using the International Mathematical and Statistical Library (IMSL) routine DDASPG based on Petzoid-Gear BDF method [IMS 1997]. The system and orbital parameters for the spacecraft along with the initial conditions used in the numerical simulations are shown in Table 5.1. Unless otherwise stated explicitly, all numerical simulations are based on the parameters stated in Table 5.1 without considering the product of inertia terms, $I_{xy} = I_{xz} = I_{yz} = 0$, in the mass moment of inertia matrix of the spacecraft.

Table 5.1: Underactuated spacecraft - Simulation parameters

Parameters	Values
Orbit	
r_p (km)	6878
μ_e (km ³ s ⁻²)	398600
Spacecraft MOI	
I_{xx} (kg m ²)	15
I_{yy} (kg m ²)	17
I_{zz} (kg m ²)	20
Initial Conditions	
$[\alpha_0, \phi_0, \gamma_0]$	$[80^\circ, -40^\circ, 40^\circ]$
$[\alpha_0', \phi_0', \gamma_0']$	$[0.001, 0.001, 0.001]$

Based on values of the spacecraft moment of inertia we can calculate nondimensional parameters $k_1 = (I_z - I_x)/I_y = 0.3$ and $k_2 = (I_z - I_y)/I_x = 0.2$. These ratios are considered for the design of control algorithms. Any change in the moment of inertia of the spacecraft is unknown to the controller. The control gains (φ_i) and the boundary layer (δ) used in all simulations for Cases I and II are shown in Table 5.2.

Table 5.2: Controller parameters used for numerical analysis

Control Gains	Case I	Case II
$[\varphi_1, \varphi_2, \varphi_3, \varphi_4]$	[0.40, 0.60, 1.50, 0.40]	[0.15, 0.40, 2.00, 0.15]
$[K_{11}, K_{12}, K_{13}, K_{14}]$	[4, 0, 0, 0]	[0.5, 0, 0, 0]
$[K_{21}, K_{22}, K_{23}, K_{24}]$	[0, -2, 2, -1]	[0, 2, 2, 1]
δ	0.0001	0.0001

It is important to note that the universal gain (η) is calculated based on all φ_i using the formula given by Eq. (5.46). The sliding plane is given by $S_u = x_2 + K x_1$, where $K = [K_1, K_2]$ is determined using LQR applied to the reduced order system in Eq. (5.40). K can be considered as a 'pseudo' feedback matrix that prescribes the required performance of the reduced order system (A_{11}, A_{12}).

Case I: For no actuation available on roll (ϕ) axis, the closed-loop eigenvalues of the reduced order system $[A_{11} - A_{12}K]$ based on values of K in Table 5.2, are:

$$\lambda_{1,2} = -0.4 \pm 1.0i; \quad \lambda_3 = -2; \quad \lambda_4 = -4 \quad (5.65)$$

Case II: For no actuation available on yaw (γ) axis, the closed-loop eigenvalues of the reduced order system $[A_{11} - A_{12}K]$ based on values of K in Table 5.2, are:

$$\lambda_{1,2} = -0.4 \pm 0.2i; \quad \lambda_3 = -2; \quad \lambda_4 = -4 \quad (5.66)$$

Clearly, from Eqs. (5.65) and (5.66), we can observe that the sliding manifold designed using K in Table 5.2 leads to stable dynamics for the unactuated states once the sliding manifold is reached. The reaching condition is ensured using the control input given by Eq. (5.45) as stated in Theorem 5.1.

First, we present the effectiveness of the proposed control strategy in stabilizing the spacecraft attitude by comparing the results with a fully actuated controller [Eq. (5.31)]. We then examine the effects of variations in spacecraft mass moment of inertia, orbit eccentricity, and external disturbances.

5.3.1 Nominal Performance

We first study the attitude motion of the spacecraft orbiting in a circular orbit (i.e. $e = 0$). Figure 5.2 shows the attitude response of the spacecraft in the presence of initial attitude disturbances (Table 5.1) for Case I when the control laws given by Eqs. (5.31) and (5.45) are used to stabilize the system.

The nonnegative constants in the control law for the fully actuated system are chosen as $\Lambda_\alpha = \Lambda_\phi = \Lambda_\gamma = 4$ and $\eta_c = 0.01$. With no control authority available on the ϕ -axis, a control algorithm specifically designed for a full actuated spacecraft fails to stabilize the *roll* motion. The proposed control law for the underactuated system [Eq. (5.45)] successfully stabilizes 3-axis attitude of the spacecraft using only two control torques (U_α and U_γ). The driving control torque required for 3-axis stabilization is also presented in Fig. 5.2. The corresponding plots of sliding surfaces and angular velocity are given in Fig. 5.3.

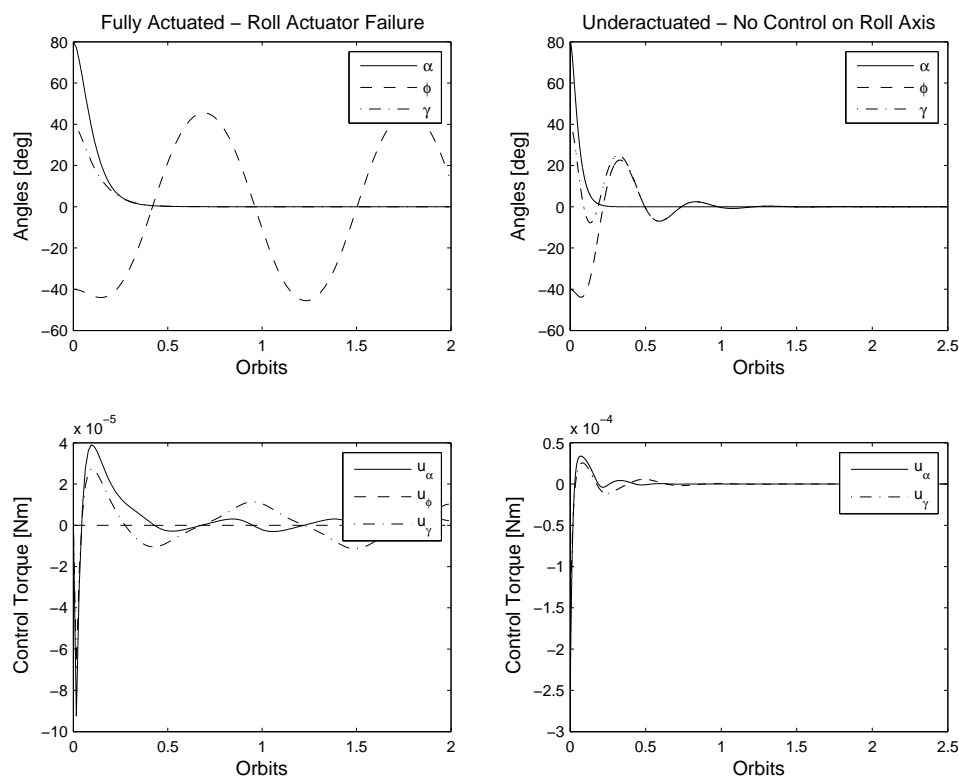


Figure 5.2: Comparison between the performance of the conventional control algorithm and the proposed controller for case I.

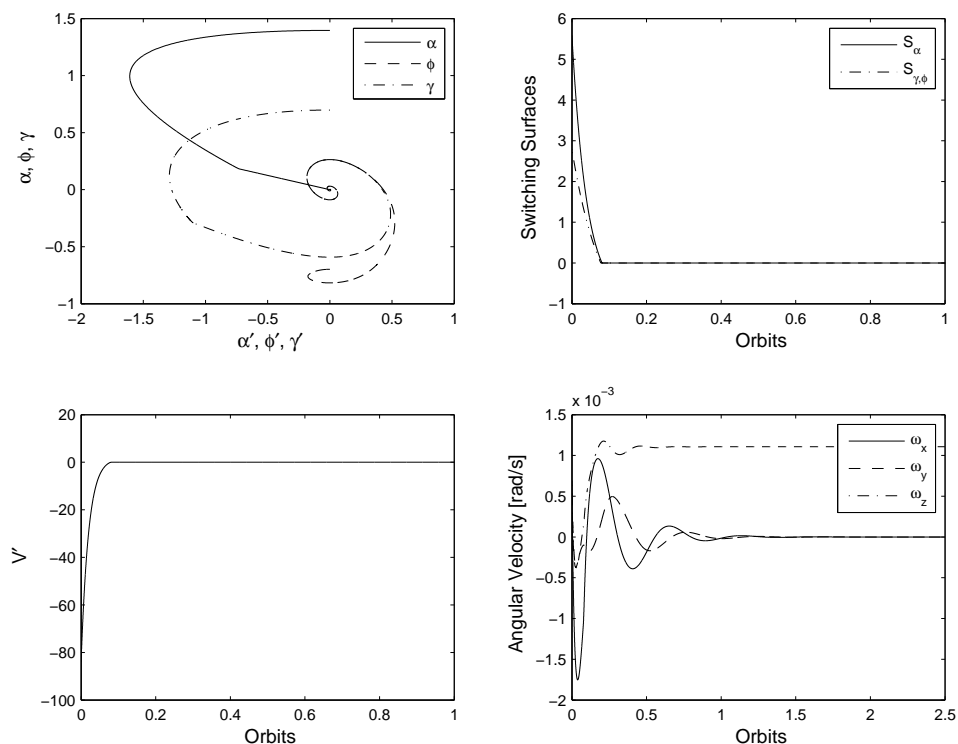


Figure 5.3: State space trajectories, sliding surfaces, Lyapunov derivative, and angular velocities for case I.

With no external disturbances acting on the spacecraft, motion of the system reaches the sliding surface $S_u = 0$ in finite time which can be analytically determined using

$$t_r \leq \frac{\|S_u(t_0)\|}{2\pi\eta} \text{ orbits} \leq 0.5 \text{ orbit} \quad (5.67)$$

where $\eta = 1.3$ from Table 5.2. The angular velocity of the spacecraft is stabilized to $\omega_x = \omega_y = 0$ and $\omega_z = 0.0011$ rad/s. According to the coordinate frames selected as shown in Fig. 5.1 the spacecraft z -axis is normal to the orbit plane and therefore ω_z would be equal to the orbital rate (when $e = 0$).

Next, we consider the case where there is no actuation available on the yaw axis (Case II). It is clearly evident in Fig. 5.4 that the control algorithm given by Eq. (5.31) fails to stabilize the yaw motion of the spacecraft with $U_\gamma = 0$. The reason for uncontrollable rotation of the spacecraft about its x -axis can be analytically determined from the zero-dynamics of the yaw equation of motion. When $\alpha = \alpha' = \phi = \phi' = 0$ the yaw

equation of motion is given by

$$\gamma'' + k_2 \sin \gamma \cos \gamma = 0 \tag{5.68}$$

where $k_2 = (I_z - I_y)/I_x$. From the solution of Eq. (5.68) and taking γ_0 and γ_0' as the initial values, the minimum value of γ' is given by

$$\gamma'_{min} = \sqrt{\gamma_0'^2 + k_2 \sin^2 \gamma_0 - k_2} \tag{5.69}$$

Therefore, the initial spin rate to avoid uncontrolled motion of the spacecraft about the x -axis can be obtained from Eq. (5.69) as

$$\gamma_0' < |\cos \gamma_0| \sqrt{k_2} \tag{5.70}$$

With respect to the uncontrollable motion of γ in Fig. 5.4, determining the spin rate (γ') at the time when *pitch* and *roll* axes stabilize, helps us verify that $\gamma' > |\cos \gamma_0| \sqrt{k_2}$. Therefore,

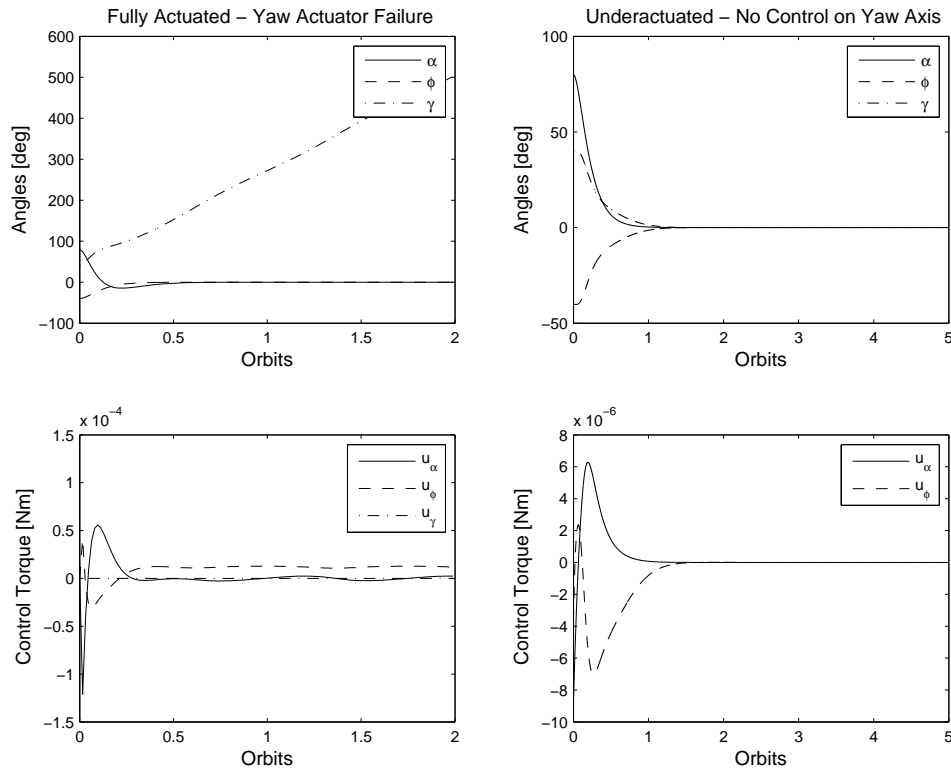


Figure 5.4: Comparison between the performance of the conventional control algorithm and the proposed controller for case II.

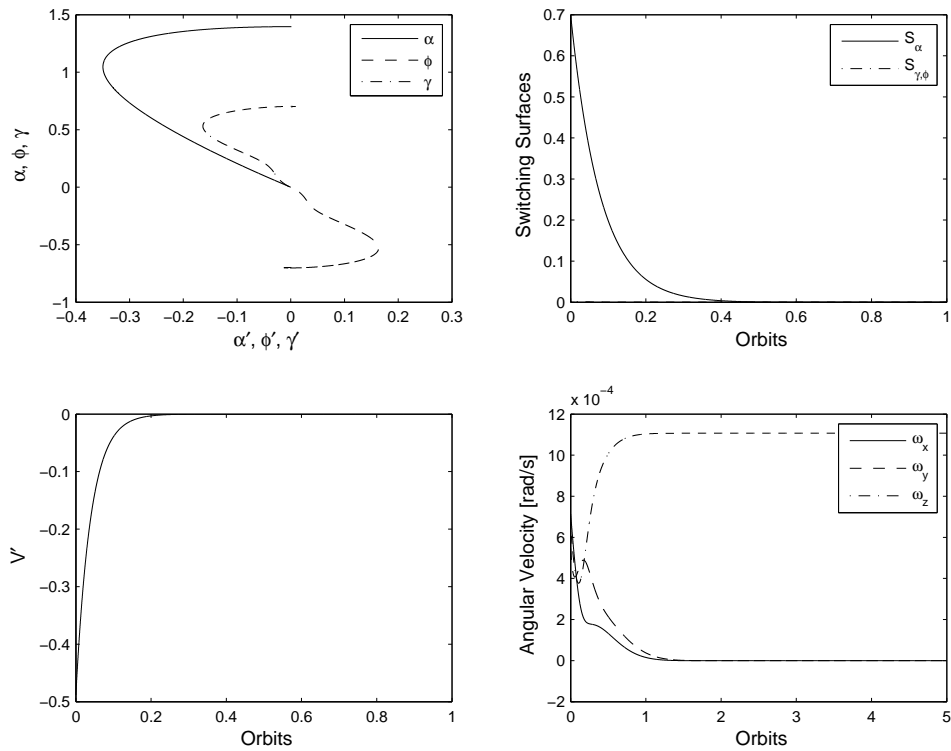


Figure 5.5: State space trajectories, sliding surfaces, Lyapunov derivative, and angular velocities for case II.

the initial attitude disturbances and the moment of inertias have a significant effect on the uncontrolled response of the system. The proposed control law for the underactuated system [Eq. (5.45)] successfully stabilizes 3-axis attitude of the spacecraft using only two control torques (U_α and U_ϕ). The finite time convergence of the system to the sliding surface, state space trajectories, and the angular velocity response of the system are shown in Fig. 5.5. The reaching time (t_r) for this case can be determined using Eq. (5.68) and the value of η from Table 5.1.

5.3.2 Variations in Spacecraft Mass Moment of Inertia

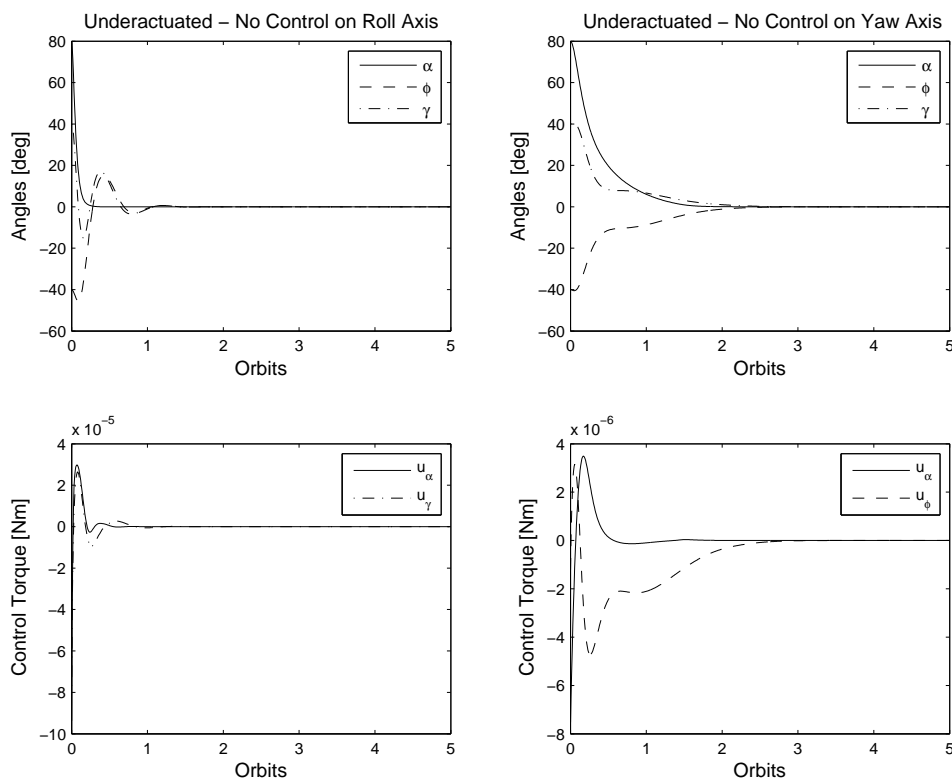
The performance evaluation of the proposed control strategy [Eq. (5.45)] presented in this section is divided into three subcategories. First, we present the effectiveness of the control strategy for attitude stabilization of an axially symmetric rigid spacecraft using two

Table 5.3: Variations in spacecraft moment of inertia

Ideal	Axis Symmetric	Product of Inertia
$\begin{bmatrix} 15 & 0 & 0 \\ 0 & 17 & 0 \\ 0 & 0 & 20 \end{bmatrix}$	$\begin{bmatrix} 17 & 0 & 0 \\ 0 & 17 & 0 \\ 0 & 0 & 20 \end{bmatrix}$	$\begin{bmatrix} 15 & 0.5 & 0.9 \\ 0.5 & 17 & 2 \\ 0.9 & 2 & 20 \end{bmatrix}$

independent control torques (Cases I and II). We then examine the efficacy of the proposed control strategy when the spacecraft is an unstable gravity gradient configuration. Finally, we illustrate the performance of the controller as affected by adding the product of inertia terms (I_{xy} , I_{xz} , I_{yz}) in the spacecraft inertia tensor.

Figure 5.6 shows controlled performance of an axis-symmetric spacecraft undergoing initial attitude disturbances stated in Table 5.1. The simulations are applied to an axisym-

Figure 5.6: Controlled performance for an axis-symmetric spacecraft ($k_1 = k_2 = 0.1765$).

metric spacecraft with inertia matrix in Table 5.3, giving $k_1 = 0.1765$ and $k_2 = 0.1765$. The control law is derived based on stable moment of inertia specified in Table 5.3. Compared to Figs. 5.2 and 5.4, there is no deterioration in the attitude response shown in Fig. 5.6.

We next examine the asymptotic convergence properties of the proposed controller on a spacecraft model with the inertia matrix containing product of inertia terms (Table 5.3). The control objective is still achieved despite the additional terms in the inertia matrix. However, the spacecraft attitude angles settle to nonzero values (Fig. 5.7). Thus, the products of inertia have an adverse effect on the satellite attitude response. When higher products of inertia terms are considered, the steady state attitude angles increase and with further increase in the products of inertia the spacecraft attitude may become unstable with the constant control gains.

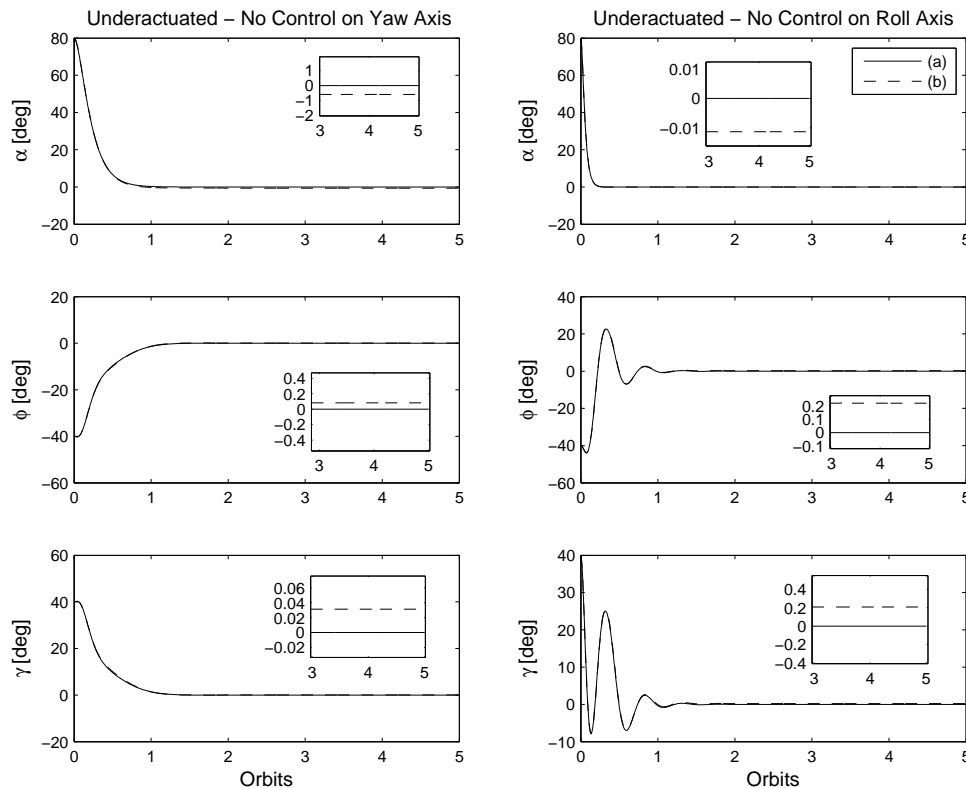


Figure 5.7: Spacecraft attitude response as affected by changes in moment inertia matrix (kg^2m). (a) $I_{xx} = 15$, $I_{yy} = 17$, $I_{zz} = 20$, $I_{xy} = I_{xz} = I_{yz} = 0$; (b) $I_{xx} = 15$, $I_{yy} = 17$, $I_{zz} = 20$, $I_{xy} = 0.5$, $I_{yz} = 2$, $I_{xz} = 0.9$

When the spacecraft is in an unstable gravity gradient configuration (for stable region, $k_1 k_2 > 0$), the inertia tensor chosen corresponds to $k_1 = 0.3$, $k_2 = -0.2$ for Case I; and $k_1 = -0.2$, $k_2 = 0.3$ for Case II (Table 5.4). Selecting different k_i to represent unstable gravity gradient configuration for cases I and II is because of the following reasons:

1. With no actuation available on the roll axis (Case I), the zero-dynamics of the roll equation of motion when $\alpha = \alpha' = \gamma = \gamma' = 0$ is given by

$$\phi'' + 4k_1 \sin \phi \cos \phi = 0 \quad (5.71)$$

Linearizing using small angle approximation we can determine the characteristic equation of the system

$$\begin{aligned} s^2 + 4k_1 &= 0 \\ s_{1,2} &= \pm 2\sqrt{-k_1} \end{aligned} \quad (5.72)$$

Hence, if $k_1 > 0$ the system will be marginally stable (complex conjugate roots), whereas, if $k_1 < 0$ the characteristic equation has one positive real root which makes the system unstable. Therefore, in order to ensure stable roll motion $k_1 > 0$ and the unstable gravity gradient configuration for this case is given by $k_1 > 0$ and $k_2 < 0$.

2. Similarly, for no actuation available on the yaw axis (Case II), the zero-dynamics of yaw equation of motion when $\alpha = \alpha' = \phi = \phi' = 0$ is

$$\gamma'' + k_2 \sin \gamma \cos \gamma = 0 \quad (5.73)$$

Linearizing using small angle approximation we can determine the characteristic equation of the system

$$\begin{aligned} s^2 + k_2 &= 0 \\ s_{1,2} &= \pm \sqrt{-k_2} \end{aligned} \quad (5.74)$$

Hence, if $k_2 > 0$ the system will have complex conjugate roots making it marginally stable, whereas, if $k_2 < 0$ the system becomes unstable due to one positive real root. Therefore, in order to ensure stable yaw motion $k_2 > 0$ and the unstable gravity gradient configuration is given by $k_1 < 0$ and $k_2 > 0$.

Table 5.4: Unstable gravity-gradient configurations

Case I	Case II
$\begin{bmatrix} 10 & 0 & 0 \\ 0 & 17 & 0 \\ 0 & 0 & 15 \end{bmatrix}$	$\begin{bmatrix} 17 & 0 & 0 \\ 0 & 10 & 0 \\ 0 & 0 & 15 \end{bmatrix}$

Figure 5.8 provides the attitude time history and the commanded control torque time history for Cases I and II for a spacecraft in unstable gravity gradient configuration. As is evident, the proposed control scheme successfully stabilizes the spacecraft attitude without any deterioration in performance. It is important to note that, the controller is not aware of the changes in inertia matrix since it is designed based on stable moment of inertias.

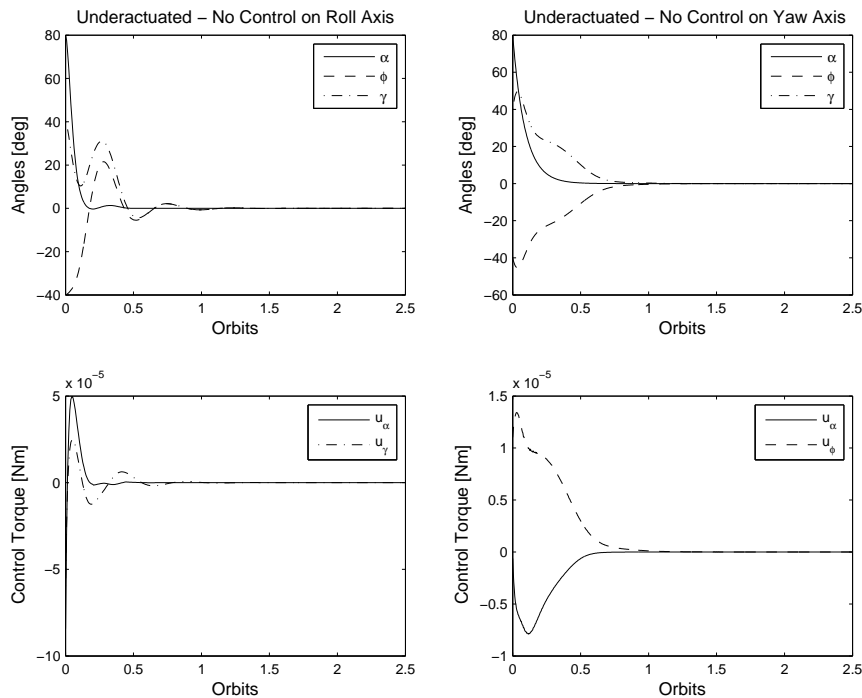


Figure 5.8: Controlled performance for unstable gravity-gradient inertia configurations. Controller designed based on stable moment of inertias ($k_1 = 0.3$, $k_2 = 0.2$) applied to a spacecraft in unstable configuration with $k_1 = 0.3$, $k_2 = -0.2$ for Case I and $k_1 = -0.2$, $k_2 = -0.3$ for Case II.

5.3.3 Eccentricity and External Disturbances

A spacecraft moving in an elliptic orbit is examined and the corresponding attitude response plots for cases I and II are shown in Figs. 5.9 and 5.10, respectively. The proposed controller effectively negates the disturbances caused by eccentricity and stabilizes the spacecraft even in an orbital eccentricity as high as $e = 0.3$. The steady state roll and yaw errors are zero while the pitch error is bounded by $|\alpha|_{max} = 0.015^\circ$ for Case I (Fig. 5.9) and $|\alpha|_{max} = 0.15^\circ$ for Case II (Fig. 5.10). This illustrates the robustness of the control law [Eq. (5.45)] to the simultaneous presence of different types of uncertainties and disturbances.

The steady state roll and yaw control inputs are null while the pitch control inputs are $|u_\alpha|_{max} = 1.5 \times 10^{-5}$ Nm for both cases I and II. The period of the steady state control is 1 orbit; this matches the simplified steady state pitch control input, $u_\alpha = 2e \sin \theta$, obtained from Eq. (5.45) considering the null steady state errors.

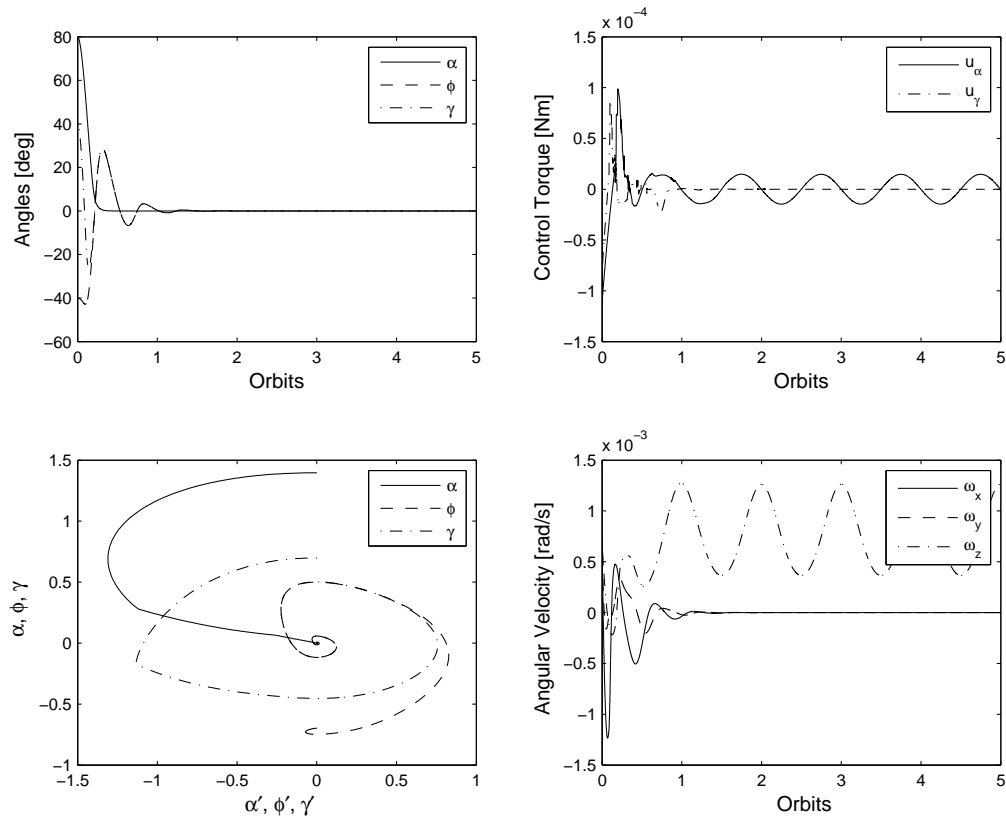


Figure 5.9: Effects of orbital eccentricity ($e = 0.3$) - Case I.

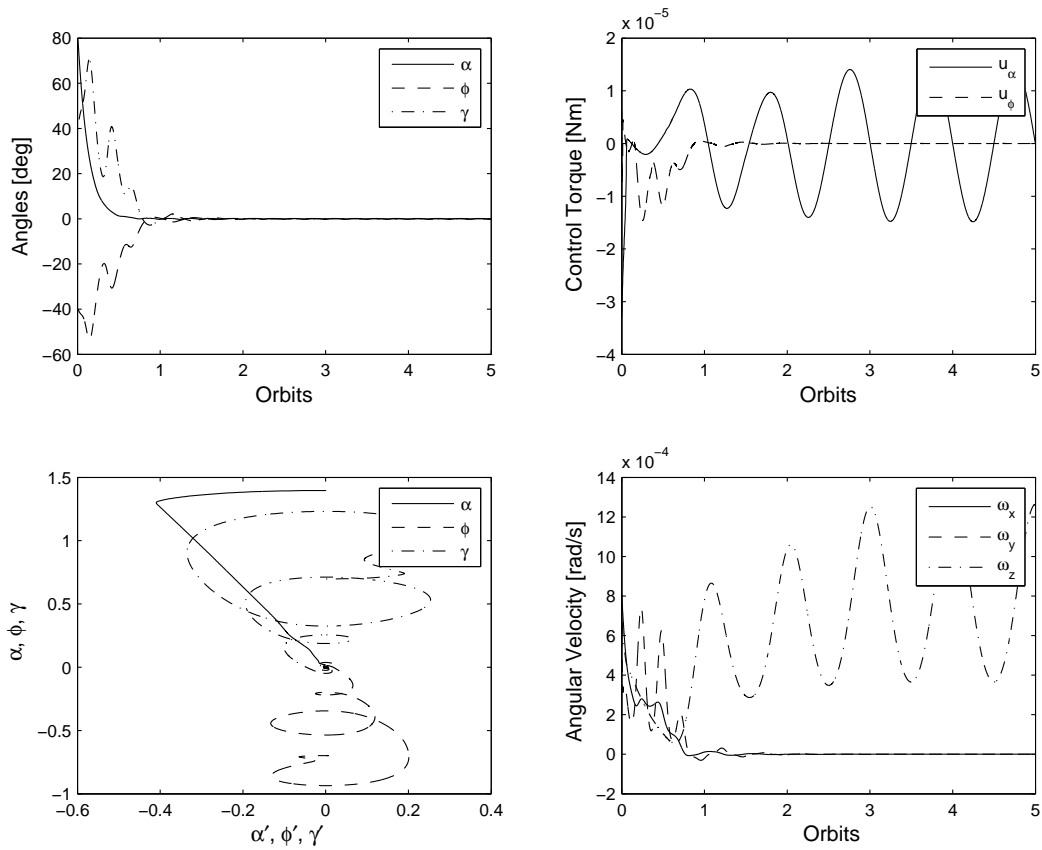


Figure 5.10: Effects of orbital eccentricity ($e = 0.3$) - Case II.

The angular velocity curves for cases I and II show a periodic behavior on ω_z . This can be explained using Eq. (5.11) with the steady state values of $\phi = \gamma = \dot{\phi} = 0$, we have $\omega_z = \dot{\theta} + \dot{\alpha}$. Since, for an elliptic orbit, $\dot{\theta} \neq 0$, and as mentioned earlier steady state α is bounded, ω_z also remains bounded ($\forall t$, Figs. 5.9 and 5.10).

We next examine the disturbance rejection aspects of the control scheme when applied in the presence of environmental disturbances due to solar radiation pressure, aerodynamic drag, and magnetic forces. The disturbances due to solar radiation pressure can be expressed as (in Nm) [Kaplan 1976],

$$\begin{bmatrix} T_{s\alpha} \\ T_{s\phi} \\ T_{s\gamma} \end{bmatrix} = S_f \begin{bmatrix} (1 \times 10^{-4}) \cos(\dot{\theta}t) \\ (2 \times 10^{-5})[1 - 2 \sin(\dot{\theta}t)] \\ (5 \times 10^{-5}) \cos(\dot{\theta}t) \end{bmatrix} \quad (5.75)$$

The external torque due to aerodynamic drag [Wie 1998] can be modeled as bias plus cyclic terms in the body-fixed control axes (in Nm),

$$\begin{bmatrix} T_{a\alpha} \\ T_{a\phi} \\ T_{a\gamma} \end{bmatrix} = 1.36 A_f \begin{bmatrix} -[4 + 2 \sin(\dot{\theta}t) + 0.5 \sin(2\dot{\theta}t)] \\ 1 + \sin(\dot{\theta}t) + 0.5 \sin(2\dot{\theta}t) \\ -[1 + \sin(\dot{\theta}t) + 0.5 \sin(2\dot{\theta}t)] \end{bmatrix} \quad (5.76)$$

where S_f and A_f are positive scaling factors. The disturbance torque simulated is of the form $T_d = T_a + T_s$. We choose $S_f = 0.01$ and $A_f = 2 \times 10^{-6}$ such that the signals described by Eqs. (5.76) and (5.75) emulates the disturbance process due to solar radiation pressure, aerodynamic drag, and magnetic forces, $\|T_d\| \leq 2 \times 10^{-5}$ Nm for a spacecraft in LEO (500 km) [Wertz & Larson 1999].

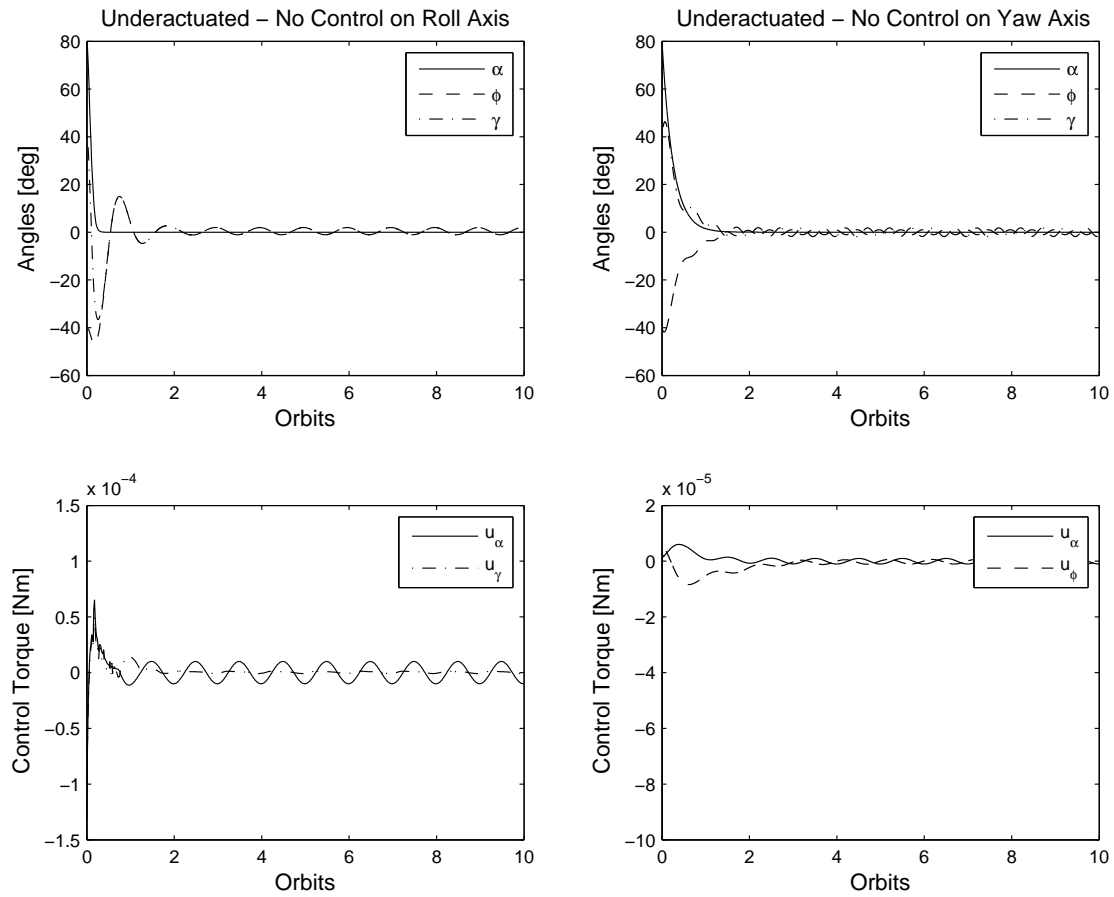


Figure 5.11: Effects of time-varying external disturbances.

Robustness of the proposed control technique to time varying disturbances is analyzed to assess the reliability of the algorithm. Figure 5.11 shows the performance of the proposed controller when the disturbances specified by Eqs. (5.75) and (5.76) are acting on the system, and the gains are set at the values listed in Table 5.2. As expected under the influence of external disturbances, the proposed controller is able to regulate the attitude motion and stabilize the errors to within the expected neighborhood of the origin, where they remain indefinitely.

During the initial phases the control signals counteract the large attitude errors and as the spacecraft is stabilized the controller smoothly tracks the disturbances and eliminate its effects as time increases. With no control on roll axis (Case I), the steady state attitude errors are $|\alpha|_{max} = 0.02^\circ$, $|\phi|_{max} = 1^\circ$, and $|\gamma|_{max} = 1.5^\circ$. For case II, the steady state attitude errors are $|\alpha|_{max} = 0.004^\circ$, $|\phi|_{max} = 1.5^\circ$, and $|\gamma|_{max} = 1.5^\circ$. The inherent robustness of the proposed control scheme stabilizes the spacecraft's attitude successfully for all cases.

5.4 Summary

In this chapter, the proposed control methodology was employed for 3-axis stabilization of a rigid spacecraft using control torques supplied by thrusters about only two of its principal axes. We considered two cases, (i) no control authority available on the roll axis, and (ii) no actuation available on the yaw axis. To verify and validate the effectiveness of the proposed control algorithm, a high-fidelity nonlinear model of the spacecraft attitude dynamics was developed which includes the mathematical models of environmental disturbances acting on the spacecraft in LEO. Numerical simulation results illustrates that the proposed control scheme can successfully regulate the attitude motion from large initial conditions and stabilize the unactuated states to within the expected neighborhood of the origin, where they remain indefinitely. Based on the results of underactuated spacecraft attitude stabilization, we present a novel attitude control system in the next chapter that utilizes only a single thruster for 3-axis attitude stabilization.

CHAPTER 6

Spacecraft Attitude Control Using Single Thruster

FEASIBILITY of achieving complete three axis attitude and angular velocity stabilization using a novel concept - A Single Thruster - is explored in this chapter. For low-cost missions using pico-satellites, the possibility of handling actuator failures without the need for redundant elements is an appealing concept. The actuator system remains minimal and complete three-axis attitude stabilization is achieved using a single thruster. A single-thruster control concept, either by design or in a contingency, is challenging because the thruster exerts both force and torque on a spacecraft. This coupling property, along with appropriate sizing and positioning of the thruster, can be utilized to carry out precise three-axis attitude maneuvers. Torques are generated using a thruster orientation mechanism with which the thrust vector can be tilted on a two axis gimbal.

The spacecraft, controlled using the proposed concept, constitutes an underactuated system (a system with fewer independent control inputs than degrees of freedom) with nonlinear dynamics. Moreover, using thruster gimbal angles as control inputs make the system non-affine (control terms appear nonlinearly in the state equation). This necessitates the control algorithms to be developed based on nonlinear control theory since linear control methods are not directly applicable. The control concept is implemented by developing a robust variable structure control algorithm based on the nonlinear hyperplanes.

The chapter is organized as follows: Section 6.1 introduces the mathematical model of the proposed spacecraft system. Nonlinear control algorithm is formulated with detailed proof of stability for the closed-loop system in Section 6.2. The results of numerical simulations incorporating different mission scenarios are presented in Section 6.3. Finally, conclusions of the study are stated in Section 6.4.

6.1 Spacecraft Model with Single Thruster

The main feature of this proposed attitude control method is that it requires only a single thruster to control yaw, roll, and pitch angle. An actuator is operationally attached to the gimbaled thruster to control the angled position of the gimbaled thruster in two orthogonal directions. A position control system sends a control signal to the actuator which moves the gimbaled thruster to an angled position in response to the control signal, and the angled position of the gimbaled thruster controls the attitude of the spacecraft.

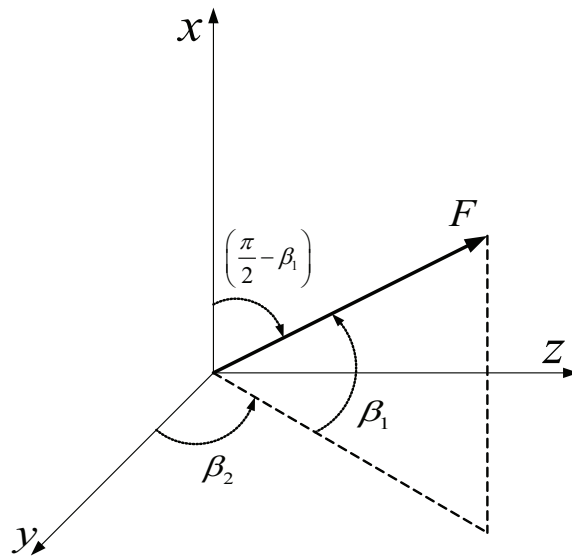


Figure 6.1: Thruster azimuth and elevation.

We consider a double-gimbal thruster that provides constant force. For a gimbaled thruster shown in Fig. 6.1, the force components can be derived as

$$\bar{\mathbf{F}} = \begin{bmatrix} F_x \\ F_y \\ F_z \end{bmatrix} = F \begin{bmatrix} \sin \beta_1 \\ \cos \beta_1 \cos \beta_2 \\ \cos \beta_1 \sin \beta_2 \end{bmatrix} \quad (6.1)$$

where F is the constant thrust level, β_1 is the elevation angle, and β_2 is the azimuth angle. Let $\vec{\mathbf{r}} = r_x \hat{i} + r_y \hat{j} + r_z \hat{k}$ be the vector representing the placement of the reaction thruster from the spacecraft center of mass. Torque components provided by the thruster can be

written as follows:

$$\tau = \begin{bmatrix} \tau_x \\ \tau_y \\ \tau_z \end{bmatrix} = \mathbf{\bar{r}} \times \mathbf{\bar{F}} = F \begin{bmatrix} r_y \cos \beta_1 \sin \beta_2 - r_z \cos \beta_1 \cos \beta_2 \\ r_z \sin \beta_1 - r_x \cos \beta_1 \sin \beta_2 \\ r_x \cos \beta_1 \cos \beta_2 - r_y \sin \beta_1 \end{bmatrix} \quad (6.2)$$

It is clearly evident from Eq. (6.2) that, when $\beta_1 = \beta_2 = 0$, the torque components are $\tau_x = -r_z F$, $\tau_y = 0$, and $\tau_z = r_x F$. Even in the equilibrium state, we have torque components provided the thruster is switched on. In order to avoid this phenomenon, the single thruster attitude control methodology proposed in this study considers the thruster to be placed with only an offset in the spacecraft y -axis ($r_x = r_z = 0$). Therefore, the torque components of the proposed single thruster system reduces to

$$\begin{bmatrix} \tau_x \\ \tau_y \\ \tau_z \end{bmatrix} = F \begin{bmatrix} r_y \cos \beta_1 \sin \beta_2 \\ 0 \\ -r_y \sin \beta_1 \end{bmatrix} \quad (6.3)$$

The complete mathematical model of the proposed single thruster attitude control system, considering the kinematics and dynamics of the spacecraft combined with the dynamics of the thruster gimbal mechanism can be written as follows (from Section 5.1.4):

$$\begin{bmatrix} x_{11}' \\ x_2' \end{bmatrix} = \begin{bmatrix} \bar{A}_{11} & \bar{A}_{12} \\ \bar{A}_{21} & \bar{A}_{22} \end{bmatrix} \left\{ \begin{bmatrix} F_1 \\ F_2 \end{bmatrix} + \begin{bmatrix} 0 \\ U \end{bmatrix} + \begin{bmatrix} d_1 \\ d_2 \end{bmatrix} \right\} \quad (6.4)$$

The above equations of motion are in dimensionless form. Therefore, the torques given by Eq. (6.3) are converted to dimensionless form by introducing the parameter $\kappa = (F r_y)/(I_{zz} \dot{\theta}^2)$. The control torque in Eq. (6.4) is given by

$$U \in \mathbb{R}^{2 \times 1} = \begin{bmatrix} U_\alpha \\ U_\gamma \end{bmatrix} = \kappa \begin{bmatrix} -\sin \beta_1 \\ \cos \beta_1 \cos \beta_2 \end{bmatrix} \quad (6.5)$$

For this case $x_{11} = \phi'$, $x_2 = [\alpha', \gamma']$, and $U \in \mathbb{R}^{2 \times 1} = [U_\alpha, U_\gamma]^T$ given by Eq. (6.5). Similarly, $F(q, q') = [F_1, F_2]^T$ where $F_1 = F_\phi$ and $F_2 = [F_\alpha, F_\gamma]^T$. The nonlinear terms in the \bar{A} matrix are given by

$$\bar{A}_{11} = \frac{\cos^2 \gamma + k_{yz} \sin^2 \gamma}{k_{yz}} \quad \text{and} \quad \bar{A}_{21} = \begin{bmatrix} \frac{(1 - k_{yz}) \sin \gamma \cos \gamma}{k_{yz} \cos \phi} \\ \frac{(1 - k_{yz}) \sin \gamma \cos \gamma \sin \phi}{k_{yz} \cos \phi} \end{bmatrix} \quad (6.6)$$

$$\bar{A}_{12} = \begin{bmatrix} \frac{(1 - k_{yz}) \sin \gamma \cos \gamma}{k_{yz} \cos \phi} & \frac{(1 - k_{yz}) \sin \gamma \cos \gamma \sin \phi}{k_{yz} \cos \phi} \end{bmatrix} \quad (6.7)$$

$$\bar{A}_{22} = \begin{bmatrix} \frac{\sin^2 \gamma + k_{yz} \cos^2 \gamma}{k_{yz} \cos^2 \phi} & \frac{\sin \phi (\sin^2 \gamma + k_{yz} \cos^2 \gamma)}{k_{yz} \cos^2 \phi} \\ \frac{\sin \phi (\sin^2 \gamma + k_{yz} \cos^2 \gamma)}{k_{yz} \cos^2 \phi} & \frac{\sin^2 \phi (\sin^2 \gamma + k_{yz} \cos^2 \gamma)}{k_{yz} \cos^2 \phi} + \frac{1}{k_{xz}} \end{bmatrix} \quad (6.8)$$

The nonlinear terms in $F_1 = F_\phi$ and $F_2 = [F_\alpha, F_\gamma]^T$ were provided in the previous chapter [Eq. (5.23)] and are not restated here for brevity. The system in Eq. (6.4) can be written in the following form:

$$\begin{bmatrix} M_{11} & M_{12} & M_{13} \\ M_{21} & M_{22} & M_{23} \\ M_{31} & M_{32} & M_{33} \end{bmatrix} \begin{bmatrix} \phi'' \\ \alpha'' \\ \gamma'' \end{bmatrix} = \left\{ \begin{bmatrix} F_\phi \\ F_\alpha \\ F_\gamma \end{bmatrix} + \begin{bmatrix} 0 \\ U_\alpha \\ U_\gamma \end{bmatrix} + \begin{bmatrix} d_\phi \\ d_\alpha \\ d_\gamma \end{bmatrix} \right\} \quad (6.9)$$

where F_ϕ , F_α , F_γ are described in Eq. (5.23), U_α and U_γ are given by Eq. (6.5), and M_{ij} are described below.

$$\begin{aligned} M_{11} &= k_{yz} \cos^2 \gamma + \sin^2 \gamma & \text{and} & & M_{23} &= M_{32} = -k_{xz} \sin \phi \\ M_{12} &= M_{21} = (k_{yz} - 1) \sin \gamma \cos \gamma \cos \phi & \text{and} & & M_{13} &= M_{31} = 0 \\ M_{22} &= k_{xz} \sin^2 \phi + k_{yz} \cos^2 \phi \sin^2 \gamma + \cos^2 \phi \cos^2 \gamma & \text{and} & & M_{33} &= k_{xz} \end{aligned} \quad (6.10)$$

To facilitate the development of nonlinear control algorithms and simplify the stability analysis, Eq. (6.9) is represented as follows

$$M(q) q'' = F(q, q') + U(\beta_1, \beta_2) + D \quad (6.11)$$

where $q \in \mathbb{R}^3 = [\phi \ \alpha \ \gamma]^T$, $M(q) \in \mathbb{R}^{3 \times 3}$, $F(q, q')$, $D \in \mathbb{R}^3$, and $U(\beta_1, \beta_2) = [0 \ U_\alpha \ U_\gamma]^T$.

6.2 Control Laws - Single Thruster System

In this section we present the control methodology for the single thruster attitude control system proposed earlier in Section 6.1. The system is underactuated, i.e., no control authority available about the y -axis (roll). This case is similar to, case II presented in Section 5.2 except for the fact that the thruster gimbal dynamics are considered along with the equations of motion. Using thruster gimbal angles as control inputs makes the system non-affine (control terms appear nonlinearly in the state equation).

6.2.1 Design of Sliding Manifold

For the single thruster attitude control system considered in this study, the control signals are the gimbal angles (β_1, β_2) that commands the movement of the thruster in a given direction to provide torques about the x -axis (yaw) and z -axis (pitch). The evolution of the gimbal angles are constrained to restrict thrust firings towards the spacecraft. The range space of the gimbal angles are bounded by: $0 \leq \beta_1 < \frac{\pi}{2}$ and $0 \leq \beta_2 < \frac{\pi}{2}$. Since the control signals are non-affine, we develop a nonlinear control algorithm based on higher-order sliding mode. By increasing the order of the system, the gimbal rates (β'_1, β'_2) can be extracted from Eq. (6.11). The control algorithm establishes the required gimbal rates and then employs a single-step integration process to obtain the corresponding angular positions. This information is sent to the actuators that control the gimbal movement to orient the thruster in the prescribed direction.

A novel nonlinear higher-order sliding surface for the single thruster attitude control system is defined in this section. First, we introduce a lower level sliding surface given by

$$S_{1T} = \bar{K}_1 M q' + \bar{K}_2 q \quad (6.12)$$

where $\bar{K}_1 \in \mathbb{R}^{2 \times 3}$ and $\bar{K}_2 \in \mathbb{R}^{2 \times 3}$ are the weighting matrices for q' and q , respectively. They have the form

$$\bar{K}_1 = \begin{bmatrix} 0 & P_2 & 0 \\ P_5 & 0 & P_6 \end{bmatrix} \quad \text{and} \quad \bar{K}_2 = \begin{bmatrix} 0 & P_1 & 0 \\ P_3 & 0 & P_4 \end{bmatrix} \quad (6.13)$$

The stability of the lower order sliding surface [Eq. (6.12)] has been previously established in Section 5.2. Taking the first derivative of S_{1T} yields

$$S'_{1T} = \bar{K}_1 M q'' + (\bar{K}_1 M' + \bar{K}_2) q \quad (6.14)$$

Now, the higher-order sliding manifold is defined as a combination of the lower-order sliding surface and its first derivative using a positive constant ζ ,

$$\sigma = S'_{1T} + \zeta S_{1T} \quad (6.15)$$

6.2.2 Control Formulation

The second phase of the design procedure is to develop a nonlinear control algorithm that can steer the trajectories of the system [Eq. (6.11)] to the high-order sliding manifold (Eq. 6.15). The algorithm should also be capable of maintaining the system states on the sliding manifold for all $t > t_r$, where t_r is the sliding surface reaching time.

The main challenge is to control the attitude of the spacecraft in the presence of uncertainties and external disturbance torques. With no control authority available in the roll axis, achieving precision attitude control becomes a difficult task in the presence of system nonlinearities, and time varying external disturbances. A simple approach is to extract the core information of the uncertainties and disturbances by using the worst case upper-bound of the disturbances in the controller design. We introduce the following term

$$\xi(q, q', q'') = \bar{K}_1[D' + F'(q, q')] + [\bar{K}_1M' + \bar{K}_2]q'' + \bar{K}_1M''q' \quad (6.16)$$

Note that $\xi(q, q', q'')$ is the lumped term containing the system nonlinearities, parameter uncertainties (moment of inertia), and external disturbances (changing operating conditions). One way to account for this in the control algorithm is to assume that the lumped disturbances are bounded and then use the upper bound in the controller design.

$$\|\xi(q, q', q'')\| \leq \rho_1 + \rho_2\|q\| + \rho_3\|q'\| \leq \varphi_3 \quad (6.17)$$

We now develop the control scheme to ensure that the sliding manifold is reached and sliding on the manifold occurs. The objective is to force the higher-order sliding surface given by Eq. (6.15) to follow a desired path given by,

$$\begin{aligned} \sigma' &= S''_{1T} + \zeta S'_{1T} = - \left[\eta_1 + \frac{\eta_2\varphi_2}{\|\sigma\| + \delta} \right] \sigma \\ &= \bar{K}_1[Mq''' + M'q''] + [\bar{K}_1M' + \bar{K}_2]q'' + \bar{K}_1M''q' = - \left[\eta_1 + \frac{\eta_2\varphi_2}{\|\sigma\| + \delta} \right] \sigma \end{aligned} \quad (6.18)$$

Taking the derivative of the equations of motion [Eq. (6.11)] along its trajectories and substituting in Eq. (6.18), we get

$$\sigma' = \bar{K}_1U' + \bar{K}_1[D' + F'(q, q')] + [\bar{K}_1M' + \bar{K}_2]q'' + \bar{K}_1M''q' \quad (6.19)$$

$$\begin{aligned}
\bar{K}_1 U' &= \begin{bmatrix} 0 & P_2 & 0 \\ P_5 & 0 & P_6 \end{bmatrix} \begin{bmatrix} 0 & 0 \\ -\kappa \cos \beta_1 & 0 \\ -\kappa \sin \beta_1 \sin \beta_2 & \kappa \cos \beta_1 \cos \beta_2 \end{bmatrix} \begin{bmatrix} \beta'_1 \\ \beta'_2 \end{bmatrix} \\
&= \begin{bmatrix} -\kappa P_2 \cos \beta_1 & 0 \\ -\kappa P_6 \sin \beta_1 \sin \beta_2 & \kappa P_6 \cos \beta_1 \cos \beta_2 \end{bmatrix} \begin{bmatrix} \beta'_1 \\ \beta'_2 \end{bmatrix} \quad (6.20)
\end{aligned}$$

Carrying out some algebraic manipulations based on Eqs. (6.18)-(6.20), the nonlinear control law capable of providing gimbale rate commands for β_1 , β_2 , and in turn control the attitude of the spacecraft is given by

$$U_{1T} = - \begin{bmatrix} -\kappa P_2 \cos \beta_1 & 0 \\ -\kappa P_6 \sin \beta_1 \sin \beta_2 & \kappa P_6 \cos \beta_1 \cos \beta_2 \end{bmatrix}^{-1} \left[\eta_1 + \frac{\eta_2 \varphi_2}{\|\sigma\| + \delta} \right] \sigma \quad (6.21)$$

where $U_{1T} = [\beta'_1 \ \beta'_2]^T$, and δ is a small positive scalar specifying the boundary layer thickness that will eliminate chatter if appropriately chosen so that the unmodeled high frequency dynamics are not excited. The scalar parameter η_2 depends on the magnitude of the disturbances and uncertainties,

$$\eta_2 = \frac{\varphi_1}{\varphi_2} (\varphi_3 + \varphi_4) \quad \forall \quad \varphi_1, \varphi_3, \varphi_4 \geq 0 \quad (6.22)$$

for some positive constants φ_1 , φ_2 , φ_3 , and φ_4 . The steps involved in adequately determining these nonnegative constants are detailed in the next section. It is also important to note that Eq. (6.16) is true regardless of any external disturbance (gravity gradient torque, solar radiation pressure, aerodynamic drag), inherent nonlinearities, and other uncertainties that arise due to changing spacecraft parameters or operating conditions.

6.2.3 Stability Analysis

In this sub-section we present stability conditions for the single thruster attitude control system, focussing primarily on robustness against disturbances. We show that the control law, Eq. (6.21), is capable of driving the closed-loop trajectory of the system towards a boundary layer on the sliding surface in finite time (Hitting Phase). Once the sliding surface is reached, the system enters into the sliding regime.

Theorem 6.1: For the single thruster attitude control mathematical model in Eq. (6.11) if, the higher-order sliding manifold is chosen as Eq. (6.15), the control law is defined as Eq. (6.21), and the bounds on the external disturbances and uncertainties on the system is assumed as given by Eq. (6.17) then the system reaches the sliding surface in finite time for a sufficiently small $\delta > 0$.

Proof: Consider a continuously differentiable Lyapunov function candidate

$$V(\sigma) = \frac{1}{2}\sigma^T\sigma \quad (6.23)$$

Taking the first derivative of $V(\sigma)$ along the trajectory of the system yields,

$$\begin{aligned} V' &= \sigma^T\sigma' = \sigma^T [S''_{1T} + \zeta S'_{1T}] \\ &= \sigma^T [\bar{K}_1 U' + \bar{K}_1 (D' + F') + (\bar{K}_1 M' + \bar{K}_2)q'' + \bar{K}_1 M''q'] \\ &= \sigma^T [\bar{K}_1 U' + \xi(q, q', q'')] \end{aligned} \quad (6.24)$$

Substituting for the gimbal rates from Eq. (6.21) in the previous equation, gives

$$\begin{aligned} V' &= \sigma^T \left[-\eta_1 \sigma - \eta_2 \frac{\varphi_2 \sigma}{\|\sigma\| + \delta} + \xi(q, q', q'') \right] \\ &\leq -\eta_1 \sigma^T \sigma + \|\sigma\| \left[-\eta_2 \frac{\varphi_2 \|\sigma\|}{\|\sigma\| + \delta} + \|\xi\| \right] \\ &\leq -\eta_1 \sigma^T \sigma + \|\sigma\| \left[-\eta_2 \frac{\varphi_2 \|\sigma\|}{\|\sigma\| + \delta} + \varphi_3 \right] \end{aligned} \quad (6.25)$$

Expressing φ_3 in terms of η_2 , φ_1 , φ_2 , and φ_4 from Eq. (6.22) and substituting in Eq. (6.25), the following simplifications can be made to the first derivative of the Lyapunov function candidate,

$$\begin{aligned} V' &\leq -\eta_1 \sigma^T \sigma - \|\sigma\| \left[\eta_2 \varphi_2 \frac{\|\sigma\|}{\|\sigma\| + \delta} - \frac{\eta_2 \varphi_2}{\varphi_3} + \varphi_4 \right] \\ &\leq -\eta_1 \sigma^T \sigma - \varphi_4 \|\sigma\| - \eta_2 \varphi_2 \|\sigma\| \left[\frac{\|\sigma\|}{\|\sigma\| + \delta} - \frac{1}{\varphi_1} \right] \end{aligned} \quad (6.26)$$

It is readily obtained from Eq. (6.26) that, if:

$$\begin{aligned} \frac{\|\sigma\|}{\|\sigma\| + \delta} - \frac{1}{\varphi_1} &\geq 0 \\ \|\sigma\| &\geq \frac{\delta}{\varphi_1 - 1} \end{aligned} \quad (6.27)$$

then $\dot{V}(\sigma) < 0$. The condition in Eq. (6.27) is only satisfied if

$$V(\sigma) > \frac{1}{2} \left(\frac{\delta}{\varphi_1 - 1} \right)^2 = \varepsilon_1 \quad (6.28)$$

Based on Eq. (6.25), where $\frac{\|\sigma\|}{\|\sigma\| + \delta} \leq 1$ ($\forall \delta \geq 0$), the gains can be selected as

$$\begin{aligned} \eta \varphi_2 - \varphi_3 &> 0 \\ \varphi_1 &> \frac{\varphi_3}{\varphi_3 + \varphi_4} \end{aligned} \quad (6.29)$$

Using this fact it can be shown that $V'(\sigma) \leq -\varepsilon_2 \sqrt{2V(\sigma)}$ for some $\varepsilon_2 > 0$. This implies that the sliding boundary layer is reached in finite time, t_r . For the case where a small (δ) is chosen, then every solution will eventually enter the set $\mathfrak{R} = \{\sigma : V(\sigma) \leq \varepsilon_1\}$ and will be uniformly ultimately bounded with respect to the ellipsoid ε_1 .

The gimbal angle rates given by Eq. (6.21) forces the attitude trajectories of the spacecraft towards a boundary layer surrounding the sliding surface σ in the state space, and the trajectories remains in the ellipsoid ε_1 thereafter. From the properties of V and V' , we conclude that $\sigma \in \mathcal{L}_2 \cap \mathcal{L}_\infty$. Here, σ is defined as $\sigma = S'_{1T} + \zeta S_{1T}$. If $(S'_{1T} + \zeta S_{1T}) \in \mathcal{L}_2 \cap \mathcal{L}_\infty$, then $S_{1T} \in \mathcal{L}_2 \cap \mathcal{L}_\infty$ and $S'_{1T} \in \mathcal{L}_2 \cap \mathcal{L}_\infty$. From Barbalat's lemma, we conclude that $\sigma \rightarrow 0$ as $t \rightarrow t_r$. Thus, $S_{1T} \rightarrow 0$ and $S'_{1T} \rightarrow 0$, which implies that $q \rightarrow 0$ and $q' \rightarrow 0$ as $t \rightarrow \infty$. This completes the proof. \square

6.3 Performance Evaluation

In this section, we give an illustrative example of the proposed single thruster scheme for the problem of attitude control of a rigid spacecraft. The results presented in Chapter 5 examined the case of attitude control using two pairs of body-fixed thrusters capable of providing two control torques. In contrast, the proposed attitude control algorithm using a single thruster employs gimbal rate steering law. In this section, the complete nonlinear equations of motion given by Eq. (6.11) and the gimbal rate steering law given by Eq. (6.21) are used to predict and validate the performance of the proposed single thruster attitude control methodology under realistic operating conditions.

Table 6.1: RyePicoSat inertia and thruster parameters.

Parameters	Values
Size (m ³)	0.1 × 0.1 × 0.1
Moment of Inertia	
I_{xx} (kg m ²)	0.0015
I_{yy} (kg m ²)	0.0017
I_{zz} (kg m ²)	0.0020
Thruster	
Max. Force, F , (μ N)	8
y -axis offset, r_y , (m)	0.15

Table 6.2: Higher-order SMC parameters.

Control Gains	Values
$[\varphi_1, \varphi_2, \varphi_3, \varphi_4]$	[1.5, 1.5, 0.5, 0.5]
$[P_1, P_2, P_3]$	[0.1, 0.1, 0.1]
$[P_4, P_5, P_6]$	[-0.1, 0.1, -0.1]
ζ	2
δ	1×10^{-6}

For precision attitude control a Micro-Electro-Mechanical System (MEMS) based col-loidal thruster [Xiong *et al.* 2002] capable of delivering thrust to the order of $5 - 30\mu\text{N}$ is selected. This thruster is mounted on a two-axis gimbal that is fixed at the end of a moment arm extending along the body-fixed y -axis. The length of the moment arm is $r_y = 0.15$ m and the thruster is only offset from the spacecraft center of mass in the y -direction ($r_x = r_z = 0$). The maximum delivered thrust is fixed at $8 \mu\text{N}$. The proposed attitude control system is for the *RyePicoSat* and Table 6.1 summarizes the spacecraft model parameters used in all numerical simulations. Based on values of the spacecraft moment of inertia we can calculate nondimensional parameters $k_1 = (I_z - I_x)/I_y = 0.3$ and

$k_2 = (I_z - I_y)/I_x = 0.2$. The control algorithm is designed based on these moment of inertia ratios. Results for varying spacecraft moment of inertia are examined by implementing the changes only in the spacecraft dynamic model and therefore, the control algorithm remains fixed for all simulations. The control gains (φ_i), sliding surface weighting matrices (\bar{K}_1, \bar{K}_2) and the boundary layer (δ) used in all simulations for Cases I and II are listed in Table 6.2.

The spacecraft is subjected to the following initial attitude disturbances about the yaw (x), roll (y), and pitch (z) axes:

$$\begin{aligned}\gamma_0 &= \phi_0 = \alpha_0 = 60^\circ \\ \gamma'_0 &= \phi'_0 = \alpha'_0 = 0\end{aligned}\tag{6.30}$$

The thruster is initially configured with the gimbal axes at its equilibrium position, $\beta_{1,0} = \beta_{2,0} = 0$. Unless explicitly stated, the spacecraft parameters specified in Table 6.1, control gains in Table 6.2, and initial conditions given by Eq. (6.30) are used in all simulations.

6.3.1 Nominal Performance

We first study the attitude motion of the spacecraft in a circular orbit at an altitude of 500 km with an orbit period $T = 5677$ seconds. The attitude response for large initial attitude errors is illustrated in Fig. 6.2. The Euler angles asymptotically approach to zero starting from non-zero initial conditions. The variations in the spacecraft angular rates during the transient phase are due to the attitude errors. The angular velocities eventually converges during steady state as the spacecraft attains a stable attitude. The angular velocity of the spacecraft about the z -axis converges to a non-zero value $\omega_z = 0.0011$ rad/s.

Based on the coordinate frames selected as shown in Fig. 5.1 the spacecraft z -axis is normal to the orbit plane. Therefore, due to the spacecraft rotation about the Earth, ω_z would be equal to the orbital frequency of the spacecraft $\dot{\theta} = \sqrt{\mu_e R^3}$, where μ_e (km^3s^{-2}) is the gravitational parameter of the Earth and $R = 6878$ km. Substituting the steady-state values the Euler angles are their rates ($\alpha = \phi = \gamma = \dot{\alpha} = \dot{\phi} = \dot{\gamma} = 0$) in Eq. (5.11) we can derive that $\omega_x = \omega_y = 0$ and $\omega_z = \dot{\theta}$. The plots of gimbal angles and the net control torques provided by the single thruster are also shown in Fig. 6.2. As evident, β_1 is the thruster elevation angle and therefore it is mainly used for controlling the pitch (α) motion (out of plane) of the spacecraft.

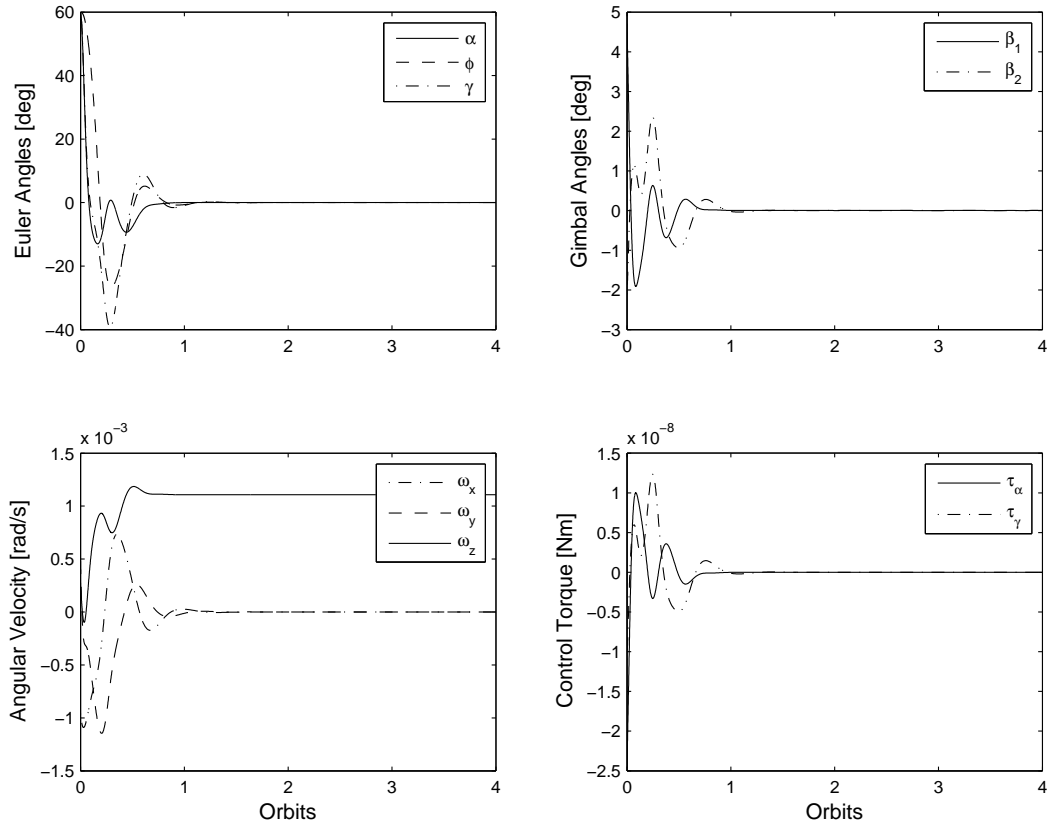


Figure 6.2: Controlled response for ideal attitude stabilization.

6.3.2 Variations in Moment of Inertia

The performance of the proposed control algorithm using a single-thruster for 3-axis attitude control is examined in this sub-section for variations in the spacecraft moments of inertia. First, we consider the case where the spacecraft is in an unstable gravity gradient configuration. Since there is no control input in the y -axis, the unstable gravity gradient configuration for this case is given by $k_1 > 0$ and $k_2 < 0$ [derived in Eq. (5.72)]. When the spacecraft is in an unstable gravity gradient configuration (for stable region, $k_1, k_2 > 0$), the inertia tensor chosen corresponds to $k_1 = 0.3$, $k_2 = -0.2$ for the inertia matrix

$$I = \begin{bmatrix} 0.0010 & 0 & 0 \\ 0 & 0.0017 & 0 \\ 0 & 0 & 0.0015 \end{bmatrix} \quad (6.31)$$

It is important to note that the control algorithm is designed based on the stable inertia configuration ($k_1 = 0.3$, $k_2 = 0.2$). Figure 6.3 illustrates the effectiveness of the proposed control methodology in stabilizing the attitude of the spacecraft. The control objective is still achieved despite such large change in the inertia matrix. Since the proposed methodology is implemented based on nonlinear higher-order sliding mode, the response profile of the gimbal angles are very smooth. This observation is consistent with the theoretical reasoning that high-order SMC eliminates control chattering.

Next, we present the effectiveness of the control algorithm for attitude stabilization of an axially symmetric rigid spacecraft using a single thruster. Figure 6.4 shows controlled performance of an axisymmetric spacecraft undergoing initial attitude disturbances stated

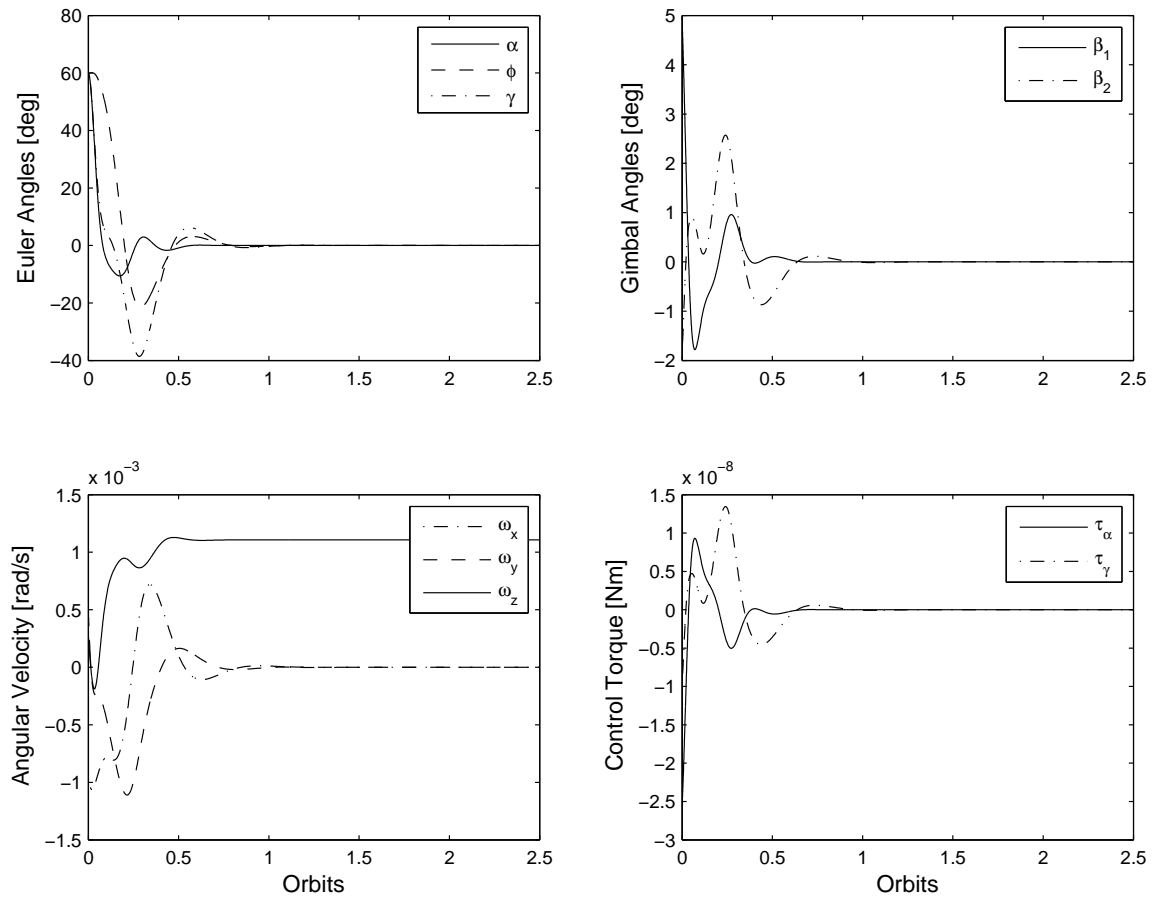


Figure 6.3: Controlled response for unstable gravity gradient configuration.

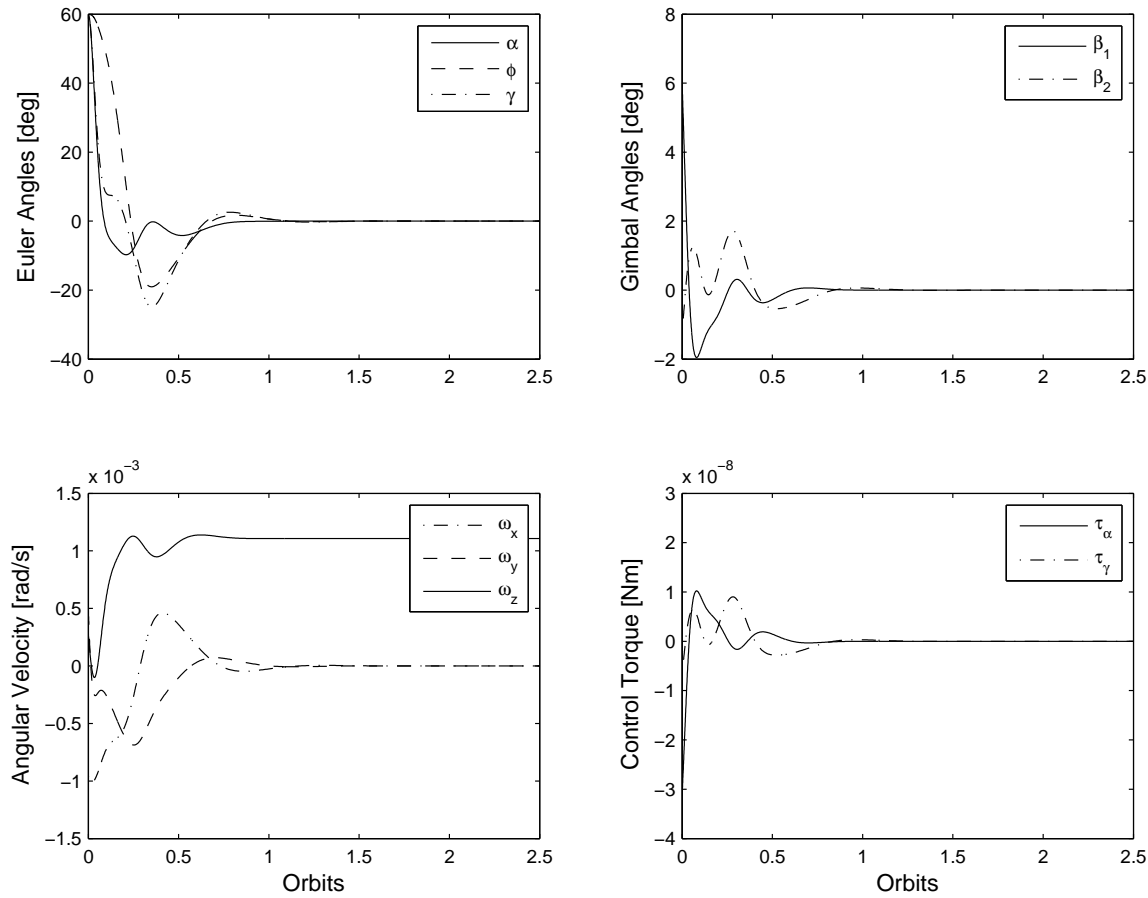


Figure 6.4: Controlled response for an axisymmetric spacecraft.

in Eq. (6.30). The simulations are applied to a rigid spacecraft with inertia matrix

$$\begin{bmatrix} 0.0017 & 0 & 0 \\ 0 & 0.0017 & 0 \\ 0 & 0 & 0.0020 \end{bmatrix} \quad (6.32)$$

The nondimensional inertia ratio are $k_1 = 0.1765$ and $k_2 = 0.1765$. The control law is designed based on stable moment of inertia specified in Table 6.1. When compared to Figs. 6.2 and 6.3, there is no deterioration in the attitude response shown in Fig. 6.4. Compared with the existing techniques for attitude control, one advantage of using high-order SMC is the tradeoff between tracking performance and control effort. Since the gimbal angle positions are obtained by integrating the rates, the control chattering is also negated.

6.3.3 Eccentricity and External Disturbances

A spacecraft moving in an elliptic orbit is examined and the corresponding attitude response is shown in Fig. 6.5. The spacecraft and control parameters used in the simulation are stated in Tables 6.1 and 6.2. The proposed controller effectively negates the disturbances caused by eccentricity and stabilizes the spacecraft even for an orbital eccentricity as high as $e = 0.3$. The steady state roll and yaw errors are zero while the pitch error is bounded by $|\alpha|_{max} = 0.05^\circ$. This illustrates the robustness of the control law [Eq. (6.21)] to the simultaneous presence of different types of uncertainties and disturbances.

To compensate for the bounded pitch motion of the spacecraft, the out of plane gimbal angle (β_1) is also bounded $|\beta_1|_{max} = 5^\circ$. The steady state yaw control torque is zero while the torque generated about the pitch axis is $|u_\alpha|_{max} = 2.2 \times 10^{-8}\text{Nm}$. The period

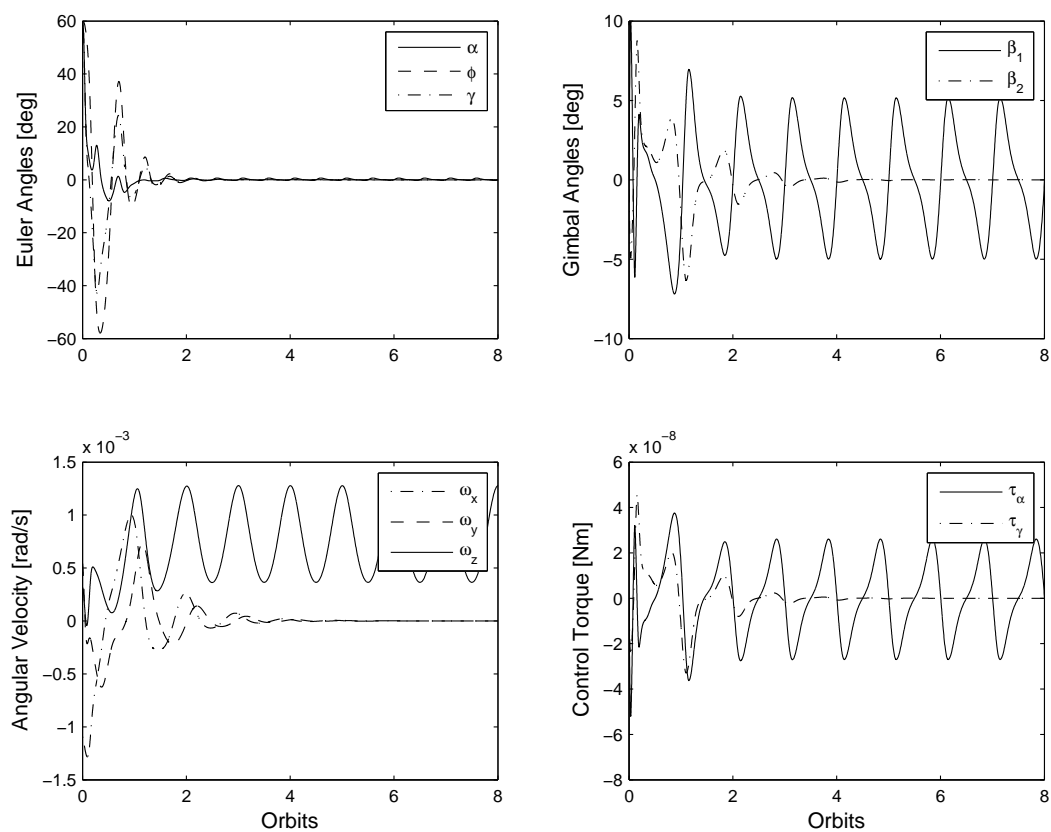


Figure 6.5: Effects of orbital eccentricity ($e = 0.3$) on controller performance.

of the steady state control torque is 1 orbit; this matches the simplified steady state pitch control input $U_\alpha = -r_y F \sin \beta_1$ obtained from Eq. (5.16), considering the null steady state errors. From the angular velocity plot, it is clearly evident that ω_z profile exhibits a periodic behavior. This can be explained using Eq. (5.11) where the steady state values of $\phi = \gamma = \dot{\phi} = 0$, we have $\omega_z = \dot{\theta} + \dot{\alpha}$. Since, for an elliptic orbit, $\dot{\theta} \neq 0$, and as mentioned earlier steady state α is bounded, ω_z also remains bounded.

Table 6.3: RyePicoSat parameters for disturbance models.

Symbol	Description	Value
ρ_d	Atmospheric density (kg/m ³)	4.89×10^{-13}
v	Orbital velocity (m/s)	7613
A_a	Aero contact surface area (m ²)	0.01
A_s	SRP contact surface area (m ²)	0.01
c	Speed of light (m/s)	3×10^8
C_D	Drag coefficient	2.50
C_g	Center of gravity	0.00
C_{pa}	Center of aerodynamic pressure	0.07
C_{ps}	Center of solar pressure	0.07
D_{res}	Residual dipole of RyeSat (A.m ²)	0.05
F_s	Solar constant (W/m ²)	1367
i_s	Sun incidence angle (deg)	0
M_e	Magnetic moment of Earth (T.m ³)	7.96×10^{15}
r	Coefficient of reflectivity	0.85

We next examine the disturbance rejection aspects of the control scheme when applied in the presence of environmental disturbances due to solar radiation pressure, aerodynamic drag, and magnetic forces. The time-varying forms of disturbance torques due to solar radiation pressure and aerodynamic drag are given by Eqs. (5.75) and (5.76), respectively. The positive scaling factors S_f and A_f have to be chosen based on the expected worst-case disturbance torques. For a pico-satellite in LEO, the worst case perturbing torques due to

solar radiation pressure, aerodynamic drag, and magnetic disturbances are given in Table 6.4. The parameters used for the calculations are given in Table 6.3 [Alger 2008].

Table 6.4: Disturbance torque models for RyePicoSat.

External Torques	Standard Formula	Value (in Nm)
Solar Radiation	$\tau_{solar} = \frac{F_s}{c} A_s (1 + r) \cos i_s (C_{ps} - C_g)$	6.14×10^{-9}
Magnetic	$\tau_{mag} = D_{res} \frac{2M_e}{R^3}$	2.49×10^{-6}
Aerodynamic	$\tau_{aero} = \frac{1}{2} \rho_d v^2 A_a C_D (C_{pa} - C_g)$	5.62×10^{-7}

Based on Table 6.4, the positive scaling factors were chosen as $S_f = 6.14 \times 10^{-9}$ and $A_f = 1.53 \times 10^{-6}$. The disturbance torque simulated is $T_d = T_a + T_s$. Figure 6.6 shows the performance of the proposed controller when the disturbances specified by Eqs. (5.75)

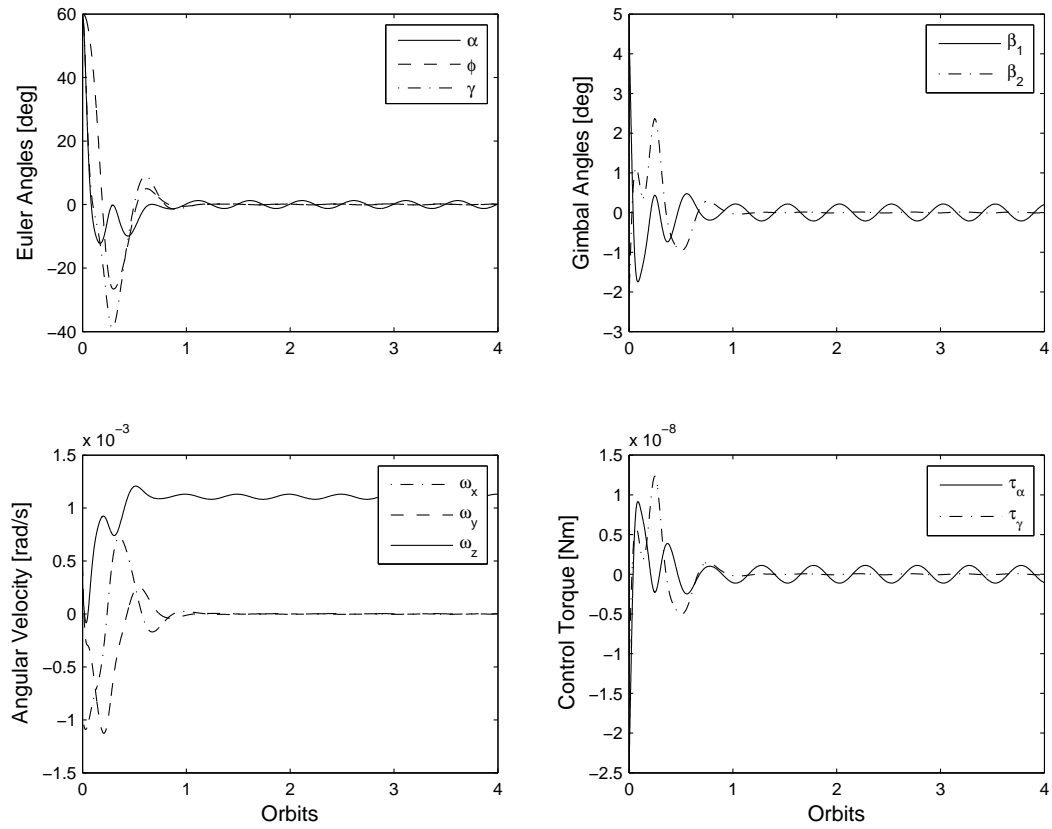


Figure 6.6: Effects of time-varying external disturbances on RyeSat.

and (5.76) are acting on the system, and the gains are set at the values listed in Table 6.2. As expected under external disturbances, the proposed controller is able to regulate the attitude motion and stabilize the errors to within the expected neighborhood of the origin, where they remain indefinitely. During the initial phase, gimbal angles are autonomously positioned to counteract large attitude errors. As the spacecraft is stabilized, gimbal angles smoothly track the disturbances and eliminate its effects as time increases.

6.4 Summary

In this chapter, a nonlinear control algorithm based on sliding mode theory was developed to stabilize the 3 axis attitude angles of a spacecraft using only a single thruster. Torques were generated using a thruster orientation mechanism with which the thrust vector can be tilted on a two-axis gimbal to provide the necessary framework for validating the proposed nonlinear control algorithm. To verify and validate the effectiveness of the proposed control algorithm, a high-fidelity nonlinear model of the spacecraft attitude dynamics was developed which includes the mathematical models of environmental disturbances acting on the spacecraft in LEO. The domains of sliding mode and the estimates of domain of attraction along with the regions of asymptotic stability are obtained utilizing Lyapunov's second method. When in sliding mode, the behavior of the system is dominated by lower-order dynamics and the effects of unmatched disturbances on the dynamic performance is studied. Numerical simulations illustrates that the proposed control scheme can successfully regulate the attitude motion from large initial conditions and stabilize the unactuated states to within the expected neighborhood of the origin, where they remain indefinitely.

Fault-Tolerant Control of Flexible Spacecraft

TETHERED satellite systems (TSS) have been proposed for a wide variety of applications ever since the first presentation of the “Shuttle-borne Skyhook” concept [Colombo *et al.* 1975]: a scientific satellite extended below the Shuttle to conduct low orbital altitude experiments. Numerous researchers have studied the dynamic aspects of TSS and many science missions have been flown to validate different tether models. The advantages of using an offset control scheme for attitude control and some important studies that examined the applicability of this approach were previously listed Section 1.3.3. Although this method has been used for many spacecraft systems, very few have accounted for unexpected severance of the tether, a major problem associated with the failure of many tethered spacecraft missions.

The initiation and process of two unscheduled events, tether severance and interference between tether and other hardware, using a high-speed computer simulation incorporating a nonlinear lumped-mass model was first investigated by [Trivailo *et al.* 1999]. Later on, [Williams *et al.* 2003] developed a flexible tether model to simulate the event of tether severance. Some of the potential problems that can occur due to tether severance include the following [Williams *et al.* 2003]: (1) The loss of tension at the severance point causes the tether to accelerate away from the platform, (2) The tether rotates around the attachment at the subsatellite, and (3) The tether becomes entangled in itself and does not rotate around the attachment at the subsatellite. A severed tether can also recoil and wrap around the platform [Blanksby & Trivailo 2000]. Although tether severance is numerically simulated in [Trivailo *et al.* 1999, Williams *et al.* 2003], the issue of attitude control using the remaining tether has not received its due attention in the literature.

In contrast, the purpose of this study is to propose a solution for TSS attitude control in a critical situation, when tether deployment suddenly stops and tether breakage occurs. For example, during stationkeeping phase of the mission, the tether might be completely severed by a hypervelocity impact with a micrometeorite. First, a detailed mathematical model is presented that consists of two identical tethers of equal length connecting the downward-deployed auxiliary mass to two distinct points that are symmetrically offset from the main satellite's mass center. An adaptive fault tolerant nonlinear control algorithm is then proposed to control the attitude of the main satellite using coordinated movement of the tether attachment points. Finally, several numerical examples are presented to demonstrate the fault recovery capability of the proposed control algorithms to counteract critical components failures and faults like tether severance, tether attachment point blocking, and sign-reversal of attachment point motion.

7.1 Proposed Tethered Satellite System

The investigation is initiated by formulating the equations of motion of the proposed TSS moving in a circular orbit. The proposed system model assumes a downward deployment of a small auxiliary mass from the satellite through a two-tether system (Fig. 7.1). Two identical tethers are attached to the satellite at two distinct points symmetrically offset from its mass center and below the satellite's principal Z axis. The other ends of the two tethers are connected to an auxiliary mass. To facilitate analytical treatment of the problem, only the case involving in-plane system motion is investigated. The coordinate frame $S-X_0 Y_0 Z_0$ passing through the system center of mass represents the orbital reference frame. The right-hand triad is formed with the X_0 -axis taken normal to the orbital plane, the Y_0 -axis taken along the local vertical, and the Z_0 -axis pointing along the local horizontal. The measured spacecraft orientation is a rotation α of the local frame about the X_0 -axis. Hence, the angle α defines the librational pitching angle with respect to the local vertical. The $S - X Y Z$ coordinate frame is used to represent the relative motion of the spacecraft with respect to the local orbital frame. For the variable length L joining the satellite mass center S and tether junction E , the angle β denotes rotation about the axis normal to the orbital plane

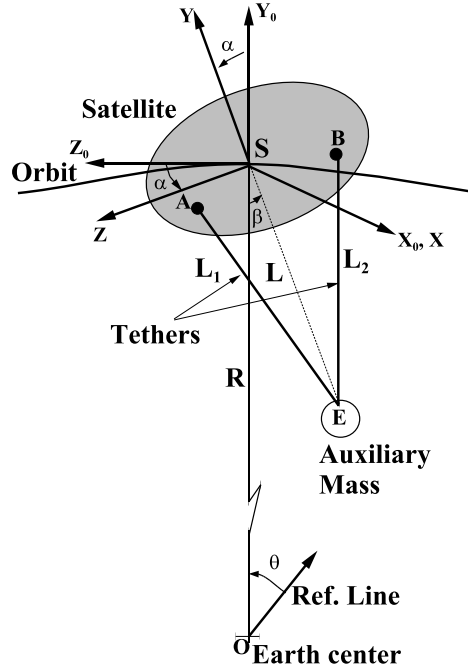


Figure 7.1: Geometry of the proposed tethered satellite system.

and is referred to as the in-plane swing angle. The satellite is assumed to be vertically above the ground station while passing over the ascending node. The corresponding nodal line represents the reference line in orbit for the measurement of the true anomaly.

Remark 7.1: Points A and B in Fig. 7.1 denote the attachment points of tether-1 and tether-2, respectively. Subscript $j = 1, 2$ denotes tether-1 and tether-2, respectively. a_k and b_k (for $k = 1, 2$) represents the horizontal and vertical offsets of tether attachment points A and B in the satellite $S - X_0 Y_0 Z_0$ coordinate frame. The stretched and unstretched tether lengths are denoted by L_j and L_{j0} , respectively. The tether lengths are nondimensionalized using a reference length, $L_{ref} = \sqrt{I_x/m_2}$. The nondimensional (length) parameters are:

$$\bar{a}_k = \frac{a_k}{L_{ref}}; \quad \bar{b}_k = \frac{b_k}{L_{ref}}; \quad l_j = \frac{L_j}{L_{ref}}; \quad l_{j0} = \frac{L_{j0}}{L_{ref}}; \quad l = \frac{L}{L_{ref}} \quad (7.1)$$

7.1.1 Energy Model and Equations of Motion

The satellite pitch angle α , the distance between the satellite mass center and the auxiliary mass (L), its associated in-plane swing angle β , and the two tether strains ε_1 and ε_2

constitute the chosen set of generalized coordinated that describe the motion of the system. The preceding generalized variables are not independent and they are related through dimensionless constraints as follows:

$$f_j = l_j - [\bar{a}_j^2 + \bar{b}_j^2 + l^2 + (-1)^j 2l\bar{h}_j]^{\frac{1}{2}} \quad (7.2)$$

where \bar{h}_j (for $j = 1, 2$) relates the satellite pitch angle (α) and tether swing angle (β) to the horizontal (\bar{a}_k) and vertical (\bar{b}_k) offsets of the tether attachment points.

$$\begin{aligned} \bar{h}_j &= \bar{a}_j \sin(\alpha - \beta) + (-1)^{j+1} \bar{b}_j \cos(\alpha - \beta) \\ l_j &= l_{j0} (1 + \varepsilon_j), \quad j = 1, 2 \end{aligned} \quad (7.3)$$

The major assumptions employed in the derivation of the model are:

1. The main spacecraft is considered to have much greater mass when compared to the tether and the subsatellite, and therefore the centre of mass of the system is assumed to coincide with the centre of mass of the main spacecraft.
2. The tether is assumed to be made of light material such as Kevlar, and, hence, is considered to have negligible mass.
3. The damping effects and transverse vibrations of the tethers are ignored. Because of relatively short tether lengths considered in this study (8 – 20m), it is assumed that the tether dynamics does not affect the orbital dynamics.

To apply the Lagrangian approach for the formulation of the system equations of motion, the expressions for the system kinetic energy (T) as well as the potential energy (V) are first obtained[Kumar & Kumar 2001]:

$$T = \frac{1}{2}M(\dot{R}^2 + \dot{\theta}^2 R^2) + \frac{1}{2}m_2 \left[\dot{L}^2 + (\dot{\theta} + \dot{\beta})^2 L^2 \right] + \frac{1}{2}I_x(\dot{\theta} + \dot{\alpha})^2 \quad (7.4)$$

$$\begin{aligned} V = & - \frac{\mu M}{R} + \frac{1}{4} \frac{\mu}{R^3} [(I_x + I_y + I_z) - 3\{I_x + (I_z - I_y) \cos 2\alpha\}] \\ & + \frac{1}{2} \frac{\mu}{R^3} m_2 [1 - 3\cos^2 \beta] L^2 + \frac{1}{2} EA \sum_{j=1}^2 L_{j0} \varepsilon_j^2 U(\varepsilon_j) \end{aligned} \quad (7.5)$$

The term $U(\varepsilon_j)$ in the potential energy expression is simply a unit function, the use of which precludes any negative strain in the tether.

$$U(\varepsilon_j)|_{j=1,2} = \begin{cases} 1, & \text{for } \varepsilon_j \geq 0 \\ 0, & \text{for } \varepsilon_j < 0 \end{cases} \quad (7.6)$$

The Lagrangian equations of motion corresponding to the various generalized coordinates indicated earlier can be obtained using the general relation

$$\frac{d}{dt} \left[\frac{\partial T}{\partial \dot{q}} \right] - \frac{\partial T}{\partial q} + \frac{\partial V}{\partial q} = Q + \sum_{j=1}^2 \Lambda_j \frac{\partial f_j}{\partial q} \quad (7.7)$$

where q denotes the vector of generalized coordinates, Q represents the generalized force corresponding to the generalized coordinate q , and Λ_j denotes the Lagrange multiplier corresponding to the j -th constraint. Substituting the generalized coordinates in Eq. (7.7) and carrying out the algebraic manipulation, we obtain the following governing nonlinear coupled ordinary differential equations of motion in dimensionless form.

Satellite Pitch (α):

$$\begin{aligned} \alpha'' - 1.5 I_r \sin(2\alpha) - \frac{\lambda_1}{l_1} l [\bar{a}_1 \cos(\alpha - \beta) - \bar{b}_1 \sin(\alpha - \beta)] \\ + \frac{\lambda_2}{l_2} l [\bar{a}_2 \cos(\alpha - \beta) + \bar{b}_2 \sin(\alpha - \beta)] = 0 \end{aligned} \quad (7.8)$$

L - in-plane swing (β):

$$\begin{aligned} \beta'' + 1.5 \sin(2\beta) + 2(1 + \beta') \left(\frac{l'}{l} \right) + \frac{\lambda_1}{l l_1} [\bar{a}_1 \cos(\alpha - \beta) + \bar{b}_1 \sin(\alpha - \beta)] \\ - \frac{\lambda_2}{l l_2} [\bar{a}_2 \cos(\alpha - \beta) + \bar{b}_2 \sin(\alpha - \beta)] = 0 \end{aligned} \quad (7.9)$$

L - dimensionless length (l):

$$l'' + \left[(1 - 3\cos^2\beta) - (1 + \beta')^2 \right] l + \frac{\lambda_1}{l_1} [l - \bar{h}_1] + \frac{\lambda_2}{l_2} [l + \bar{h}_2] = 0 \quad (7.10)$$

Tether Strain (ε_1):

$$EA_1 L_{10} \varepsilon_1 U(\varepsilon_1) = \Lambda_1 l_{10} \quad (7.11)$$

Tether Strain (ε_2):

$$EA_2 L_{20} \varepsilon_2 U(\varepsilon_2) = \Lambda_2 l_{20} \quad (7.12)$$

The tether strains given in Eqs. (7.11) and (7.12) can be nondimensionalized by using the following expression

$$\lambda_j = \frac{\Lambda_j}{m_2 L_{ref}^2 \Omega^2} \quad j = 1, 2 \quad (7.13)$$

Substituting Eq. (7.13) into Eqs. (7.11) and (7.12),

$$\begin{aligned} \lambda_1 &= C_1 \varepsilon_1 U(\varepsilon_1) \\ \lambda_2 &= C_2 \varepsilon_2 U(\varepsilon_2) \end{aligned} \quad (7.14)$$

where $C_1 = C_2 = EA/(m_2 L_{ref}^2 \Omega^2)$ is the tether rigidity parameter, EA (in N) is the modulus of rigidity of the tether, and $I_r = (I_y - I_z)/I_x$ is the satellite mass distribution parameter. In this study, a model of the tether dynamics that neglects tether flexibility is adopted for the control law design. Such models are often used in tether control law design because of their simplified mathematical representations and computational efficiency. The nonlinear, coupled ordinary differential equations of motion in dimensionless form described by Eqs. (7.8)-(7.14) being complex, numerical integration was resorted to for simulation of the satellite's attitude response. Tether offsets \bar{a}_1 and \bar{a}_2 are the control input terms which are embedded in the equations of motion to form the closed loop system.

7.1.2 Offset Control Methodology

The attitude stabilization problem considered here is to determine a control algorithm capable of coordinating the motion of tether (offset motion) attachment points which can stabilize the attitude of the main satellite to an asymptotically stable equilibrium point. From Eqs. (7.8)-(7.14), it is clearly evident that offset positions \bar{a}_1 and \bar{a}_2 are difficult to extract from the coupled equations to design a control law. Choosing the two offset velocities \bar{a}'_1 and \bar{a}'_2 as control inputs and integrating them to obtain offset positions simplifies the control design procedure. Moreover, an offset position specification scheme may result in velocities that are impossible to implement through conventional motors. On the other hand, the maximum offset velocities required for control could be easily lowered by adjusting the control gains within the control algorithm. In order to extract the offset velocities from the equations of motion, we differentiate Eq. (7.8). First consider,

$$\alpha'' = 1.5 I_r \sin(2\alpha) + C_1 E_1 \bar{A}_1 l - C_2 E_2 \bar{A}_2 l \quad (7.15)$$

where E_j and \bar{A}_j are given by

$$E_j = \left[\frac{1}{l_{j0}} - \frac{1}{l_j} \right]; \quad \frac{\lambda_j}{l_j} = C_j E_j; \quad \bar{A}_j = \bar{a}_i \cos(\alpha - \beta) + (-1)^j \bar{b}_j \sin(\alpha - \beta) \quad (7.16)$$

Analytical differentiation of Eq. (7.15) provides a detailed representation of the satellite pitch dynamics and the offset velocities can be explicitly obtained.

$$\alpha''' = I_r f_0(x) + \sum_{j=1}^2 (-1)^{j+1} C_j [E_j \bar{A}_j l' + E_j \bar{A}_j' l + E_j' \bar{A}_j l] \quad (7.17)$$

The derivative terms in Eq. (7.17) can be rearranged to extract \bar{a}'_1 and \bar{a}'_2 using,

$$\begin{aligned} f_0(x) &= 3 \cos(2\alpha) \alpha' \\ \bar{A}_j' &= \bar{a}'_j \cos(\alpha - \beta) - \bar{h}_j (\alpha' - \beta') \end{aligned} \quad (7.18)$$

$$E_j' = \left[\frac{\bar{a}_j + (-1)^j \sin(\alpha - \beta)}{l_j^3} \right] \bar{a}'_j + \frac{l l' + (-1)^j (\bar{h}_j l' + \bar{A}_j (\alpha' - \beta'))}{l_j^3} \quad (7.19)$$

Based on Eqs. (7.16)-(7.19), the following nonlinear terms can be introduced

$$f_0(x) = 3 \cos(2\alpha) \alpha' \quad (7.20)$$

$$f_1(x) = E_1 A_1 l' - E_1 \bar{h}_1 (\alpha' - \beta') l + \bar{A}_1 \frac{l l' - (\bar{h}_1 l' + \bar{A}_1 (\alpha' - \beta'))}{l_1^3} \quad (7.21)$$

$$f_2(x) = -E_2 A_2 l' - E_2 \bar{h}_2 (\alpha' - \beta') l - \bar{A}_2 \frac{l l' + (\bar{h}_2 l' + \bar{A}_2 (\alpha' - \beta'))}{l_2^3} \quad (7.22)$$

$$g_1(x) = \bar{A}_1 \left[\frac{\bar{a}_1 - l \sin(\alpha - \beta)}{l_1^3} \right] l + E_1 \cos(\alpha - \beta) l \quad (7.23)$$

$$g_2(x) = -\bar{A}_2 \left[\frac{\bar{a}_2 + l \sin(\alpha - \beta)}{l_2^3} \right] l - E_2 \cos(\alpha - \beta) l \quad (7.24)$$

The modified form of the pitch equation of motion explicitly showing the two offset velocities \bar{a}'_1 and \bar{a}'_2 as control inputs is given by:

$$\alpha''' = I_r f_0(x) + C_1 f_1(x) + C_2 f_2(x) + C_1 g_1(x) \bar{a}'_1 + C_2 g_2(x) \bar{a}'_2 \quad (7.25)$$

7.2 Design of Control Laws

In this section, we present the theoretical basis for incorporating TSS attitude control using coordinated motion of tether offsets into the nonlinear control framework. Firstly, the methods and analysis tools of sliding mode nonlinear control are developed that are robust to nonlinear model errors. The formulation of the nominal sliding mode controller is then improved using adaptive approximation in the presence of model uncertainties.

7.2.1 Nominal Sliding Mode Control

Sliding mode control is a robust nonlinear feedback control methodology that belongs to a kind of variable-structure control system in which the structure between switching surfaces is changed to achieve desired performance. Sliding mode control is insensitive to external disturbances [Slotine & Li 1991b] and therefore one can consider it to implement the offset control scheme for TSS. The group of state variables used to construct the sliding surface are α , α' , and α'' . The sliding surface S is defined as

$$S = \alpha'' + p_2\alpha' + p_1\alpha \quad (7.26)$$

where p_1 and p_2 are positive constants. The basic idea is to alter the system dynamics such that the trajectory of the system is steered onto the sliding manifold described by $S = 0$.

Next, the control law is derived based on Lyapunov stability theorem. The control algorithm that forces the motion of the states to be along the sliding manifold $S = 0$ can be determined by choosing the Lyapunov energy function defined as follows:

$$V = \frac{1}{2}S^2 \quad (7.27)$$

Differentiating V we get,

$$V' = SS' = S(\alpha''' + p_2\alpha'' + p_1\alpha') \quad (7.28)$$

Substituting for α''' from Eq. (7.25) in Eq. (7.28) we get,

$$V' = S[I_r f_0(x) + C_1 f_1(x) + C_2 f_2(x) + C_1 g_1(x) \bar{a}'_1 + C_2 g_2(x) \bar{a}'_2 + p_2\alpha'' + p_1\alpha'] \quad (7.29)$$

The objective of a Lyapunov function incorporated based on sliding mode technique is to find a control law such that $S S'$ is always negative-definite ($S S' < 0$).

$$\begin{aligned} I_r f_0(x) + C_1 f_1(x) + C_2 f_2(x) + p_2 \alpha'' + p_1 \alpha' + C_1 g_1(x) \bar{a}'_1 \\ + C_2 g_2(x) \bar{a}'_2 = -\eta \text{sat}(S) - kS \end{aligned} \quad (7.30)$$

where η and k are positive constants. The saturation function $\text{sat}(S)$ is used to suppress the control chatter [Fernandez & Hedrick 1987]. Substituting Eq. (7.30) into Eq. (7.29), V' becomes negative-definite. Hence, the system is stable and its trajectory will approach the sliding plane while converging toward the origin.

$$V' = -\eta |S| - kS^2 \leq 0 \quad (7.31)$$

Rearranging the terms in Eq. (7.30), the control laws can be obtained as

$$\bar{a}'_1 = \frac{D_1}{D_1^2 + D_2^2} D_3 \quad \text{and} \quad \bar{a}'_2 = \frac{D_2}{D_1^2 + D_2^2} D_3 \quad (7.32)$$

where

$$\begin{aligned} D_1 &= C_1 g_1(x) \\ D_2 &= C_2 g_2(x) \\ D_3 &= -\eta \text{sgn}(S) - kS - I_r f_0(x) - C_1 f_1(x) - C_2 f_2(x) - p_2 \alpha'' - p_1 \alpha' \end{aligned} \quad (7.33)$$

For the existence of the control inputs described by Eq. (7.32), $D_1^2 + D_2^2$ must be non-zero in the region of interest. After carrying out some simplifications, the region Ω_S ($\Omega_{S_1} \cap \Omega_{S_2}$) of singularity in which $D_1^2 + D_2^2 = 0$ is given by

$$\begin{aligned} \Omega_{S_j} &= \left\{ D_j^2 = C_j^2 \left\{ \frac{1}{\bar{a}_j} \cos(\alpha - \beta) + \frac{\bar{b}_j}{\bar{a}_j} [1 - \sin(\alpha - \beta)] \right\}^2 = 0 \right\} \\ &= \left\{ \left[\frac{1}{\bar{a}_j} \cos(\alpha - \beta) + \frac{\bar{b}_j}{\bar{a}_j} [1 - \sin(\alpha - \beta)] \right] = 0 \right\} \\ &= \left\{ \alpha - \beta = (4n + 1) \frac{\pi}{2} \right\} \end{aligned} \quad (7.34)$$

where $j = 1, 2$ and $n \in J$, is a set of integers. The control law is well defined as long as the trajectory of the closed-loop system does not enter the region Ω_s . The control inputs \bar{a}_1 and \bar{a}_2 are obtained by numerically integrating the expressions in Eq. (7.32), and are then substituted in Eq. (7.8) to complete the closed-loop dynamics of the system.

7.2.2 Adaptive Sliding Mode Control

In TSS, parameter uncertainties can pose numerous problems in the control tasks, causing inaccuracy and instability in the control system. Adaptive control deals with situations in which some of the parameters are unknown or slowly time-varying. The basic idea is to estimate these unknown parameters online and then use the estimated parameters in place of the unknown parameters in the feedback control law. Two different types of adaptive control for the TSS are considered in this section.

Case I Exact parameter representation is considered based on constant system parameters I_r , C_1 , and C_2 . Adaptive control law is developed based on the nominal nonlinear control law designed in Sec. 7.2.1. Although the true values of C_1 and C_2 are equal, we evaluate the controller when their estimated values could differ.

Case II Modified system parameters represented as $\eta_1 = \frac{I_r}{C}$ and $\eta_2 = \frac{1}{C}$, where $C = C_1 = C_2$, are considered. This is a valid assumption because the two tethers considered in this study are made of the material. Hence, their respective rigidity parameters will be approximately the same.

The tether rigidity parameters are denoted separately with subscripts 1 and 2, to induce tether failure into the model. For example, to consider the failure of tether 2, we set $C_2 = 0$ in the plant. In both cases, the control laws are designed to be fault-tolerant based on passive methods; that is, information regarding the failure of tether 2 is not detected and passed to the control algorithm.

7.2.2.1 Fault Tolerant Adaptive Control (Case I)

In this case, I_r , C_1 , and C_2 are considered to be unknown constant parameters. The parameter estimation errors are given by

$$\tilde{I}_r = \hat{I}_r - I_r, \quad \tilde{C}_1 = \hat{C}_1 - C_1, \quad \tilde{C}_2 = \hat{C}_2 - C_2 \quad (7.35)$$

The adaptive algorithm is developed based on the same sliding surface given by Eq. (7.26). A candidate Lyapunov function is defined as follows:

$$V = \frac{1}{2}S^2 + \frac{1}{2\gamma_r}\tilde{I}_r^2 + \frac{1}{2\gamma_1}\tilde{C}_1^2 + \frac{1}{2\gamma_2}\tilde{C}_2^2 \quad (7.36)$$

where γ_r , γ_1 , and γ_2 are positive constants. Taking the first derivative of V along the trajectory of the system gives,

$$V' = SS' + \frac{\tilde{I}_r \tilde{I}_r'}{\gamma_r} + \frac{\tilde{C}_1 \tilde{C}_1'}{\gamma_1} + \frac{\tilde{C}_2 \tilde{C}_2'}{\gamma_2} \quad (7.37)$$

Substituting for α''' from Eq. (7.25) in S' , we get

$$\begin{aligned} S' &= I_r f_0(x) + C_1 f_1(x) + C_2 f_2(x) + C_1 g_1(x) \bar{a}'_1 + C_2 g_2(x) \bar{a}'_2 + p_2 \alpha'' + p_1 \alpha' \\ &= (\hat{I}_r - \tilde{I}_r) f_0(x) + (\hat{C}_1 - \tilde{C}_1) f_1(x) + (\hat{C}_2 - \tilde{C}_2) f_2(x) + (\hat{C}_1 - \tilde{C}_1) g_1(x) \bar{a}'_1 \\ &\quad + (\hat{C}_2 - \tilde{C}_2) g_2(x) \bar{a}'_2 + p_2 \alpha'' + p_1 \alpha' \end{aligned}$$

The adaptive law components and control algorithm components are split as per:

$$\begin{aligned} \hat{I}_r f_0(x) + \hat{C}_1 [f_1(x) + g_1(x) \bar{a}'_1] + \hat{C}_2 [f_2(x) + g_2(x) \bar{a}'_2] \\ + p_2 \alpha'' + p_1 \alpha' = -\eta \text{sat}(S) - kS \end{aligned} \quad (7.38)$$

$$\begin{aligned} \frac{\tilde{I}_r \hat{I}_r'}{\gamma_r} + \frac{\tilde{C}_1 \hat{C}_1'}{\gamma_1} + \frac{\tilde{C}_2 \hat{C}_2'}{\gamma_2} - S [\tilde{I}_r f_0(x) + \tilde{C}_1 f_1(x) + \tilde{C}_2 f_2(x) \\ + \tilde{C}_1 g_1(x) \bar{a}'_1 + \tilde{C}_2 g_2(x) \bar{a}'_2] = 0 \end{aligned} \quad (7.39)$$

Substituting Eqs. (7.38) and (7.39) in Eq. (7.37) will ensure that V' is negative-definite: $V' = -\eta|S| - kS^2 \leq 0$. The parameter update laws are obtained by collecting terms in Eq. (7.39) and solving them separately.

$$\begin{aligned} \hat{I}_r' &= \gamma_r S f_0(x) \\ \hat{C}_1' &= \gamma_1 S [f_1(x) + g_1(x) \bar{a}'_1] \\ \hat{C}_2' &= \gamma_2 S [f_2(x) + g_2(x) \bar{a}'_2] \end{aligned} \quad (7.40)$$

The expressions for offset velocities can be determined by rearranging terms in Eq. (7.38).

$$\bar{a}'_1 = \frac{\hat{D}_1}{\hat{D}_1^2 + \hat{D}_2^2} \hat{D}_3 \quad \text{and} \quad \bar{a}'_2 = \frac{\hat{D}_2}{\hat{D}_1^2 + \hat{D}_2^2} \hat{D}_3 \quad (7.41)$$

where

$$\begin{aligned} \hat{D}_1 &= \hat{C}_1 g_1(x) \quad \text{and} \quad \hat{D}_2 = \hat{C}_2 g_2(x) \\ \hat{D}_3 &= -\eta \text{sgn}(S) - kS - \hat{I}_r f_0(x) - \hat{C}_1 f_1(x) - \hat{C}_2 f_2(x) - p_2 \alpha'' - p_1 \alpha' \end{aligned} \quad (7.42)$$

The update laws in Eq. (7.40) provide an estimate of the unknown parameters \hat{I}_r , \hat{C}_1 , and \hat{C}_2 which are subsequently provided to the offset velocity control schemes given by Eq. (7.41). The offset positions are obtained by integrating Eq. (7.41).

7.2.2.2 Fault Tolerant Adaptive Control (Case II)

For the TSS considered in this study both the tethers are made of the same material and therefore, the assumption that $C = C_1 = C_2$ is a valid one. Hence, instead of estimating \hat{I}_r , \hat{C}_1 , and \hat{C}_2 separately, we follow a modified system parameter representation for developing a new adaptive control law for the TSS. The spacecraft pitch motion given by Eq. (7.25) can be reexpressed in the following form

$$\eta_2 \alpha''' = \eta_1 f_0(x) + [f_1(x) + f_2(x) + g_1(x) \bar{a}'_1 + g_2(x) \bar{a}'_2] \quad (7.43)$$

where $\eta_1 = I_r/C$ and $\eta_2 = 1/C$. The new system parameter estimates are

$$\tilde{\eta}_1 = \hat{\eta}_1 - \eta_1, \quad \tilde{\eta}_2 = \hat{\eta}_2 - \eta_2 \quad (7.44)$$

To examine the convergence property of α , consider a Lyapunov function candidate, that includes adaptive parameters and control variables, defined as follows:

$$V = \frac{1}{2} |\eta_2| S^2 + \frac{1}{2} \gamma_1 \tilde{\eta}_1^2 + \frac{1}{2} \gamma_2 \tilde{\eta}_2^2 \quad (7.45)$$

where γ_1 and γ_2 are positive constants. Of course, in this study, η_2 is always positive. Taking the derivative of V , adding and subtracting $\hat{\eta}_1 f_0(x)$ and $\hat{\eta}_2(p_2 \alpha'' + p_1 \alpha')$, and collecting terms gives,

$$\begin{aligned} V' = S[& \hat{\eta}_1 f_0(x) + g_1(x) \bar{a}'_1 + g_2(x) \bar{a}'_2 + f_1(x) + f_2(x) + \hat{\eta}_2(p_2 \alpha'' + p_1 \alpha')] \\ & - \tilde{\eta}_1 S f_0(x) - \tilde{\eta}_2 S(p_2 \alpha'' + p_1 \alpha') + \gamma_1 \tilde{\eta}_1 \hat{\eta}'_1 + \gamma_2 \tilde{\eta}_2 \hat{\eta}'_2 \end{aligned} \quad (7.46)$$

To make $V' \leq 0$, the parameter update laws are chosen to cancel unknown terms:

$$\hat{\eta}'_1 = \gamma_1^{-1} S f_0(x), \quad \hat{\eta}'_2 = \gamma_2^{-1} S(p_2 \alpha'' + p_1 \alpha') \quad (7.47)$$

The control inputs are obtained by solving the preceding expression [Eq. (7.46)] for \bar{a}'_1 and \bar{a}'_2 , and the adaptive control laws that guarantee asymptotic stability for the system are given by,

$$\bar{a}'_1 = \frac{g_1(x)}{g_1^2(x) + g_2^2(x)} g_0(x) \quad \text{and} \quad \bar{a}'_2 = \frac{g_2(x)}{g_1^2(x) + g_2^2(x)} g_0(x) \quad (7.48)$$

where the adaptive system parameters are specified in the term $g_0(x)$,

$$g_0(x) = \eta \text{sat}(S) + kS + \hat{\eta}_1 f_0(x) + \hat{\eta}_2(p_2 \alpha'' + p_1 \alpha') \quad (7.49)$$

For the existence of control laws in Eq. (7.48), $g_1^2(x) + g_2^2(x)$ must be non-zero in the region of interest $\Omega_S (\Omega_{S_1} \cap \Omega_{S_2})$ as formulated in Eq. (7.34).

7.2.3 Tether Failure

In this study, we only consider the failure of tether 2, represented by L_2 in the geometry of the TSS described in Figure 7.1. Tether breakage is implemented by setting $C_2 = 0$ in the system equations of motion. Therefore,

$$\begin{aligned} \beta'' + 1.5 \sin(2\beta) + 2(1 + \beta') \left(\frac{l'}{l}\right) + \frac{\lambda_1}{l\bar{l}_1} [\bar{a}_1 \cos(\alpha - \beta) + \bar{b}_1 \sin(\alpha - \beta)] &= 0 \\ \alpha'' - 1.5I_r \sin(2\alpha) - \frac{\lambda_1}{l} l [\bar{a}_1 \cos(\alpha - \beta) - \bar{b}_1 \sin(\alpha - \beta)] &= 0 \\ l'' + [(1 - 3\cos^2\beta) - (1 + \beta')^2] l + \frac{\lambda_1}{l_1} [l - \bar{h}_1] &= 0 \end{aligned} \quad (7.50)$$

The effects of this failure on the control strategies considered in this study are:

1. For the case of nominal sliding mode control, if tether 2 fails, it is assumed that the failure is detected and the information is passed to the control system. This method reacts to tether failure actively by properly reconfiguring its control actions so that the stability and performance of the entire system can still be acceptable. Hence, the control law given by Eq. (7.32) simplifies to

$$\bar{a}'_1 = \frac{D_3}{D_1} \quad \text{and} \quad \bar{a}'_2 = 0 \quad (7.51)$$

In order to achieve a successful control system reconfiguration, this methodology relies heavily on the real-time fault detection and isolation scheme (not considered in this study) for precise information regarding the status of the components (actuators and sensors) and operating conditions of the system.

2. For the adaptive fault-tolerant control laws considered in cases I and II, tether failure ($C_2 = 0$) is incorporated in the system model but the failure information is not provided to the control laws. Instead of using an explicit failure detection and isolation algorithm, this methodology is based on the adaptive control theory where the controller is constantly updating itself.

In this study, we do not account for collision dynamics of the tether with itself or the second tether, and hence the consequence of tether entanglement is not assessed. Similarly for the case of tether severance, tether recoil and wrapping of the remaining tether around the main satellite is not considered.

7.3 Dynamical Features of Proposed TSS

An important principle governing the dynamics of TSS is the presence of changing gravitational and centrifugal accelerations as the distance from the Earth's center changes. For two-tether systems, the net restoring force is capable of stabilizing TSS about the local vertical and the difference in the forces experienced by the main satellite and the subsatellite keeps the two tethers under tension. The combined effects of these properties tend to keep the system in a desired configuration without the use of thrusters or other actuators. The motion of the subsatellite can be controlled efficiently using two tethers and the added benefit of redundancy in the case of tether severance makes this system reliable with respect to control hardware failures. Main dynamical features of a two-tether satellite system are: (1) Traveling Waves, and (ii) Tether Severance.

7.3.1 Traveling Waves

Traveling waves along two tethers where both tethers are aligned along the local vertical was simulated using a VRML animation of a two-tethered system in [Williams *et al.* 2003]. The tension at the two attachment points cause the tethers to be pulled apart at the main satellite end. This initiates traveling waves along each of the tethers. When these waves reach the subsatellite, it is reflected and begins to travel back towards the main satellite. Thus, a complex set of lateral oscillations begins to propagate, that consists of a large set of superimposed traveling waveforms. A major drawback of this phenomenon is that the two tethers can overlap after the traveling wave is reflected off the subsatellite. Therefore, control schemes that can suppress these lateral modes of tether vibrations are required to avoid the chances of tether entanglement. Since this study deals with short tethers (< 100 m), the system is not prone to the problem of entanglement of the tethers.

7.3.2 Tether Severance

Severance may occur either as a result of interference (due to tether dynamics during retrieval), or as a result of some other event such as collision with a micrometeorite [Trivailo *et al.* 1999]. Assuming that the tether mass is negligible in comparison to that

of the subsatellite mass; then, it is plausible that, after failure, the portion of the tether connected to the main satellite goes slack. In this case the motion is unstable and the remaining tether may recoil and wrap around the main satellite. The velocity field originated after failure creates increasing tension on the tether due to tether mass and finite values of phase speed at which the longitudinal waves propagate [Bergamaschi 1982]. Before failure, the tether is in a stressed equilibrium due to the mass of the main satellite and its own inertia. After failure, the elastic energy stored in part of the tether connected to the subsatellite is converted in kinetic energy. Therefore, it is important to ensure that the tether is severed at points sufficiently close to the main satellite. Two solutions suggested by [Bergamaschi 1982] are: (i) use a tether with increased cross-section in its terminal part so that the probability of failure near the sub-satellite is as small as possible, and (ii) connect the terminal part to the remained of the tether by means of a damper, in order to absorb the longitudinal elastic waves propagating toward the main satellite.

7.4 Performance Evaluation

To study the effectiveness and performance of the proposed attitude control strategies, the detailed system response is numerically simulated using the set of governing equations of motion [Eqs. (7.8)-(7.14)] in conjunction with the proposed control laws Eqs. (7.32), (7.41), and (7.48). The equilibrium and desired states of the system are $\alpha_e = \alpha_d = 0$, $\alpha'_e = \alpha'_d = 0$, $\alpha''_e = \alpha''_d = 0$. For simulation of the attitude response, the system parameters are chosen in dimensionless form. This enhances the scope for application of these results, regardless of the satellite size. The equations were nondimensionalized with respect to the subsatellite mass m_2 , the tether reference length l_{ref} , and the orbital rate Ω . The nondimensional system parameters and initial conditions considered in this study are indicated in Table 7.1.

Figure 7.2 shows the uncontrolled response of the TSS with tether breakage and the presence of initial disturbances specified in Table 7.1. Although the trajectories stay bounded, they experience sustained and repeated oscillations. As discussed earlier, this phenomenon can make the system unstable. The tensile stress due to gravity gradient is large enough

Table 7.1: TSS Simulation parameters

Parameters	Values
Mass ratio, I_r	1
Unstretched tether lengths, l_{j0}	$l_{10} = l_{20} = 10$
Tether rigidity parameter, C_j	$C_1 = C_2 = 2 \times 10^7$
Initial offset	
Local horizontal, \bar{a}_{j0}	$\bar{a}_{10} = \bar{a}_{20} = 0.2$
Local vertical, \bar{b}_{j0}	$\bar{b}_{10} = \bar{b}_{20} = 0.5$
Initial conditions $\{\alpha, \alpha', \beta, \beta'\}$	$\{0, 0.1, 0, 0.01\}$
Occurrence of tether breakage	at 0.1 orbit

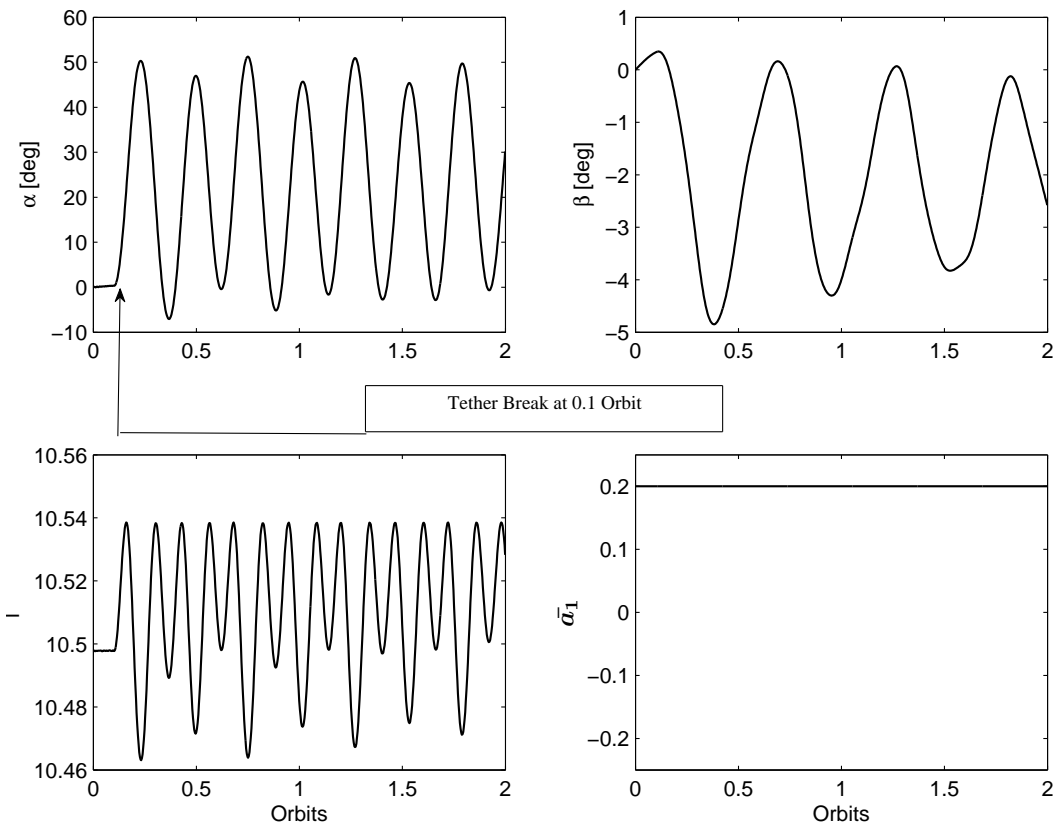


Figure 7.2: Uncontrolled response of TSS subjected to initial errors and tether failure.

to prevent tension loss at the main satellite end, and therefore the Coriolis force causes the repeated oscillations in the attitude dynamics of the system. The objective is to bring the pitch motion of the spacecraft back to its equilibrium position ($\alpha_e = 0$).

7.4.1 Nominal Sliding Mode Control

Figure 7.3 shows the controlled response of the system using the nominal sliding mode offset control scheme. The controller was simulated using the following parameters:

$$p_1 = 300n, p_2 = 0.4n, \eta = 0.4, k = 10 \quad (7.52)$$

The values of n are fine-tuned to get a good response of the satellite pitch angle. For $n = 47,000$, it is clearly evident from Fig. 7.3 that the sliding mode controller is able to stabilize the attitude motion of the satellite. It is also interesting to note that even for high gains used in the sliding surfaces, the tether offset variations remain within ± 0.2 initially

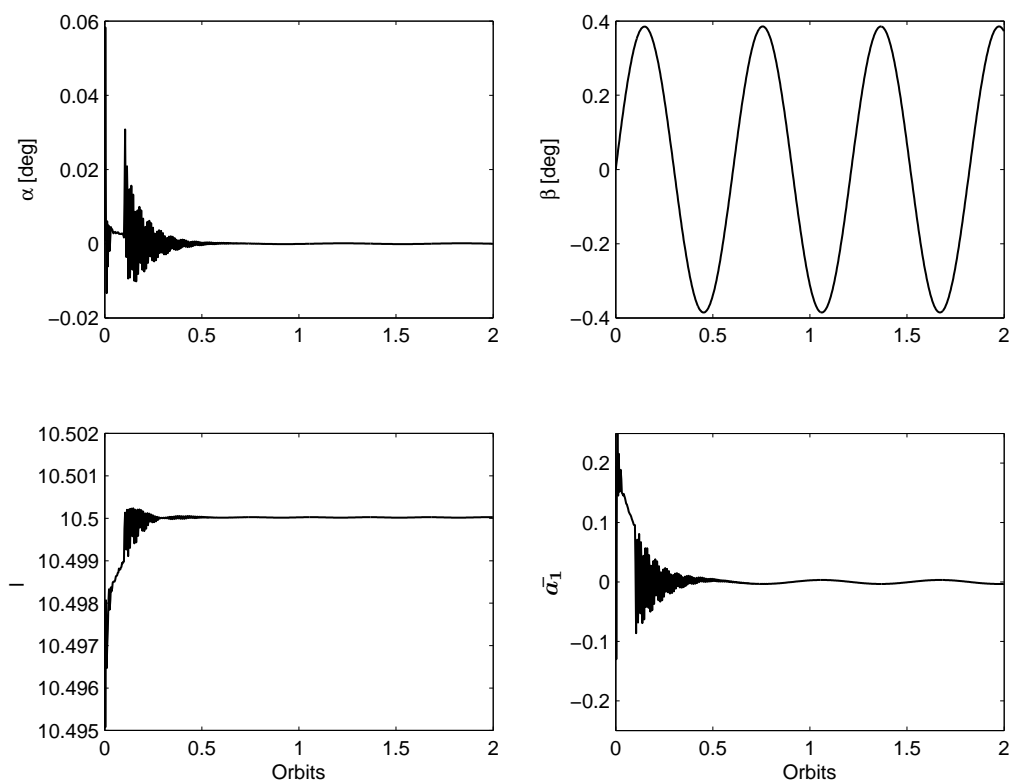


Figure 7.3: Controlled response of TSS with tether breakage at 0.1 orbit.

and gradually settle down to a value of zero. The offset regulator does not return the system to the equilibrium state corresponding to the terminal position of the attachment point $\bar{a}_{10} = 0.2$. Due to severance of tether-2, the equilibrium position of the system will pertain to $\bar{a}_{10} = 0$, since the offset corresponding to tether-2 does not exist. The nominal SMC has proven to be very effective in stabilizing the pitch motion of the satellite. The control algorithm developed in this study is also applicable to non-circular orbits. However, it is well known for dumbbell systems that elliptical orbits do not have stable equilibrium points [Fujii & Ichiki 1997]. The system is not stabilizable at the local vertical, but rather enters into a controlled periodic motion about the desired equilibrium point.

We next examine the effect of adding external disturbances to the system between specified orbit ranges. The disturbance model is described by

$$\alpha'' = g(\alpha, \alpha', \beta, \beta', l, l', \bar{a}_1, \bar{a}_2) + d_1 \quad (7.53)$$

where $d_1 = 4$ is a lumped disturbance which include the parameter variations and other

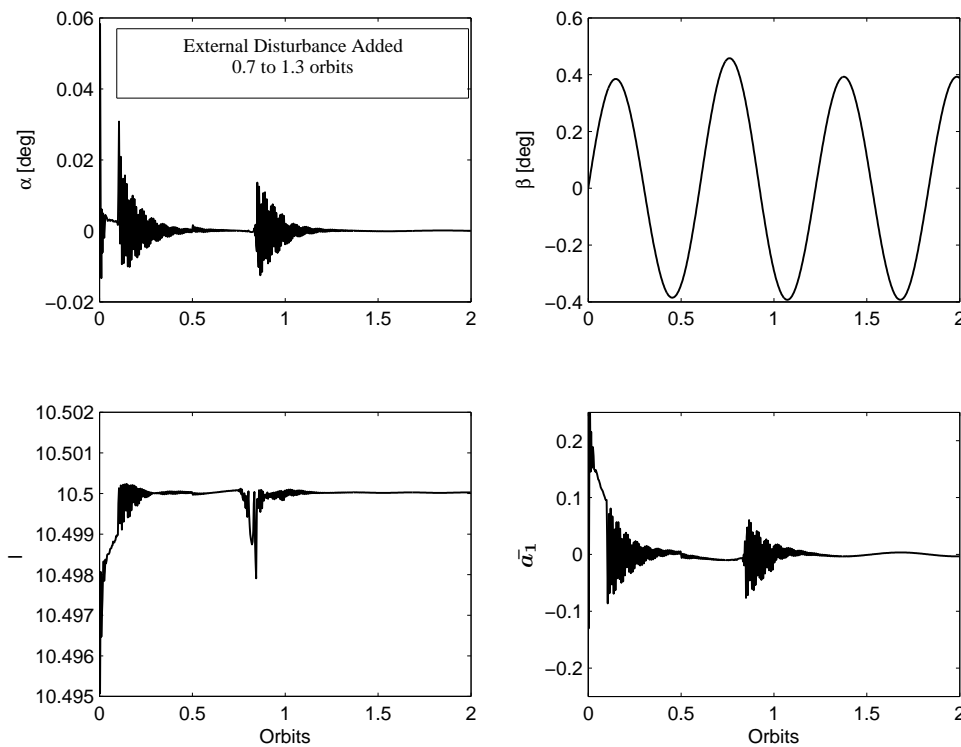


Figure 7.4: Effect of external disturbances and tether breakage.

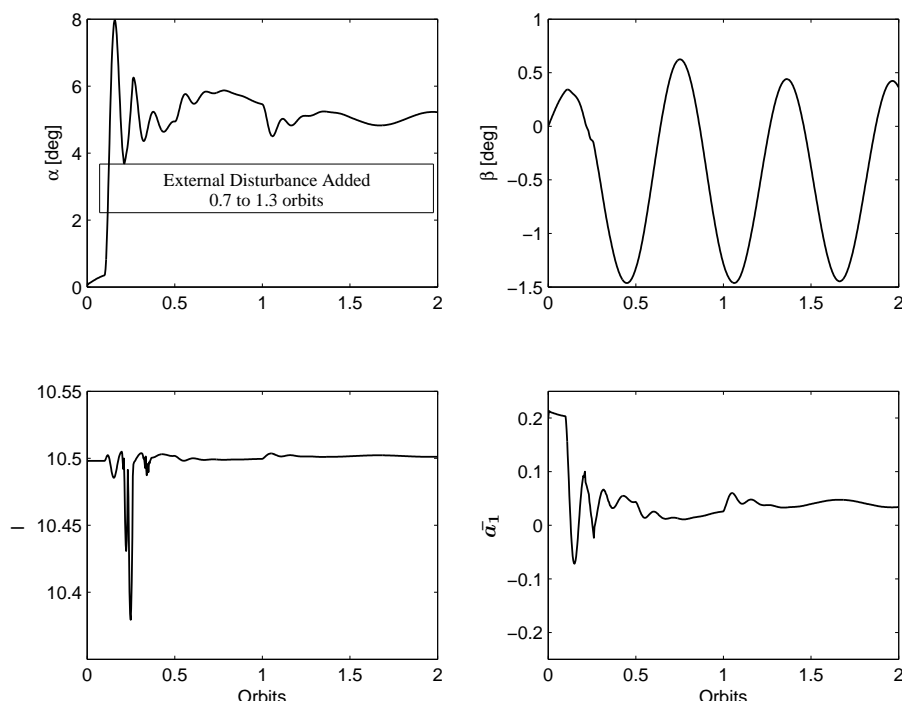


Figure 7.5: Effect of external disturbances on linear controller.

external disturbances. This disturbance is nondimensional and is activated for a specified time frame, 0.7 to 1.3 orbits. For a TSS constituting a microsatellite 60 kg, $I_x = 18.2 \text{ kg}\cdot\text{m}^2$ and an auxiliary mass ($m_2 = 10 \text{ kg}$) in a 500 km circular orbit, this disturbance torque will be approximately equal to $2 \times 10^{-4} \text{ N}\cdot\text{m}$. The addition of external disturbance is expected to cause certain variations in the response of the system, and the performance of sliding mode controller is investigated for this scenario. Figure 7.4 shows that the proposed control strategy is able to overcome the external disturbances and progressively reduce the attitude errors. This is achieved with very smooth control actuation.

The advantage of using a nonlinear controller under such circumstances can only be observed if the control responses are compared with the performance of a linear controller. The linear controller to vary the tether offset is a proportional-derivative law:

$$\bar{a}_1 = -(\mu_1 \alpha' + \nu \alpha) \quad \text{and} \quad \bar{a}_2 = (\mu_1 \alpha' + \nu \alpha) \quad (7.54)$$

The linear control gains are chosen as $\mu_1 = 0.001$ and $\nu = 20$. The nonlinear control law developed in Eq. (7.32) was linearized and compared to Eq. (7.54), and then the gains were

selected based on p_1 and p_2 in Eq. (7.52). Rather than adopting a trial and error procedure, the above mentioned method is more systematic for comparison of both the control laws. The controlled response of using a linear controller for the TSS undergoing initial in-plane attitude disturbances and external disturbances when the system is subjected to tether failure at 0.1 orbit is shown in Fig. 7.5. It is clearly evident that the proposed sliding mode controller has an advantage over the linear controller when external disturbances are added to the system. The linear controller is ineffective in damping the pitch response of the main satellite (α).

7.4.2 Fault-tolerant Adaptive Control

We next investigate the effect of model uncertainties on the performance of the system. For case I, an adaptive control law proposed in Eq. (7.41) is used for simulating the attitude response. The controller was numerically simulated with the system mathematical model using the following sliding plane parameter values:

$$p_1 = 300n, \quad p_2 = 0.4n, \quad \eta = 0.4, \quad k = 5 \quad (7.55)$$

The value of $n = 420$ was chosen for the adaptive controller, compared with the large value chosen for the nominal sliding mode controller [Eq. (7.52)]. The initial parameter estimates are taken as follows:

$$\hat{I}_{r_0} = 0.5, \quad \hat{C}_{1_0} = 2 \times 10^5, \quad \text{and} \quad \hat{C}_{2_0} = 2 \times 10^5 \quad (7.56)$$

The parameters of the plant are considered to be the same as mentioned in Table 7.1. Figure 7.6 presents the response of the system using the adaptive control law in Eq. (7.41). Tether 2 fails after 0.1 orbit. When compared with the controller response obtained using the sliding mode controller in Fig. 7.3, it is clearly evident that the adaptive controller performs better in damping the oscillations of the pitch attitude. The overshoot and frequency of oscillations in the pitch motion is also found to be reduced considerably when compared with Fig. 7.3. Another important point to note here is the use of low-value gains when compared with the nominal sliding mode controller. The plot of parameter estimates are shown in Fig. 7.7. The constants for the adaptation laws were chosen as

$$\gamma_r = 1.8, \quad \text{and} \quad \gamma_1 = \gamma_2 = 1.2 \quad (7.57)$$

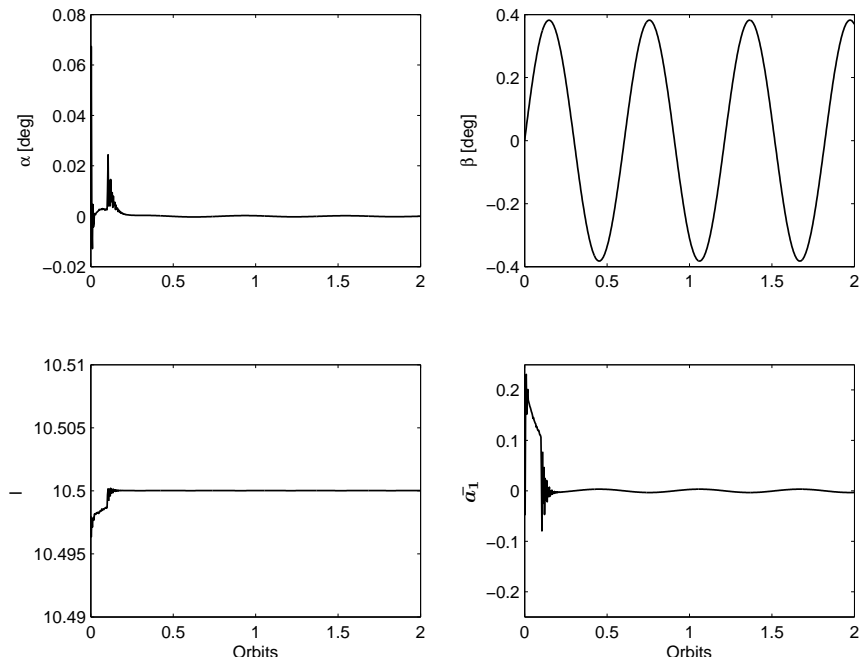
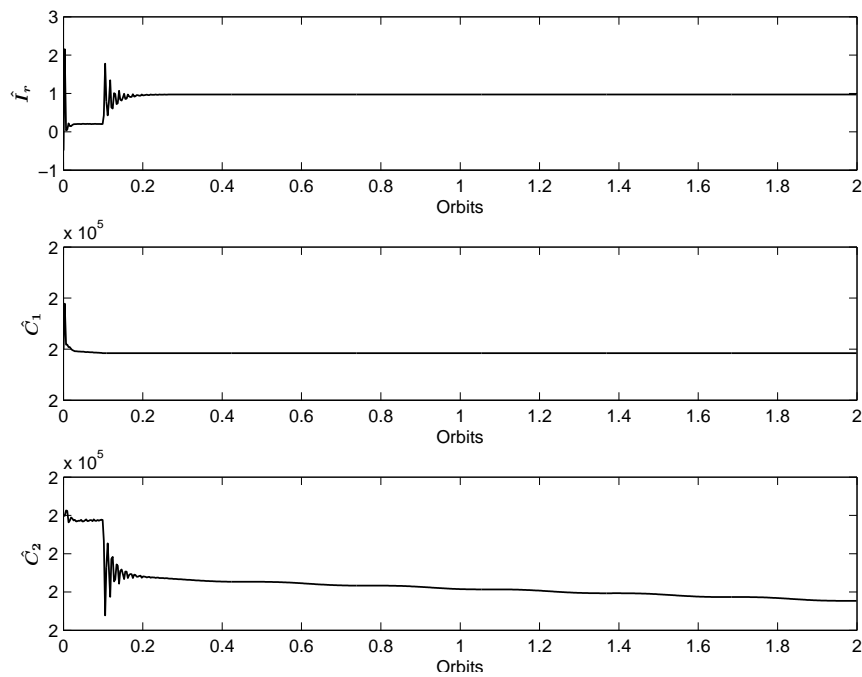


Figure 7.6: Controlled system response using adaptive control law - Case I.

Figure 7.7: Parameter estimates \hat{I}_r , \hat{C}_1 , and \hat{C}_2 .

When tether 2 fails, the estimate of the satellite mass distribution parameter, \hat{I}_r , reaches a value close to 3 and then settles to a value of 1. The values of \hat{C}_i does not vary much, but a much lower value is used for the controller than that used in the system. Therefore, the control laws stabilize the pitch motion of the TSS.

For case II, an adaptive control law described by Eq. (7.48) is simulated and the results are presented next. The following sliding plane constants and adaptive gains were used:

$$p_1 = 4, p_2 = 4, \eta = 0.01, k = 2, \gamma_1 = 0.0012, \gamma_2 = 0.08 \quad (7.58)$$

The initial parameter estimates are assumed to be:

$$\begin{aligned} \hat{\eta}_1|_{initial} &= \frac{I_{r0}}{C_0} = \frac{0.5}{2 \times 10^5} \\ \hat{\eta}_2|_{initial} &= \frac{1}{C_0} = \frac{1}{2 \times 10^5} \end{aligned} \quad (7.59)$$

The controlled response of the system after undergoing initial inplane disturbances and breakage of tether 2 is shown in Fig. 7.8. It is evident that the trajectory of α is very

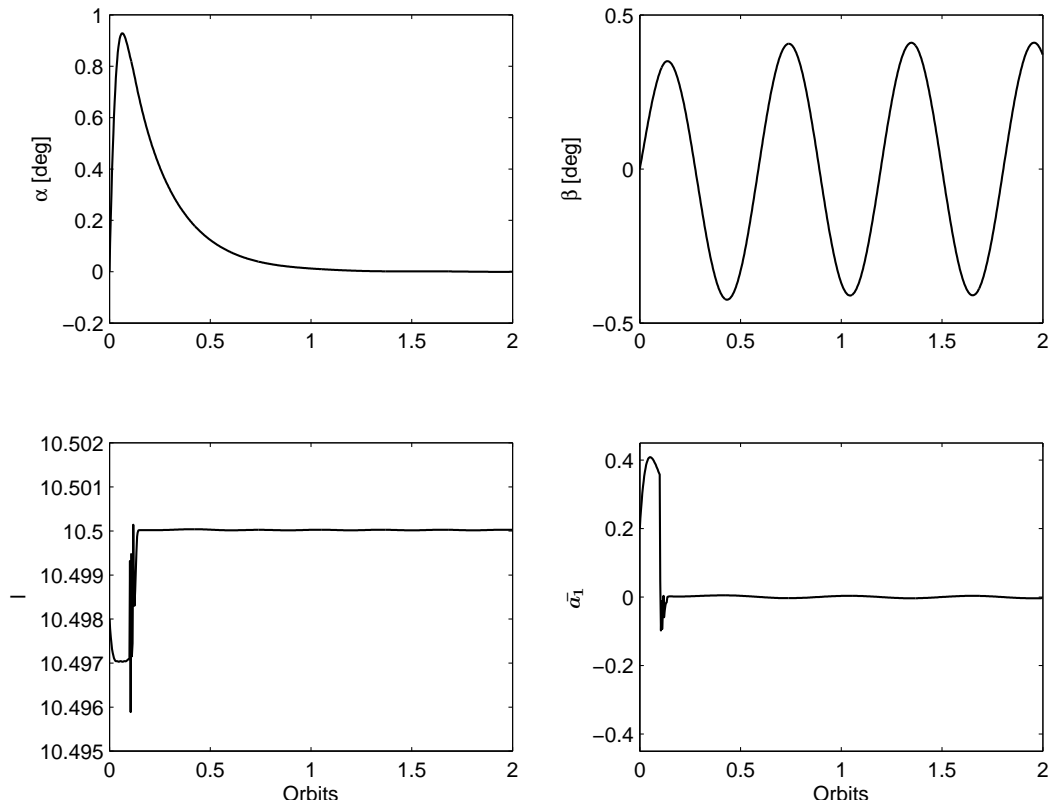
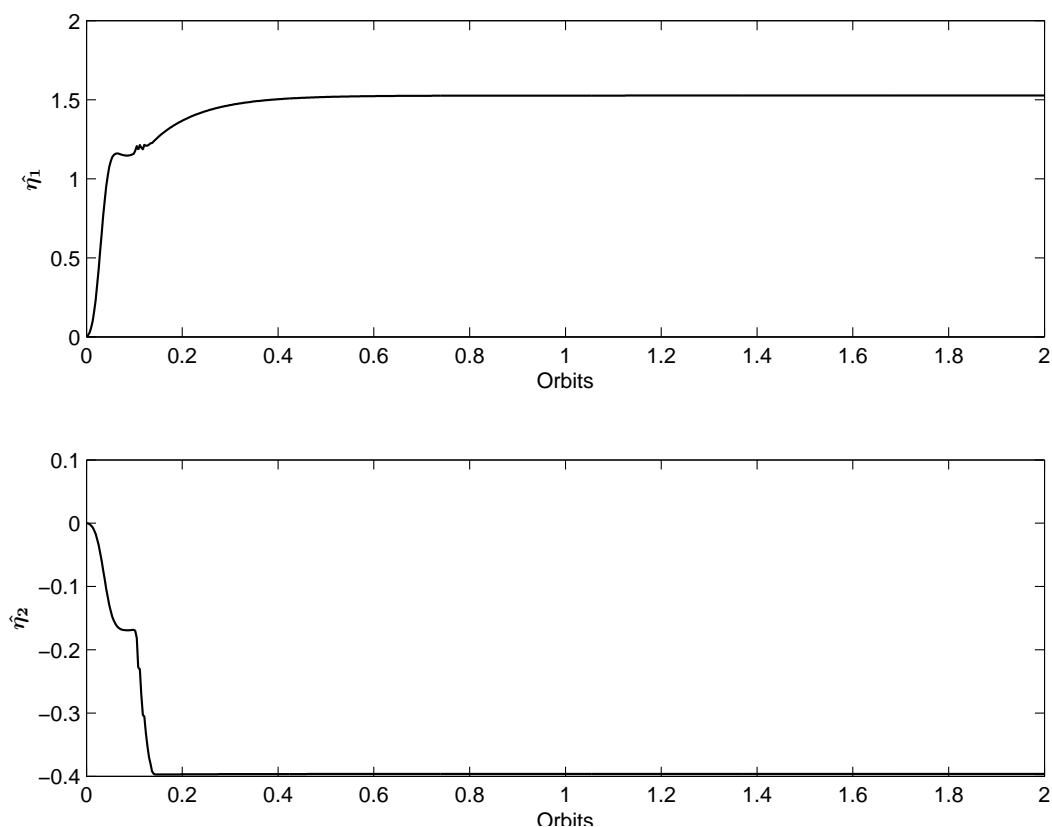


Figure 7.8: Controlled system response using adaptive control law - Case II.

Figure 7.9: Parameter estimates $\hat{\eta}_1$ and $\hat{\eta}_2$.

smooth, unlike the responses obtained from using sliding mode control (Fig. 7.3) and case I adaptive control (Fig. 7.6).

One can clearly see from Fig. 7.8 that the system requires more settling time, compared with Figs. 7.3 and 7.6. The tradeoff is the use of much lower gains, compared with the sliding mode control and adaptive control developed in case I. This is clearly visible by comparing Eqs. (7.52) and (7.55) to Eq. (7.58). The control input \bar{a}_1 clearly counteracts for the failure of tether 2 and hence reduces its effect on the response of α . Slight distortions in the response of α occur, although it is not very clear in Fig. 7.8. The variation of system parameters represented by $\hat{\eta}_1 = \hat{I}_r/\hat{C}$ and $\hat{\eta}_2 = 1/\hat{C}$ is shown in Fig. 7.9. These values, although extremely high compared with the ideal case (Table 7.1), prove the robustness of this adaptive control scheme.

7.4.2.1 Random Initial Conditions

We next examine the results from a wider range of system parameters and initial disturbances to make the conclusions more generally applicable. The adaptive fault-tolerant control scheme (case II) is tested for random system parameters. The saturation limits for the controller is set at $\bar{a}_1 = \pm 0.4$. For the random simulations, the control gains were chosen as

$$p_1 = 6, \quad p_2 = 6, \quad \eta = 0.1, \quad \phi = 0.3, \quad K = 3 \quad (7.60)$$

Figure 7.10 shows the range of system parameters that gave successful results for two sets of initial condition disturbances: 1) $\alpha'_0 = 0.1$, $\beta'_0 = 0.01$, and 2) $\alpha'_0 = 0.01$, $\beta'_0 = 0.01$. Tether breakage at 0.1 orbit was simulated. It can be clearly observed from Fig. 7.10 that for the case of $\alpha'_0 = 0.01$ and $\beta'_0 = 0.01$, a wider range of system parameters were successful in controlling the response of the system during the failure of one of the tethers. The initial unstretched length of the tether, l_{j0} , had no effect on the analysis. For any initial tether length, the range of \bar{a}_j and \bar{b}_j remains the same. As the disturbance was increased to $\alpha'_0 = 0.1$ and $\beta'_0 = 0.01$, the maximum initial offset available was $\bar{a}_j = 0.27$ for $\bar{b}_j = 0.6$.

Keeping initial disturbances the same, we then examined the effect of control gains on a range of system parameters. Figure 7.11 shows the range of system parameters that were successful in controlling the response of the system for two cases: 1) $K = 3$, and 2) $K = 5$. Using $K = 5$, for $\bar{b}_j = 0.6$, the maximum available initial offset increases to 0.32 as opposed to the case of $\bar{a}_j = 0.27$ for $K = 3$. The range of system parameters for which the fault-tolerant adaptive control provides successful results depend on the gains and the initial disturbances considered. For larger disturbances, range of system parameters decreases.

7.4.2.2 Tether Attachment-Point Blocking

Tether attachment-point blockage was first studied by [Grassi *et al.* 1994] where they studied a control system that integrates a reaction wheel and a mobile attachment point on-board each of two tethered platforms. They considered a breakdown case in which the attachment-point control system on the mother satellite stops work and only the daughter satellite attachment point provides the two satellite pitch and roll control. For the fault-tolerant adaptive controller developed in case II, we next incorporate a more likely fault

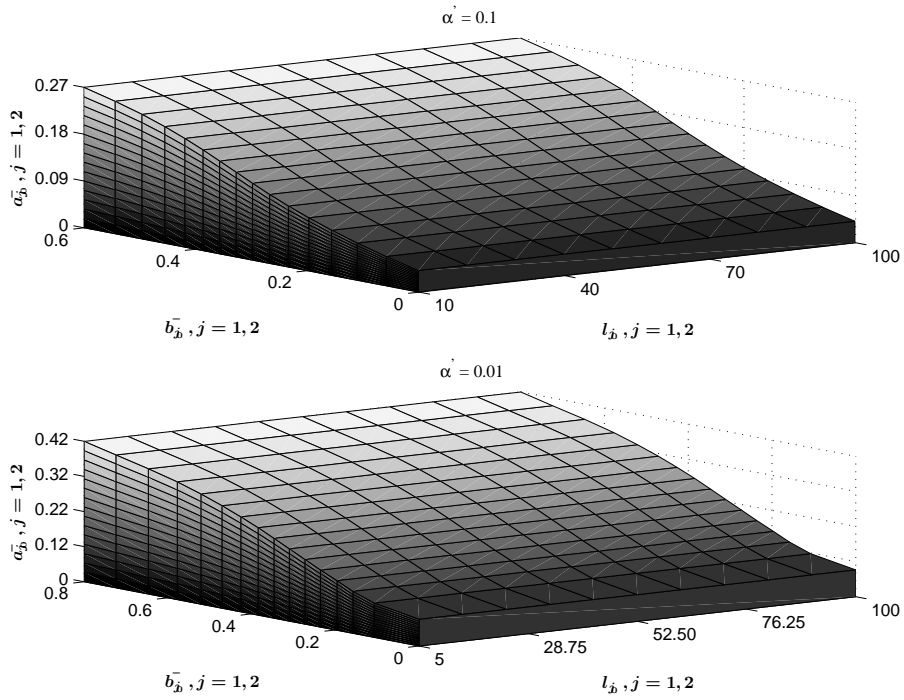


Figure 7.10: Range of parameters with stable solution for $\alpha'_0 = 0.1$ and 0.01 .

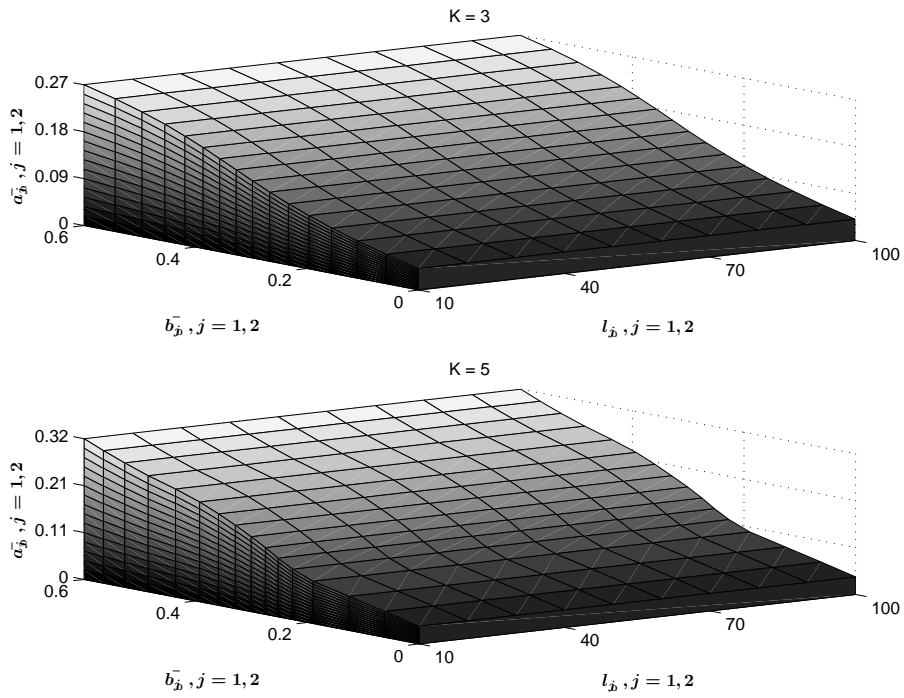


Figure 7.11: Range of parameters with stable solution for gains $K = 3$ and 5 .

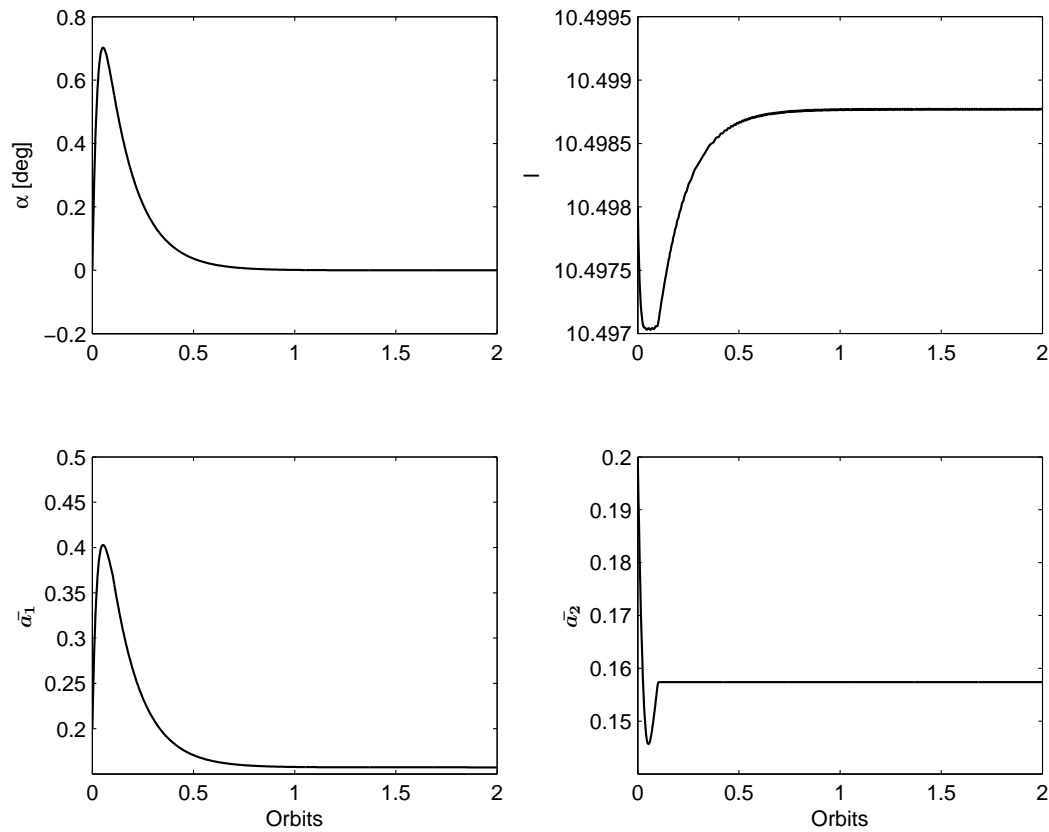


Figure 7.12: Blockage of \bar{a}_2 attachment point is simulated at 0.1 orbit.

scenario in which one of the offset jams in position. An abrupt stop of the tether attachment point \bar{a}_2 at 0.1 orbit is simulated and the results are shown in Fig. 7.12. No modifications were made to the control law in Eq. (7.48), to accommodate for offset blockage. It can be clearly observed that \bar{a}_1 overshoots to a value of 0.4 as soon as \bar{a}_2 is jammed at 0.17; \bar{a}_1 eventually settles at 0.17 after controlling the pitch attitude of the main satellite in accordance with the geometry of the system. As expected, even when one of the offsets is stuck in position, the fault-tolerant controller proposed in this study demonstrates excellent performance in providing pitch control.

7.4.2.3 Tether Attachment-Point Sign Reversal

We consider the case in which one of the tether attachment points starts moving with sign reversal. Although the control laws provide the correct signal, a fault in the actuator

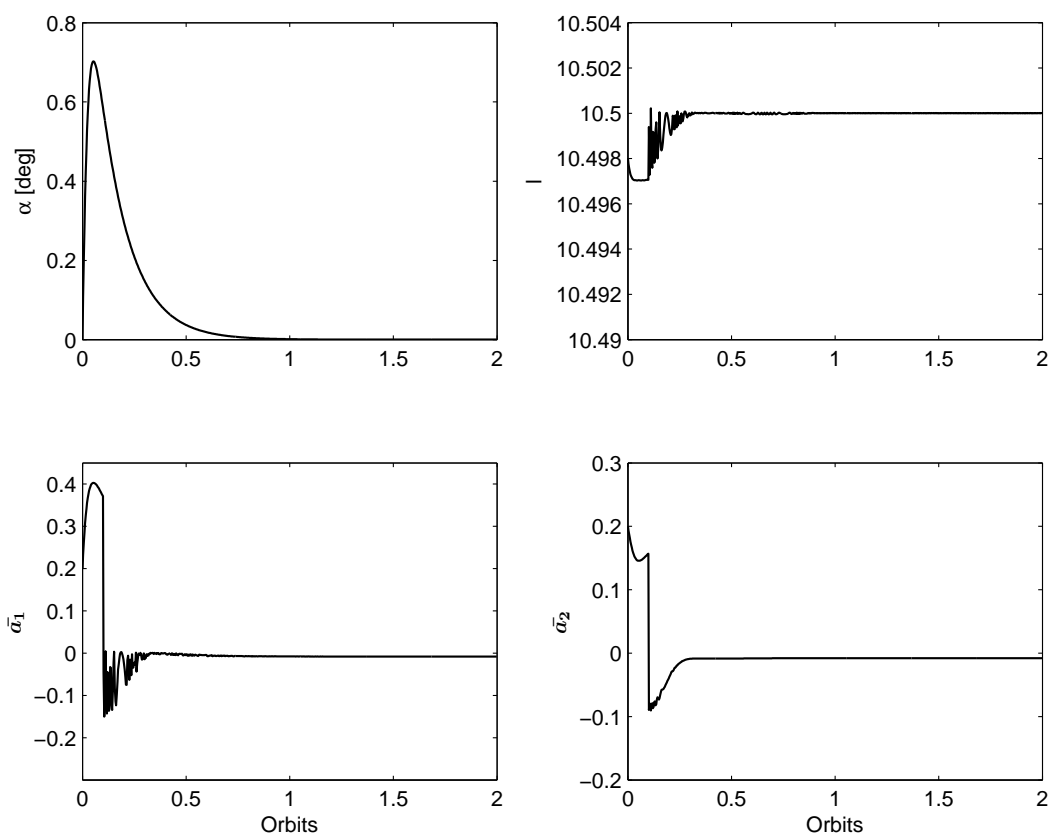


Figure 7.13: Sign reversal of \bar{a}_2 attachment point is simulated at 0.1 orbit.

can reverse the motion of the tether attachment point. Figure 7.13 shows the librational motion of the main satellite for a case in which \bar{a}_2 starts moving with sign reversal after 0.1 orbit. The proposed fault tolerant control methodology can effectively damp the oscillations present in the pitch attitude even when an offset start moving with sign reversal.

The preceding results bring out powerful features of the proposed adaptive controllers (cases I and II). The performance of the controller does not deteriorate even when the system parameters are changing and yet provides a better attitude response, as seen in Figs. 7.6 and 7.8. It is seen that in the closed-loop dynamics, the estimated parameters do not converge to their true values in Figs. 7.7 and 7.9. Furthermore, the proposed controllers perform satisfactorily even in the case of a slack tether. Overall, tether offset variations using sliding mode control prove to be an excellent control strategy for TSS even when one of the tether fails.

7.4.3 Quantitative Analysis

Based on the results obtained in this section, it is important to examine whether the maximum tether offset variations required for the fault-tolerant adaptive controllers can satisfy the requirements of real satellites. Depending on the size of the satellite, the actual tether offset will be a_1 in dimension. The maximum tether offset a_1 required for various sizes of satellites are presented in Table 7.2.

For SPARTNIK, a diameter of 0.51m gives a maximum of 0.2m for a_1 and a_2 . The requirement from the simulation in dimensionless form is $\bar{a}_1 = 0.4$, which can be converted to $a_1 = 0.1\text{m}$ in dimensions using the satellite parameters in Table 7.2. This clearly falls under the maximum available value of 0.2m. Similarly for nanosatellites and picosatellites, the maximum tether offset requirements are met very comfortably. The maximum speed requirements for the offsets vary from 0.3m/s for a microsatellite to 0.7m/s for a picosatellite (Table 7.2). For the practical realization of the proposed control strategy, several issues, including power and weight requirements, must be taken into account.

7.5 Summary

One advantage of employing a two-tether satellite system over a single-tether system is the level of redundancy introduced into the system if one of the tethers were to be severed. However, as discussed in Sec. 8.3, there are some ill effects that must be taken into account when a tether breaks. There is a huge possibility that the remaining tether could collide with itself and lead to tether entanglement. These cases were not considered in the simulations. Fault-tolerant adaptive stabilization of a TSS using an offset control scheme in the presence of tether failure was presented in this chapter.

The numerical integration of the governing nonlinear equations of motion establishes the feasibility of the proposed tether offset variation strategy. The equations of motion were developed using the Lagrangian approach. Based on a nominal sliding mode technique, two different types of nonlinear adaptive controllers were designed. A nonadaptive controller based on sliding mode technique was also developed for comparing a linear proportional-derivative control law when external disturbance is added to the system.

Table 7.2: Maximum tether offset requirements for various satellite systems.

	Microsatellite	Nanosatellite	Picosatellite
Mass, kg	40	8.335	1
Auxiliary mass, kg	5	1	0.09
Size, m	Diameter = 0.51 Height = 0.25	Diameter = 0.4 Height = 0.3	Length = 0.1 Height = 0.1 Depth = 0.1
Moment of Inertia, kg.m ²	$I_x = 0.324$ $I_y = 0.303$ $I_z = 0.486$	$I_x = 0.137$ $I_y = 0.178$ $I_z = 0.176$	$I_x = 0.001$ $I_y = 0.002$ $I_z = 0.001$
Maximum tether offset, m	0.1	0.14	0.4
Maximum offset speed, m/s	0.3	0.2	0.7

The adaptive sliding mode controller developed using modified representation of system parameters (case II) outperforms the other control strategies developed in this study. Use of low sliding mode gains and better adaptation to tether failure are the advantages of this approach. The adaptive controller was also tested for cases when one of the tether attachment point abruptly stops moving and when one of the offsets moves with sign reversal. This control strategy demonstrated excellent performance in all the fault and failure cases considered.

The proposed control scheme can stabilize the satellite's attitude within a quarter of an orbit using tether offsets to the order of one-tenth of a meter for small satellites. Overall, the numerical results clearly establish the robustness of the proposed adaptive offset control scheme in regulating the satellite dynamics of a two-tether system in the event of breakage of one of the tethers.

Conclusions

SPACECRAFT are potentially subjected to unexpected anomalies and failures of actuators during their mission lifetime. With recent advances in computer hardware and computational techniques, fault recovery can be accomplished autonomously onboard spacecraft. Taking inspiration from the existing theory of nonlinear control, we have developed a fault tolerant control system for the *RyePicoSat* missions to cope with actuator faults whilst maintaining the desirable degree of overall stability and performance. In this chapter we review the contributions of the fault tolerant control techniques developed in this thesis. We breakdown the contributions based on the techniques presented in the previous chapters to outline possible future directions in fault tolerant control research for space systems. The discussion is concluded with a few final remarks.

8.1 Summary of Contributions

Autonomous multiple spacecraft formation flying space missions demand the development of reliable control systems to ensure rapid, accurate, and effective response to various attitude and formation reconfiguration commands. To enable capabilities that would never be achievable by single large spacecraft, several missions and mission statements by NASA and other bodies such as the European Space Agency have identified formation flying as a means of reducing cost and adding flexibility to space-based programs. Keeping in mind the complexities involved in the technology development to enable spacecraft formation flying, the objective of the space program initiated by Space Systems Dynamics and Control (SSDC) laboratory at Ryerson University, is to design a fault tolerant control algorithm that augments the AOCS on-board a spacecraft to ensure that these challenging formation flying missions will fly successfully.

8.1.1 Fault Tolerant Reconfigurable Spacecraft Formations

Spacecraft formation flying has become an important field of research in the space industry due to cost benefits and mass savings that arise from this mode of operation. Development and implementation of robust and reliable control algorithms for controlling the formation are necessary to ensure that the advantages of formation flying are effectively exploited. Autonomous coordinated control, precise formation-keeping, and reconfiguration of formation geometry in the presence of actuator faults are areas critical to the success of any proposed mission involving spacecraft flying in formation.

Although nonlinear control algorithms have been published in the literature for formation flying in LEO, very few have addressed fault recovery, robustness, and adaptation with thruster saturation, simultaneously. We considered several scenarios of thruster faults that can introduce constant or state-dependant disturbances into the overall closed-loop system causing the dynamics of the follower spacecraft to deviate largely from its nominal regime. A fault tolerant control scheme was developed to enable autonomous fault recovery in the presence of various thruster faults. Numerical results presented in Chapter 2 clearly establish the robustness of the proposed fault tolerant control methodology for enabling sub-millimeter precision spacecraft formation flying in the presence of subsystem faults, model uncertainties, and time varying disturbances.

8.1.2 Control of Underactuated Spacecraft Formations

Relative motion control of spacecraft formations using thrusters in a fully actuated configuration is a well understood and an extensively studied problem. On the other hand, despite the recent advances, very few researchers have addressed the prospects of using reduced inputs (underactuated configuration) to illustrate formation acquisition and reconfiguration maneuvers. For configurations with no radial axis input, the controllers available in the literature are based on linearized relative motion dynamics and only work in a small neighborhood of the origin. For controlling formations with reduced inputs, significant investigation is required to establish the regions of asymptotic stability for the follower spacecraft and also guarantee a closed stable relative orbit around the leader spacecraft.

We developed a nonlinear control strategy capable of precision formation control to study two configurations of reduced inputs, where no control force is available in the (1) radial direction, and (2) along-track direction. In particular, the second case, not examined in the literature previously, was challenging because it fails the linear controllability test and hence required the use of nonlinear control techniques. The case of no control authority in the radial direction was also demonstrated using hardware-in-the-loop simulations performed on the SSCDC Satellite Airbed Formation Experiment (SAFE) testbed simulating formation acquisition. The theoretical and experimental results presented in this chapter clearly indicate that the proposed control scheme represents a practical design approach for multiple spacecraft formations to deal with the problem of formation maintenance and reconfiguration maneuvers for the case where the radial or along-track thrusters fail.

8.1.3 Fault Tolerant Attitude Control of Spacecraft

Space mission to validate technology developments and new concepts are very risky and expensive. This ultimately hinders the development of attitude and orbit control research. The trend for spacecraft related research has been to simulate space systems in a laboratory environment to reduce risk and cost. Simulations provide valuable knowledge for validating concepts and missions. Many of these simulations are software-based architectures. At Ryerson University we have developed a hardware-in-the-loop reaction wheel assembly simulator to provide a more realistic demonstration of expected performance of the proposed fault tolerant control techniques as compared with software-based architectures.

Hardware-in-the-loop simulation was accomplished using a reaction wheel assembly with on-board control electronics to test actuator performance. Two configurations of reaction wheel assembly developed by the SSCDC laboratory at Ryerson University were examined: 1) Traditional four wheel setup in which three reaction wheels are aligned with the spacecraft principal body axes and the fourth wheel in a skewed configuration; and 2) Four reaction wheels in a pyramid configuration. The reaction wheel testbed is primarily setup to verify the generation of correct reaction torques as demanded by the control algorithm to get a physical feel of attitude control. Faults of reaction wheels were modeled as additive and multiplicative. Abrupt failure of one or two wheels in the assembly were also considered.

The proposed control law does not require an explicit fault detection and isolation mechanism and therefore failure time instants, patterns, and values of actuator failures remain unknown to the designer. The stability conditions for robustness against model uncertainties and disturbances were derived using Lyapunov theory to establish the regions of asymptotic stabilization. The benefits of the control algorithm were analytically authenticated and also validated using numerical simulations. The hardware-in-the-loop reaction wheel simulation results clearly established the robustness of the proposed control algorithm for precise attitude tracking in the event of reaction wheel faults and failures.

8.1.4 Attitude Control of Underactuated Spacecraft

Fault tolerant attitude control of spacecraft with redundant reaction wheels examined in Chapter 4 required the development of a reconfigurable control scheme that can redistribute control actions to remaining operational wheel upon failure of one or more reaction wheels (depending on the reaction wheel configuration). A constraint inherent in the proposed methodology is that the reaction wheel configuration, after wheel failure, is still capable of providing independent control torques in all three principal body-fixed coordinates of the spacecraft. For spacecraft equipped with momentum exchange devices, like reaction wheels or control moment gyros, three axis attitude controllability is impossible with fewer than three devices providing torques in two orthogonal directions.

If the spacecraft is equipped with minimal set of thrusters (three pairs distributed on three axes of the body frame of the spacecraft), complete failure of any single pair prevents the spacecraft from performing arbitrary attitude maneuvers using a conventional control algorithm modeled based on minimal actuator configuration. In this case, a sufficient degree of attitude dexterity can be made available using a control law reconfiguration. With a view to counteract the challenges posed by failure of control actuators, we developed a control scheme that can provide three axis attitude stabilization for spacecraft using torques supplied by thrusters about only two of its principal axes. We considered two cases, 1) no control authority available on the roll axis, and 2) no actuation available on the yaw axis. Numerical simulations illustrated that the proposed control scheme can successfully regulate the attitude motion from large initial conditions and stabilize the spacecraft.

8.1.5 Spacecraft Attitude Control Using a Single Thruster

Based on the results obtained from the proposed underactuated configurations, the most important contribution of Chapter 6 is the formulation of a novel single thrust control strategy for pico-satellites to achieve 3-axis attitude control. A nonlinear control algorithm was developed to stabilize the three axis attitude angles and angular velocities of spacecraft using a single thruster. Torques are generated using a thruster orientation mechanism with which the thrust vector can be tilted on a two-axis gimbal to provide the necessary framework for validating the proposed nonlinear control algorithm.

With recent renewed interest to return to the Moon, NASA has proposed a new series of Crew Exploration Vehicle capable of carrying astronauts to the Moon. The control concept using a single-thruster can be conceived as a last-ditch emergency backup system, in the absence of nominal control capacity, to execute attitude maneuvers during de-orbit and descent phases (for descent to the lunar surface, or, attaining a heat-shield-forward attitude trajectory during atmospheric reentry). For low-cost missions using pico-satellites, the possibility of handling actuator failures without the need for redundant elements is even more appealing. The actuator system remains minimal and complete three-axis attitude stabilization is achieved using a single thruster.

8.1.6 Fault Tolerant Attitude Control of Tethered Spacecraft

The advent of tethered satellite systems marks the beginning of a new era in space research. Several interesting space applications of tethers have been proposed and several mission have been flown; some missions were successful and others were unsuccessful. Some of the major causes of failure of these missions were found to be associated with tether deployment and tether breakage. Researchers have tried to solve these problems using a high-performance tether deployment system and multistrand tethers; however, the problems of tether deployment and breakage still exist. The scope of Chapter 7 was to emphasize the challenges associated with the attitude stabilization of a two-tether system when tether deployment suddenly stops and tether breakage occurs. We examined the attitude control of a spacecraft using two identical tethers of equal length connecting a downward-deployed

auxiliary mass. The tethers are connected to two distinct points symmetrically offset from the spacecraft's mass center. The objective was to control the attitude of the spacecraft through regulated motion of the tether attachment point. A fault tolerant adaptive sliding mode control scheme was developed to stabilize the attitude of the spacecraft in the event of breakage of one of the tethers. Furthermore, a likely scenario in which one of the two tether attachment points suddenly stops moving was also incorporated to test the effectiveness of the proposed control algorithm.

8.2 Future Work

Developing attitude and orbit control software for spacecraft to ensure operational safety has several potential future directions. We have identified three main directions for future research. To have a complete fault tolerant 'intelligent' spacecraft, it is necessary to evaluate the impact of sensor failures and develop methodologies that can enhance existing attitude estimation algorithms. This provides ample scope for developing output feedback control laws, an area virtually unexplored in the current literature. Another issue of great practical importance is experimental validation of proposed techniques. Simulation of the complete spacecraft with on-board control electronics is essential to verify and understand the limitations of various subsystems. Finally, we present some further applications that would be helpful in analyzing the performance of the proposed control scheme in this thesis.

8.2.1 Improved Fidelity Attitude Estimation

Many nonlinear filtering methods have been applied to the problem of spacecraft attitude and orbit determination in the last two decades. Multiplicative extended Kalman filter has been widely used in attitude estimation algorithms, but it can fail in cases that have highly nonlinear dynamics or measurement models. Other methods available in the literature are simple linear filter based algorithms that do not provide optimal results. When measuring a particular state variable, a single type of sensor for that variable may not be able to meet all the required performance specifications. The idea of blending data from various attitude and orbit sensors using a single state estimation algorithm is known as *sensor fusion*.

To increase the level of autonomy for space missions and to reduce the cost of ground support, a method for autonomous fault detection and isolation of spacecraft sensor systems needs to be examined. The objective is to first detect the presence and location of the faults and then calculate the attitude estimate utilizing the remaining operational sensors by reconfiguring the algorithm architecture. Nonlinear observers are an attractive alternative for applications where the spacecraft is subjected to changing operating conditions and nonlinearities of the dynamic model or measurement model are severe, or when a good *a priori* estimate of the states are unavailable.

8.2.2 Experimental Validation and Prototyping

Air bearings offer one of many solutions to the problem of simulating the functional space environment in a laboratory setup. Simulation of the spacecraft motions using a spherical three axis air bearing platform with sensors, actuators, and control electronics mounted on it plays a vital role in the development and testing of spacecraft attitude control systems. This can provide a true measure of chosen controller gain parameters, on-board subsystem malfunctions, and various interface incompatibilities. The primary objective of air-bearing tests is precise representation of spacecraft dynamics. With the problem of accurate plant model addressed, experimenters can use this simulator to evaluate various attitude control schemes. Performance of the control algorithms can be verified based on three axis pointing and tracking maneuvers.

8.2.3 Applications

Finally, we recommend other spacecraft applications that can benefit from the fault tolerant control schemes presented in this thesis. The proposed control framework can be applied directly to some of these applications while the others would only require some minor changes to the control structure. The following suggestions can help the selection of future research topics.

- Distributed Consensus Network. Spacecraft formation flying in the presence of actuator faults can be made more appealing by extending the leader-follower configuration

examined in this thesis to a distributed consensus network. Then, the proof of stability will be more challenging than simply proving the stability of the tracking error between a leader and a follower spacecraft. An advantage of the distributed network is that loss of one spacecraft does not represent a single point of failure for the mission.

- Coordinated attitude and orbit control. The problem of orbit control for multiple spacecraft in formation has been investigated in this thesis with consideration of actuator faults. Further refinement and extension to this problem is possible by examining the synchronization of spacecraft considering the coupled effects of relative attitude and orbit position. Synchronization performance must now be established based on six-degree of freedom and cross-coupling concept.
- Artificial Intelligence. The concept of artificial intelligence (AI) and ‘learning/expert systems’ could be exploited for developing autonomous on-board identification and isolation of actuator and sensor faults. The basic framework developed in this thesis can be adopted by adding an AI retrofit component to detect and isolate faults.

8.3 Concluding Remarks

As missions become more ambitious, spacecraft attitude control will require more versatility, which may not be realizable with conventional feedback control algorithms. In the past, not many missions had the option of using on-board fault tolerant reconfiguration control algorithms because of each control processor unit’s cost, performance factor, and weight. However, with the development of smaller and cheaper micro-processors, several different control algorithms can be combined to obtain a more precise evaluation of spacecraft attitude and orbit parameters. Overall, the re-design goals set in the initial stages of the study was successfully validated. Successful implementation of the proposed methodology will greatly enhance the reliability of the spacecraft, while allowing for potentially significant overall mission cost reduction.

Bibliography

- [Aeyels 1985] Aeyels, D., “Stabilization by smooth feedback of the angular velocity of a rigid body,” *Systems and Control Letters*, Vol. 6, No. 1, 1985, Pages: 59–63. 14
- [Ahmed *et al.* 1998] Ahmed, Jasim, Coppola, Vincent T., & Bernstein, Dennis S., “Adaptive asymptotic tracking of spacecraft attitude motion with inertia matrix identification,” *Journal of Guidance, Control, and Dynamics*, Vol. 21, No. 5, 1998, Pages: 684–691. 13
- [Alger & Kumar 2008] Alger, M.W.R., & Kumar, K.D., “A Design and Development of Pico- and Femto-satellites,” *International Journal of Manufacturing Research*, Vol. 3, No. 1, 2008, Pages: 48–79. 6
- [Alger 2008] Alger, M.W.R. *Design and development of power and attitude control subsystems for RyeSat*. Master’s thesis, Ryerson University, Toronto, ON, September 2008. 207
- [Alwi *et al.* 2008] Alwi, H., Edwards, C., Stroosma, O., & Mulder, J.A., “Fault tolerant sliding mode control design with piloted simulator evaluation,” *Journal of Guidance, Control, and Dynamics*, Vol. 31, No. 5, 2008, Pages: 1186–1201. 119
- [Bainum *et al.* 1985] Bainum, P.M., Woodard, S., & Juang, J.-N., “The Development of Optimal Control Laws For Orbiting Tethered Platform Systems,” *Proceedings of the AAS/AIAA Astrodynamics Conference, AAS 85-360*, Vol. 58, Vail, CO, August 12-15, 1985, Pages: 219–314. 16
- [Beletsky & Levin 1993] Beletsky, V.V., & Levin, E.M., *Dynamics of Space Tether Systems*, Vol. 83, Advances in the Astronautical Sciences, 1993. 15
- [Bergamaschi 1982] Bergamaschi, S., “Tether Motion After Failure,” *Journal of the Astronautical Sciences*, Vol. 30, No. 1, 1982, Pages: 49–59. 223

- [Bevilacqua & Romano 2008] Bevilacqua, R., & Romano, M., “Rendezvous maneuvers of multiple spacecraft using differential drag under J2 perturbation,” *Journal of Guidance, Control, and Dynamics*, Vol. 31, No. 6, 2008, Pages: 1595–1607. 12
- [Bharadwaj *et al.* 1998] Bharadwaj, S., Osipchuk, M., Mease, K.D., & Park, F.C., “Geometry and inverse optimality in global attitude stabilization,” *Journal of Guidance, Control, and Dynamics*, Vol. 21, No. 6, 1998, Pages: 930–939. 13
- [Bialke 1998] Bialke, Bill, “High fidelity mathematical modeling of reaction wheel performance,” *Proceedings of the 1998 Annual AAS Rocky Mountain Guidance and Control Conference, Advances in the Astronautical Sciences, AAS 98-063*, Vol. 98, Breckenridge, CO, Feb. 4-8, 1998, Pages: 483–496. 114
- [Blanksby & Trivailo 2000] Blanksby, C., & Trivailo, P., “Collision Dynamics of Space Tethers,” *Journal of Guidance, Control, and Dynamics*, Vol. 23, No. 6, 2000, Pages: 1078–1081. 209
- [Boskovic *et al.* 2004] Boskovic, J.D., Li, S.M., & Mehra, R.K., “Robust tracking control design for spacecraft under control input saturation,” *Journal of Guidance, Control, and Dynamics*, Vol. 27, No. 4, 2004, Pages: 627–633. 13
- [Bošković *et al.* 1999] Bošković, J.D., Li, Sai-Ming, & Mehra, R.K., “Intelligent Control of Spacecraft in the Presence of Actuator Failures,” *Proceedings of the 38th IEEE Conference on Decision and Control*, Vol. 5, Phoenix, AZ, Dec. 7-10, 1999, Pages: 4472–4477. 13
- [Brockett 1984] Brockett, R.W., “Asymptotic stability and feedback stabilization,” *Differential Geometric Control Theory*, R.W. Brockett, R.S. Millman, H.H. Sussmann (eds.), Birkhauser, Boston, 1984, Pages: 181–208. 14
- [Byrnes & Isidori 1991] Byrnes, C.I., & Isidori, A., “On the attitude stabilization of rigid spacecraft,” *Automatica*, Vol. 27, No. 1, 1991, Pages: 87–95. 14

- [Cai *et al.* 2008] Cai, W., Liao, X.H., & Song, Y.D., “Indirect robust adaptive fault-tolerant control for attitude tracking of spacecraft,” *Journal of Guidance, Control, and Dynamics*, Vol. 31, No. 5, 2008, Pages: 1456–1463. 13, 77, 112, 117, 118
- [Chen & Saif 2007] Chen, Wen, & Saif, Mehrdad, “Observer-based Fault Diagnosis of Satellite Systems Subject to Time-varying Thruster Faults,” *Journal of Dynamic Systems, Measurement and Control*, Vol. 129, No. 3, 2007, Pages: 352–356. 13
- [Chobotv 2002] Chobotv, V.A., *Orbital Mechanics*, AIAA Education Series, AIAA, Reston, VA, 2002. 11
- [Clohessy & Wiltshire 1960] Clohessy, W., & Wiltshire, R., “Terminal guidance systems for satellite rendezvous,” *Journal of the Astronautical Sciences*, Vol. 27, No. 9, 1960, Pages: 653–658. 10
- [Colombo *et al.* 1975] Colombo, G., Gaposchkin, E. M., Grossi, M. D., & Weiffenbach, G. C., “SKYHOOK: A Shuttle-borne Tool For Low-Orbital-Altitude Research,” *Meccanica*, Vol. 10, No. 1, 1975, Pages: 3–20. 209
- [Coron & Keraï 1996] Coron, J.M., & Keraï, E.L., “Explicit feedback stabilizing the attitude of a rigid spacecraft with two control torques,” *Automatica*, Vol. 32, No. 5, 1996, Pages: 669–677. 14
- [Cosmo & Lorenzini 1997] Cosmo, M.L., & Lorenzini, E.C., *Tethers in Space Handbook*, 3 édition, 1997. 16
- [Crassidis & Landis Markley 1996] Crassidis, J.L., & Landis Markley, F., “Sliding mode control using modified Rodrigues parameters,” *Journal of Guidance, Control, and Dynamics*, Vol. 19, No. 6, 1996, Pages: 1381–1383. 13
- [Crosby 2009] Crosby, N.B., “Solar extreme events 2005-2006: Effects on near-Earth space systems and interplanetary systems,” *Advances in Space Research*, Vol. 43, 2009, Pages: 559–564. 4

- [Damaren 2007] Damaren, C.J., “Almost periodic relative orbits under J2 perturbations,” *Proceedings of the Institution of Mechanical Engineers, Part G (Journal of Aerospace Engineering)*, Vol. 221, No. G5, 2007, Pages: 767–774. 11
- [de Queiroz *et al.* 2000] de Queiroz, Marcio S., Kapila, Vikram, & Yan, Qiguo, “Adaptive nonlinear control of multiple spacecraft formation flying,” *Journal of Guidance, Control, and Dynamics*, Vol. 23, No. 3, 2000, Pages: 385–390. 12
- [Demourant & Chretien 2008] Demourant, Fabrice, & Chretien, Jean-Pierre, “Relative motion control for along-track formation flight in low earth orbit: Linear synthesis with non-linear actuators,” *Proceedings of the 3rd International Symposium on Formation Flying, Missions, and Technologies, ESA SP-654*, Noordwijk, Netherlands, April 23-25, 2008. 68
- [Edwards & Spurgeon 1998] Edwards, C., & Spurgeon, S.K., *Sliding Mode Control - Theory and Applications*, Taylor and Francis Ltd, London, UK, 1998. 39, 78, 82, 172
- [Eyer & Damaren 2009] Eyer, J.K., & Damaren, C.J., “Quasi-periodic relative trajectory generation for formation flying satellites,” *Journal of Guidance, Control, and Dynamics*, Vol. 32, No. 4, 2009, Pages: 1403–1407. 11
- [Fan & Bainum 1988] Fan, R., & Bainum, P.M., “Dynamics and Control of a Space Platform with a Tethered Subsatellite,” *Journal of Guidance, Control, and Dynamics*, Vol. 11, No. 4, 1988, Pages: 377–381. 16
- [Feng *et al.* 2002] Feng, Yong, Yu, Xinghuo, & Man, Zhihong, “Non-singular terminal sliding mode control of rigid manipulators,” *Automatica*, Vol. 38, No. 12, 2002, Pages: 2159–2167. 39, 49
- [Fernandez & Hedrick 1987] Fernandez, B.R., & Hedrick, J.K., “Control of Multivariable Nonlinear Systems by the Sliding Mode Method,” *International Journal of Control*, Vol. 46, No. 3, 1987, Pages: 1019–1040. 217
- [Folta *et al.* 2002] Folta, D., Bristow, J., Hawkins, A., & Dell, G., “NASA’s autonomous formation flying technology demonstration, Earth Observing-1,” *First Interna-*

- tional Symposium on Formation Flying Missions and Technologies*, Centre National d'Etudes Spatiales, Toulouse, France, Oct 29-30, 2002. 10
- [Fragopoulos & Innocenti 2004] Fragopoulos, D., & Innocenti, M., "Stability considerations in quaternion attitude control using discontinuous Lyapunov functions," *IEE Proceedings-Control Theory and Applications*, Vol. 151, No. 3, 2004, Pages: 253–258. 109
- [Fu & Abed 1993] Fu, Jyun.-H., & Abed, E.H., "Linear feedback stabilization of nonlinear systems with an uncontrollable critical mode," *Automatica*, Vol. 29, No. 4, 1993, Pages: 999–1010. 71
- [Fujii & Ichiki 1997] Fujii, H.A., & Ichiki, W., "Nonlinear Dynamics of the Tethered Subsatellite System in the Station Keeping Phase," *Journal of Guidance, Control, and Dynamics*, Vol. 20, No. 2, 1997, Pages: 403–406. 226
- [Golikov 2003] Golikov, A., "Evolution of Formation Flying Satellite Relative Motion: Analysis Based on the Theona Satellite Theory," *Proceedings of the 17th International Symposium on Space Flight Dynamics*, Moscow, Russia, June 16-20, 2003. 11
- [Grassi & Cosmo 1996] Grassi, M., & Cosmo, M.L., "Atmospheric Research with the Small Expendable Deployer System: Preliminary Analysis," *Journal of Spacecrafts and Rockets*, Vol. 33, No. 1, 1996, Pages: 70–78. 16
- [Grassi *et al.* 1994] Grassi, M., Moccia, A., & Vetrella, S., "Tethered System Attitude Control After Attachment Point Blocking," *Acta Astronautica*, Vol. 32, No. 5, 1994, Pages: 355–362. 232
- [Gurfil 2005] Gurfil, Pini, "Relative motion between elliptic orbits: Generalized boundedness conditions and optimal formationkeeping," *Journal of Guidance, Control, and Dynamics*, Vol. 28, No. 4, 2005, Pages: 761–767. 11
- [Hadaegh *et al.* 1998] Hadaegh, F.Y., Lu, W-M., & Wang, P.K.C., "Adaptive control of formation flying spacecraft for interferometry," *Proceedings of the 8th*

- IFAC/IFORS/IMACS/IFIP Symposium on Large Scale Systems: Theory and Applications*, Vol. 1, Rio Patras, Greece, July 15-17, 1998, Pages: 117–122. 12
- [Hall 2003] Hall, C.D., “When spacecraft went point,” *Advances in the Astronautical Sciences*, AAS 03-505, Vol. 116, Big Sky, MT, Aug 3-7, 2003, Pages: 79–86. 2
- [Han & Pechev 2009] Han, C., & Pechev, A.N., “Time-varying underactuated attitude control design with feedback linearization using two pairs of gas jet actuators,” *Proceedings of the 9th Biennial Conference on Engineering Systems Design and Analysis*, Vol. 2, Haifa, Israel, July 7-9, 2009, Pages: 479–484. 14
- [Harding 1966] Harding, C.F. “Effect of gravity gradient torque on the motion of the spin axis of an asymmetric vehicle,” . Rapport technique, NASA, Washington, D.C., 1966. NASA CR-433. 15
- [Hill 1878] Hill, G.W., “Researches in the lunar theory,” *American Journal of Mathematics*, Vol. 1, 1878, Pages: 5–26. 10
- [Hu & Ng 2007] Hu, Yan-Ru, & Ng, Alfred, “Robust control of spacecraft formation flying,” *Journal of Aerospace Engineering*, Vol. 20, No. 4, 2007, Pages: 209–214. 11
- [IMS 1997] International Mathematical and Statistical Library (IMSL), Math Library, Visual Numerics Inc., Houston, TX, 1997. 177
- [Inalhan *et al.* 2002] Inalhan, Gokhan, Tillerson, Michael, & How, Jonathan P., “Relative dynamics and control of spacecraft formations in eccentric orbits,” *Journal of Guidance, Control, and Dynamics*, Vol. 25, No. 1, 2002, Pages: 48–59. 11
- [Isidori 1995] Isidori, A., *Nonlinear Control Systems*, 3 édition, 1995. 70
- [Jiang *et al.* 2010] Jiang, Ye, Hu, Qinglei, & Ma, Guangfu, “Adaptive Backstepping Fault-Tolerant Control for Flexible Spacecraft with Unknown Bounded Disturbances and Actuator Failures,” *ISA Transactions*, Vol. 49, No. 1, 2010, Pages: 57–69. 13

- [Jin *et al.* 2008] Jin, J.H., Ko, S.H., & Ryoo, C.-K., “Fault tolerant Control for Satellites with Four Reaction Wheels,” *Control Engineering Practice*, Vol. 16, No. 10, 2008, Pages: 1250–1258. 13
- [Jost & Chlouber 1995] Jost, R.J., & Chlouber, D., “Plasma Motor Generator (PMG) Mission Report,” *Proceedings of the Fourth International Conference on Tethers in Space*, Science and Technology Corp., Hampton, VA, April 10-14, 1995, Pages: 149–163. 16
- [Kaplan 1976] Kaplan, M.H., *Modern Spacecraft Dynamics and Control*, John Wiley and Sons, New York, NY, 1976. 188
- [Kim & Deraspe 2003] Kim, Y.V., & Deraspe, G., “Resolving RADARSAT-1 momentum wheels failure problem,” *Proceedings of 54th International Astronautical Congress of the International Astronautical Federation (IAF)*, Bremen, Germany, Sep 29 - Oct 3, 2003. 5
- [Kline-Schoder & Powel 1993] Kline-Schoder, R.J., & Powel, J.D., “Precision Attitude Control for Tethered Satellites,” *Journal of Guidance, Control, and Dynamics*, Vol. 16, No. 1, 1993, Pages: 168–174. 16
- [Krishnan *et al.* 1994] Krishnan, H., Reyhanoglu, M., & McClamroch, N.H., “Attitude stabilization of a rigid spacecraft using two control torques: A nonlinear control approach based on spacecraft attitude dynamics,” *Automatica*, Vol. 30, No. 6, 1994, Pages: 1023–1027. 14
- [Kristiansen & Nicklasson 2009] Kristiansen, Raymond, & Nicklasson, Per Johan, “Spacecraft formation flying: A review and new results on state feedback control,” *Acta Astronautica*, Vol. 65, No. 11-12, 2009, Pages: 1537–1552. 11, 33
- [Krstic & Tsotras 1999] Krstic, M., & Tsotras, P., “Inverse optimal stabilization of a rigid spacecraft,” *IEEE Transactions on Automatic Control*, Vol. 44, No. 5, 1999, Pages: 1042–1049. 13

- [Kruk *et al.* 2002a] Kruk, Jeffrey W., Class, Brian F., Rovner, Dan, Westphal, Jason, Ake, Thomas B., Moos, H. Warren, Roberts, Bryce, & Fisher, Landis, “FUSE In-orbit Attitude Control with Two Reaction Wheels and No Gyroscopes,” *Proceedings of SPIE - The International Society for Optical Engineering, Future EUV/UV and Visible Space Astrophysics Missions and Instrumentation Conference*, Vol. 4854, Waikoloa, HI, Aug. 22-23, 2002, Pages: 274–285. 107
- [Kruk *et al.* 2002b] Kruk, J.W., Class, B.F., Rovner, D., Westphal, J., Ake, T.B., Moos, H.W., Roberts, B., & Fisher, L., “FUSE in-orbit attitude control with two reaction wheels and no gyroscopes,” *Proceedings of SPIE - The International Society for Optical Engineering*, Vol. 4854, Waikoloa, HI, Aug 22-23, 2002, Pages: 274–285. 3
- [Kumar & Kumar 2001] Kumar, K.D., & Kumar, K., “Attitude Maneuver of Dual Tethered Satellite Platforms through Tether Offset Change,” *Journal of Spacecrafts and Rockets*, Vol. 38, No. 2, 2001, Pages: 237–242. 16, 212
- [Kumar & Misra 2009] Kumar, K.D., & Misra, A.K., *Design of Fault Tolerant and Intelligent Attitude Control System for Micro and Nanosatellites*, Yearly Report - CSA FTC Project - 28/7005971, Ryerson University, Toronto, Canada, 2009. xxv, 140
- [Kumar & Nakajima 2000] Kumar, K.D., & Nakajima, A., “Angular Momentum Damping of Debris Through Tether System,” *Proceedings of 22nd International Symposium on Space Technology and Science*, edited by Y. Arakawa, Morioka, Japan, May 28 - Jun 4, 2000, Pages: 1780–1785. 16
- [Kumar *et al.* 2007] Kumar, K.D., Bang, H.C., & Tahk, M.J., “Satellite formation flying using along-track thrust,” *Acta Astronautica*, Vol. 61, No. 7-8, 2007, Pages: 553–564. 12
- [Kumar 2006a] Kumar, K.D., *Fundamentals of Dynamics and Control of Space Systems*, Ryerson University, Toronto, Canada, 2006. 164

- [Kumar 2006b] Kumar, K.D., “Review of Dynamics and Control of Nonelectrodynamic Tethered Satellite Systems,” *Journal of Spacecraft and Rockets*, Vol. 43, No. 4, 2006, Pages: 705–720. 15
- [Lam *et al.* 2001] Lam, Q., Sanneman, P., Stamatakos, N., Vogt, B., & Kim, J., “A Mixed-Mode Attitude Control System Strategy for Actuator Failure Accommodation,” *Proceedings of the AIAA Guidance, Navigation, and Control Conference and Exhibit, AIAA Paper 2001-4156*, Montreal, Canada, Aug. 6-9, 2001. 107
- [Lawden 1954] Lawden, D., “Fundamentals of Space Navigation,” *Journal of the British Interplanetary Society*, Vol. 13, No. 2, 1954, Pages: 87–101. 10
- [Leonard *et al.* 1989] Leonard, C.L., Hollister, W.M., & Bergmann, E.V., “Orbital formationkeeping with differential drag,” *Journal of Guidance, Control, and Dynamics*, Vol. 12, No. 1, 1989, Pages: 108–113. 12
- [Li *et al.* 2010] Li, Shihua, Ding, Shihong, & Li, Qi, “Global set stabilization of the spacecraft attitude control problem based on quaternion,” *International Journal of Robust and Nonlinear Control*, Vol. 20, No. 1, 2010, Pages: 84–105. 13
- [Lim & Bang 2009] Lim, Hyung-Chul, & Bang, Hyochoong, “Adaptive control for satellite formation flying under thrust misalignment,” *Acta Astronautica*, Vol. 65, No. 1-2, 2009, Pages: 112–122. 12
- [Lim *et al.* 2003] Lim, Hyung-Chul, Bang, Hyo-Choong, Park, Kwan-Dong, & Park, Pil-Ho, “Tracking control design using sliding mode techniques for satellite formation flying,” *Journal of Astronomy and Space Sciences*, Vol. 20, No. 4, 2003, Pages: 365–374. 63, 73
- [Liu *et al.* 2006] Liu, Hui, Li, Junfeng, & Hexi, Baoyin, “Sliding mode control for low-thrust Earth-orbiting spacecraft formation maneuvering,” *Aerospace Science and Technology*, Vol. 10, No. 7, 2006, Pages: 636–643. 12, 63, 73

- [Ludwig 1967] Ludwig, G.H., “Relative Advantages of Small and Observatory Type Satellites,” *Proceedings of AIAA Space Program Issues of the 70’s Meeting, AIAA 67-634*, Seattle, WA, Aug 28-30, 1967. 6
- [Luo *et al.* 2005] Luo, W., Chu, Y.C., & Ling, Keck-Voon, “H inverse optimal attitude-tracking control of rigid spacecraft,” *Journal of Guidance, Control, and Dynamics*, Vol. 28, No. 3, 2005, Pages: 481–493. 13
- [Massey & Shtessel 2005] Massey, Timothy, & Shtessel, Yuri, “Continuous traditional and high-order sliding modes for satellite formation control,” *Journal of Guidance, Control, and Dynamics*, Vol. 28, No. 4, 2005, Pages: 826–831. 12, 63, 73
- [Misra & Modi 1983] Misra, A. K., & Modi, V. J., “Dynamics and Control of Tether Connected Two-body Systems - A Brief Overview,” *Space 2000, edited by L.G. Napolitano, AIAA*, Washington, D.C., 1983, Pages: 473–514. 15
- [Misra & Modi 1986] Misra, A. K., & Modi, V. J., “A Survey on the Dynamics and Control of Tethered Satellite Systems,” *Proceedings of First (NASA/AIAA/PSN) International Conference on Tethers in Space, AAS 86-246*, Vol. 62, Arlington, VA, September 17-19, 1986, Pages: 667–719. 15
- [Modi *et al.* 1990] Modi, V.J., Lakshmanan, P.K., & Misra, A.K., “Offset Control of Tethered Satellite Systems: Analysis and Experimental Verification,” *Acta Astronautica*, Vol. 21, No. 5, 1990, Pages: 283–294. 16
- [Modi *et al.* 1991] Modi, V.J., Lakshmanan, P.K., & Misra, A.K., “Offset Control Strategy for the Space Station Based Tethered Payload,” *Journal of the Astronautical Sciences*, Vol. 39, No. 2, 1991, Pages: 205–232. 16
- [Modi *et al.* 1992] Modi, V.J., Lakshmanan, P.K., & Misra, A.K., “On the Control of Tethered Satellite Systems,” *Acta Astronautica*, Vol. 26, No. 6, 1992, Pages: 411–423. 16

- [Modi *et al.* 1998] Modi, V.J., Gilardi, G., & Misra, A.K., “Attitude Control of Space Platform Based Tethered Satellite System,” *Journal of Aerospace Engineering*, Vol. 11, No. 2, 1998, Pages: 24–31. 16
- [Modi 1990] Modi, V.J., “Spacecraft Attitude Dynamics: Evolution and Current Challenges,” *Acta Astronautica*, Vol. 21, No. 10, 1990, Pages: 689–718. 16
- [Morin & Samson 1997] Morin, P., & Samson, C., “Time-varying exponential stabilization of a rigid spacecraft with two control torques,” *IEEE Transactions on Automatic Control*, Vol. 42, No. 4, 1997, Pages: 528–534. 14
- [Morin 1996] Morin, P., “Robust stabilisation of the angular velocity of a rigid body with two controls,” *European Journal of Control*, Vol. 2, No. 1, 1996, Pages: 51–56. 14
- [Murugesan & Goel 1987] Murugesan, S., & Goel, P. S., “Fault-tolerant spacecraft attitude control system,” *Sadhana*, Vol. 11, No. 1-2, 1987, Pages: 233 – 261. 18
- [NASA 1998] NASA, *Lewis Spacecraft Mission Failure Investigation Board*, Final Report, No. 98-109, National Aeronautics and Space Administration, Washington, D.C., 1998. 2
- [NASA 2007] NASA, “Lewis Spins Out Of Control,” *System Failure Case Studies*, Vol. 1, No. 8, 2007. 2
- [Neeck *et al.* 2005] Neeck, S.P., Magner, T.J., & Paules, G.E., “NASA’s small satellite missions for Earth observation,” *Acta Astronautica*, Vol. 56, No. 1-2, 2005, Pages: 187–192. 10
- [Pongythithum *et al.* 2005] Pongythithum, R., Veres, S.M., Gabriel, S.B., & Rogers, E., “Universal adaptive control of satellite formation flying,” *International Journal of Control*, Vol. 78, No. 1, 2005, Pages: 45–52. 12, 55
- [Popov 1973] Popov, V.M., *Hyperstability of Control Systems*, Springer, Berlin, 1973. 46
- [Pradhan *et al.* 1999] Pradhan, S., Modi, V.J., & Misra, A.K., “Tethered Platform Coupled Control,” *Acta Astronautica*, Vol. 44, No. 5, 1999, Pages: 243–256. 16

- [Purdy *et al.* 1997] Purdy, W., Coffey, S., Barnds, W.J., Kelm, B., & Davis, M., “TiPS: Results of a Tethered Satellite Experiment,” *Proceedings of the AAS/AIAA Astrodynamics Conference, AAS 97-600*, Vol. 97, Sun Valley, ID, August 4-7, 1997, Pages: 3–23. 16
- [Ren & Beard 2004] Ren, W., & Beard, R.W., “Formation feedback control for multiple spacecraft via virtual structures,” *IEEE Proceedings: Control Theory and Applications*, Vol. 151, No. 3, 2004, Pages: 357–368. 12
- [Richardson & Mitchell 2003] Richardson, D.L., & Mitchell, J.W., “A third-order analytical solution for relative motion with a circular reference orbit,” *Journal of the Astronautical Sciences*, Vol. 51, No. 1, 2003, Pages: 1–12. 11
- [Roberts *et al.* 2004] Roberts, B.A., Kruk, J.W., Ake, T.B., Englar, T.S., Class, B.F., & Rovner, D.M., “Three-axis attitude control with two reaction wheels and magnetic torquer bars,” *Proceedings of AIAA Guidance, Navigation, and Control Conference, AIAA 2004-5245*, Vol. 4, Providence, RI, Aug 16-19, 2004, Pages: 2465–2472. 3
- [Robertson & Stoneking 2003] Robertson, B., & Stoneking, E., “Satellite GN and C anomaly trends,” *Guidance and Control 2003, Advances in the Astronautical Sciences, AAS 03-071*, Vol. 113, Breckenridge, CO, Feb 5-9, 2003, Pages: 531–542. 2, 4
- [Rycroft & Crosby 2001] Rycroft, M., & Crosby, N., *Smaller satellites: Bigger Business? Concepts Applications and Markets for Micro/Nanosatellites in a New Information World*, Kluwer Academic Publishers, 2001. 10
- [Sabol *et al.* 2001] Sabol, C., Burns, R., & McLaughlin, C.A., “Satellite formation flying design and evolution,” *Journal of Spacecraft and Rockets*, Vol. 38, No. 2, 2001, Pages: 270–278. 35, 36
- [sat nd 2009] sat nd, “Satellite Outages and Failures: TOPEX/Poseidon satellite failure description,” *Satellite News Digest*, retrieved from: <http://sat-nd.com/failures/topex.html>, Nov 18, 2009. 5

- [Scharf *et al.* 2004] Scharf, D.P., Hadaegh, F.Y., & Ploen, S.R., “A Survey of Spacecraft Formation Flying Guidance and Control (Part II): Control,” *Proceedings of the American Control Conference*, Boston, MA, June 30 - July 2, 2004, Pages: 2976–2985. 11, 35
- [Schaub & Alfriend 2001] Schaub, H., & Alfriend, Kyle T., “J2 invariant relative orbits for formation flying,” *Celestial Mechanics and Dynamical Astronomy*, Vol. 79, No. 2, 2001, Pages: 77–95. 11
- [Schaub & Junkins 2003] Schaub, H., & Junkins, J.L., *Analytical Mechanics of Space Systems*, AIAA Education Series, Reston, VA, 2003. 11, 34, 37, 112, 113
- [Schaub & Lappas 2009] Schaub, H., & Lappas, V.J., “Redundant Reaction Wheel Torque Distribution Yielding Instantaneous L_2 Power-Optimal Attitude Control,” *Journal of Guidance, Control, and Dynamics*, Vol. 32, No. 4, 2009, Pages: 1269–1276. 107
- [Schaub *et al.* 1999] Schaub, H., Vadali, S.R., Junkins, J.L., & Alfriend, K.T., “Spacecraft Formation Control Using Mean Orbit Elements,” *Journal of the Astronautical Sciences*, Vol. 48, No. 1, 1999, Pages: 69–87. 11
- [Schweighart & Sedwick 2002] Schweighart, Samuel A., & Sedwick, Raymond J., “High-fidelity linearized J2 model for satellite formation flight,” *Journal of Guidance, Control, and Dynamics*, Vol. 25, No. 6, 2002, Pages: 1073–1080. 11
- [Shen & Tsiotras 1999] Shen, H., & Tsiotras, P., “Time-optimal control of axisymmetric rigid spacecraft using two controls,” *Journal of Guidance, Control, and Dynamics*, Vol. 22, No. 5, 1999, Pages: 682–694. 14
- [Shyu *et al.* 1998] Shyu, Kuo-Kai, Tsai, Yao-Wen, & Lai, Chiu-Keng, “Sliding mode control for mismatched uncertain systems,” *Electronics Letters*, Vol. 34, No. 24, 1998, Pages: 2359–2360. 80
- [Singh 1987] Singh, S.N., “Nonlinear adaptive attitude control of spacecraft,” *IEEE Transactions on Aerospace and Electronic Systems*, Vol. 23, No. 3, 1987, Pages: 371–379. 77

- [Slotine & Li 1991a] Slotine, J.J., & Li, W., *Applied Nonlinear Control*, Prentice-Hall, Upper Saddle River, NJ, 1991. 169
- [Slotine & Li 1991b] Slotine, J.J.E., & Li, W., *Applied Nonlinear Control*, Prentice-Hall, Upper Saddle River, NJ, 1991. 216
- [Smith 1995] Smith, H.F., “The First and Second Flights of the Small Expendable Deployer System (SEDS),” *Proceedings of the Fourth International Conference on Tethers in Space*, Science and Technology Corp., Hampton, VA, April 10-14, 1995, Pages: 43–55. 16
- [Sontag & Sussmann 1988] Sontag, E.D., & Sussmann, H.J., “Further comments on the stabilizability of the angular velocity of a rigid body,” *Systems and Control Letters*, Vol. 12, No. 3, 1988, Pages: 213–217. 14
- [Spurgeon & Davies 1993] Spurgeon, S.K., & Davies, R., “A nonlinear control strategy for robust sliding performance in the presence of unmatched uncertainty,” *International Journal of Control*, Vol. 57, No. 5, 1993, Pages: 1107 – 1123. 83, 176
- [Stansbery & Cloutier 2000] Stansbery, D.T., & Cloutier, J.R., “Nonlinear Control of Satellite Formation Flight,” *Proceedings of AIAA Guidance, Navigation, and Control Conference and Exhibit, AIAA-2000-4436*, Denver, CO, Aug 14-17, 2000. 12
- [Starin *et al.* 2001a] Starin, R.S., Yedavalli, R.K., & Sparks, A.G., “Design of a LQR controller of reduced inputs for multiple spacecraft formation flying,” *Proceedings of the American Control Conference*, Arlington, VA, Jun 25-27, 2001. 12
- [Starin *et al.* 2001b] Starin, R.S., Yedavalli, R.K., & Sparks, A.G., “Spacecraft formation flying maneuvers using linear-quadratic regulation with no radial axis inputs,” *AIAA Guidance, Navigation, and Control Conference and Exhibit, AIAA 2001-4029*, Montreal, Aug 6-9, 2001. 67
- [Sweeting *et al.* 2004] Sweeting, M.N., Hashida, Y., Bean, N.P., Hodgart, M.S., & Steyn, H., “CERISE microsatellite recovery from first detected collision in low Earth orbit,” *Acta Astronautica*, Vol. 55, No. 2, 2004, Pages: 139–147. 3

- [Tafazoli 2005] Tafazoli, S. “On attitude recovery of spacecraft using nonlinear control,” . PhD thesis, Concordia University, Montreal, Quebec, Canada, April 2005. 4, 5
- [Tandale & Valasek 2006] Tandale, Monish D., & Valasek, John, “Fault-Tolerant Structured Adaptive Model Inversion Control,” *Journal of Guidance, Control, and Dynamics*, Vol. 29, No. 3, 2006, Pages: 635–642. 13
- [Tomlin *et al.* 1995] Tomlin, D.D., Mowery, D.K., Musetti, B., & Cibrario, B., “TSS Mission 1 Flight Dynamics Anomalies,” *Proceedings of the Fourth International Conference on Tethers in Space*, Science and Technology Corp., Hampton, VA, April 10-14, 1995, Pages: 119–132. 16
- [Trivailo *et al.* 1999] Trivailo, P., Fujii, H.A., & Blanksby, C., “Safety Implications of Unscheduled Situations in the Operation of Tethered Satellite Systems from International Space Station,” *Acta Astronautica*, Vol. 44, No. 7, 1999, Pages: 701–707. 209, 222
- [Tschauner 1967] Tschauner, J., “Elliptic Orbit Rendezvous,” *AIAA Journal*, Vol. 5, No. 6, 1967, Pages: 1110–1113. 11
- [Tsiotras & Doumtchenko 2000] Tsiotras, P., & Doumtchenko, V., “Control of Spacecraft Subject to Actuator Failures: State-of-the-Art and Open Problems,” *Journal of the Astronautical Sciences*, Vol. 48, No. 2, 2000, Pages: 337–358. 14
- [Tsiotras *et al.* 1995] Tsiotras, P., Corless, M., & Longuski, J.M., “A novel approach to the attitude control of axisymmetric spacecraft,” *Automatica*, Vol. 31, No. 8, 1995, Pages: 1099–1112. 14
- [Tsiotras *et al.* 2001] Tsiotras, P., Shen, H., & Hall, C., “Satellite attitude control and power tracking with energy/momentum wheels,” *Journal of Guidance, Control, and Dynamics*, Vol. 24, No. 1, 2001, Pages: 23–34. 109
- [Tudoroiu & Khorasani 2007] Tudoroiu, N., & Khorasani, K., “Satellite Fault Diagnosis Using a Bank of Interacting Kalman Filters,” *IEEE Transactions on Aerospace and Electronic Systems*, Vol. 43, No. 4, 2007, Pages: 1334–1350. 13

- [Tyc & Han 1995] Tyc, G., & Han, R.P.S., “Attitude Dynamics Investigation of the OEDIPUS-A Tethered Rocket Payload,” *Journal of Spacecraft and Rockets*, Vol. 32, No. 1, 1995, Pages: 133–141. 16
- [Tyc *et al.* 1997] Tyc, G., Vigneron, F.R., Jablonski, A.M., Han, R.P.S., Modi, V.J., & Misra, A.K., “Flight Dynamics Results from the OEDIPUS-C Tether Mission,” *Proceedings of the AIAA/AAS Astrodynamics Conference*, AIAA Paper 96-3573, San Diego, CA, July 29-31, 1997, Pages: 39–50. 16
- [Vadali *et al.* 2008] Vadali, S.R., Sengupta, P., Yan, H., & Alfriend, K.T., “Fundamental frequencies of satellite relative motion and control of formations,” *Journal of Guidance, Control, and Dynamics*, Vol. 31, No. 5, 2008, Pages: 1239–1248. 12
- [Vadali 1986] Vadali, S.R., “Variable-structure control of spacecraft large-angle maneuvers,” *Journal of Guidance, Control, and Dynamics*, Vol. 9, No. 2, 1986, Pages: 235–239. 13
- [Vaddi & Vadali 2003] Vaddi, S.S., & Vadali, S.R., “Linear and Nonlinear Control Laws for Formation Flying,” *Advances in the Astronautical Sciences*, Vol. 114, No. 1, 2003, Pages: 171–188. 11
- [Vaddi *et al.* 2003] Vaddi, Sesha S., Vadali, Srinivas R., & Alfriend, Kyle T., “Formation flying: Accommodating nonlinearity and eccentricity perturbations,” *Journal of Guidance, Control, and Dynamics*, Vol. 26, No. 2, 2003, Pages: 214–223. 11
- [Vaddi 2003] Vaddi, V.V.S.S. “Modelling and control of satellite formations,” . PhD thesis, Texas A&M University, College Station, TX, May 2003. 34, 77
- [van Pelt 2009] van Pelt, M., *Space Tethers and Space Elevators*, Copernicus Books, New York, 2009. 15
- [Vassar & Sherwood 1985] Vassar, R.H., & Sherwood, R.B., “Formationkeeping of a pair of satellites in circular orbit,” *Journal of Guidance, Control, and Dynamics*, Vol. 8, No. 2, 1985, Pages: 235–242. 67

- [Vignal & Pernicka 2006] Vignal, Pierre, & Pernicka, Henry, “Low-thrust spacecraft formation keeping,” *Journal of Spacecraft and Rockets*, Vol. 43, No. 2, 2006, Pages: 466–475. 11
- [Wallsgrove & Akella 2005] Wallsgrove, R.J., & Akella, M.R., “Globally stabilizing saturated attitude control in the presence of bounded unknown disturbances,” *Journal of Guidance, Control, and Dynamics*, Vol. 28, No. 5, 2005, Pages: 957–963. 13
- [Wang & Zhang 2007] Wang, Zhaokui, & Zhang, Yulin, “Design and verification of a Robust formation keeping controller,” *Acta Astronautica*, Vol. 61, No. 7-8, 2007, Pages: 565–574. 63, 73
- [Wen & Kreutz-Delgado 1991] Wen, J.T.-Y., & Kreutz-Delgado, K., “The attitude control problem,” *IEEE Transactions on Automatic Control*, Vol. 36, No. 10, 1991, Pages: 1148–1162. 13
- [Wertz & Larson 1999] Wertz, J.R., & Larson, W.J., *Space Mission Analysis and Design*, Microcosm and Kluwer, New York, NY, 3rd édition, 1999. 189
- [Wie 1998] Wie, B., *Space Vehicle Dynamics and Control*, AIAA Inc., Reston, VA, 1998. 111, 170, 189
- [Williams *et al.* 2003] Williams, P., Blanksby, C., Trivailo, P., Fujii, H.A., & Kojima, H., “Dynamics and Control of Platform-Supported-Two-Tether-Subsatellite System,” *Proceedings of the 10th JRS/AAS/CSA Symposium, International Conference of Pacific Basin Societies (ISCOPS), AAS 03-378*, Vol. 117, Tokyo, Japan, December 10-12, 2003, Pages: 245–264. 209, 222
- [Won & Ahn 2003] Won, Chang-Hee, & Ahn, Hyo-Sung, “Nonlinear orbital dynamic equations and state-dependent riccati equation control of formation flying satellites,” *Journal of the Astronautical Sciences*, Vol. 51, No. 4, 2003, Pages: 433–449. 12
- [Wong *et al.* 2002] Wong, Hong, Kapila, Vikram, & Sparks, Andrew G., “Adaptive output feedback tracking control of spacecraft formation,” *International Journal of Robust and Nonlinear Control*, Vol. 12, No. 2-3, 2002, Pages: 117–139. 12

- [Xing & Parvez 2001] Xing, G.Q., & Parvez, S.A., “Nonlinear attitude state tracking control for Spacecraft,” *Journal of Guidance, Control, and Dynamics*, Vol. 24, No. 3, 2001, Pages: 624–626. 13
- [Xing *et al.* 2007] Xing, Jian-Jun, Tang, Guo-Jin, Xi, Ao-Ning, & Li, Hai-Yang, “Satellite formation design and optimal stationkeeping considering nonlinearity and eccentricity,” *Journal of Guidance, Control, and Dynamics*, Vol. 30, No. 5, 2007, Pages: 1523–1528. 11
- [Xiong *et al.* 2002] Xiong, J., Zhou, Z., Ye, X., Wang, X., Feng, Y., & Li, Y., “A colloid micro-thruster system,” *Microelectronic Engineering*, Vol. 61-62, 2002, Pages: 1031–1037. 200
- [Xu *et al.* 2007] Xu, Yunjun, Fitz-Coy, Norman, Lind, Rick, & Tatsch, Andrew, “ μ Control for satellites formation flying,” *Journal of Aerospace Engineering*, Vol. 20, No. 1, 2007, Pages: 10–21. 11
- [Yan *et al.* 2000] Yan, Qiguo, Yang, Guang, Kapila, Vikram, & de Queiroz, Marcio S., “Nonlinear dynamics and output feedback control of multiple spacecraft in elliptical orbits,” *Proceedings of the American Control Conference*, Vol. 2, Chicago, IL, Jun 28-30, 2000, Pages: 839–843. 11
- [Yan *et al.* 2009] Yan, Hui, Alfriend, Kyle T., Vadali, Srinivas R., & Sengupta, Prasenjit, “Optimal design of satellite formation relative motion orbits using least-squares methods,” *Journal of Guidance, Control, and Dynamics*, Vol. 32, No. 2, 2009, Pages: 599–604. 36
- [Yeh *et al.* 2002] Yeh, Hsi-Han, Nelson, Eric, & Sparks, Andrew, “Nonlinear tracking control for satellite formations,” *Journal of Guidance, Control, and Dynamics*, Vol. 25, No. 2, 2002, Pages: 376–386. 12, 63, 73
- [Yuqiang *et al.* 1998] Yuqiang, Wu, Xinghuo, Yu, & Zhihong, Man, “Terminal sliding mode control design for uncertain dynamic systems,” *Systems and Control Letters*, Vol. 34, No. 5, 1998, Pages: 281–287. 49

- [Zedd 1997] Zedd, M.F., “Experiments in Tether Dynamics Planned for ATEX’s Flight,” *Proceedings of the AAS/AIAA Astrodynamics Conference, AAS 97-601*, Vol. 97, Sun Valley, ID, August 4-7, 1997, Pages: 25–44. 16
- [Zhihong *et al.* 1994] Zhihong, Man, Paplinski, A.P., & Wu, H.R., “Robust MIMO terminal sliding mode control scheme for rigid robotic manipulators,” *IEEE Transactions on Automatic Control*, Vol. 39, No. 12, 1994, Pages: 2464 – 2469. 49
- [Zohdy *et al.* 1992] Zohdy, M., Fadali, M.S., & Liu, J., “Variable structure control using system decomposition,” *IEEE Transactions on Automatic Control*, Vol. 37, No. 10, 1992, Pages: 1514–1517. 70